Search for the Higgs boson produced in association with a Z boson and decaying to a pair of bottom quarks with the ATLAS experiment at LHC

Lion Alio

CPPM-T-2014-04

AIX-MARSEILLE UNIVERSITÉ
Faculté Des Sciences
163, avenue de Luminy
13288 Marseille cedex 09

THÈSE DE DOCTORAT

Spécialité : Physiques et Sciences de la Matière
présentée par

Lion ALIO

en vue d'obtenir le grade de docteur d'Aix-Marseille Université

Search for the Higgs boson produced in association with a Z boson and decaying to a pair of bottom quarks with the ATLAS experiment at LHC

Soutenue le 12/11/2014 devant le jury composé de :

Dr.	Isabelle RIPP-BAUDOT	Rapporteur
Dr.	Song-Ming WANG	Rapporteur
Dr.	Eric KAJFASZ	Examinateur, président du jury
Prof.	Gordon WATTS	Examinateur
Dr.	Laurent VACAVANT	Directeur de thèse
Dr.	Yann COADOU	Co-directeur de thèse

To my family,

Acknowledgements

First of all, I want to express my best gratitude to Laurent Vacavant. Thank you infinitely for your patience, your invaluable help and your great knowledge that followed me since my Master 2 and years of PhD. It's my greatest pleasure to work with you and in ATLAS group at CPPM.

My most sincere gratitudes goes next for Yann Coadou, my co-supervisor. I cannot express enough my thanks for your unconditionally help, your support, your patience, your kindness. All of your advices always guide me, they will follow me to my future.

A great thanks for my reviewers, Song-Ming Wang and Isabelle Ripp-Baudot, for the work you have been accomplished for your corrections and suggestions. Thank you Eric Kajfasz, the director of CPPM, for creating a great and friendly environment for researcher and PhD students to work with, and participate in my committee as my examiner. I also express my thanks to my second examiner , Pr. Gordon Watts, to give me many advices and suggestions.

An immense thanks to the "Japanese trio": Yoshikazu Nagai, Kazuya Mociduki and Kenji Kiuchi. It was my pleasure to works with you in the Higgs search group. A special thanks to Yoshikazu, in the past 3 years you seemed to be my "unofficial" supervisor in many subjects and aspects. I appreciate very much the invaluable helps from Kenji. And a great thanks to Kazuya, for his helps in many technical problems, I wish you have a good continuation in our ATLAS group at CPPM.

I express my gratefulness for the great helps from members of Higgs search group in ATLAS Collaboration, especially Daniel Buescher and Nicholas Morange, for their outstanding helps in some technical details, that lead me to reach the end of the analysis. A big thank to David Jamin and other members in Academia Sinica group, with their great help to achieve our analysis. I also thank the other Higgs group members, Jean Francois Grivaz, Paolo Francavilla, the Higgs conveners and others, who give me many valuable advices and give me chances to communicate and learn many things. A great cheers to all for delivering a great works on Higgs search that have come fruitful. It's my pleasure to work with such an outstanding group, thank you for everything and wish you the best to continue your research.

Thank you for my senior colleagues in CPPM: George Add, Steve Muanza, Fabrice Hubaut, Emmanuelle Monnier, Alexander Rozanov, Emmanuel le Guirrec, Edith Knoops... for many advices and suggestions during 3 years of my thesis. I also appreciate the supports from other people at CPPM, who did their best to deliver a good and comfortable working environment. It is my honor to work and contribute in such a great research center with such kind people.

It is a pleasure to mention my fellow PhD students and friends at CPPM for giving your great helps and supports, for following together through the life of PhD. I miss all the funs

we have together: coffees, travels, dinners, jokes... that we've enjoyed the past three years. I want to thank Nicolas, Nancy, Emilie, Mathieu, Thomas, Michael, Elodie, Carine, Margaux, Raymond, Aurore, Fanny, and many other PhD students. I wish you luck and all the best to your future career.

Last but not least, my family also contribute great supports for my thesis. My great thanks for my parents, Y Trou and Huong, my sisters, Elaine and Thuy, and especially my wife, Huong, who is always with me all the time toward the end.

Contents

Introduction

All kinds of visible matter in the Universe are well-described by the so-called Standard Model of particle physics, which describes the elementary components of matter as well as their interactions. Over four decades, a wonderful theoretical description was built, and all its predictions were proven by various experiments in the world with high accuracy. However, the Standard Model is not renormalizable if particles have mass, which is already proven. A possible solution to solve this problem in the Standard Model context is to assume that the masses of particles are generated by the existence of the Higgs mechanism. This mechanism predicts the existence of a new boson in the Standard Model: the Higgs boson, whose mass is not predicted by theory and has to be determined experimentally. The Higgs boson is a puzzle piece that is need to complete the description of the Standard Model of particles.

The search for the Higgs boson was carried out by various experiments: at LEP in the 90s decade of the last century, at the Tevatron from the end of 80s till 2011, and at the LHC since 2010. The Higgs boson search is divided into various channels based on its production and decay channels. A major breakthrough occured in 2012 when the ATLAS and CMS experiments at LHC found the Higgs boson through its decays to bosons ($H \to \gamma\gamma$, $H \to Z^*Z$, $H \to WW^*$) at a mass of $\sim$125 GeV. This thesis will focus on the search for the Higgs boson in the channel where the Higgs boson decays to a pair of b-quarks and is produced in association with a Z boson decaying to two neutrinos. The Higgs mechanism, the constraints for the existence of Higgs boson and its discovery will be reviewed in the first chapter.

The data collected in the proton-proton collisions at the LHC in the year of 2012 are used for this search. The center-of-mass energy of the collisions is 8 TeV. This thesis uses the data collected from the ATLAS detector. The detailed descriptions of LHC and ATLAS detector, as well as their operation will be found in the second chapter.

The $ZH \to \nu\bar{\nu}b\bar{b}$ channel contains a pair of b-quarks and two neutrinos in the final state. The two neutrinos go through without being detected, leaving missing transverse energy in the detector. The two b-quarks will form jets in the detector. Thus identifying jets originating from b-quarks is vital for this analysis. This technique is referred to as b-tagging. The details of b-tagging algorithms and how to apply them to this Higgs analysis will be discussed in the third chapter.

The work on the missing transverse energy measurements and its triggers is also important as this will help identifying the events that contain Z decays to two neutrinos and help reducing the backgrounds. In this work a new missing transverse energy trigger for the Higgs boson search will be studied, along with the other already existing triggers, and it is expected to increase the sensitivity of the Higgs boson search. The chapter four will detail the trigger

parametrization, as well as application of missing transverse energy triggers in the Higgs analysis in the $ZH \to \nu\bar{\nu}b\bar{b}$ channel.

Finally, the detailed analysis of the search of Higgs boson in the $ZH \to \nu\bar{\nu}b\bar{b}$ channel will be discussed in chapter five. We will go through various steps of the analysis: object identification and selection, modelling and reduction of the backgrounds, as well as estimating the systematic uncertainties. We will study the effect of the new missing transverse energy trigger on the search for the Higgs boson.

Chapter 1

Theory context

1.1 Standard Model of Particle Physics

Since the beginning of the twentieth century, physics has witnessed huge achievements in many aspects, with the birth of the two grand pillars: General Relativity and Quantum Mechanics. The former shows a good prediction of the macroscopic universe (such as the dynamic of galaxies) while the latter describes well the microscopic world (such as the atomic world) with high accuracy. Quantum Mechanics was developped in early 20th century by Shrödinger [1], Heisenberg, Born [2], Planck, etc... for the non-relativistic formulation. The relativistic version of Quantum Mechanics was completed by Dirac [3], which lead to the prediction of anti-particles. Quantum Mechanics (non-relativistic or relativistic) can only describe one particle, later developments of quantum theory included fields, and is usually referred to as Quantum Field Theory. This theory can also depict interactions in sub-atomic physics, such as Quantum Electrodynamics (QED), which was researched by Feynman, Schwinger and Tomonaga [4–6], the theory of weak interaction, proposed early by Fermi [7], later developed and unified with the electromagnetic interaction (usually referred to as Electro-Weak unification) by Glashow, Salam and Weinberg [8–10]. The theory of Quantum Chromodynamics (QCD) for strong interactions was completed by the work of Wilson in confinement of quarks [11] and Gross, Wilczek and Politzer in asymptotic freedom [12–14].

In parallel with the development of Quantum Field Theory and theories of fundamental interactions, the discovery of elementary particles also obtained huge achievements. The baryons and mesons are found (p, n are examples of baryons, and $\pi^{\pm}$, $K^{\pm}$ are mesons), and can be grouped in an *eightfold way*, developed by Gell-Mann, Ne'eman and Nishijima [15]. This lead to the birth of the quark model of particles, proposed by Gell-Mann and Zweig [16, 17], which predicted that the baryons and mesons are composed of quarks. The baryons and mesons discovered at that time needed the existence of three quarks, however the Glashow–Iliopoulos–Maiani mechanism [18] predicted the existence of a fourth quark, called *charm* quark (or c-quark), later discovered at SLAC and BNL [19, 20]. Moreover, the observation of CP violation by Cronin and Fitch [21] can only be explained with the presence of another two quarks, which was theorized by Kobayashi and Maskawa [22]. The two quarks were named bottom (or beauty) and top (notation b and t, respectively), and both particles were discovered at Fermilab [23–25]. Last but not least, the observation of weak bosons at CERN [26, 27] confirmed the theory prediction of weak interaction.

All the achievements of theories of elementary particle physics together with Quantum Field Theory, forms the Standard Model (SM) of particle physics nowadays. Most of the experimental data are well predicted with high precision using this model, making it one of the well-established theories in history. However, the Standard Model is still missing the piece to complete the Electro-Weak picture: the Higgs boson. With the presence of Higgs boson, the puzzle of Spontaneous Symmetry Breaking in Electro Weak theory will be resolved in the SM. These problem will be discussed in this chapter.

We will begin with a brief introduction to elementary particles in section 1.1.1 and their interactions in 1.1.2. The formulation of Standard Model will be described in 1.1.3. Then, the Higgs mechanism will be discussed in 1.2, the experimental limits in 1.3, and its discovery at LHC in 1.3.4.

1.1.1 Particle hierarchy in the Standard Model

The Standard Model includes three types of interaction: electromagnetic, weak and strong interactions. A fourth interaction is at play in nature, gravitation, but the gravitational interaction is not included in the Standard Model but in General Relativity context (which will not be discussed here).

Fermions are particles of spin one-half, which obey the Fermi-Dirac statistic. These particles are the elemental components which form all of observed matter. The fermions in the SM can be divided into two categories:

- **Quarks**: There are six quarks discovered as introduced earlier which are named: *up* (u), *down* (d), *charm* (c), *strange* (s), *top* (t), *bottom or beauty* (b). Quarks cannot be observed in free states, they can only be seen in their compound states of hadrons. There are two types of hadrons: baryons, which are formed by three quarks and mesons formed by a quark-antiquark pair. Quarks have *color*, which characterizes their strong interaction.

- **Leptons**: There are also six leptons discovered: three charged leptons *electron* (e), *muon* (μ) and *tau* (τ), along with their associated neutrinos ν_e, ν_μ, ν_τ which possess very small masses. Unlike quarks, leptons have no color.

Quarks can exchange strong interaction with other quarks thanks to their instrinsic color. They can also interact with each other via weak and electromagnetic forces. Leptons cannot have strong interaction since they do not have color but they interact with other particles via electromagnetic and weak interactions except the neutrinos, which can only exchange weak force.

The quarks and leptons, as well as their characteristics, are summarized in Table 1.1. All fermions have their own anti-fermions with the same mass and spin but with opposite charges. We can list the fermions into 3 generations, with each generation containing two quarks with different charge, a charged lepton and its associated neutrino, for example: the first generation will contain u, d, e and ν_e. From the first generation to others, the masses of fermions increase, which suggests us that the first generation is the most stable, and in result most of the observed matter in the universe is composed by those fermions. The fermions of higher generations can only be observed in the astroparticle phenomena or in particle collisions.

Fermions	1st generation		2nd generation		3rd generation		Electric charge	L	B
	Name	Mass [GeV]	Name	Mass [GeV]	Name	Mass [GeV]			
Quarks	u	2.3×10^{-3}	c	1.28	t	173.5	2/3	0	1
	d	4.8×10^{-3}	s	95.5×10^{-3}	b	4.18	$-1/3$	0	1
Leptons	e	0.5×10^{-3}	μ	105.7×10^{-3}	τ	1.77	-1	1	0
	ν_e	$< 2 \times 10^{-9}$	ν_μ	$< 0.19 \times 10^{-6}$	ν_τ	$< 18.2 \times 10^{-6}$	0	1	0

Table 1.1: Quarks and leptons categorized in three generations with their corresponding masses, charges, number of lepton (L) and baryon (B). Quarks masses are masses of the "bare" quarks. The anti-particles associated with each fermion have opposite charge [28]. The details of neutrino masses can be found in Ref. [29].

1.1.2 Bosons and interactions

Bosons are particles with integer spin and they obey the Bose-Einstein statistic. All interactions among fermions in the Standard Model are governed by bosons as follows:

- **Electromagnetism** (EM): mediated by the photon, denoted by γ, also known as the particle of light. This particle is massless and stable, therefore it has infinite range. All fermions with non-zero electric charge can interact with the others via electromagnetic interaction. One example of this interaction is the movement of electron around the atomic nucleus.
- **Weak interaction**: All fermions in the Standard Model are affected by the weak force via the exchange of $W^{\pm}$ bosons with charge ±1 and Z boson with neutral charge. Unlike the photon, all weak bosons are heavy, therefore the range of weak interaction is finite and short. An example for this interaction is the radioactive β decay of neutron to proton, electron, and anti-neutrino.
- **Strong interaction**: This type of interaction is mediated by eight gluons and it exchanges color between quarks and gluons. This is the interaction responsible for quark confinement. Although all the gluons are massless, their interaction range is finite. The strong interaction is observed via the bond among the protons and neutrons inside the nucleus, and jet creation in particle detectors.

Table 1.2 summarizes some details of each interaction. In Quantum Field Theory, like the other interactions, gravitation is supposed to have its own quanta, called graviton with zero mass, zero charge and spin 2. Nevertheless such particles have not been detected yet by experiments. Moreover the strength of gravitation is extremely small compared to other interactions in SM (10^{25} times smaller than the weak interaction). Thus in the Standard Model context, gravitation is alway neglected.

1.1.3 Formulation of Standard Model

The interactions in the Standard Model can be described by symmetry groups based on Quantum Field Theory and gauge symmetry [30]:

$$SU(3)_c \otimes SU(2)_L \otimes U(1)_Y$$

Interaction	Boson	Spin	Mass [GeV]	Relative Strength	Range [m]
Strong	8 gluons	1	0	1	10^{-15}
Electromagnetic	γ	1	0	10^{-2}	∞
Weak	$W^{\pm}$, Z	1	80.4, 91.2	10^{-13}	10^{-18}
Gravitation	graviton (?)	2	0	10^{-38}	∞

Table 1.2: The fundamental interactions in SM and some properties of their mediator bosons [28]. The gravitation is not included in SM but it is still counted as fundamental interaction.

- $U(1)_Y$: group of hypercharge, characterized by the quantum number Y
- $SU(2)_L$: Group of isospin in weak interaction, which affects only the left-handed particles, characterized by two weak-isospin quantum numbers: T and T_3
- $SU(3)_c$: Symmetry group that describes the strong interaction and Quantum Chromodynamics (QCD). The notation c refers to the color exchange between quarks and gluons.

All fermions and bosons are supposed to have zero mass so that the Standard Model is a renormalizable theory[1]. However the experimental results show that quarks, charged leptons and weak bosons have mass. A solution for this issue is the Higgs mechanism, which will be discussed later.

In theory, one can represent the interactions of particles in SM using Quantum Field Theory by introducing the Lagrangian:

$$\mathcal{L}_{SM} = \mathcal{L}_{bosons} + \mathcal{L}_{fermions} + \mathcal{L}_{Higgs} + \mathcal{L}_{Yukawa}$$

The $\mathcal{L}_{bosons}$ represents the gauge bosons with their self-interactions and field strengths. The term $\mathcal{L}_{fermions}$ represents the kinematics of fermions, as well as the interaction between fermions and gauge bosons. $\mathcal{L}_{Higgs}$ shows the Higgs field (described in section 1.2.5) and $\mathcal{L}_{Yukawa}$ describes the Yukawa interactions, which generate masses of fermions. All of these terms are detailed in the next section.

1.2 Higgs mechanism

1.2.1 Electroweak unification

The Electroweak theory unifies the electromagnetic and weak interactions. The theory is based on the symmetry group $SU(2)_L \times U(1)_Y$. This unification requires that two leptons in the same family must be arranged in the same representation of the group (for example e and ν_e). The three families of leptons are organized as doublets represented as:

$$\begin{pmatrix} e \\ \nu_e \end{pmatrix} \begin{pmatrix} \mu \\ \nu_\mu \end{pmatrix} \begin{pmatrix} \tau \\ \nu_\tau \end{pmatrix}$$

[1]The renormalization is the procedure that removes the divergences in theoretical calculation [31].

However, we can observe the disparity between the leptons in each doublet: while e, μ, τ have mass, the neutrinos are massless in the SM[2]. Plus, the theory predicted the 4 bosons associated to the group $SU(2)_L \times U(1)_Y$ are massless, in contradiction to experimental results, which observed the weak bosons are massive (shown in Table 1.2). The most accepted explanation for these paradoxes is the Higgs mechanism, which will be discussed in the next section.

1.2.2 The Higgs mechanism

The Higgs mechanism introduces a boson field with non-zero weak isospin and weak hypercharge interacting with particles (boson and fermions). This mechanism is used to explain the masses of fermions and weak bosons [33–35]. This field is in fact a complex doublet of scalar fields:

$$\Phi = \begin{pmatrix} \Phi^+ \\ \Phi_0 \end{pmatrix} \tag{1.1}$$

The Lagrangian of this field is written in the form:

$$\mathcal{L} = (\mathcal{D}_\mu \Phi)^\dagger (\mathcal{D}^\mu \Phi) - V(\Phi^\dagger \Phi) \tag{1.2}$$

$$V(\Phi^\dagger \Phi) = \mu^2 \Phi^\dagger \Phi + \lambda (\Phi^\dagger \Phi)^2 \tag{1.3}$$

- The first term in the Lagrangian denotes the kinematic part of the field, which contains the interaction between the field Φ and gauge bosons of the group $SU(2)_L \times U(1)_Y$. $\mathcal{D}_\mu$ is the covariant derivative needed for local gauge invariance under the transformation of the group:

$$\mathcal{D}_\mu = \partial_\mu + ig\frac{\tau^a}{2}W_\mu^i + ig^{'}\frac{Y}{2}\frac{\tau^a}{2}B_\mu, \tag{1.4}$$

  where the bosons $W^{\mu i}(i = 1, 2, 3)$ are the bosons of group $SU(2)_L$ with coupling constant g and group generators τ^a (Pauli matrices), B_μ is the boson of group $U(1)_Y$ with coupling constant $g^{'}$ and Y is the hypercharge.

- The second term in the Lagrangian is the potential of the field Φ. This term is invariant under the gauge transformation $SU(2)_L$. The term μ^2 can be understood as mass of the field Φ, and λ is considered as the self-coupling of the field Φ, λ must be larger than 0 so that the self-coupling term of the potential is bounded.

With this choice of kinematic term and potential term, the Lagrangian of the field Φ is invariant under the group transformation $SU(2)_L \times U(1)_L$.

There are two possibilities of the term μ^2 that can alter the behavior of the potential $V(\Phi^\dagger \Phi)$:

- $\mu^2 > 0$: The potential V has a paraboloic shape and the equilibrium state where $V = 0$ can only be found at Φ=0. We can also say that there is only one VEV (*vacuum expectation value*). The potential is symmetric, and no symmetry breaking is observed.

[2]Neutrinos actually have mass but very small [32]. There is no proven mechanism to generate their mass yet.

- $\mu^2 < 0$: Now the potential V has a form of "Mexican hat" and the equilibrium state of V can be located anywhere as long as the value of the field satisfies $\langle \Phi_{VEV} \rangle = -\frac{\mu^2}{2\lambda}$ (Fig. 1.1). In this case we say that the symmetry is broken (spontaneous symmetry breaking).

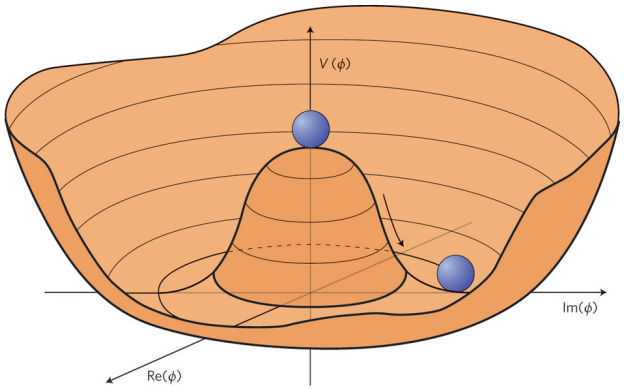

Figure 1.1: The shape of potential $V(\Phi)$ in the complex plane of Φ for the case $\mu^2 < 0$.

Generally we can choose a specific solution of Φ as the following:

$$\Phi = \begin{pmatrix} 0 \\ \frac{\nu}{\sqrt{2}} \end{pmatrix}$$

where $\nu = \frac{\sqrt{-\mu^2}}{\lambda}$.

One example for spontaneous symmetry breaking is in ferromagetism: For ferromagnetic material, it is invariant under the spatial rotations. The considered parameter is the magnetic polarization. Above the Curie temperature, this parameter is zero, so no magnetic polarization and the symmetry is conserved. Under the Curie temperature, the polarization is non-vanishing, causing the magnetization to point to a certain direction. The rotation along this direction is symmetric while the other rotations are spontaneously broken.

1.2.3 Masses of weak bosons

Developing the Φ_{VEV} around the minimun of V, we rewrite:

$$\Phi_{VEV} = \frac{1}{\sqrt{2}} \begin{pmatrix} 0 \\ \nu + H \end{pmatrix} \tag{1.5}$$

where H is the Higgs field in vacuum. Then we can replace the field in eq. 1.5 into the expression of eq. 1.2 using the covariant derivative in eq. 1.4. Considering the mass terms in the Lagrangian[3] we obtain:

$$\mathcal{L}_{mass} = \frac{g^2\nu^2}{4} W^+W^- + \frac{g^2 + g'^2}{8} \frac{(gW^3 - g'B)^2}{\sqrt{g^2 + g'^2}} - \mu^2|H|^2 \tag{1.6}$$

[3]the mass term in Lagrangian has the form $\frac{1}{2}m^2\phi^\dagger\phi$

with $W^{\pm} = \frac{1}{\sqrt{2}}(W^1 \pm iW^2)$. The bosons W^3 and B can also be represented by introducing Z and γ:

$$\begin{pmatrix} \gamma \\ Z \end{pmatrix} = \begin{pmatrix} \cos\theta_W & \sin\theta_W \\ -\sin\theta_W & \cos\theta_W \end{pmatrix} \begin{pmatrix} B \\ W^3 \end{pmatrix} \tag{1.7}$$

Here, we introduce the Weinberg angle θ_W with $\cos\theta_W = \frac{g}{\sqrt{g^2+g'^2}}$. Experimental results show the value $\sin\theta_W \approx 0.23$ [28].

Applying the representation of (γ, Z) of equation 1.7 in equation 1.6, we can observe the mass associated with each boson by identifing:

$$M_W = \frac{g\nu}{2},\ M_Z = \frac{\sqrt{g^2+g'^2}\nu}{2},\ M_\gamma = 0,\ M_H = \sqrt{-2\mu^2}.$$

The $W^{\pm}$ bosons only couple with the left-handed fermions, while the Z boson and γ can be coupled with both left-handed and right-handed fermions.

1.2.4 Masses of fermions

The spontaneous symmetry breaking generated masses of weak bosons, but it takes no responsibility for masses of fermions. They are from the interactions between fermion fields and Higgs field described by the Yukawa Lagrangian:

$$\mathcal{L}_{Yukawa} = C_f \bar{\Psi}_L \Phi \Psi_R + \text{Hermitian conjugate terms} \tag{1.8}$$

where Ψ_L and Ψ_R are left-handed doublet and right-handed singlet fermion fields, respectively. C_f is the Yukawa coupling constant to the fermion field f. This form of Lagrangian is invariant under the transformation of $SU(2)_L \times U(1)_Y$. The mass of fermion is proportional to the Yukawa coupling:

$$M_f = \frac{C_f \nu}{\sqrt{2}}.$$

The SM contains 3 generations of quarks so the Yukawa coupling constant must be 3×3 matrices in the interaction eigenstates and these matrices are not necessarily diagonal. However we need the diagonal matrices since the physical particles (which correspond to mass eigenstates) are needed. Therefore a transformation that changes those coupling constants from the interaction eigenstates to the mass eigenstates is required, and of course, this transformation must be a unitary matrix and mixes 3 generations of quarks. This matrix is called the Cabibbo-Kobayashi-Maskawa (CKM) matrix V^{CKM} [22, 36]:

$$V^{CKM} = \begin{pmatrix} V_{ud} & V_{us} & V_{ub} \\ V_{cd} & V_{cs} & V_{cb} \\ V_{td} & V_{ts} & V_{tb} \end{pmatrix} \tag{1.9}$$

and the transformation between the interaction eigenstates and mass eigenstates of quarks can be written as:

$$q'^i = V_{ij}^{CKM} q^j$$

where q'^i is the quark vector in weak interaction eigenstates, and q^j is the vector in mass eigenstates, i, j is the index of quark (u, d, etc...). The CKM matrix also tells us the

probability of quark transition from a quark to another quark via weak force exchange, which is proportional to $|V_{ij}|^2$. Each element V_{ij}^{CKM} in the CKM matrix represents the coupling constant of the charged weak current to quarks i and j. The CKM matrix can also be parametrized using different constraints in SM, with three mixing angles and one complex phase. This phase is needed to explain the CP-violation discovered in kaon-system [21]. Currently the best value of *magnitude* of each element of CKM matrix[4] is [28]:

$$\begin{bmatrix} |V_{ud}| & |V_{us}| & |V_{ub}| \\ |V_{cd}| & |V_{cs}| & |V_{cb}| \\ |V_{td}| & |V_{ts}| & |V_{tb}| \end{bmatrix} = \begin{bmatrix} 0.97427 \pm 0.00015 & 0.22534 \pm 0.00065 & 0.00351^{+0.00015}_{-0.00014} \\ 0.22520 \pm 0.00065 & 0.97344 \pm 0.00016 & 0.0412^{+0.0011}_{-0.0005} \\ 0.00867^{+0.00029}_{-0.00031} & 0.0404^{+0.0011}_{-0.0005} & 0.999146^{+0.000021}_{-0.000046} \end{bmatrix}.$$

From these values, one can observe that the top quark decays almost 100% to b quark and W boson. The matrix is almost diagonal.

The existence of neutrino masses suggests that a similar version of CKM matrix should be applied for the lepton sector,which is so-called Pontecorvo-Maki-Nakagawa-Sakata (PMNS) matrix [37, 38].

1.2.5 The Higgs boson

The Higgs boson associated to the Higgs field in Higgs mechanism is expected to exist. This is the consequence from the Goldstone theorem [39], which predicts the existence of the massive scalar field after the symmetry breaking of the gauge group $SU(2)_L \times U(1)_Y$. This boson is spin 0.

Take a look again in the Lagrangian of eq. 1.2, considering only the Higgs field and note that ν is constant, it can be written as:

$$\mathcal{L} = |\partial_\mu H|^2 - \mu^2 \frac{(\nu + H)^2}{2} - \lambda \frac{(\nu + H)^4}{4}$$

Expanding the last two terms in the Lagrangian, then we obtain the mass terms of the Higgs:

$$M_H = \frac{1}{2}(-\mu^2)H^2,$$

and the self-interaction of Higgs field:

$$\frac{\mu^2}{\lambda}H^3 + \frac{\mu^2}{4\nu^2}H^4.$$

The value of μ^2 has to be negative so that the symmetry breaking can happen, however its value is still needed to be determined. And in the SM context, this value is not predicted. Searches could put limits on the Higgs mass, allowing us to specify the regions where the Higgs mass is discoverable. The hunt is now over, as we will discuss later.

[4] These values are obtained from global fit in SM.

1.2.6 Summary

All discovered particles (fermions and bosons) are categorized as in Figure 1.2, classifying the generations of fermions and some of their characteristics (mass, spin, charge). The particles in the first generation are the most stable and they compose most of the observed matter in the universe (for example, atoms contain electrons moving around the nucleus which is formed by protons and neutrons, which are composed internally by up and down quarks). The particles in second and third generations possess much higher masses than those in the first generation, therefore they are likely to decay to the first generation within a very short lifetime and can only be observed in high-energy experiments. The neutrinos are supposed to have zero mass and cannot change their flavor in the Standard Model. However the discovery of neutrino oscillations proved that neutrinos must have non-zero mass, and from experimental constraints, these masses are very small.

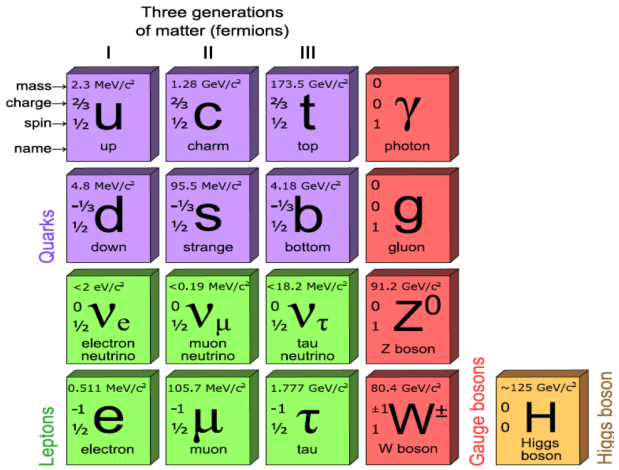

Figure 1.2: Particle hierarchy in Standard Model with their characteristics.

There are three fundamental interactions mediated by 12 bosons (1 γ for EM, 3 weak bosons ($W^{\pm}, Z$) for weak force and 8 gluons for strong interaction) in SM. Quarks can exchange all types of interaction, and leptons cannot have strong interaction as they have no color. The bosons must have no mass in order to have gauge invariance, nevertheless the weak bosons are observed with heavy mass, which can be explained by the spontaneous symmetry breaking of the Electro-Weak symmetry. This phenomenon predicts the existence of the Higgs boson, which also generates masses for all fermions in the SM.

1.3 Search for the Higgs boson

As we have seen in section 1.2, after the spontaneous symmetry breaking, masses of particles in the Standard Model can be generated by introducing the Higgs mechanism. However the mass of the Higgs boson is determined by an arbitrary parameter μ^2, and in the Standard Model context, this parameter is unknown by the theory. The experimental search was recently performed at LEP, HERA, and Tevatron afterwards. Currently the Higgs search is continued at the LHC.

1.3.1 Theoretical constraints

The Higgs mass is not predicted in the SM, however the theoretical calculations can be used to derive limits. All the Higgs mass constraints are based on the equation of renormalisation group. We will not go through the detailed calculations here, those works can be found in [40, 41].

The results of these calculations can be summarized in Figure 1.3. The allowed region for the existence of the Higgs boson is between the limit of pertubative regime and the vacuum stability. From this constraint, if we search for the Higgs boson at TeV scale, the Higgs boson mass is allowed in the range of $50 < M_H < 800$ GeV.

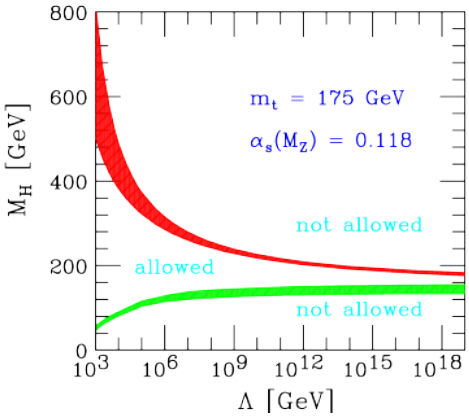

Figure 1.3: Theory constraint of Higgs mass as a function of energy scale Λ. The red line is the limit from pertubative regime and the green line is the limit of vacuum stability. The allowed Higgs region is between the red and green lines [41].

1.3.2 Direct experimental constraints

The experimental constraints on the Higgs mass were obtained by particle colliders: LEP, Tevatron.

LEP was an e^+e^- collider at center-of-mass energy of 209 GeV maximum, operated for over ten years from 1989 to 2000 with an integrated luminosity of 2.5 fb^{-1}. LEP searched for the Higgs boson in $e^+e^- \to Z^* \to ZH$. The data collected from LEP allowed to put a lower limit on the Higgs mass with 95% of confidence level at 114.4 GeV [42].

The Tevatron used proton-antiproton collisions with energy at center-of-mass 1.96 TeV to perform its Higgs search. The Higgs search was composed from several production and decay modes. The data collected showed the exclusion of Higgs mass in range of $90 < m_H < 109$ GeV and $149 < m_H < 182$ GeV using the Higgs boson decays to $b\bar{b}, WW^*, ZZ^*$, $\tau\tau, \gamma\gamma$ depending on the production mode (Fig. 1.4) [43].

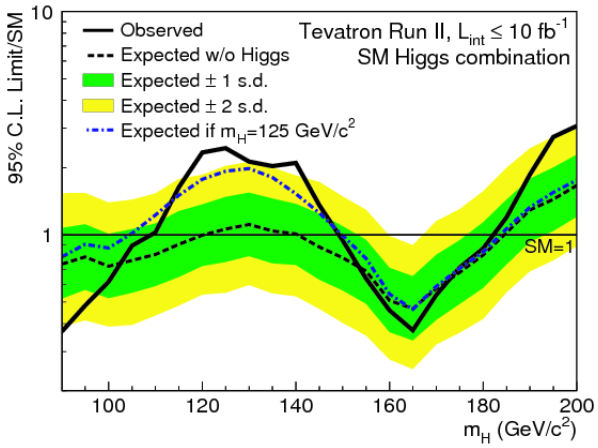

Figure 1.4: The limit of SM Higgs boson production at Tevatron with 95% confidence level. The regions where CL < 1 are excluded [43].

1.3.3 Indirect experimental constraints

The indirect constraints are used as complementary to direct constraints of Higgs search based on quantum properties of particle physics. One method uses the mass of $W^{\pm}$ boson and top quark to put limits on the Higgs mass. The corrections of $W^{\pm}$ boson mass depend on Higgs mass logarithmically. Figure 1.5 shows that a small variation on $W^{\pm}$ boson mass can cause a large deviation of Higgs mass, and constrains the region where the Higgs mass is allowed.

Another constraint method that is still using the previous electroweak parameters dependence on Higgs mass is the difference of χ^2 between the theoretical prediction and measurements, the $\Delta\chi^2$ (this constraint is only available for SM Higgs boson). Figure 1.6 shows that the most probable value of Higgs mass (the minimum $\Delta\chi^2$) is 90^{+35}_{-26} at 68% CL. The upper limit of the Higgs is found at $m_H = 158$ GeV at 95% CL.

1.3.4 Higgs search at Large Hadron Collider

The production of Higgs bosons at low mass ($m_H < 150$ GeV) at LHC can be done in the following channels (Fig. 1.7):

- Gluon-gluon fusion: the Higgs boson is created in the virtual loop of top quarks.
- Weak boson fusion: Collisions of quarks produce the weak bosons, then the two weak bosons can be fused together to create the Higgs boson (only available for $W^+W^- \to H$ or $ZZ \to H$).
- Associate production with a pair of top quarks.
- Weak boson strahlung: A pair of quark-antiquark collides, producing a virtual weak boson. Then this virtual weak boson will radiate a Higgs boson.

The cross-sections for each production mode of Higgs boson as a function of Higgs mass are shown in Figure 1.8 at the center-of-mass energy $\sqrt{s} = 8$ TeV (detailed Higgs production

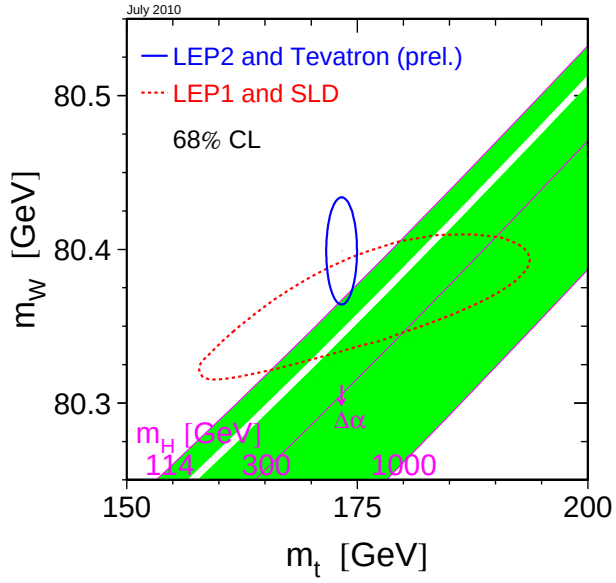

Figure 1.5: W boson mass as a function of top quark mass. The red and blue contours are of 68% confidence level. The green zone shows the value of Higgs mass available in SM for different masses of W and t [44].

cross section can be founded in Ref. [45]). The gluon-gluon fusion is the dominant production channel[5]. Then the second dominant production mode is the weak boson fusion. The two production channels of weak boson bremstrahlung have lower cross-section than the previous two, however they are still higher than the $t\bar{t}$ channel.

The search for Higgs boson at LHC uses all of these production channels, and utilizes channels of Higgs decays which can be detected (Fig. 1.9) if we are to search for Higgs boson with low mass ($m_H < 149$ GeV as the exclusion from Tevatron). The decay channels that are being studied at LHC are $H \to b\bar{b}$, $H \to \tau\tau$, $H \to ZZ^*$, $H \to WW^*$, $H \to Z\gamma$ and $H \to \gamma\gamma$. As one can see from the branching ratio, the most abundant decay channel for Higgs search would be the $H \to b\bar{b}$ with 57.7% of branching ratio ($m_H \sim 130$ GeV), but one should deal with large backgrounds from hadronic production. The three channels $H \to ZZ^*$, $H \to WW^*$ and $H \to \gamma\gamma$ can produce more visible signals, but need to face the low branching ratio.

Results of the search for Higgs boson at LHC The Higgs search has come fruitful after a long run of searching for almost five decades. In the year 2012, the combination of Higgs search using Higgs decay channels $H \to ZZ^* \to 4\ell$, $H \to WW^* \to \ell\nu\ell\nu$ and $H \to \gamma\gamma$ at the ATLAS and CMS experiments using data of 2011 and 2012 (4.8 fb^{-1} of data collected in 2011 and 5.8 fb^{-1} in 2012) showed the existence of Higgs-like particle with mass = 126.0 $\pm$ 0.4 (stat.) $\pm$ 0.4 (syst.) GeV [46, 47] (Figures 1.10, 1.11), with the significance of 5.9 standard deviations, corresponding to a background fluctuation probability of 1.7×10^{-9}.

[5]At LHC the dominant collision is gluon-gluon, while in Tevatron the collisions are mostly quark-quark.

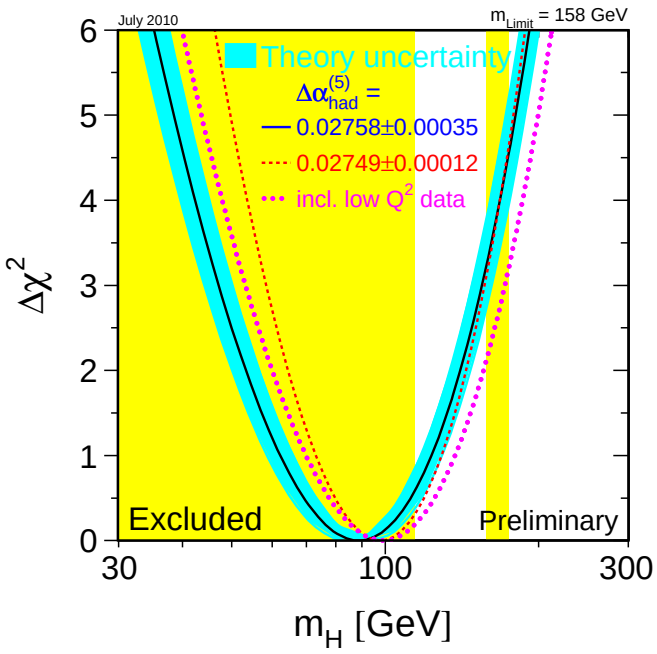

Figure 1.6: $\Delta\chi^2$ between theory and measurement as a function of Higgs mass using fit from electroweak parameters [44]. The yellow bands are the excluded region at 95% CL from LEP and Tevatron. The blue band is theoretical uncertainty.

These results confirm the existence of the Higgs boson and also confirm the coupling between the Higgs boson and the other known bosons in the Standard Model.

In the end of 2013, the results of Higgs search with mass around 125 GeV decaying to a pair of τ leptons (combining leptonic and hadronic decay mode of τ) with the ATLAS and CMS experiments once again confirm the existence of the Higgs particle [48, 49] and the coupling between Higgs boson and leptons [50].

1.4 Conclusion

The Standard Model is a successful theory to describes the hierarchy of fermions (quarks and leptons) as well as interactions between them mediated by bosons. However, it does not explain the origin of particle masses. This can only be solved by introducing the Higgs mechanism in the SM, which proposes the interaction between particles and the Higgs field to generate masses of particles. Nevertheless, the mass of the Higgs boson is not predicted, and determining this mass is one of the keys to complete the SM. Various constraints from theory and experiments allowed to reduce the region to search for the Higgs boson. Search for the Higgs boson was a primary objective at LEP and Tevatron precedently and LHC at present. Various channels and production modes are being analyzed at LHC, and the Higgs boson was found in 2012 through its decays to bosons and leptons at a mass of ∼125 GeV. However the Higgs boson decay to quarks needs confirmation to assure that the discovered

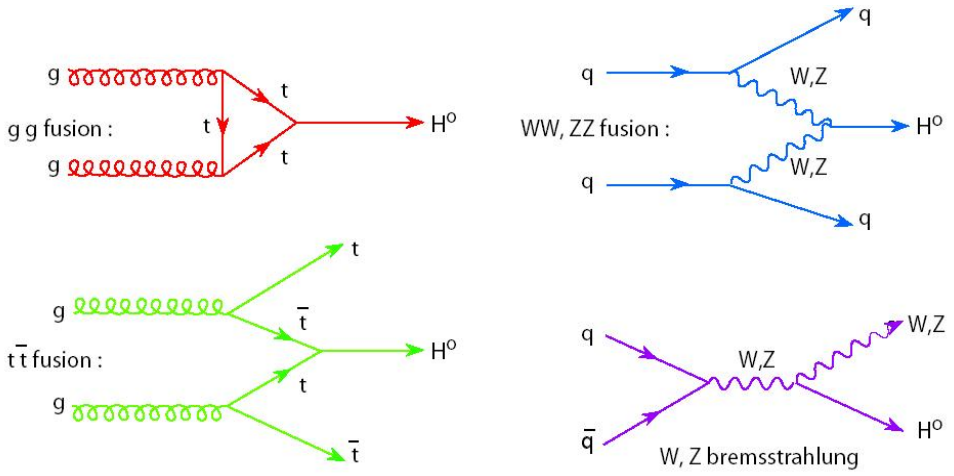

Figure 1.7: Feynman diagrams for each of Higgs boson production modes.

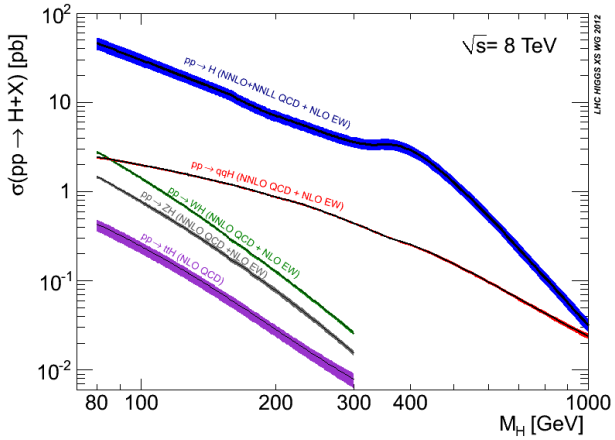

Figure 1.8: Cross sections of Higgs boson production as a function of Higgs mass at $\sqrt{s} = 8$ TeV collision at LHC [45].

Higgs boson is the one predicted by the SM.

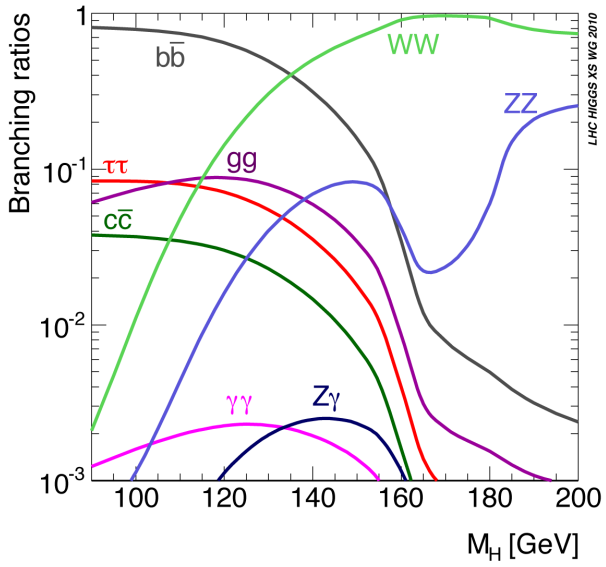

Figure 1.9: Branching ratio of each decay mode of Higgs boson as function of Higgs mass [45].

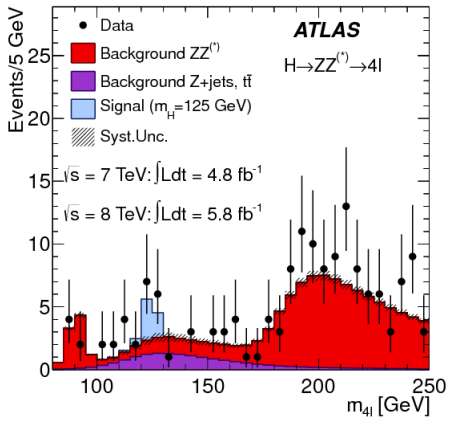

Figure 1.10: Distribution of 4-lepton invariant mass for the combination of 7 and 8 TeV data sample. The background expectations are shown in red and purple region, the signal of Higgs boson is also shown in blue, the data is represented by black points [46].

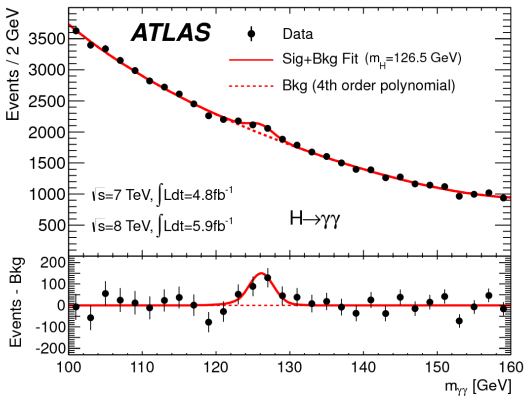

Figure 1.11: Distribution of di-photon invariant mass for the combination of 7 and 8 TeV data sample. [46]

Chapter 2

Experimental description

Our experimental framework is based on the Large Hadron Collider and proton-proton collision phenomenology. The Higgs analysis we pursue will be held at the ATLAS detector. In this chapter we will introduce the operation of the Large Hadron Collider and its objectives. The full description of the ATLAS detector will also be discussed here with all the components, performance, and physics object reconstruction.

2.1 The Large Hadron Collider

The Large Hadron Collider (LHC) is currently the world's largest particle collider in terms of center-of-mass energy. This grand machine is located at CERN, at the France-Switzerland border, near Geneva. The LHC is designed to test the modern theories of particle physics at high energy scale, verifying theoretical predictions of interactions among particles and properties of them. The machine also serves the goal of discovering new physics such as supersymmetry, and searching for new particles like the Higgs boson.

The LHC was constructed using the tunnel from the LEP collider, which spans 27 km of circumfence. It was designed to collide protons at the center-of-mass energy $\sqrt{s}$ =14 TeV. In 2010 and 2011 the LHC operated at $\sqrt{s}$ =7 TeV, and in 2012 at $\sqrt{s}$ =8 TeV. The LHC was shut down for the year of 2013 for two years for upgrading. The machine is supposed to run at $\sqrt{s}$ =13 TeV in 2015, and in the near future of 2018, it should operate at full energy at $\sqrt{s}$=14 TeV.

Particle collisions at LHC are mainly proton-proton. There are alternatives, such as:

- Collision of e^+e^- as in LEP, $p\bar{p}$ as in Tevatron and ep as in HERA
- Collision with a fixed target.

The reasons for this choice are as follows:

- The proton, much heavier than electrons (about 1836 times heavier), can be accelerated in the LHC synchrotron ring to reach higher energy thanks to its much lower synchrotron radiation loss: synchrotron radiation loss for a particle with mass m is proportional to $1/m^4$, so we can evaluate that the energy loss per turn of proton is 10^{13} times lower than for electrons, therefore can be neglected.

- The protons are much easier to produce than the antiprotons. At Tevatron, the antiprotons were produced by colliding proton beams with a metal target with a rate of millions of protons collided to produce one antiproton. Therefore a high instantaneous luminosity[1] from proton-antiproton collisions is hard to achieve.

The LHC can also be used for heavy ion collisions (mainly Pb).

Using proton-proton collisions can also lead to disadvantages, which will be discussed later also in this chapter.

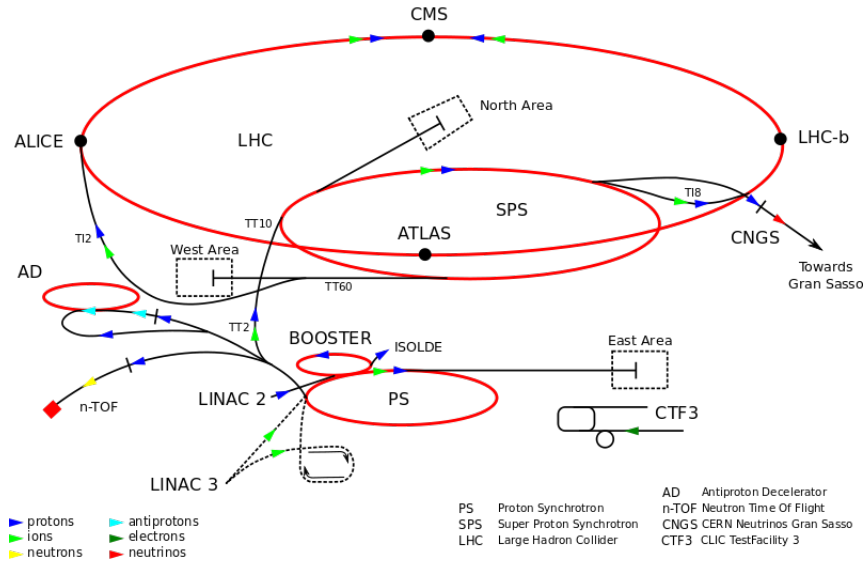

Figure 2.1: The CERN accelerator complex

For the collisions at LHC, proton beams are accelerated through the system of existing accelerators at CERN before entering the LHC ring (Fig. 2.1). At the first stage, the protons are created from ionizing hydrogen gas. The linear accelerator (LINAC 2) accelerates proton beams up to 50 MeV, then they are boosted up to 1.8 GeV by the Booster and injected to the Proton Synchrotron (PS). Here the protons are accelerated up to an energy of 25 GeV. After that, the proton beams are accelerated up to 450 GeV by another bigger synchrotron accelerator, the Super Proton Synchrotron (SPS) before being injected to the LHC as the final stage of accelerating chain. Proton bunches then are accelerated and collided at four intersection points (which correspond to the locations of four main detectors at LHC that will be described later).

The trajectories of proton beams are bended and maintained inside the LHC ring by the magnetic field generated by the system of superconducting magnets. This magnetic field sets the limit to the maximum energy that the protons can reach inside the LHC ring. For 7 TeV beam, the LHC operates at the nominal magnetic field of 8.3 T. Since the proton beams are to be accelerated into opposite directions to collide, the LHC cannot rely on one single bending magnetic field. Instead, the magnetic field is designed with two superconducting dipole magnets and two beam pipes as described in Figure 2.2, where the magnetic field in a

[1] defined from number of collions produced per unit of time $N = \mathcal{L} \cdot \sigma$, where σ is cross-section. The unit of instantaneous luminosity is $\mathrm{cm}^{-2}\mathrm{s}^{-1}$.

pipe is opposite to the other pipe. The two superconducting dipole magnets and two pipes lie in the cryostat cooled down by super-fluid helium down to a temperature of 1.9 K.

There are also the system of quadrupole magnets which aim to keep the beam focused and multipole magnets for beam corrections.

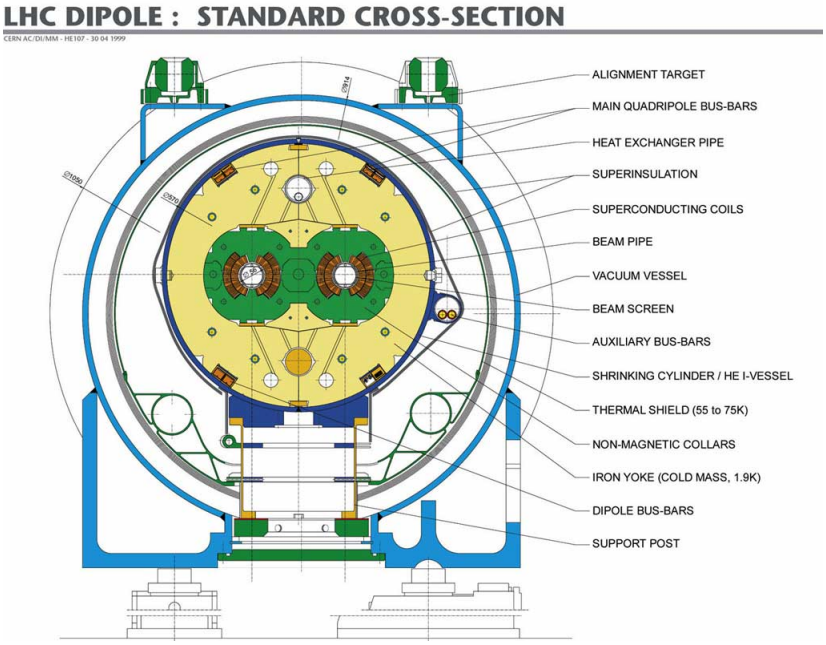

Figure 2.2: Transverse cut of a dipole magnet used at LHC.

The number of collisions per second at LHC is given by the formula $N_{events} = \mathcal{L} \times \sigma$, where $\mathcal{L}$ is defined as the luminosity of the machine (in $\text{cm}^{-2}\text{s}^{-1}$), and σ is the cross section of the considered physic process. The luminosity depends on the colliding beams characteristics and can be written as follows:

$$\mathcal{L} = \frac{N^2 \cdot B \cdot f_{rev}}{4\pi \cdot \sigma_x \sigma_y} F,$$

where:

- N is the number of protons per bunch.
- B is the number of proton bunches per beam
- f_{rev} is the revolution frequency of the bunches
- σ_x, σ_y are the widths of the Gaussian distribution of the beam in the transverse plane
- F is the geometrical correction to adjust the crossing angle of the two beams at the colliding point.

Another quantity of luminosity that we also use often is the *integrated* luminosity, which is defined as the integration over time $\mathcal{L}_{int} \equiv \int \mathcal{L}(t)dt$. This quantity yields the unit of cm^{-2},

which is the inverse of the cross-section's unit (in cm^2, or barn[2]). So in LHC operation, we usually use the units of integrated luminosity as pb^{-1}, fb^{-1}, etc...

The main features for LHC operation in 2010, 2011, 2012 and nominal operation are shown in Table 2.1. The integrated luminosity measured by the ATLAS detector is summarized in Figure 2.3.

Table 2.1: Main parameters of the LHC during operations in 2010, 2011, 2012 and nominal feature.

Parameter	2010	2011	2012	nominal
$\sqrt{s}$ [GeV]	7	7	8	14
Number of protons per bunch	$1.2 \cdot 10^{11}$	$1.45 \cdot 10^{11}$	$1.7 \cdot 10^{11}$	$1.15 \cdot 10^{11}$
Number of bunches	368	1380	1380	2808
Bunch spacing [ns]	150	75/50	50	25
Bunch revolution frequency [kHz]	11	11	11	11
Peak luminosity $[cm^{-2}s^{-1}]$	2.1×10^{32}	3.7×10^{33}	7.7×10^{33}	$1. \times 10^{34}$
Integrated luminosity/year	48 pb^{-1}	5.6 fb^{-1}	23 fb^{-1}	100 fb^{-1}

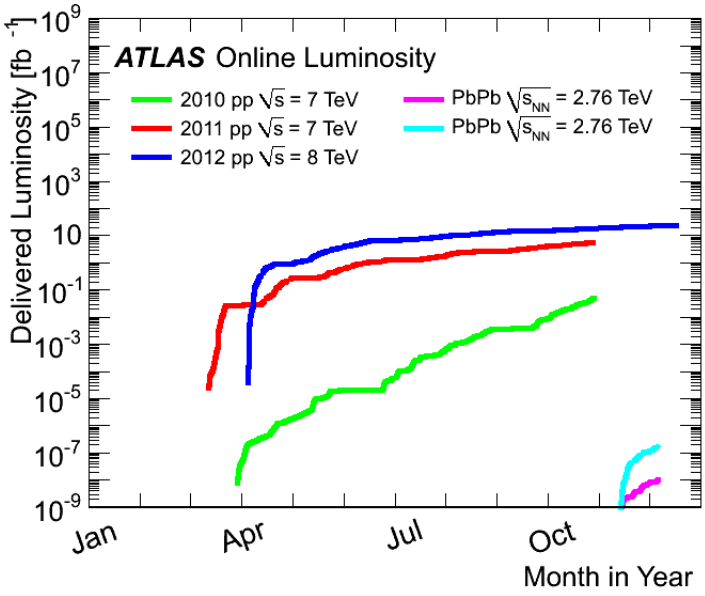

Figure 2.3: Integrated luminosity (in fb^{-1}) recorded by the ATLAS detector in 2010, 2011 and 2012.

Various experimental projects on modern physics are operated at four main experiments at LHC:

- ATLAS: A Toroidal LHC ApparatuS: general purpose experiment.
- CMS: Compact Muon Solenoid: same purpose as ATLAS.

[2] 1 barn = $10^{-24} cm^2$

- ALICE: A Large Ion Collider Experiment: Mainly observe heavy ion collisions and study the quark-gluon plasma.
- LHCb: This experiment focuses on studying the parameters of CP violation via the decays of b-hadrons and on probing new physics via precision measurements.

2.2 Proton–proton collisions at LHC

The proton-proton (pp) collisions at LHC are able to reach high energy and high luminosity, but not without paying a price: unlike electrons or positrons, which are *real* elementary particles, the protons are composed by quarks and gluons (or so-called partons), thus the real collisions at LHC are from the collisions between partons. Those partons carry some fraction of energy of proton, consequently not all the interactions happen at the same center-of-mass energy $\sqrt{s}$ but rather a wide range of $\sqrt{s}$. Plus, interactions between quarks and gluons are not perturbative and cannot be calculated precisely in QCD theory. The fraction of energy of parton inside the proton is characterized by the parton distribution functions (PDF), which are also not possible to evaluate and can only be determined using experimental data fitting (at HERA and Tevatron, for example).

The cross-sections for various physics processes using pp collisions at LHC are presented in Figure 2.4. The elastic collisions do not produce any new kind of particles and new physics and are not considered here. For the inelastic part, the partons inside protons can interact and form new particles in the process, for example: W, Z or t, Higgs, etc...(we usually call such processes as *hard scattering processes*). As the center-of-mass energy rises, the cross-section of creating new particles increases, resulting in a better chance for them to be detected.

The complexity of proton-proton collision at LHC leads to the following phenomena:

Underlying events Apart from the events from the hard scattering processes during pp collisions, other events also come from the remnants of interacting protons which can also be detected. Those kind of events are referred to as *underlying events* (UE). The modeling of UE at LHC is crucial for the measurements of high momentum processes, because they can affect those measurements by impacting on the calibration of the energy of jets for instance.

Pile-up There is more than one pp collision occuring in each bunch crossing, contributing more events to our interesting processes (for example, production of W and Z bosons, heavy quarks, etc...) (Fig. 2.5). We define these kinds of events as in-time *pile-up* events. The response time from sub-detectors can be higher than the bunch spacing (25 ns), so pile-up events from preceding and following collisions can contribute signals. Such pile-up events are called *out-of-time* pile up. Events from pile-up are different from the underlying events since they are independent from the interesting interactions. The pile-up at LHC is characterized by the mean number of interactions per bunch crossing (denoted by $\langle\mu\rangle$). For 2012 data, the $\langle\mu\rangle$ is observed to be significantly higher than in 2011 data. (Fig. 2.6).

Jets The partons can emit gluons that might generate further gluons or quark-antiquarks pairs. These processes are called parton showers. As those showers expand, the strong inter-

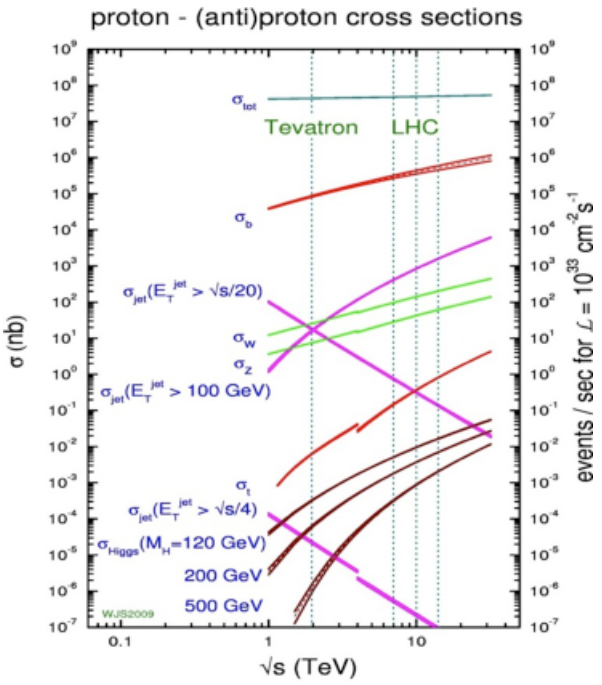

Figure 2.4: Cross-sections of various processes at Tevatron (proton-antiproton collision) and at LHC (proton-proton collision) as a function of $\sqrt{s}$ [51].

action coupling increases and this leads to *hadronization* (see Fig. 2.7), which creates more stable particles. Collisions at LHC produce very high energy-momentum quarks and gluons. The resulting cascade of particles generated in the hadronization focus in a narrow space in some specific direction. Such particle showers are usually called *jet*. Jet measurements are important at LHC as these are the key for studying the multijet at TeV scale (constrain PDF, strong coupling constant α_s), they are also the important signals and backgrounds for the study of new physics (SUSY, Beyond the Standard Model, etc...).

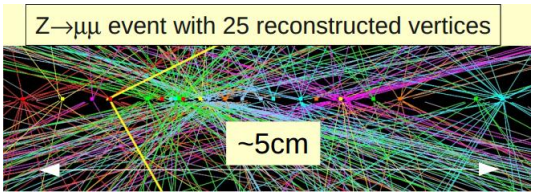

Figure 2.5: Example of pile-up events (marked by colors) in the collisions that produce a Z boson with two observed leptons (in yellow line) using ATLAS detector.

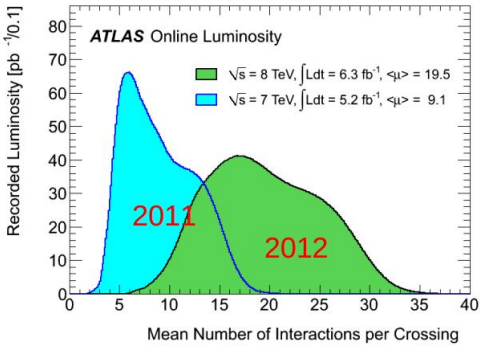

Figure 2.6: Luminosity as a function of mean number of interactions per crossing ($\langle\mu\rangle$) for 2011 and 2012 data taking recorded by the ATLAS detector.

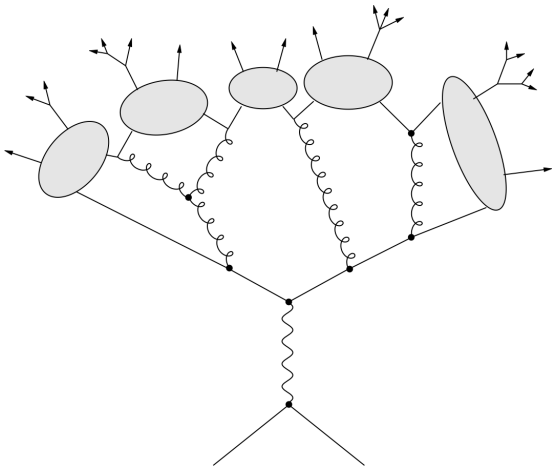

Figure 2.7: The model of hadronization: the quarks produced from collision generate the parton shower, the shower will eventually convert to hadrons as the strong coupling constant rises.

2.3 The ATLAS experiment

2.3.1 General description

ATLAS is one of the two detectors for general-purpose experiments at LHC. It is the biggest detector ever built with 46 m long, 25 m of height and 7000 t of weight. The construction began in 1997 in a cavern ∼100 m underground.

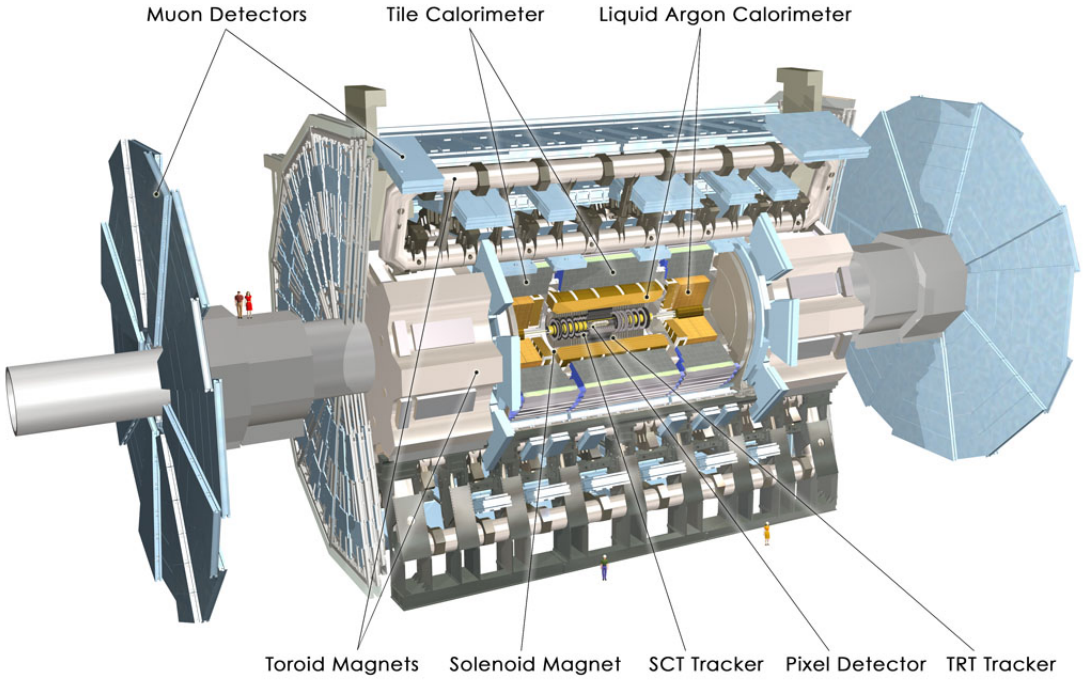

Figure 2.8: Overview of ATLAS detector and its sub-detector system.

The overview of ATLAS detector is displayed in Figure 2.8. ATLAS has a cylindrical form, with the center located at the interaction point of pp collisions. It contains a system of sub-detectors:

- Inner detector (inner tracker): The closest detector system to the interacting point and surrounded by a solenoidal magnet which generates a strong magnetic field (about 2 T).
- Electromagnetic and hadronic calorimeters: Identify and measure energy of electrons and photons (in EM calorimeter), as well as the energy of jets (measured also in hadronic calorimeter).
- Muon spectrometer: surrounded by the air-core toroid magnet. The muon spectrometer allows to trigger the muons as well as high-precision measurement of muon tracks.

The principle of detecting particles in ATLAS detector is summarized in Figure 2.9. Charged particles like electrons, muons, etc leave tracks in the tracking system, allowing the detector to reconstruct their trajectories and momentum. In EM calorimeters, electrons and

photons will deposit all their energy to the system and can be measured, the other particles like hadrons and muons will traverse through this part of calorimeter system and deposit part of their energy. All hadrons will generate hadronic showers in the hadronic calorimeters and deposit their energy in it, so that their energy is measured by the calorimeters. The muons will traverse through all the tracking system and calorimeters but are detected by the muon spectrometer, therefore their momentum can be reconstructed and measured.

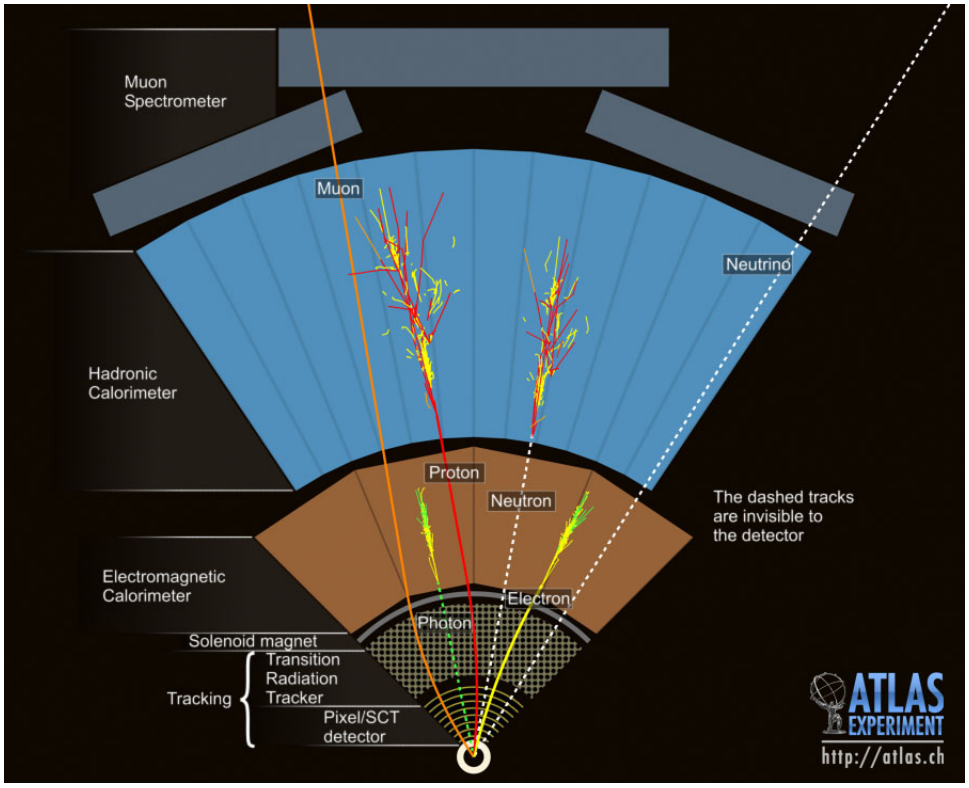

Figure 2.9: Particle detections in the sub-detector system of ATLAS.

The neutrinos escape the ATLAS detector without being detected. Details of measuring energy and momentum of neutrinos will be discussed in chapter 4.

ATLAS coordinate system The ATLAS coordinate system is defined as follows: along the beam direction of protons is the longitudinal axis, the z-axis. The $x-y$ plane (transverse plane) is perpendicular to the beam direction with the x-direction pointing to center of LHC ring, and y-axis pointing upward. We define the azimuthal angle ϕ with respect to the x axis, θ is the polar angle with respect to the z axis. We also define the pseudo-rapidity as:

$$\eta = -\ln \arctan(\theta/2).$$

The rapidity is also used with the definition:

$$y = \frac{1}{2}\ln\frac{E+p_z}{E-p_z},$$

where E is the energy of the particle and p_z is the component of momentum of particle along the z-axis. The distance ΔR is defined as: $\Delta R = \sqrt{(\Delta\phi)^2 + (\Delta\eta)^2}$.

ATLAS performance requirements Table 2.2 summarizes the performance requirements of the ATLAS detector in each detector component.

Detector component	Resolution	η coverage	
		For measurement	For L1 trigger
Inner detector	$\sigma_{p_T}/p_T = 0.05\% p_T \oplus 1\%$	$\|\eta\| < 2.5$	-
EM calorimeter	$\sigma_E/\mathrm{E} = 10\%\mathrm{E} \oplus 0.7\ \%$	$\|\eta\| < 3.2$	$\|\eta\| < 2.5$
Hadronic calorimeter	$\sigma_E/E = 50\%E \oplus 3\%$	$\|\eta\| < 3.2$	$\|\eta\| < 3.2$
Forward calorimeter	$\sigma_E/E = 100\%E \oplus 10\ \%$	$3.1 < \|\eta\| < 4.9$	$3.1 < \|\eta\| < 4.9$
Muon spectrometer	$\sigma_{p_T}/p_T = 10\%$ at $p_T = 1$ TeV	$\|\eta\| < 2.7$	$\|\eta\| < 2.4$

Table 2.2: Requirements of ATLAS detector performance.

2.3.2 Inner detector

The Inner Detector (ID) [52] is also known as the tracking system of the ATLAS detector, it is responsible for measuring and reconstructing trajectories of charged particles with high quality including their momenta, primary/secondary vertices, impact parameters in an enviroment of high density of tracks thanks to its high granuality. The ID is surrounded by a 2 T magnetic field generated by a solenoid magnet.

The Inner Detector is composed by three main components: Pixel Detector, Semi-Conductor Tracker (SCT) and Transition Radiation Tracker (TRT). They cover a region of $|\eta| < 2.5$ in the ID, which is shown in Figure 2.10. The detailed description of these component detectors will be discussed in the following subsections.

2.3.2.1 Pixel detector

The pixel detector [53] is the closest detector to the collision point along the beam line (also shown in Figure 2.10). This sub-detector is constructed based on a technology that can sustain a very high radiation level around the collision point, and can also deliver measurements with low noise, high occupancy, high efficiency and very high precision.

The pixel detector is formed by three barrel layers (numbered from 0 to 2)[3] surrounding the beam pipe and three end-cap layers (also numbered from 0 to 2) in each side, covering a region of $|\eta| < 2.5$, aiming to measure at least three space points to reconstruct tracks of charged particles. The distances of each barrel layer with respect to the beam pipe axis are 50.5 mm, 88.5 mm and 122.5 mm, respectively. For the end-cap region, the layers are installed at the corresponding distances of 495 mm, 580 mm and 650 mm with respect to the center of the detector. The area of detection is composed of 1744 modules with 1456 in the barrel region and 288 in the end-cap region, containing more than 80 million pixels (67 million in barrel region and 13 million in end-cap region). Each module (Fig. 2.11) is a block covering an area of 6.08×1.64 cm^2 composed of:

- Silicon sensor layer: contains the diode in the reverse polarization, which detects particles via the electron-hole creation when charged particles pass through.

[3]The innermost layer of the pixel detector barrel (0^{th}) is called *b*-layer.

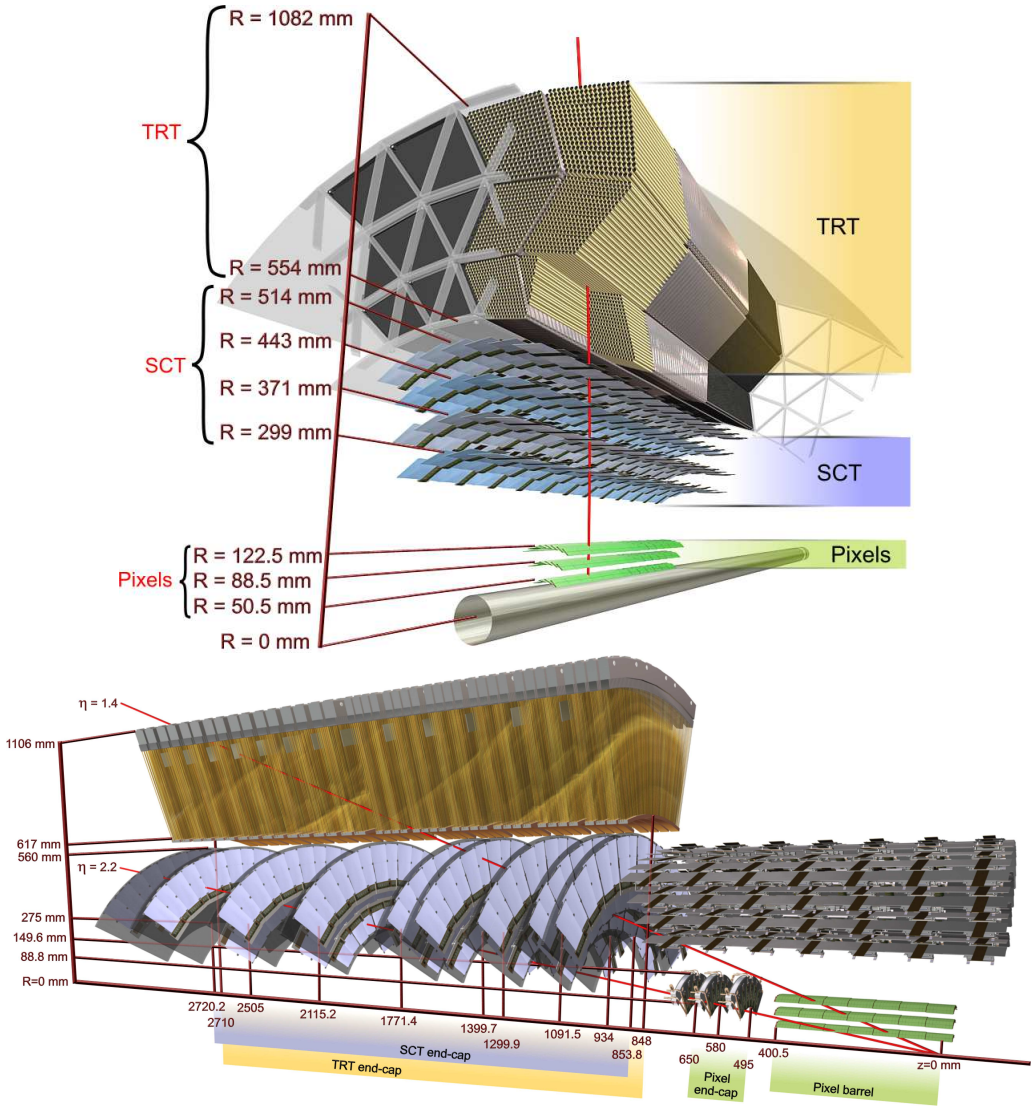

Figure 2.10: The layouts of barrel region (top) and endcap region (bottom) of Inner Detector.

- Readout electronic layer containing 16 Front-End (FE) chips with 2880 readout channels in each chip, with a total 46080 channels. Each channel associates with a *pixel*. The pixel size is of 50×400 μm in $r-\phi$ and z directions.

- Control card connected to the FE chips and using Module Control Chip (MCC). This card receives signals from FE chips and delivers them to the data acquisition.

In the barrel region, the modules are mounted on a cooling and mechanical support system called *staves*; the staves are designed such that they form a geometry providing full coverage without gap in each layer. The number of modules, staves and distance from the beam pipe are summarized in Table 2.3.

In each of end-cap regions, the layers are formed as disks, and each disk consists of eight sectors with six modules attached (so 48 modules on each disk). Those six modules are divided into two groups of three on each side (long side of the module is along the R-

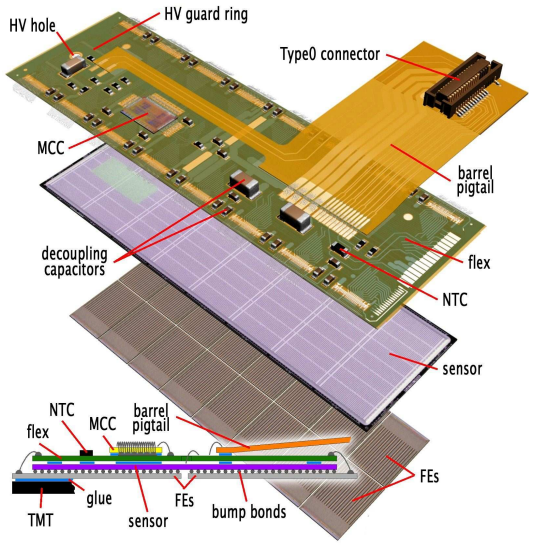

Figure 2.11: Layout of pixel module in ATLAS pixel detector.

Layer	Distance from beam pipe [mm]	Number of staves	Number of modules
0	50.5	22	286
1	88.5	38	494
2	122.5	52	676

Table 2.3: Properties of each layer in barrel region of ATLAS pixel detector

direction) with the modules on the back side rotated by a tilt angle of 7.5° in ϕ-direction so that the full coverage of detection can be guaranteed.

The instrinsic resolutions of pixel detector are 10 μm in the $R-\phi$ plane and 115 μm along the z-axis. These are good resolutions in order to separate tracks from long-lived particles (b or c-hadrons) and deliver a good reconstruction of primary and secondary vertices in both transverse plane and longitudinal direction. This will be very useful for our analysis.

2.3.2.2 Semi-Conductor Tracker

The Semi-Conductor Tracker (SCT) [54, 55] surrounds the pixel detector. Like the pixel detector, it is designed to sustain a high level of radiation. It is a semiconductor p-in-n silicon microstrip detector because silicon is fast and can sustain under long-term high luminosity operation.

The SCT is composed of four barrel layers and nine disks on each end-cap side (see Fig. 2.10). Four barrels contain a total of 2112 SCT modules with more than 3.2 million readout channels. On eighteen disks from both end-cap sides, there are 1976 modules in total with more than 3 millions readout channels. The modules are mounted on a light support material of carbon fibers (Fig. 2.12), composed of 2 sensors on each side rotated by a small angle of 40 mrad with respect to each others so that the hits ambiguity is reduced.

The modules of SCT cover an area of 63 m^2 and provide at least four space point measurements. The SCT delivers instrinsic hit resolutions of 17 μm in $R-\phi$ plane and 580 μm

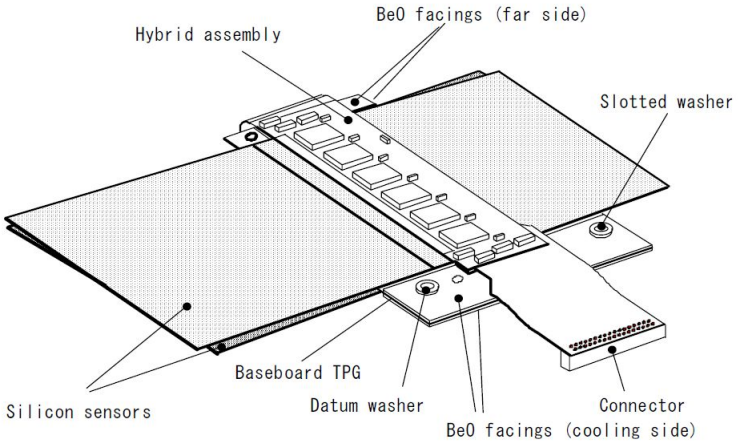

Figure 2.12: Layout of SCT barrel module.

along the z-direction in the barrel region while in the end-cap the resolutions are 17 μm in $R-\phi$ plane and 580 μm in the radial direction R.

2.3.2.3 Transition Radiation Tracker

The Transition Radiation Tracker (TRT) [56] is the outermost component of ATLAS ID made from more than 350000 drift tubes of 4 mm diameter called straw tubes, covering a region of $|\eta| < 2$. The strawtubes are arranged along the beam axis in the barrel region with 144 cm length while in end-cap region, they are installed along the radial axis with 37 cm length. The TRT in the barrel region consists of three cylindrical rings with 32 modules on each. There are three different types of barrel modules installed from the innermost to outermost radius.

Each strawtube is filled with a gas mixture of $Xe/CO_2/O_2$. The anode is installed at the center of the strawtube with a 31 μm-diameter tungsten wire plated gold, and the cathode is the surface of the strawtube. The passing charged particle will ionise the gas mixture in the tube and the charge drift will be collected at the anode. Figure 2.13 shows the principle of determining the charged particle trajectory in TRT. The drift time of the ion in the tube depends on the distance between the anode and the primary ionisation and provide the resolution of 130 μm in $R-\phi$ plane. Unlike pixel detector or SCT, the TRT provides only measurements in $R-\phi$ plane.

In addition to bringing a good momentum resolution for charged tracks, as it spans up to a radius of 1 m, the TRT plays an important role in electron identification because the electrons deposit more energy in the gas mixture inside the strawtube than the other heavier particles (pions, hadrons, etc...) thanks to the higher transition radiation absorbed in strawtubes[4].

[4]The radiation transition of an ultra-relativistic charged particle is proportional to the Lorentz factor $\gamma = E/m$.

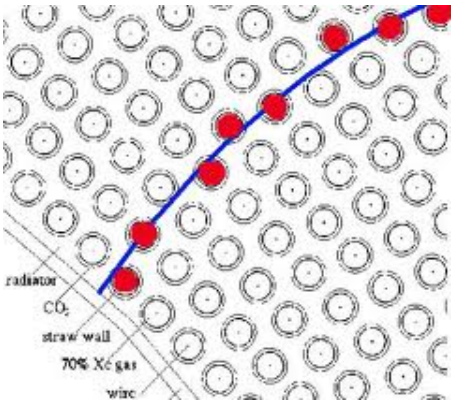

Figure 2.13: Principle of detecting charged particle in TRT.

2.3.2.4 The ID cooling system

Chips and modules in pixel detector and SCT generate large amount of heat in ATLAS detector since the high granularity will need high density of electronics. The heat emitted from the ID can be up to 85 kW at nominal luminosity, so controlling the conditions of electronic system is essential to maintain the operation of detector and protect the detector from unexpected damages.

The pixel detector and SCT use the same cooling system using C_3F_8 as the coolant due to their high radiation resistance, non-toxic and inflammable. The silicon sensors can operate at -7° to minimise damage from radiation. Both pixel detector and SCT operate in a dry N_2 gas flow to remove the possible humidity on sensors and FE electronics.

Unlike pixel detector and SCT, the TRT operates at room temperature, and it uses C_6F_{14} as the coolant. Additionally, the volume of TRT is filled with CO_2 to suppress the contamination of the mixture gas inside the straw with other molecules.

2.3.3 Calorimetry system

The ATLAS detector calorimetry system [57] is built with different technologies to deliver measurements with good energy resolution, good position precision and cover a large range of pseudo-rapidity $|\eta| < 4.9$. The calorimetry system is composed of three main parts: Electromagnetic, hadronic and forward calorimeters (Fig. 2.14), which serve different purposes in measurements:

- EM calorimeter (EM): for energy measurement and identification of electrons and photons. It also takes part in jet reconstruction/energy and missing transverse energy.
- Hadronic calorimeter: Used for jet reconstruction, jet energy measurements and also measure the missing transverse energy.
- Forward calorimeter (FCal): attached to the end-cap cryostats, this part of calorimeter is used for forward jet and missing transverse energy measurements.

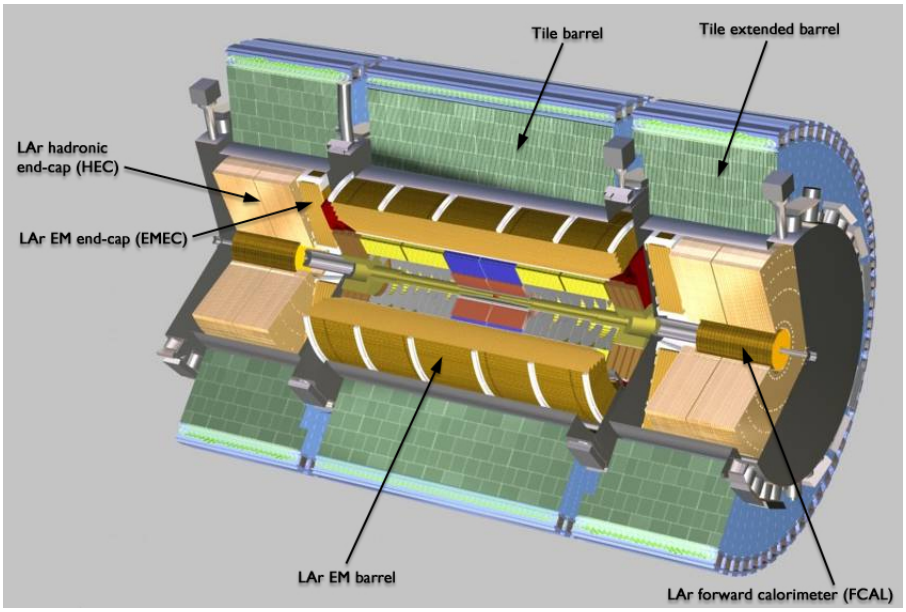

Figure 2.14: Layout of ATLAS Calorimetry system.

2.3.3.1 Electromagnetic calorimeter

The EM calorimeter is designed to absorb energy of particles like electrons and photons. Its high granularity provides a high precision measurement of energy and position of absorbed particles. The calorimeter is divided into three regions: a barrel region for $|\eta| < 1.375$ and two end-cap regions covering $1.375 < |\eta| < 3.2$. The EM barrel and end-cap are made of lead absorbers and copper electrodes, and gaps between them are filled with liquid argon (LAr).

The barrel EM calorimeter is split into three layers as shown in Figure 2.15. The first layer is the closest to the ID and has a high granularity of thin strips (with the size of $\Delta\eta \times \Delta\phi = 0.0031 \times 0.098$) which provides a good resolution to separate electrons/photons from π^0. The second layer has larger radiation length compared to the first one such that it can absorb the majority of energy of the electrons and photons up to 50 GeV, its cell size in η direction is bigger than the first layer (0.0245 compared to 0.0031) but smaller in ϕ direction (0.0245 compared to 0.098). Particles with high energy can reach the third layer and are stopped here, at this point the clusters created by particles in calorimeter are wide enough to double the size of cells in η direction without losing the resolution. In the region of $|\eta| < 1.8$ the Pre-Sampler (PS) is installed in front of EM barrel to correct the energy loss in the ID.

The EM end-cap (EMEC) covers the higher region of pseudo-rapidity. In each side of end-cap, the EMEC is divided into inner wheel (coverage of $2.5 < |\eta| < 3.2$) and outer wheel ($1.375 < |\eta| < 2.5$). The voltage applied on the EMEC and the LAr gap size vary with respect to radius so that the response of signal in η direction is uniform.

2.3.3.2 Hadronic calorimeter

The hadronic calorimeter absorbs the energy of particles that pass through the EM calorimeter (usually hadrons), covering a range of $|\eta| < 3.2$, it is composed of two compartments: Tile Calorimeter (TileCal) and LAr hadronic end-cap calorimeter.

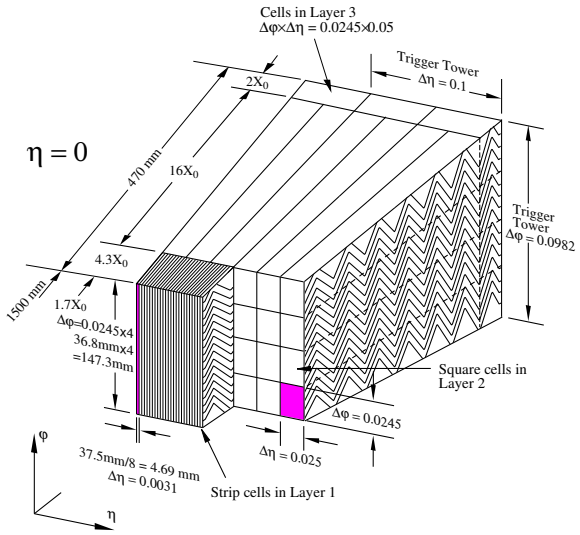

Figure 2.15: A schematic view of the three samplings of the ATLAS barrel elec- tromagnetic calorimeter system.

Tile Calorimeter The Tile hadronic calorimeter is located right behind the EM calorimeter. It uses steel as absorber and scintillating plastic tiles as active material (Fig. 2.16). It is divided into three parts: barrel part, covering a range of $|\eta| < 1$, and two end-cap barrels on each side covering the region $0.8 < |\eta| < 1.7$.

LAr hadronic end-cap calorimeter Like the EMEC, the hadronic end-cap calorimeter (HEC) is installed within the same cryostat. It has two independent wheels on each side of the end-cap, located right after the EMEC. It extends the coverage up to $|\eta| < 3.2$, also overlaping with the forward calorimeter to ensure the material density at the transition region. It uses copper as absorber and liquid argon as medium.

2.3.3.3 LAr forward calorimeter

The LAr Forward Calorimeters (FCal) provide measurement of jets in the forward region, and also play an important role in estimating missing transverse energy. They are located on both sides of the end-cap and contain both EM and hadronic calorimeters. The range of pseudo-rapidity extended by the FCal is up to $|\eta| < 4.9$ and also overlaps with HEC, therefore ensuring good coverage.

The FCal is divided into three modules as shown in Figure 2.17: The module that is closer to the interaction point is for EM detection, which uses copper as absorber. The other two modules are placed right after the EM modules and use tungsten as absorber for hadronic absorption. All three modules use the same cryostat as the other end-cap calorimeters.

2.3.4 Muon spectrometer

The muon spectrometer is the outermost part of the ATLAS detector and covers other sub-detectors. Figure 2.18 illustrates the layout of the muon spectrometer and its four compo-

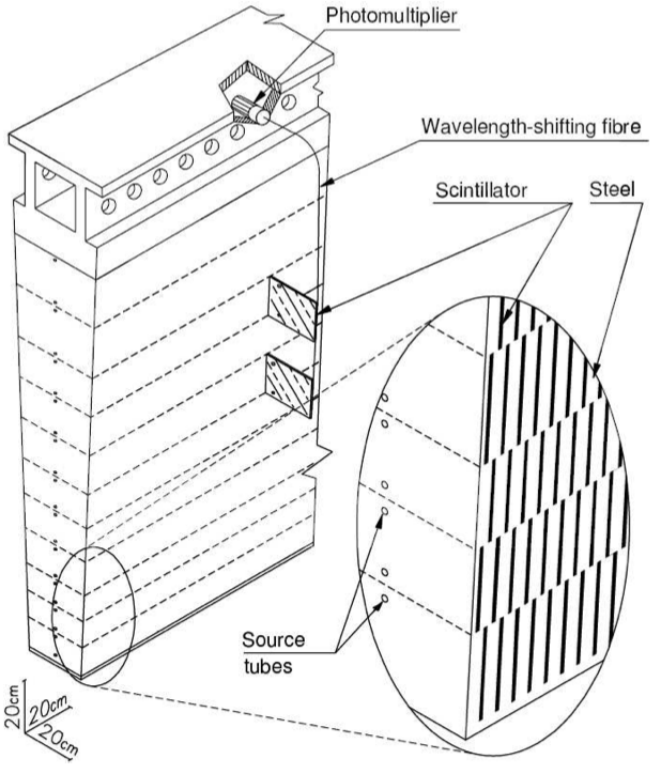

Figure 2.16: A schematic view of Tile hadronic calorimeter.

nents: Monitored drift tubes (MDT), Cathode strip chambers (CSC), resistive plate chambers (RPC) and thin gap chambers (TGC). All these components operate under the toroidal magnetic field generated by three air-core toroids, with a long barrel toroid located in the central region and two end-cap toroids in the end-cap region to cover the higher range of pseudo-rapidity. The magnetic field is constructed such that it is always perpendicular to the muon trajectory. The muon spectrometer provides a high precision standalone measurement of muon momentum.

The MDT covers all the region of $|\eta| < 2.7$ with a barrel and two end-caps. At the innermost layer end-cap region ($2.0 < |\eta| < 2.7$), the MDTs are replaced by the CSCs. The MDT is composed by drift tubes (with diameter of 29.970 mm) containing the gas mixture of Ar/CO_2, and a tungsten-rehnium wire as anode with 50 μm thickness placed at center (Fig. 2.19). There are approximately 1150 MDT chambers with 350000 read-out channels with resolution of single tube about 80 μm.

The CSC is the multiwire proportional chambers with cathodes segmented into strips (Fig. 2.20). The anode wires are placed in radial direction and perpendicular with the cathode strips, allowing measurements in both directions. The CSC allows the read-out of high rates of particles with the maximum counting rate of 1000 Hz/cm^2. The CSC replace the MDT in the region of $2.0 < |\eta| < 2.7$ because the particle flux in this region is beyond the maximum readout rate of MDT (with only 150 Hz/cm^2). The resolution of measurements of the wires is $\sim$60 μm, and 5 mm in the transverse plane (ϕ direction).

The RPC in the barrel region (covering $|\eta| < 1.05$) and TGC in end-cap regions (covering

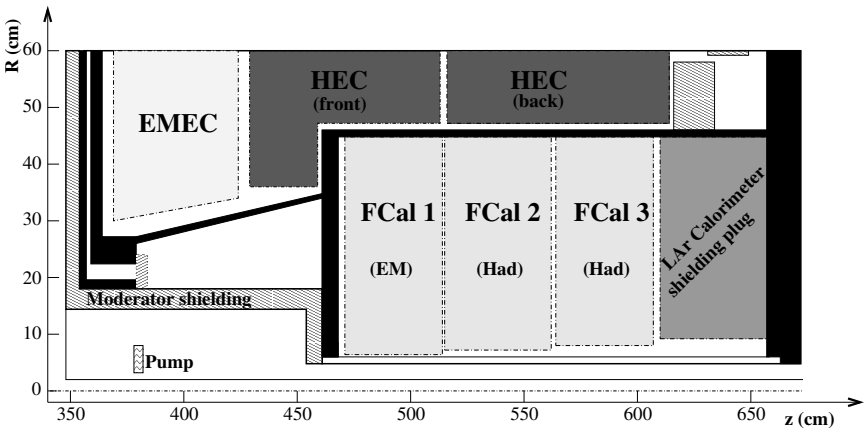

Figure 2.17: A schematic view of the LAr forward calorimeter and its modules.

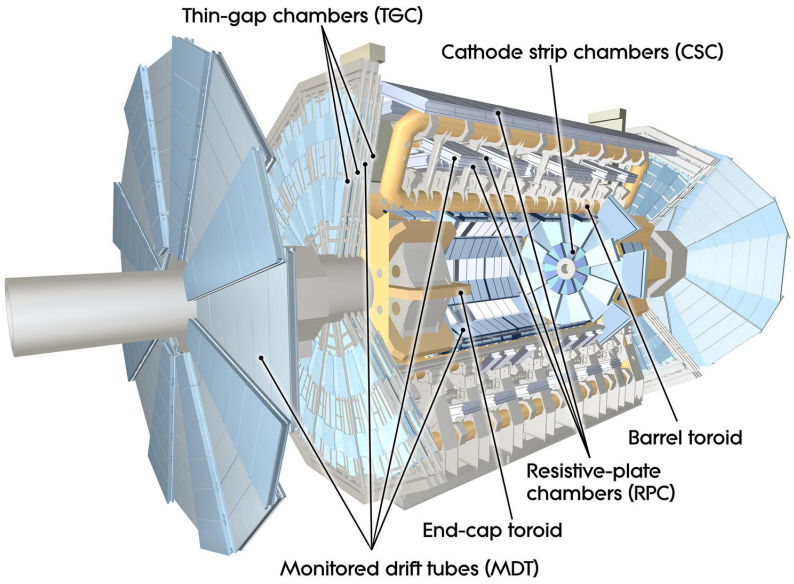

Figure 2.18: Layout of ATLAS Muon Spectrometer.

$1.05 < |\eta| < 2.4$) are used for triggering purpose. The timing resolution of the two are very high, of 1.5–4 ns, which allows to identify the bunch crossing (the bunch space of LHC is 25 ns). They also pre-define the threshold of transverse momentum for trigger selection. The resolution in RPC is 10 mm in z-direction and for TGC are 6 mm in R and 7 mm in ϕ.

2.4 ATLAS Trigger system

The bunch spacing of pp collisions at LHC is 25 ns, which delivers an extremely high event rate that costs huge computing resource and storage to write. The ATLAS trigger system is designed to reduce such high event rate to about 500 Hz so that the events can be written in storage, serving the purpose of selecting rare interesting events (from very rare processes or new physics) out of large background from pp collisions.

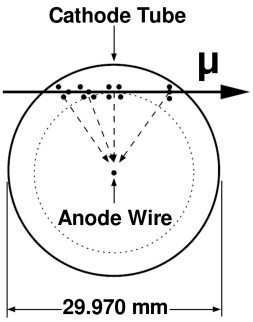

Figure 2.19: Cut-view of a drift tube in MDT. Muons passing through the tube ionise the gas mixture filled in the tube and the ions are collected at the anode placed at center

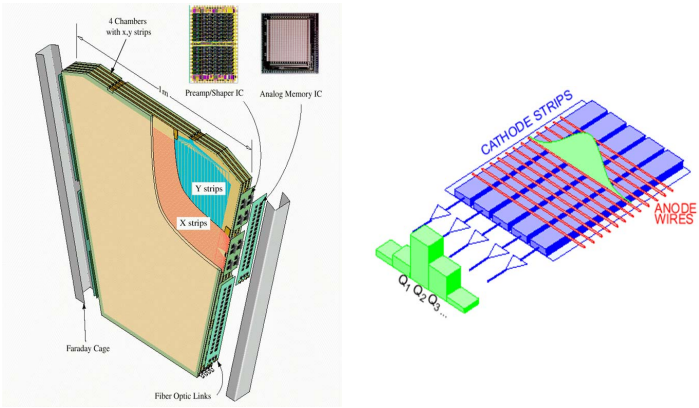

Figure 2.20: Overview of a CSC (left) with anode wires and cathode strips placed perpendicular to each others (right).

Figure 2.21 illustrates the trigger system in ATLAS detector: the system is divided into three stages: Level 1 (L1), Level 2 (L2) and Event Filter (EF). The L2 and EF are often referred to as High Level Trigger (HLT). The detailed description of these three levels will be discussed in the following subsections.

2.4.1 First Level Trigger

The Level 1 receives signals from calorimeter and muon system. Its main purpose is to reduce the event rate from 40 MHz to about 75 kHz with a latency of 2.5 μs (all the data from all sub-detectors will be stored in the pipelines during this latency). The decision on L1 trigger is based on the energy thresholds of the objects in sub-detectors like EM clusters, electrons, muons, photons, jets, missing transverse energy, etc... The algorithms used to compute these objects are based on the trigger towers of 0.1×0.1 granularity in $\Delta\eta\times\Delta\phi$ [58]. All the information about these objects will be identified as "Region of Interest" (RoI) at L1 trigger, and later transferred to L2 for further processing.

The limit number of L1 configurations (or L1 items) available at anytime is 256, and each L1 item is the combination of certain L1 thresholds. A prescale factor can also be specified

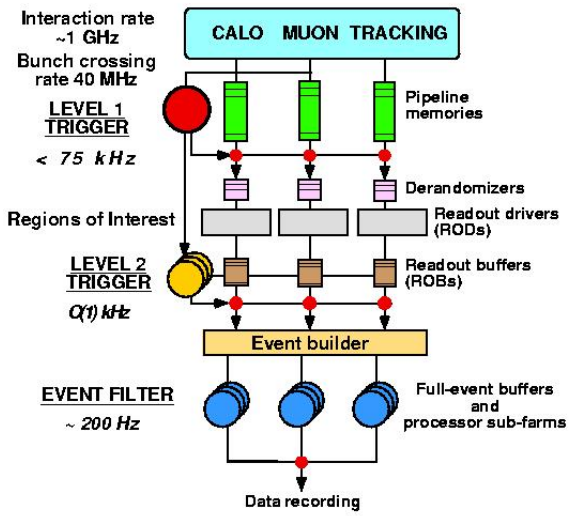

Figure 2.21: Overview of ATLAS trigger system.

for these L1 items[5].

Data-taking is divided into time intervals of the order of one minute, called luminosity blocks. These luminosity blocks are the smallest size of data which can be monitored and available for physics analysis. Within a luminosity block, the information of L1 trigger like trigger configuration and prescale factors remains unchanged.

2.4.2 Second Level Trigger

The L2 trigger [59] is a software-based system using a farm of PCs to run the selection algorithms. It accesses all information from all sub-detectors in the RoI identified by L1 to create a seed of information of each trigger accepted by L1 containing p_T threshold and $\eta - \phi$ position, using this seed to construct a RoI window, the size of this window depends on the type of triggered object.

The L2 triggers use refined algorithms with more optimal calibrations that improve the resolution. The L2 has the ability to access the information that is not available at L1 (for example the track reconstruction in ID); further rejection as well as higher purity can be achieved at L2 using information from sub-detector systems.

The L2 provides additional rejection compared to L1, reducing the event rate from 75 kHz to $\sim$ 2 kHz during operation of detector. The latency of L2 is about 10 μs, and the average time for processing is about 40 ms, including data transferring time.

2.4.3 Event Filter

The Event Filter [59] is the final online selection performed by software algorithm. It receives the information from L2 and uses them as seed for a more refined analysis. The

[5]The prescale factor is defined as only 1 event over N events pass for further HLT processing

EF uses algorithms more similar to offline reconstruction, which is more complex, providing more rejection at EF.

The EF receives the events at a rate of 2 kHz, with a processing time of 4s per event during nominal operation, and will further reduce the rate to less than 1 kHz. The output rate of EF is limited by offline computing resources and budget.

Chapter 3

Identification of *b*–jets

The goal of our analysis is to identify the Higgs boson in the decay mode $H \to b\bar{b}$, the two b quarks ending up as jets in the detector. Thus the identification of jets originated from b hadron (called b-tagging) in the ATLAS detector plays an important role in our analysis. The b-tagging is not only useful for the search of Higgs boson in $H \to b\bar{b}$ but also important in the other searches for new physics (SUSY, discover new particles for example). In this chapter we discuss the b-tagging algorithms, some studies we realized and the use of b-tagging in our analysis.

The b-tagging algorithms rely on reconstructed tracks in detector that are associated to jets (so-called track-to-jet association). This chapter introduces a new track-to-jet association: the ghost-association, and we later study how the b-tagging algorithms perform using this new association.

Finally, the application of b-tagging in our Higgs analysis will be described: which algorithm is the best choice and how to deal with possible differences in data and in simulation.

3.1 Jet algorithms in ATLAS detector

As b-tagging algorithms operate on jets stemming from the fragmentation of b-quarks, let us first give some basic information about the jet reconstruction in the ATLAS detector.

3.1.1 Introduction

Jets are created in the detector from the hadronization of quarks and gluons in a very localized space, typically in a cone whose axis close to the initial quark/gluon direction.

Almost all the physics studies in ATLAS involve jet reconstruction. Generally there is no universal jet finder algorithm, the jet finder depends on the physics processes that we want to study (for instance, in $t\bar{t}$ process, we are interested in narrow jets while in measurement of cross–section of jets from QCD processes, we prefer wide jets). The basic guidelines for jet reconstruction are discussed in Ref. [60].

Jets are reconstructed in ATLAS calorimeter system based on the clusters of energy deposited in calorimeters. They could also be partially reconstructed using tracks in the Inner Detector to get an independent jet measurement from calorimeters.

3.1.2 Standard jet algorithm: anti-k_t

3.1.2.1 Jet algorithm

All objects (such as tracks, particles, or more often clusters in calorimeters) can be clustered together to reconstruct jets using jet algorithm. The most used jet algorithm in ATLAS is anti–k_t [61,62]. This algorithm is a fixed–cone jet finder which follows a sequential recombination algorithm for all the input objects based on the following quantity:

$$d_{ij} = \min(\frac{1}{k_{T,i}^2}, \frac{1}{k_{T,j}^2})\frac{\Delta R_{ij}^2}{R^2} \tag{3.1}$$

where i, j is the index of the 2 arbitrary objects, $k_{T,i}$ is the transverse momentum of the object i, ΔR_{ij} is the distance in $\phi - \eta$ plane between object i and j, R can be understood as the radius parameter for the algorithm, and d_{ij} can be understood as "distance" between the two objects i, j. We also define the quantity $d_i = 1/k_{T,i}^2$ which is the distance between the object i and the beam.

When the minimum value in the list of distances d_{min} is some d_{ij}, then the objects i and j are combined into a new object k, therefore recreating the list of objects.

If $d_{min} = d_i$, the object i is considered as a final jet. This method is repeated until all jets are found.

The distance R is chosen to control the size of the jets, common chosen value of R is 0.4 for narrow jets, and R =0.6 for wide jets.

There are other jet algorithms available that we don't use in our study: k_t and Cambridge/Aachen. The principle of k_t is the same as anti–k_t but uses the transverse momentum k_t^2 in the jet finding algorithm instead of using $1/k_t^2$. For the Cambridge/Aachen, particles and tracks are clustered using spatial separation, not considering momenta nor energies.

3.1.2.2 Jet calibration

The jet energy measured in the calorimeter should be calibrated to the energy at particle level because notably of the energy loss when particles pass the cracked region ($1.37 < |\eta| < 1.52$) or out-of-cone losses. ATLAS provides jet calibration using correction factors derived from Monte Carlo simulation. This is also called *Jet Energy Scale Calibration* [63]. In this method each jet is corrected by a factor as a function of p_{T} and η of jet. The corrections depend on pile-up and jet origin.

3.1.3 Active area of jets

Most of the time we are interested in the jets originating from the hard scattering processes. However the underlying event (UE) and pile-up in the collision can affect our jet measurements because particles from those events can contribute to jet clusters in the calorimeters. The high pile-up can also form jets that overlap with other jets, resulting in ambiguities. To deal with this issue, we introduce the concept of *active area of jet*.

The principle of finding the active area of jets relies on the following steps [64]:

- Get a uniform distribution of low–energy particles (less than 0.01 MeV) called *ghost particles* in rapidity and azimuth.

- All the constituents, including these ghost particles, are then clustered to create jets.
- Since the energy of ghost particles are low, they don't change the result of clustering jets, but more important, these jets contain extra ghost particles, so we can measure the area of the jets by counting the number of ghost particles (present in the jets) times the average area that a single ghost particle fills in calorimeter.

An example of jet areas using the principle above is shown in Figure 3.1. All the jets with high momentum have a circular shape area with certain radius R, while other jets with much lower p_{T} have the crescent shape area.

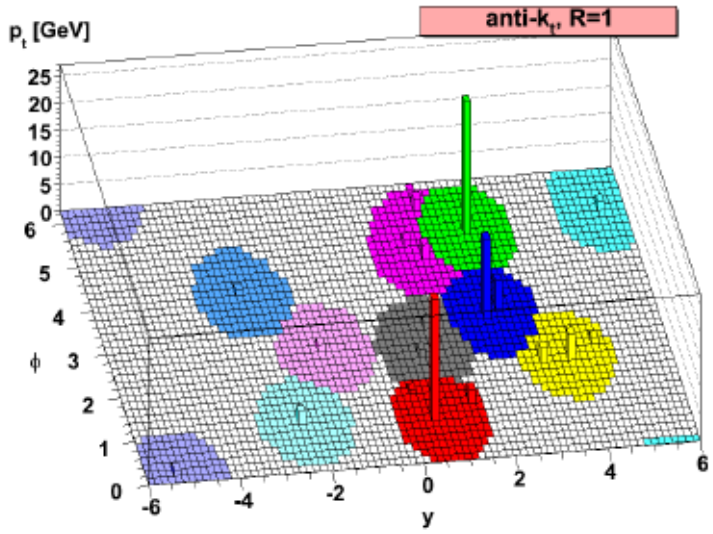

Figure 3.1: Sample of parton-level event with many ghost particle uniformly distributed clustered with anti–k_t algorithm.

The active area of jet is applied to study the jet substructure since the real jet may be originating from more than one particle. The other application is to develop a method of pile-up substraction. All of these applications are detailed in Ref. [64]

Jet Vertex Fraction Most of the time we are interested in jets originating from the primary vertex (which is usually from hard scattering processes in ATLAS detector (see 2.2)), nevertheless the pile-up and underlying events in pp collisions also produce jets, affecting the jet measurement (Fig. 3.2). To distinguish jets from primary vertex and jets from pile-up, we use the quantity called jet vertex fraction (JVF) defined as the sum of p_{T} of all matched tracks from a given vertex divided by the total p_{T} of tracks matched to jet:

$$\mathrm{JVF}(\mathrm{jet}, \mathrm{vertex_j}) = \frac{\sum_k p_{\mathrm{T}}(\mathrm{track_k^{jet}}, \mathrm{vertex_j})}{\sum_n \sum_p p_{\mathrm{T}}(\mathrm{track_p^{jet}}, \mathrm{vertex_n})}$$

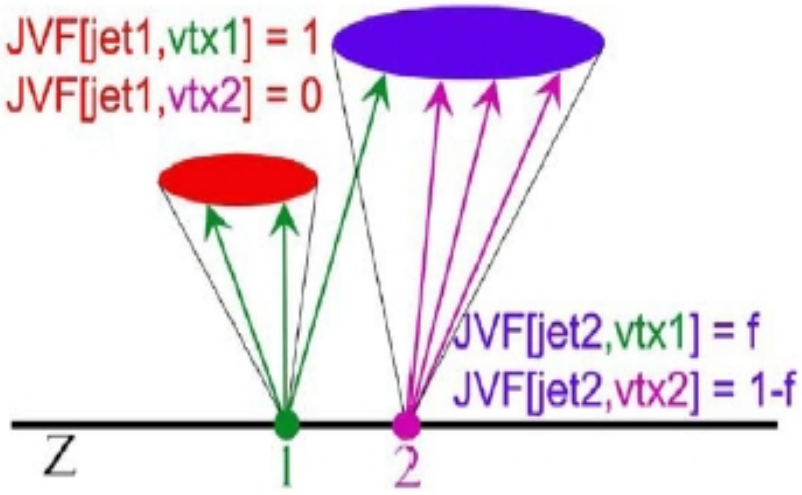

Figure 3.2: Illustration of jet vertex fraction of jet with respect to the given vertices.

The JVF is defined for each jet with respect to each vertex. If jets are from pile-up, the JVF should be zero. Else if they are originated from primary vertex, this quantity will take the value 1. And if no track matched to the jet, we set the JVF to be -1.

3.1.4 Association of tracks to jet

3.1.4.1 Principle of track-to-jet association

Association of tracks to jet is important in our study because tracks are one of the key ingredients in the construction of the b-tagging algorithms. Tracks reconstructed can also participate in jet reconstruction.

After selecting tracks we can associate them to jet. In most of the studies in ATLAS we use the cone matching using the quantity ΔR(jet,track): the track will be associated to a jet if the distance ΔR between the track and the axis of jet in calorimeter fulfills $\Delta R(\text{jet}, \text{track}) < 0.4$. However this method is not optimal because the higher transverse momentum of jet, the more collimated the tracks in jet are (Fig.3.3). Therefore, for a high-p_{T} jet, the cone is too big and collects backgrounds from noise, pile-up, etc... A solution for this issue is to have the cone ΔR varied as a function of p_{T} of jet. In ATLAS, we use $R = 0.239 + e^{-1.22-1.64\cdot 10^{-5}\cdot p_{\mathrm{T}}}$ [65] with p_{T} in MeV, which has been defined to collect 95% of the b hadron hadronization products, regardless of the p_{T}.

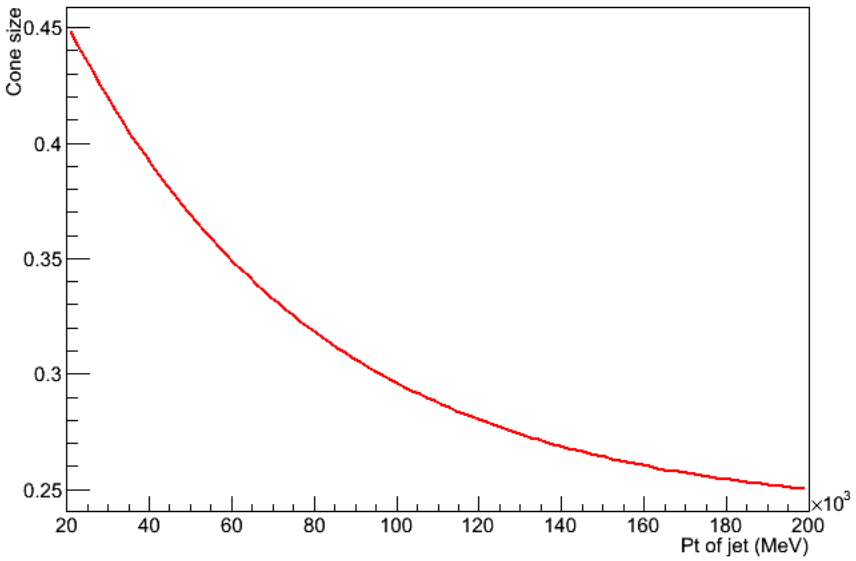

Figure 3.3: ΔR of cone of jet as function of transverse momentum p_{T} of jet

3.1.4.2 Ghost association of tracks to jet

Motivation In the case of isolated jets and low pile–up, the cone–based algorithms (anti–k_t, etc...) can associate well tracks/particles to jet.

In the high pile–up case (appear quite often in high luminosity collisions, especially after the year 2011, when luminosity is more than 3.7×10^{33} cm^{-2}s^{-1}, and particularly in 2012 the luminosity is 7.7×10^{33} cm^{-2}s^{-1}), the jets may no longer be isolated. In addition, the jets can have substructure. The cone–based algorithms cannot associate particles/tracks to a certain jet when regions of tracks/particles in the calorimeters lie in the intersection area of the two jets.

More over, in many situation (especially in boosted regime: boosted top, boosted Higgs, etc...), there always exist situations ($H \to b\bar{b}$ decay, for example) that require b–tagging to work on these jets.

Principle of ghost-association Using the same principle of finding active area of jets described in section 3.1.3, we can construct the algorithm to associate tracks to jets using tracks with low energy (also called *ghost tracks*), so called ghost-association of tracks to jet:

- Create a list of ghost tracks using the same η, ϕ of real actual existing tracks but with low energy,
- Using these ghost tracks and all the other constituents, run the jet clustering algorithm,
- Using the information from calorimeter and from clustering algorithm, we can find the region where ghost track ends up in calorimeter (region of ghost track in calorimeter is

very small) and therefore, tell which real tracks (which the ghosts represent) belong to which jet (Fig. 3.4).

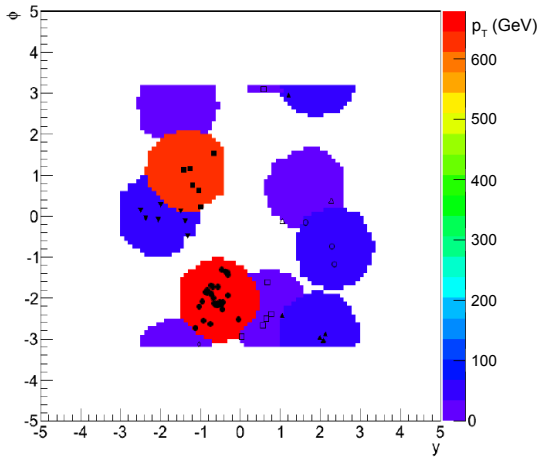

Figure 3.4: Event display in y/ϕ plane showing anti-k_t jets with $\Delta R = 1$ and displaying the use of ghost tracking. Different pattern marks (open or plain circles, triangles, etc...) correspond to tracks belonging to different jets, the colors correspond to p_{T} of jets.

Advantages of ghost-association jet algorithm The ghost-association can solve the ambiguity problem of associating tracks in the border regions of non-isolated jets.

The jet-vertex-fraction (see in section 3.1.4.1) requires association of tracks to jet, and currently use the cone algorithm. However this is not correct if the jets are from pile-up since it is assumed that the jets are cone-shaped and those jets are side–by–side to other jets. Ghost-association algorithm allows to run JVF on subjets, and therefore remove subjets with pile-up dominant.

The ghost–association jet algorithm provides an infrared-safe track matching to non-isolated jets, which is common for the case $g \to b\bar{b}$, $H \to b\bar{b}$.

In this chapter, we will study the performance of b-tagging on ghost-association jets.

3.2 *b*-tagging in ATLAS detector

3.2.1 Introduction

3.2.1.1 Physics motivation

In the Standard Model, it can be seen easily that except for the top quark, the bottom quark's mass is much higher than the others. That means other heavier particles can be coupled with b quark, and decay preferably to this quark flavour, such as top quark (with almost 100% decay to b quark and W boson), the scalar Higgs boson (decay to pair of b quarks is dominant in low mass region), or the other unknown particles (fourth generation quarks, SUSY particles, etc...).

Consequently, identifying the jets that come from the hadronization of b quarks, as well as identifying the other particles originating from the collision, will lead us to reconstruct the initial decayed particles, identifying their properties. Therefore b-tagging has a the key role to discover and study the new physics such as searching for Higgs boson, SUSY.

3.2.1.2 Properties of *b*-jets in detector

In theory, the b quarks have a lifetime of the order of 1.5 ps, therefore they can travel a distance of $c\tau \approx 450\ \mu m$ (in the rest frame) before decaying to other products. For instance, a b hadron in a jet with transverse momentum p_{T} of 50 GeV can have a significant flight path length $\langle l \rangle = \beta\gamma c\tau$, traveling around 4 mm in the transverse plane before decaying, this distance is significant enough to be measured in the detector.

There is a large fraction of b hadron which decay into c hadrons, which will decay into lighter hadrons. Along the b hadron path, at the point where b hadron decays, one can determine the displaced tracks and secondary vertex, therefore measure the track impact parameter, which is the closest distance of tracks to the primary vertex point (Fig. 3.5).

The large mass of b hadrons (more than 4 GeV) implies that the open angles and transverse momenta of the decay products with respect to b hadron flight direction will be different from other jets. The b-jets will have a wider cone, higher number of constituent particles and large invariant mass.

In addition, b–quark fragmentation is hard, that means the b hadron retains about 70% of the b quark momentum.

There is another important characteristic of b hadron decay: semi-leptonic decay. This decay mode has a branching ratio of 36% for each lepton flavour (e, μ or τ), and including cascade decays like $B \to D \to lX$. This decay mode has high purity and low correlations with the track-based algorithms, which can be used for checking and calibrating purposes on data.

3.2.2 Key ingredients for *b*-tagging

Using the properties of b hadrons in detector discussed in section 3.2.1.2, one can establish the b-jet identification algorithms based on the following means:

- Measuring the impact parameters (IPs) of the tracks coming from B hadron decay products (the distance of closest approach of the track to the primary vertex point). As shown in Fig. 3.5, tracks from b-jets tends to have large IPs compared to the tracks coming from primary vertex.

- Using the flight distance of b hadron, one can measure this distance by reconstructing the secondary vertices created by the decay products. The existence of a secondary vertex is a strong hint of b-jet appearance. Moreover, the secondary vertex contains a large fraction of b-jet energy.

- Utilizing the semi-leptonic decay of b hadron: because the b hadrons have hard fragmentation and high mass, the leptons in jets also have large transverse momentum, therefore large momentum relative to the jet axis. In this context we won't discuss much the detail (more in reference [59]) of semi-leptonic tagging.

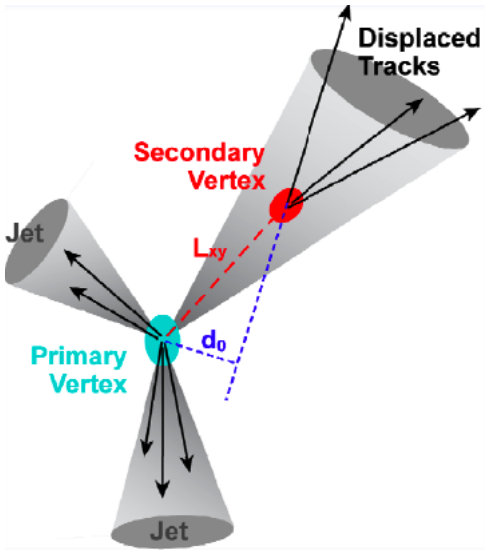

Figure 3.5: Figure of b-jet decay products: displaced tracks and secondary vertex.

3.2.2.1 Tracks

The most important ingredient for b-tagging is track reconstruction because they are key objects to reconstruct vertices (primary/secondary vertex), as well as measuring the impact parameters. Tracks to be associated to jet must pass the good quality selection mentioned in section 3.1.4.1. There is another selection of track in order to use them for b-tagging purpose (usually called b-tagging quality): we aim to select the well-measured tracks and reject fake tracks from long-lived particles (K_S, Λ and other hyperon decays) and interactions in detector (gamma conversions, for example), so the extra requirements are: at least 2 hits in pixel detector and one of them must be in the b-layer, the other requirements are $|d_0| <$ 1 mm and $|z_0 - z_{PV}| \sin\theta < 1.5$ mm. This selection is applied on all the IP-based b-tagging algorithms (summarized in Table 3.1).

Table 3.1: Track selection for IP–based b-tagging algorithms

Variables	Cut value
p_{T}	>1 GeV
$\lvert d_0 \rvert$	$<$ 1 mm
$\lvert z_0 - z_{PV} \rvert \sin\theta$	$<$ 1.5 mm
$\lvert \eta \rvert$	$\leq$ 2.5
Number of hits in b-layer	$\geq$ 1
Number of hits in Pixel Detector	$\geq$ 2

For the secondary vertex (SV) based algorithms, we use looser track selection [66] so as to optimize the efficiency to reconstruct decay products of neutral particles with long lifetime (K^0, Λ^0, etc).

For ghost-association, the tracks will pass an additional selection in order to obtain good quality before applying the b–tagging algorithms. This additional track selection for ghost-association algorithm is shown in Table 3.2.

Table 3.2: List of variables of track selection for ghost-association and their cut values.

Variables	Cut value
p_{T}	> 0.5 GeV
$\lvert\eta\rvert$	≤ 2.5
$\lvert d_0\rvert$	5. mm
$\lvert z_0 - z_{PV}\rvert \sin\theta$ for b-tagging	< 100 mm
Number of hits in Pixel	≥ 1
Number of hits in SCT	≥ 6
Number of hits in Si	≥ 6
χ^2/N_{dof} [a]	5

[a] This is the quality of the fit of track reconstruction

3.2.2.2 Primary vertex

The primary vertex (PV) from the hard scattering process plays a vital role in any b-tagging procedures since this is the first element to be determined in order to measure the other quantities relative to it, such as IP of tracks and the displaced vertices. The reconstruction of PV bases on the track reconstruction following 3 steps:

- Vertex finding: build vertex candidates from tracks.
- Choice of PV: pick-up one of the primary vertex candidates: By default in ATLAS, the vertex maximizing $\Sigma_{\mathrm{tracks}} p_{\mathrm{T}}^2$ is chosen.
- Vertex fitting: Reconstruct the position of primary vertex, so as their covariance matrix, then recalculate track parameters using the vertex constraint, and refit the incident track parameters. The fitting uses the adaptive vertex fitting algorithm [67].

3.2.2.3 Impact parameter

The impact parameter is the distance of closest approach of the track to the primary vertex as mentioned earlier. It is the key point to distinguish the tracks from the displaced vertices from tracks from the primary vertex. To measure the impact parameter, in the ATLAS coordinate system, we define the following quantities:

- The transverse impact parameter d_0, it is the impact paramenter in the $r-\phi$ (transverse plane)

- z_0: the coordiate along the z-axis of the point of closest approach
- $z_0 \sin\theta$: often used as the longitudinal IP

To have an idea how well the impact parameters are reconstructed, one can divide the IP of a track by the error of its measurement (it is the combination of the IP resolution and error of reconstruction of PV). This quantity is called IP significance:

$$\frac{d_0}{\sigma(d_0)} = \frac{d_0}{\sqrt{\sigma^2(d_0^{track}) + \sigma_{PV}^2}} \tag{3.2}$$

Signing impact parameter There are two possibilities of track position with respect to jet direction:

- Tracks that intersect the jet flight axis "downstream" the PV (which is more likely compatible with the fact that those tracks start from a displaced vertex in the direction of flight as expected for b hadron),
- Tracks intersecting the jet flight axis "in front of" (or "upstream") the PV (Fig. 3.6).

To distinguise these two cases, we define the sign of impact parameter using the jet direction $\vec{P_{jet}}$ (measured in calorimeter), the direction $\vec{P_{trk}}$ and track position $\vec{X_{trk}}$ (at the point of closest approach to the position $\vec{X_{PV}}$ primary vertex), then the sign of the impact parameter is calculated as:

$$\text{sign}_{3D} = \text{sign}(\vec{P_{jet}} \times \vec{P_{trk}}) \cdot (\vec{P_{trk}} \times (\vec{X_{trk}} - \vec{X_{PV}}))) \tag{3.3}$$

Figure 3.7 shows the two-dimentional distribution of signed transverse IP significance and signed longitudinal IP significance using MC simulation for tracks in $b-$ and light-jets. We can observe that the $b-$jets tend to have positive sign. These properties will be used in several b-tagging algorithms which will be discussed later.

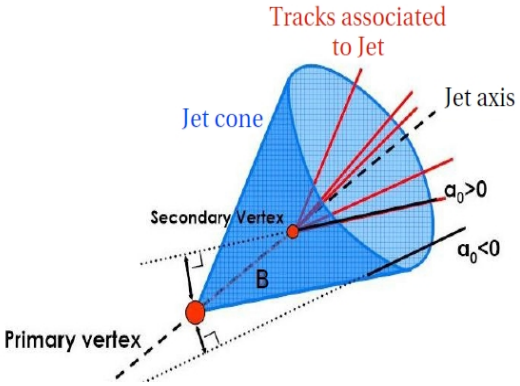

Figure 3.6: The impact parameter sign for different position of track: positive (negative) if the point of minimun approach of tracks to the primary vertex is in the same direction (opposite direction) that the jet with respect to the primary vertex.

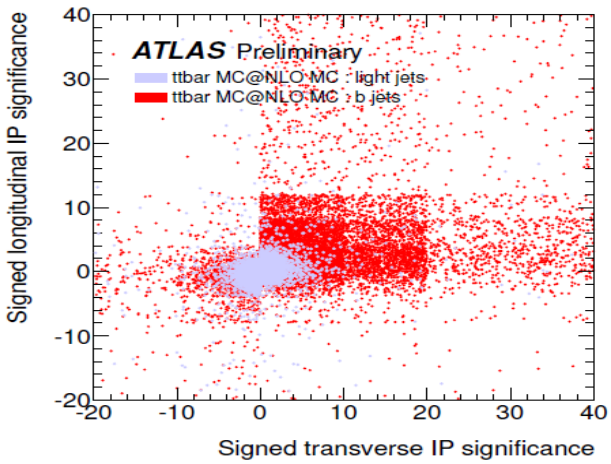

Figure 3.7: Signed longitudinal IP significance vs signed transverse IP significance for tracks in b-jets (red) and light-jets (grey).

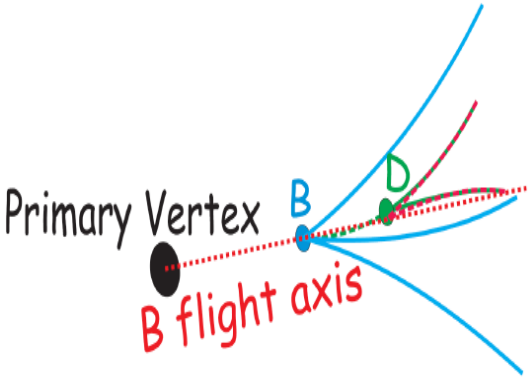

Figure 3.8: Decay chain inside a b-jet and the fit for multi-vertex using b hadron flight axis [68].

Figure 3.9: Inclusive vertex fit inside a jet [68].

3.2.2.4 Secondary vertices

b hadrons usually decay weakly to c hadrons (note that $|V_{cb}|^2 \gg |V_{ub}|^2$), which then decays later to lighter products. As a result, the typical topology of the particles in a b-jet is a decay chain with at least two vertices, one is from b hadron decay and the other from c-hadron decay (Fig. 3.8).

Attempting to resolve the b- and c-vertices separately from the decay chain is very difficult because of the following reasons:

- The probability to have at least two reconstructed charged particles both from b- and c-hadron decays is hard to reach 100% efficiency, because of the charged particle multiplicities as well as the limited track reconstruction efficiency caused by the interactions in the detector.

- The resolution of the relevant track parameters, especially at low transverse momenta,

are not sufficient to separate the two very close vertices efficiently.

Therefore the main approach consists in reconstructing an inclusive secondary vertex, a kind of average of the two vertices. It is based on the default reconstruction of fitting a single geometrical vertex. This method is to select displaced tracks that form a good vertex, only tracks associated to jets and far from primary vertex are chosen, then all these tracks are combined to obtain an inclusive single vertex (Fig. 3.9). This hypothesis is not correct completely, but a good approximation for a large fraction of cases. The b-tagging algorithms using it are $SV0$ and $SV1$ (see later).

In ATLAS, an algorithm was developped to attempt to reconstruct the two vertices. It is based on kinematical approach by assuming that PV, b- and c- hadron decay vertices lie on the same line, which is the flight path of the b hadron. This method has several advantages, such as the ability to reconstruct the incomplete topologies, increasing the chance to separate b/c vertices, and improving rejection against light quark jets. This algorithm is called $JetFitter$.

3.2.3 *b*-tagging algorithms

Now we have gathered all the necessary ingredients for constructing b-tagging algorithms. In this section we will discuss about various standard b-tagging algorithms, as well as the combined b-tagging algorithms. The performances of b-tagging algorithm is included as well.

We will refer to the b-tagging algorithms as "taggers".

3.2.3.1 Likelihood ratio formalism

Some of b-tagging algorithm that we will introduce later uses the likelihood ratio method. This method is done as follows:

- Measure value X_i of a discriminating variable and use it to compare with the pre-defined smoothed and normalized distributions for two hypotheses of b- and light-jet, $b(X_i)$ and $u(X_i)$. The $b(X_i)$ and $u(X_i)$ functions can be the probability density functions (PDF). Each tagger has its proper PDF.

- Calculate the weight of jet defined as:

$$W_{jet} = \Sigma_{i=1}^{N_{track}} \ln W_i = \Sigma_{i=1}^{N_{track}} \ln \frac{b(X_i)}{u(X_i)},$$

  where N_{track} is the number of individual track in jet.

3.2.3.2 *IP3D* algorithm

The principle of $IP3D$ algorithm is to use the signed transverse IP significance $d_0/\sigma(d_0)$ and signed longitudinal IP significance $z_0/\sigma(z_0)$ (Fig. 3.7) and their correlation (2D PDF). The information are combined via a likelihood ratio.

3.2.3.3 *SV0* algorithm

This b-tagging algorithm is based on the 3-dimensional distance between PV and an inclusive reconstructed secondary vertex divided by the error on its measurement. This quantity, called $SV0_{weight} = L_{3D}/\sigma(L_{3D})$, shows how well the SVs being reconstructed. It is signed like the IPs. We can see from Fig. 3.10 that the low decay length significance region is dominated by c- and light jets, and the b-jets takes advantage in high decay length significance region. Thus we can use this discrimination to place a cut of $SV0_{OP}$ to decide:

- If $SV0_{weight} > SV0_{OP}$: the jet is tagged as b,
- If $SV0_{weight} \leq SV0_{OP}$: the jet is tagged as non-b.

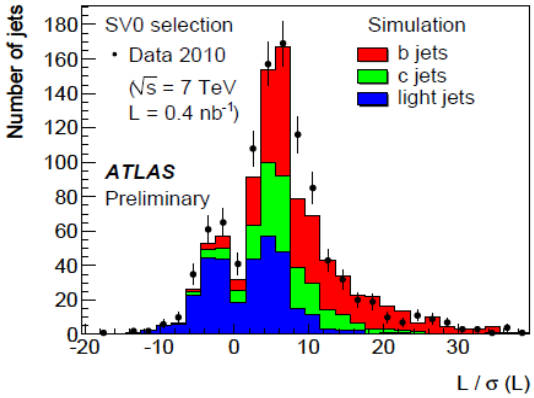

Figure 3.10: The 3-dimensional decay length significance and signed with respect to the jet axis for secondary vertices reconstructed in data events (markers). The expected events from simulation is normalized to the number of jets in data and superimposed [66].

Varying the value of $SV0_{OP}$ allows us to adjust the operating point of this algorithm, *i.e* defining its performance.

3.2.3.4 *SV1* algorithm

The $SV1$ algorithm is also a likelihood ratio algorithm and takes advantages of the following secondary vertex properties:

- The invariant mass of all tracks associated to the vertex.
- The ratio of the sum of the energies of the tracks originated from the vertex to the sum of the energies of all the tracks in the jet.
- The number of vertices in the jet (excluding the vertex of neutral decays or material interaction).
- The distance between the jet axis and the line connecting the PV to the SV.

3.2.3.5 *JetFitter* algorithm

This algorithm exploits the weak decay of b- and c- hadron inside the jet as introduced earlier in Sec.3.2.2.4. A Kalman filter is used to find the line on which b- and c-vertices lie, as well as their position, giving an approximated flight path of b hadron. Thus the b- and c-vertices don't have to be merged (compare with the case of $SV0$ and $SV1$ that using inclusive reconstructed vertex) even if they contain only a single track. More detail this algorithm can be found in references [59, 68].

3.2.3.6 Combined taggers

There are algorithms which combine previous algorithms using different methods:

- $IP3D + SV1$: This algorithm can be achieved by summing the weights of the $IP3D$ and $SV1$ algorithms.
- $IP3D + JetFitter$ (or $JetFitterCombNN$): This combination use the artificial neural network techniques with Monte Carlo simulation traning samples and other variables describing the topology of the decay chain [59].
- $MV1$: This is an artificial Neural Network (NN) combination of the $IP3D$, $SV1$ and $JetFitterCombNN$ weights. MV1 is the recommended algorithm for all ATLAS physics analyses in Run 1.
- $MV1c$: This algorithm is similar to $MV1$, but with a better rejection of c-jets.

For the $VH \to b\bar{b}$ analyses, the b–tagging algorithm $MV1c$ is used instead of $MV1$. This is because the c-jet mis-tag rate is high in $MV1$ since this algorithm is trained only with b-jets and light-jets as background and didn't include the presence of c-jet. The $MV1$ is optimized only for discriminating b-jets from light jets.

3.2.4 Performance of *b*–tagging algorithms

In this studies, only jets with p_{T} >15 GeV and $|\eta|$ <2.5 are chosen to be taggable jets (jets that will be used for b-tagging). The events which don't contain a primary vertex are neglected. We use the sample of simulated $t\bar{t}$ events, which were generated with the MC@NLO generator assuming the mass of top quark is 172.5 GeV.

3.2.4.1 Labelling of jet

To estimate the performance of b-tagging algorithms, we need to specify the type of particles from which the jet originates: this is called *jet labelling*.

Jets are labelled as a b-jets if a b quarks with $p_{\mathrm{T}} > 5$ GeV is found in a cone of $\Delta R = 0.3$ around the jet direction. We also have the same labelling definition for c-jets. If neither b or c quark are founded, then the τ lepton is looked for, and jet will be labelled as τ-jet. If the jets don't contain b, c quarks or τ lepton, they will be labelled as light-jets.

3.2.4.2 Statistical use

We need to determine how well the b-tagging algorithm can be used to identify a jet as b-jet. Indeed, the actual flavour of jets can never be identified with 100% certainty due mostly to experimental limitations. So we can only tell the *performance* of a b-tagging algorithm using statistical concept.

For b-tagging algorithm study, we define two quantities: the b-tagging efficiency and the mis-tagging rate. The b-tagging efficiency ϵ_b is defined as the fraction of taggable jets labelled as b-jets which are tagged as b-jets by the algorithm. The mis-tagging rate is the fraction of taggable jets not labelled as b-jets but are tagged as b-jets. In the performance study we will use the *light-jet rejection* (labelled as r_u) instead of mis-tagging rate: it is defined as the inverse of mis-tagging rate.

3.2.4.3 Performance of b-tagging algorithm

We define a pair of (ϵ_b, r_u) as an operating point of the b-tagging algorithm. The performace of b-tagging is obtained by varying continuously the operating points of each tagger (i.e cut on its discriminating variable). The b–tagging performance for various algorithms is shown in Figures 3.11 and Table 3.3. For the b–tagging efficiency of 70%, we can observe that the taggers $IP3D$ and $JetFitter$ have mis-tagging rates larger than 3%, while the other combined taggers can achieve a mistag rate around 1%, especially the $MV1$ tagger, which has mistag rate of 0.7%: this tagger shows the best performance overall.

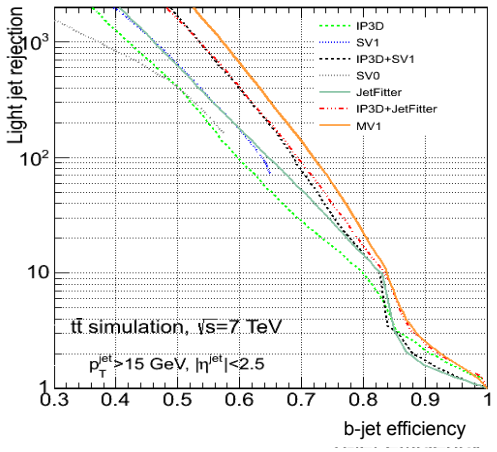

Figure 3.11: b-tagging performance for different taggers, based on simulated $t\bar{t}$ events.

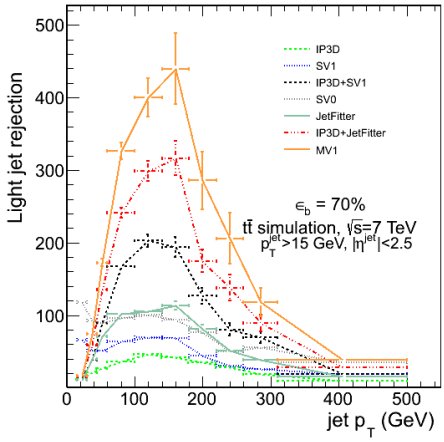

Figure 3.12: Light jet rejection as function of jet transverse momentum p_{T} for b-tagging efficiency $\epsilon_b = 70\%$, based on simulated $t\bar{t}$ events.

The performance of b-tagging strongly depends on the kinematics of the sample, which can be seen in Figure 3.12 which shows the light jet rejection as the function of jet p_{T} for various b-tagging algorithms with the b-tagging efficiency ϵ_b =70% (for all p_{T}^{jet} bins). We notice that the tagging performance is optimal for 100 GeV $< p_{\mathrm{T}}^{jet} <$ 200 GeV. This can be explained as follows: for low p_{T}^{jet}, tracks in jets have relatively low momentum and therefore

Table 3.3: Examples of b-tagging performances for $JetFitter$, $MV1$ taggers for anti-k_t jet algorithm: light-jet rejection for various b-tagging efficiencies.

Efficiency (%)	$JetFitter$	$MV1$
50	619.69 ± 12.06	2882.39 ± 121.01
55	330.95 ± 4.71	1397.2 ± 40.8
60	178.43 ± 1.86	666.94 ± 13.46
65	97.12 ± 0.75	302.86 ± 4.12
70	52.43 ± 0.29	140.35 ± 1.29
75	27.52 ± 0.11	60.03 ± 0.36
80	14.34 ± 0.04	22.58 ± 0.08
85	3.404 ± 0.004	6.85 ± 0.01

the multiple scattering processes wil reduce the resolution of impact parameter, while at high p_{T}^{jet} tracks are more collimated which will affect negatively measurements in the pixel detector and also in the b-layer, reducing the performance [59].

3.3 *b*-tagging performance using ghost– association jet algorithm

3.3.1 Comparison with the standard jet algorithm

As mentioned earlier, the b-tagging can be applied directly to the jets using ghost-association of tracks (we refer as ghost-association jets), like the case of jets using cone matching (we refer as standard jets). Our main goal in this study is to check the b-tagging performance of algorithms applying on the ghost-association jets algorithm and compare them to the b-tagging performance on the standard jets.

The b–tagging performance for ghost-association jet and standard one are displayed in Figure 3.13 and Table 3.4, showing the light rejection in terms of the b–tagging efficiency for tagger $MV1$ for both algorithm. Overall results show that the b-tagging performance on ghost-association jet is lower than the performances for standard jet.

These results may due to the track selection for ghost–association on jet, which selects less tracks to be used for b-tagging algorithms, hence affecting the overall performance on b-tagging. For instance, at the b-efficiency of 70%, the light–jets rejection on standard jet for $MV1$ tagger is around 140, but for the ghost-association jet, the light-jet rejection is reduced to 72.5, meaning a huge lost of 50% of performance (more detail at Table 3.5).

3.3.2 Modification of track selection for ghost-association

The lower b-tagging performances on ghost-association jet in comparison to the standard one may come from the tighter track selection for ghost-association, which allows less tracks to be associated to jets, and therefore less tracks to be used for b-tagging purpose. We

Table 3.4: b-tagging performance for $JetFitter$ and $MV1$ for ghost-association: light-jet rejection for various b-tagging efficiencies.

Efficiency (%)	$JetFitter$	$MV1$
50	439.711 ± 7.21	1724.61 ± 56
55	227.71 ± 2.68	809.26 ± 17.99
60	122.42 ± 1.06	368.88 ± 5.53
65	65.05 ± 0.41	168.72 ± 1.71
70	33.84 ± 0.15	72.5 ± 0.5
75	17.08 ± 0.05	27.59 ± 0.11
80	5.93 ± 0.01	8.61 ± 0.02
85	1.814 ± 0.001	2.959 ± 0.003

Table 3.5: Ratio of light-jet rejections for $JetFitter$ and $MV1$ for ghost-association jets with respect to standard ones.

Efficiency (%)	$JetFitter$	$MV1$
50	0.71	0.598
55	0.688	0.579
60	0.686	0.553
65	0.67	0.557
70	0.645	0.517
75	0.621	0.46
80	0.413	0.381
85	0.533	0.432

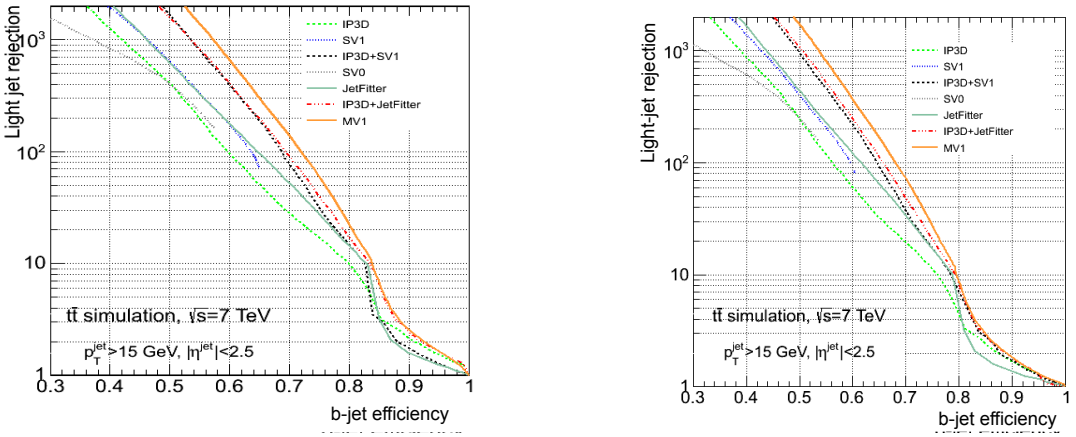

Figure 3.13: The b-tagging performance for anti-k_t algorithm (left) and ghost-association (right).

attempt to modify some cut used for track selection for ghost-association shown in Table 3.2 so that the tracks selected for ghost-association is as close as possible to the same condition of track selected for standard jets (especially on track used for b-tagging in Table 3.1). We will study the effect of each individual cut to see how the b-tagging performance changes.

There is an important notice that we should pay attention: if we want to change the track selection, *the calibration of probability distribution function for each taggers should be redone*, and as a result, this procedure can have an impact on the performance. This study doesn't include the recalibration, so these results we obtain with the modification of track selection should be taken with grain of salt. More over, when the recalibration is done for the likelihood and Neural Network (NN), the more complicated taggers that rely much on the likelihood and NN (like $MV1$, $JetFitter + IP3D$, etc) are sensitive to this modification, and the other taggers not using the likelihood nor NN (like $SV0$) will not be affected much.

From here, to simplify the comparison procedure between the b-tagging performance on ghost-association jets and on standard ones, we divide the light–jet rejection of certain b-tagging algorithm's performance for ghost-association jets by the rejection of the same algorithm for standard jets, this ratio will vary as function of b-tagging efficiency.

3.3.2.1 Modification of requirement on the number of hits

We attempt to modify the requirement on the number of hits of tracks for ghost-association to be looser and closer to the cut values for IP-based b-tagging track selection. We change those cuts as the following:

- Number of hits in Pixel from $\geq$1 to $\geq$2.
- Number of hits in SCT from $\geq$6 to $\geq$0.
- Number of hits in Si from $\geq$6 to $\geq$7.

Now we compare the b-tagging performance on ghost-association jets versus the performance on standard jets after modifying the number of hits. The results is shown in the Figure 3.14, the left figure is just the ratio between the performance for the track selection in the previous comparison, the right one is the results after the modification. The dip in the ratio of light-jet rejection around 80-85% is caused from the difference from the drop on the b-tagging performance between the two association methods. This drop is come from the separation of regions in the b-tagging performance: in the region where b-jet efficiency 85-100%, the instrinsic resolution of detector cannot distinguish b-jet and light-jet, so the discrimination is poor and light rejection increase slowly, in the region where b-jet efficiency 0–85%, the detector can distinguish b-jet from light jet thanks to the decay products of b-hadrons, therefore the light rejection increase greatly.

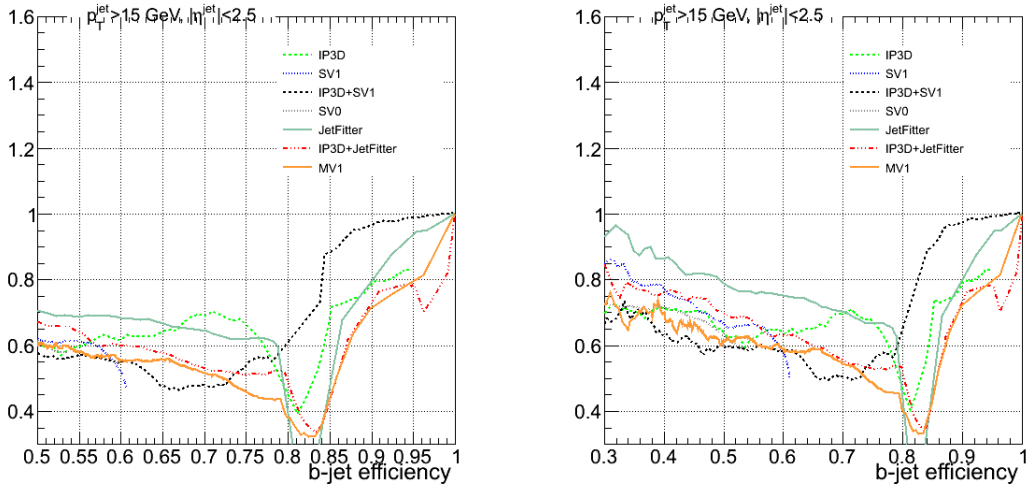

Figure 3.14: Comparison of performance of b-tagging on ghost-association jets with respect to standard jets for the original selection (left) and after number of hits modification (right).

We can observe a slight improvement of b-tagging performance on ghost-association jets for all the taggers, although the overall performance is still lower than the case of standard jets. Further details of these improvements are shown in Table 3.6 for this modification on number of hits over the original track selection.

3.3.2.2 Modification of longitudinal impact parameter cuts

In this part we will check the b–tagging performance differences with modification on variable of longitudinal impact parameter z_0. To be more specific, we drop the cut on longitudinal IP $|z_0 - z_{PV}| \sin\theta$, and we keep the requirements on the number of hits in the inner detector same as section above.

The results on Fig 3.15 and on the Table 3.7 shows an immerse improvements of b-tagging performance on ghost-association after the modification on longitudinal IP variable. The tagger $MV1$ now is very close to the performance on the nominal standard jets, and

Table 3.6: Comparison of b-tagging performance (ratio of r_u) between ghost-association jet and standard jet for tagger $MV1$ after the number of hits modification

Efficiency (%)	Ratio for $JetFitter$	Ratio for $MV1$
50	0.792	0.612
55	0.762	0.611
60	0.753	0.588
65	0.732	0.589
70	0.704	0.544
75	0.668	0.487
80	0.451	0.404
85	0.539	0.438

slightly better for ϵ_b $\geq$70%. The $JetFitter$ tagger, is now giving better performance on standard jets, for b-efficiency less than 80%.

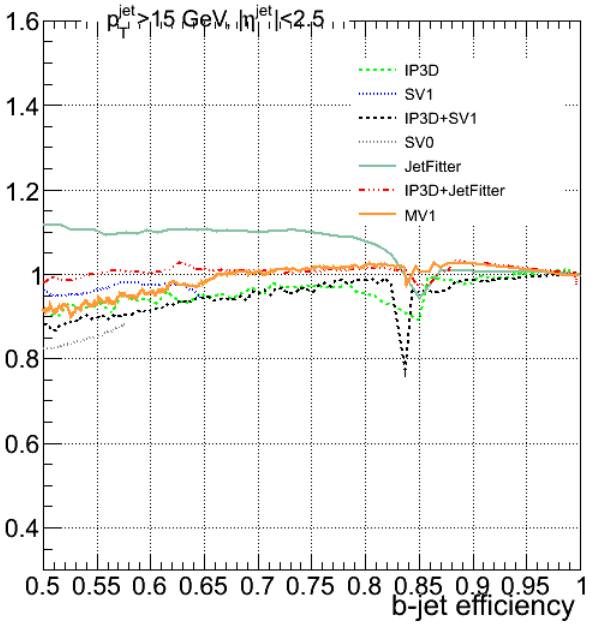

Figure 3.15: Ratio of r_u of ghost-association jets with respect to standard jets when both the requirements on number of hits and the z_0 cut are changed.

So removing the cuts on the longitudinal impact parameter for track selection for ghost-association has a huge impact on its b-tagging performance. This shows that the planned track selection for ghost-association was too tight: we were loosing tracks which were important for b-tagging. Now the b-tagging performances on ghost-association jets may approach (or surpass) the performances on standard jets. Further tests with other modifications on track

Table 3.7: b-tagging performance for taggers $JetFitter$, $MV1$ for the number of hits and z_0 cuts modification.

Efficiency (%)	JetFitter	MV1
50	694.46 ± 14.32	2637.66 ± 105.93
55	365.59 ± 5.47	1295.25 ± 36.45
60	197.2 ± 2.2	636.94 ± 12.56
65	107.7 ± 0.9	296.84 ± 3.99
70	57.57 ± 0.34	141.02 ± 1.31
75	30.29 ± 0.13	60.83 ± 0.37
80	15.49 ± 0.05	23.01 ± 0.08
85	3.213 ± 0.004	6.89 ± 0.01

Table 3.8: b-tagging performance for taggers $JetFitter$, $MV1$ for the number of hits, z_0 and d_0 cuts modification.

Efficiency (%)	$JetFitter$	$MV1$
50	680.12 ± 13.87	2543.83 ± 100.33
55	355.25 ± 5.24	1271.88 ± 35.46
60	191.56 ± 2.07	604.27 ± 11.61
65	104.48 ± 0.83	284.08 ± 3.74
70	55.71 ± 0.32	134.114 ± 1.21
75	29.13 ± 0.12	57.85 ± 0.3412
80	15.02 ± 0.04	21.78 ± 0.08
85	3.075 ± 0.003	6.44 ± 0.01

selection will be studied in the next sections.

3.3.2.3 Modification on transverse impact parameter

We maintain the previous modifications for number of hits and longitudinal IP cuts, then modify the transverse impact parameter d_0. The modification on d_0 will be taken as following: remove the significance of d_0 cut, and change the value of d_0 for b-tagging quality cut from 5 to 2 mm.

The results of this modification (Fig. 3.16, Tab. 3.8) show that the $JetFitter$ tagger still has better performance for ghost-association jet, although it has lower performance than the case without d_0 modification. For the $MV1$ case, the performance is a bit lower than the case in which d_0 cuts aren't modified yet. This can be explained as the new cut on d_0 for b-tagging is tighter and therefore allows less track to be used for b-tagging. We will have another test with looser d_0 cut, which will be discussed in later sections.

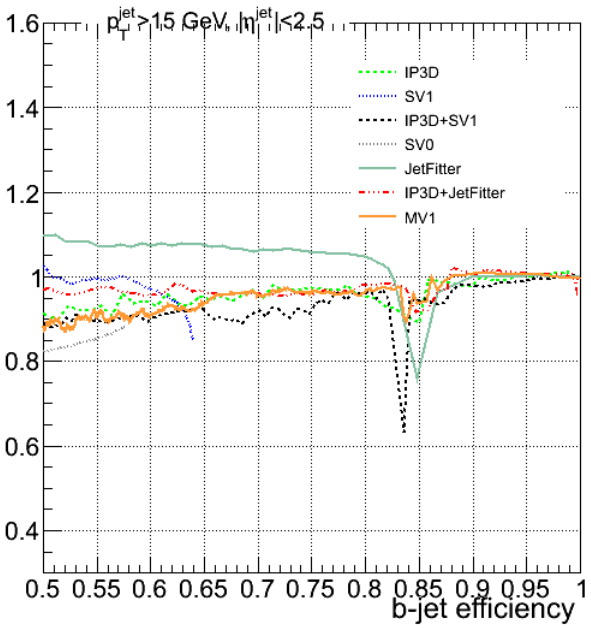

Figure 3.16: Ratio of r_u of ghost-association jets with respect to standard jets for number of hits, z_0 cuts and d_0 cuts modification.

3.3.2.4 Modification of transverse momentum of tracks

At this point, recall that we modified track selection for number of hits, longitudinal IP z_0 cuts and transverse IP d_0 cuts as the following:

- Number of hits on Pixel ≥ 2, on SCT ≥ 0, on Si ≥ 7.
- No cut on longitudinal IP $|z_0 - z_{PV}| \sin\theta$ (including b-tagging quality).
- d_0 cut for b-tagging quality = 2 mm, drop d_0 significance cut.

We keep these cuts and change the requirements on the track p_{T}.

Requiring $p_{\mathrm{T}} > 1$ GeV Currently the selection applies cut of p_{T} at > 0.5 GeV, we will increase this threshold to 1 GeV. Therefore our track selection for ghost-association is closer to the track selection for b-tagging quality (see Table 3.1).

The results for this modification are displayed in Figure 3.17, Table 3.9), showing a huge impact on the performance of *JetFitter* tagger on ghost-association jet: It is better than the performance on the standard jet, plus, even greater than the performance on ghost-association for the modification of number of hits and z_0 cuts.

Requiring $p_{\mathrm{T}} > 2$ GeV We have already seen some improvements of b–tagging performances of *JetFitter* algorithms when increasing the cut of transverse momentum to 1 GeV. It is interesting to see how the b-tagging performs on ghost-association jets if we extend the

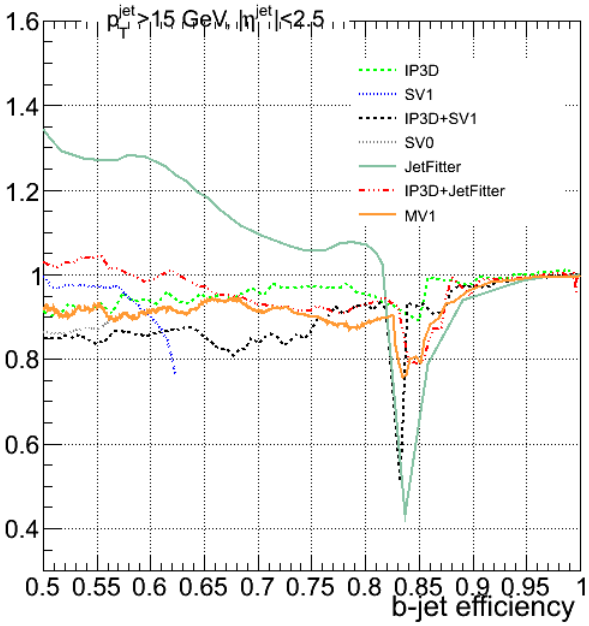

Figure 3.17: Ratio of r_u of ghost-association jets with respect to standard jets for number of hits, z_0, d_0 and $p_T > 1$ GeV.

lower threshold of p_T from 1 GeV to 2 GeV. The purpose is to find if there exist another cut on p_T which allows higher b-tagging performance.

For convenience, we still keeps the previous selection for number of hits, z_0 and d_0 cuts. The only modification here is the cut $p_T > 2$ GeV.

The results in figure 3.18 shows a significant reduction of performance for almost all the taggers ($MV1$, $JetFitter$, etc) compared to the modification of $p_T > 1$ GeV for ghost-association jets, except the $IP3D$ tagger. However the $IP3D$ tagger shows an overall improvement compared to the last modification, especially for b-efficiency > 65 %, its performance is already better than the one for standard jets. This is interesting and imply that we should consider having a specific and tighter cut on p_T for $IP3D$. The other taggers shows that this p_T modification doesn't reach their best performance. So this modification implies that there exist another threshold for p_T of tracks between $1 < p_T < 2$ GeV that we can achieve the better performance for all the taggers (like $MV1$, $JetFitter$, $JetFitterCombNN$).

Requiring $p_T > 1.5$ GeV The results in Figure 3.19 shows that the overall performance for $JetFitter$, $MV1$ is lower than the case of $p_T > 1$ GeV, however like the case of $p_T > 2$ GeV, the tagger $IP3D$ on ghost-association jet is actually higher than on standard jet. If we have a comparison between the two modifications of p_T (Figure 3.20) (compare the performance for $p_T > 2$ GeV and for $p_T > 1.5$ GeV), we can observe that the overall performance of all taggers for $p_T > 2$ GeV is lower than the case of $p_T > 1.5$ GeV. This part can be concluded that the optimal modification for achieving high performance for $IP3D$ tagger on ghost-association jet is $p_T > 1.5$ GeV.

Table 3.9: b-tagging performance for taggers $JetFitter$, $MV1$ for the number of hits, z_0 and d_0 cuts modification.

Efficiency (%)	$JetFitter$	$MV1$
50	837.36 ± 18.98	2640.7 ± 106.1
55	421.84 ± 6.78	1295.33 ± 36.45
60	227.58 ± 2.68	608.07 ± 11.72
65	115.42 ± 0.97	283.01 ± 3.72
70	57.57 ± 0.34	128.05 ± 1.13
75	29.1 ± 0.12	54.05 ± 0.31
80	15.37 ± 0.05	19.95 ± 0.07
85	2.62 ± 0.002	5.44 ± 0.01

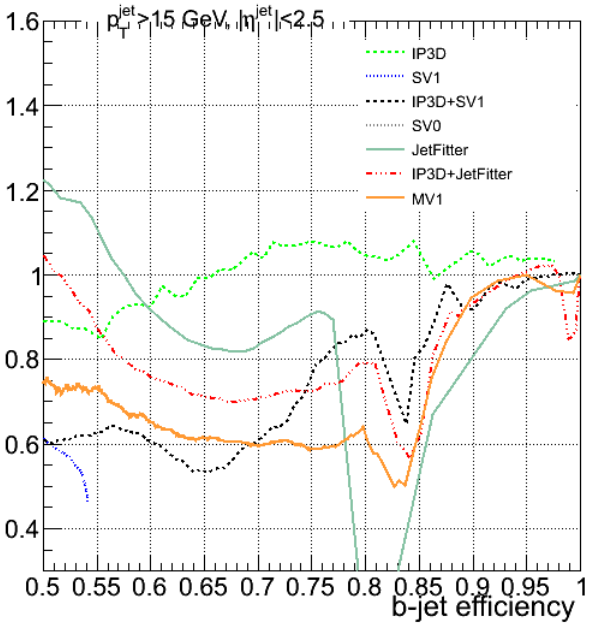

Figure 3.18: Ratio of r_u of ghost-association jets with respect to standard jets for number of hits, z_0, d_0 and $p_{\mathrm{T}} > 2$ GeV.

3.3.2.5 Additional test of transverse impact parameter for *b*-tagging quality

We attempt to modify the cut of transverse impact parameter d_0 for b-tagging quality and see how it affects the performance on ghost-association jets. We keep the previous modifications (number of hits, impact parameter of tracks) and the transverse momentum of tracks has to be > 1 GeV. For this test we will require no cut on d_0 for b-tagging quality.

The obtained results are illustrated in Figure 3.21, suggesting that the b-tagging performance are better than with cut on d_0 for b-tagging, nevertheless it should be noted that we

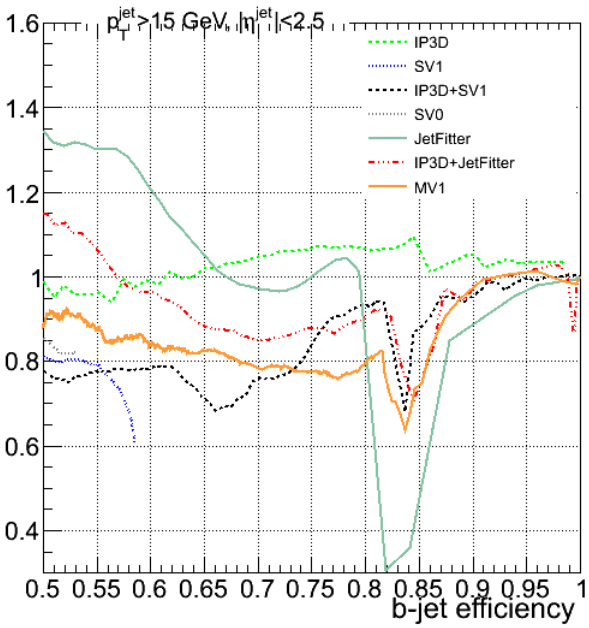

Figure 3.19: Ratio of r_u of ghost-association jets with respect to standard jets for number of hits, z_0, d_0 and $p_{\mathrm{T}} > 1.5$ GeV.

have allowed more tracks from the background jets to be included in the procedure, therefore more jets (mostly light jets) will be included, hence the light rejection increase.

3.3.2.6 Modification on IP-based *b*-tagging quality track selection

The results for the modification of $p_{\mathrm{T}} > 1.5$ GeV show a strong effect for the performance of $IP3D$ tagger. In this part, we will see if the modification on IP-based b-tagging quality track selection on transverse momentum of track has any effect on the b-tagging performance on ghost-association jets. We relax on the based selection for $JetFitter$ and $SV0$ tagger.

We keep all the other cuts for IP-based b-tagging quality track selection in Table 3.1 ($i.e$ d_0, z_0, number of hits...), and modify the cut of p_{T}, from 1 GeV to 1.5 GeV. This modification is expected to change the b-tagging performance on standard jets as well since it will affect on the algorithms using impact parameters.

One important point to be reminded that to change the track selection for b-tagging like this, we actually should recalibrate the b-tagging procedure. Hence the results of performances may change. However this part is not included in this study, so we will just focus on the b-tagging performance comparison between ghost-association jets and standard ones.

Compare the *b*-tagging performance on standard jets before and after the p_{T} modification on IP-based selection We make the comparison of b-tagging performance on standard jets between before and after modification of p_{T}. The results is shown in Figure 3.22, show that except the non-related IP taggers ($SV1$, $SV0$, $JetFitter$), all the taggers

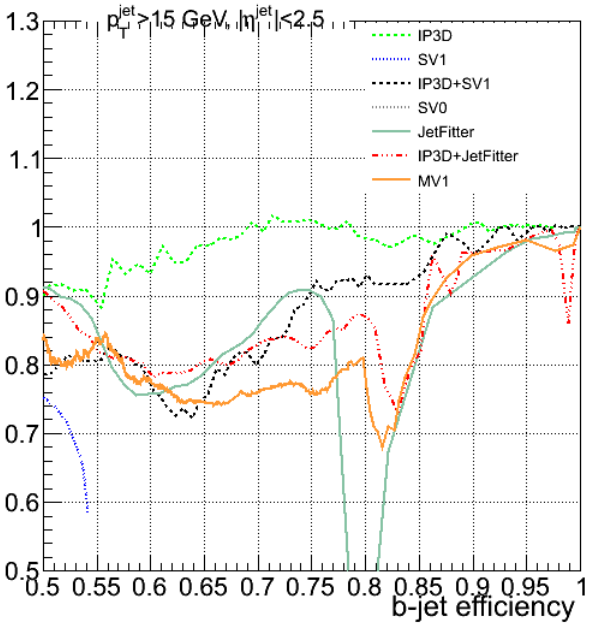

Figure 3.20: Ratio of r_u for $p_{\mathrm{T}} > 2$ GeV with respect to $p_{\mathrm{T}} > 1.5$ GeV for ghost-association after modification of number of hits, z_0, d_0.

related to the IP-based algorithms increase their performance after applying the new cut on p_{T} for IP-based track selection. However the impact is small (a few percent).

Compare the *b*-tagging performance between ghost-association jets and standard jets This comparison of performance is between the two kinds of jets will be based on the following modification: one is $p_{\mathrm{T}} > 1.5$ GeV for IP-based b-tagging quality, the other is $p_{\mathrm{T}} > 1$ GeV for track selection on ghost-association jet. Figure 3.23 shows the results of the comparison. If we compare to the figure 3.17, the results are pretty similar, with the *JetFitter* achieving better performance, while the other taggers are slightly lower. This is expected since we perform the b-tagging on ghost-association jets and standard jets at the same IP-based selection, although the performance on ghost-association jets increases, but the performance on standard jets increases as well.

Compare the *b*-tagging performance on ghost-association jets for p_{T} of track >1.5 GeV This comparison of performance will take $p_{\mathrm{T}} > 1.5$ GeV on track selection of ghost-association, then we will see if this cut provide any improvements on overall b-tagging performance. The results shown in Figure 3.24 show that no improvements is observed.

3.3.3 Conclusion

After various test on b-tagging performance of ghost-association jet by modifying the track selection for ghost-association, we can conclude that the track selection applied for ghost-

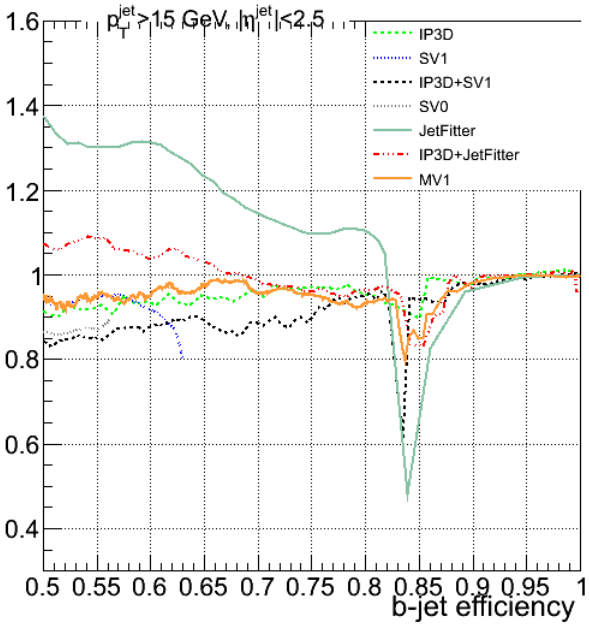

Figure 3.21: Ratio of r_u of ghost-association jets with respect to standard jets for number of hits, z_0, d_0 and $p_{\mathrm{T}} > 1$ GeV and no d_0 cut for b-tagging quality.

association is actually too tight, therefore we lose tracks that are interesting for b-tagging. If we loosen the criteria, then the b-tagging performance for ghost-association come closer to the standard algorithm. The best selection that we can apply for the ghost-association in order to achieve the optimal performance is:

- Drop the cut on IPs for b-tagging quality
- p_{T} of tracks > 1 GeV
- For IP-based selection: $p_{\mathrm{T}}^{track} > 1.5$ GeV
- Keep the IP-based selection, but change $p_{\mathrm{T}}^{track} > 1.5$ GeV for track selection of ghost-association.

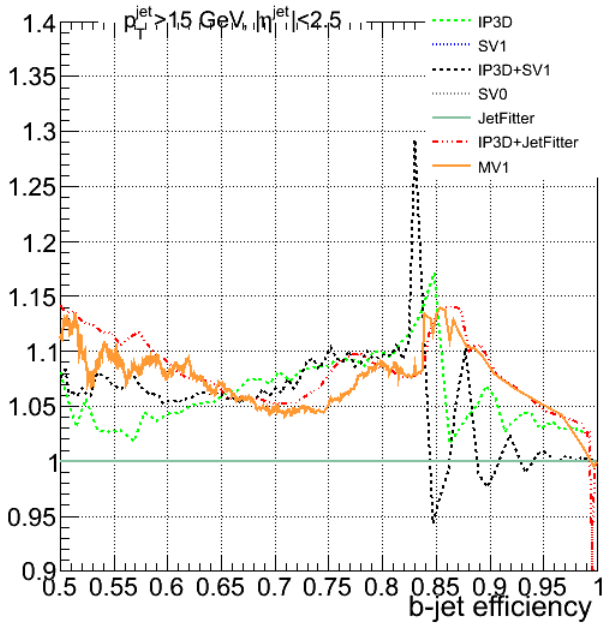

Figure 3.22: Ratio of b-tagging performance for standard jets where the numerator is the performance for p_{T} of IP-based selection greater than 1.5 GeV, and the denominator is before applying this modification.

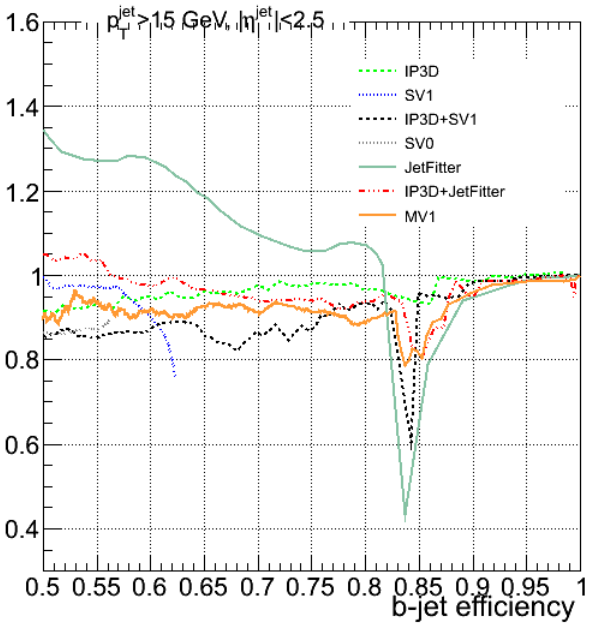

Figure 3.23: Ratio of b-tagging performance between ghost-association jets and standard jets for $p_{\mathrm{T}} > 1.5$ GeV for IP-based quality and $p_{\mathrm{T}} > 1$ GeV of track selection for ghost-association.

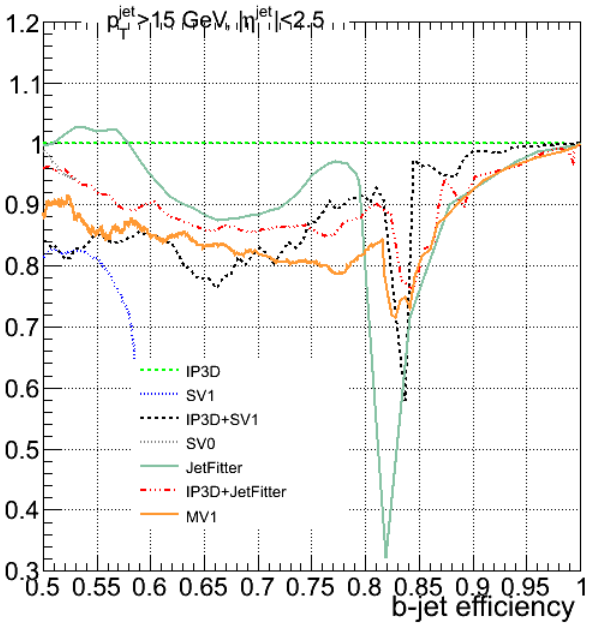

Figure 3.24: Ratio of b-tagging performance for ghost-association jets, the numerator is the performance for p_{T} of ghost-association with $p_{\mathrm{T}} > 1.5$ GeV for track selection, and the denominator is before applying this modification ($p_{\mathrm{T}} > 1$ GeV). The modification of $p_{\mathrm{T}} > 1.5$ GeV on the IP-based selection is applied.

3.4 Applying *b*-tagging for Higgs analysis

3.4.1 Calibration of *b*-tagging algorithms in data

The performance of the b-tagging we studied so far are all defined in MC simulation. Then some questions arise: how can we tag a jet in data? How do we know that the performance of an algorithm will be the same in data and in simulation? To overcome this problem, we need a procedure that checks the agreement between the data and MC, called *calibration* of the algorithm.

There are two quantities to be calibrated with data: b-tagging efficiency and mis-tagging rate.

Efficiency in data For the measurement of b-tagging efficiency in data ATLAS uses two kinds of samples:

- Soft-muon tagging in di-jet events: The QCD processes in pp collisions can be used as a source of b-jet, but the fraction of $b\bar{b}$ production is much smaller. The requirement of muon in jets increases the fraction of events containing b-jet since the semi-leptonic decay of b quark can produce μ. Therefore the efficiency of b-jet tagging can be measured in data using this muon identification. The measurements can be done with two methods: p_{T}^{rel} and $System8$ [69]. Those two methods were used at the start of LHC.

- $t\bar{t}$ events: the LHC is the factory of $t\bar{t}$ production. The decay of top quark to b quark with $\sim$100% of branching ratio is very useful to calculate the b-tagging efficiency: one can count the number of jets tagged as b-jets and divided by the number of $t\bar{t}$ events. The measurement of b-tagging efficiency on this sample has advantage over the soft-muon events because it provides an enviroment with high multiplicity of jets and also b-jet with high p_{T}, which is more common in physics analyses. This is also the sample that currently in use for b-tagging calibration [70].

When the b-tagging efficiency on data ϵ_{data} is extracted and so does on the MC ϵ_{MC}, the scale factor can be calculated as $\epsilon_{data}/\epsilon_{MC}$. The simulation will be scaled by this factor to reproduce the performance in data. The result of efficiency calibration is presented in Figure 3.25 for the calibration using $t\bar{t}$ events, for the $MV1$ tagger:

Mis-tagging rate calibrating For measuring the mis-tagging rate on data, we use the inclusive jet samples where heavy flavours is a small fraction. The measurement use two methods: one is based on the negative impact parameter significance of tracks, and the other is based on the invariant mass of tracks associated to the reconstructed secondary vertex [71]. These measurements are performed in different binning of jet p_{T} and η (Fig. 3.26).

3.4.2 Applying in Higgs analysis

Distinguishing b-jets from c- and light-jets is crucial in our Higgs analysis in the channel $H \to b\bar{b}$. The b-tagging algorithm $MV1c$ is used instead of $MV1$ tagger because of its superior c-jet rejection.

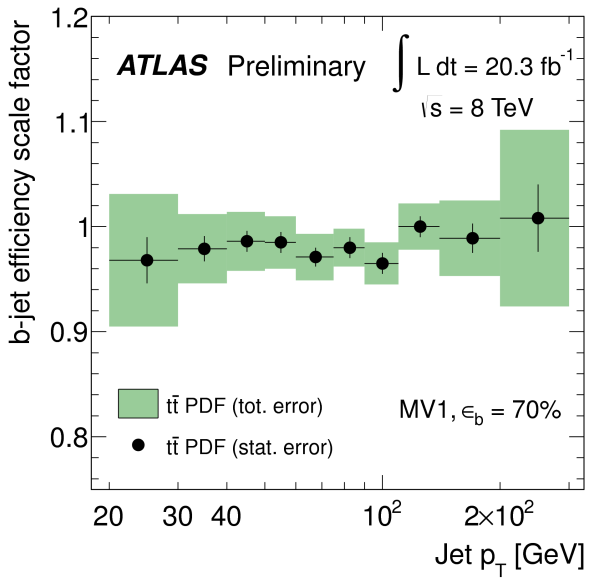

Figure 3.25: The b-tagging efficiency scale factor of data-to-MC for the b-tagging algorithm $MV1$ with 70% of b-tagging efficiency using $t\bar{t}$ events at each bin of p_{T} of jet. The green band represents the total uncertainty of the combination of the two methods [70].

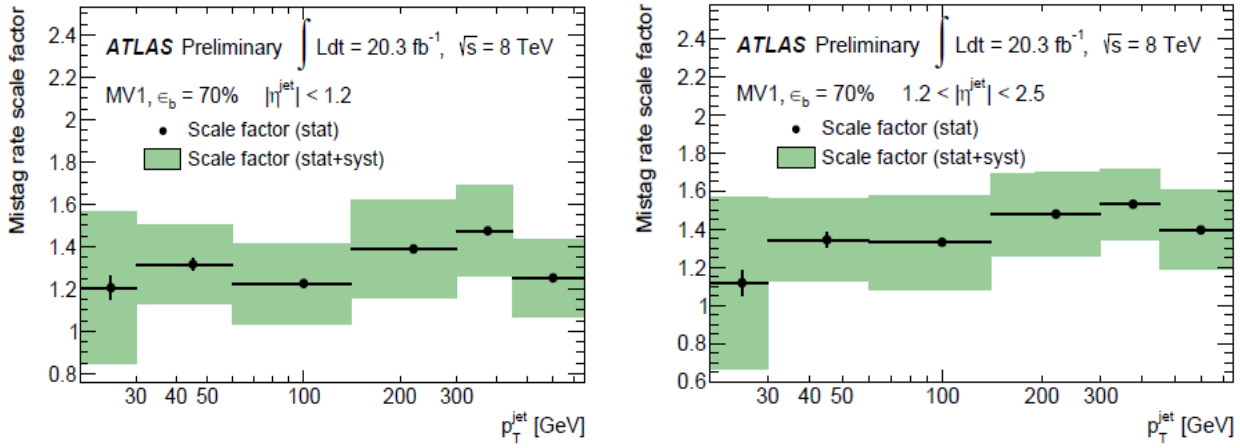

Figure 3.26: The mis-tag rate scale factor for the b-tagging algorithm $MV1$ with 70% of b-tagging efficiency using the negative impact parameter of tracks at each bin of p_{T} of jet for $|\eta| < 1.2$ (left) and $1.2 < |\eta| < 2.5$ (right). The green band represents the total uncertainty of the combination of the two methods [71].

In order to gain higher sensitiviy, using the operating points, we divide the b-tagging into 3 categories: Loose, Medium and Tight, corresponding to the working point value cuts and b-jet efficiencies described in table 3.10. This tagger has been calibrated such that applying operating point is inclusive: if the b-tagged jet satisfies the "Tight" requirement, is also passes the "Loose" criteria. Moreover these categories can be used in an exclusive way, such as requiring the tagged jet to be "Medium not Tight".

Table 3.10: Efficiencies and their corresponding calibrated operating points for $MV1c$ algorithm, used for the VH analyses in Run 1.

Category	Working point	Efficiency
80 Loose (L)	0.4050	79.85
70 Medium (M)	0.7028	70.00
60	0.8353	59.99
50 Tight (T)	0.9237	49.99

For calibration purpose, the dilepton $t\bar{t}$ events has been used. The b-jet efficiency is calibrated using a method called combinatorial likelihood method [70]. The weight distribution is calibrated such that the efficiencies in MC sample and in data matches each other. The calibration for c- and light-jets efficiencies is done using the D^* [72] and di-jet samples [73] respectively. The continuous and pseudo-continuous[1] calibration is described in [74].

3.5 Conclusion

In this chapter we have studied the b-tagging performance for various algorithms applying on the jets reconstructed by ghost-association algorithm, and compared thems to the performance on the jets reconstructed by standard jet algorithm. These works was done with Monte Carlo samples of $t\bar{t}$.

At the first look,the b-tagging performances of taggers on the ghost-association jets were lower than on the standard jets. This was to the fact that the track-selection on ghost-association is tight in the selection of number of hits in Inner Detector, and also on the longitudinal IP z_0 selection. We can actually modify those cuts to check how they affect on the b-tagging performances.

After some tests on various cuts, we reached the conclusion that the b-tagging performance on ghost-association is optimal for the following modifications of track selection for ghost-association:

[1]Instead of calibrating single working point, the continuous calibration divides the working points in 5 bins: [100, 80, 70, 60, 50, 0]. The scale factor for calibration is calculated using the pseudo-continuous approach, cumulative input: $SF_i' = \frac{\epsilon_i^{MC} SF_i - \epsilon_{i+1}^{MC} SF_{i+1}}{\epsilon_{i+1}^{MC} - \epsilon_{i+1}^{MC}}$ where ϵ_i^{MC}, SF_i is efficiency on MC and scale factor of i^{th} bin, respectively.

- No cut on longitudinal and transverse impact parameters variable (z_0 and d_0) for b-tagging quality: This will lead to the overall improvements of all the taggers on ghost-association
- Transverse momentum for track $p_{\mathrm{T}} > 1$ GeV: This cut allows the $JetFitter$ tagger to have the best performance on ghost-association
- For IP-based selection: Transverse momentum for track $p_{\mathrm{T}} > 1.5$ GeV: This will allows the $IP3D$ tagger to have better performance, and hence, all the IP-related algorithms are also improved
- Another option: keep the IP-based selection like the original, but change $p_{\mathrm{T}} > 1.5$ GeV for track selection of ghost-association, this will improve the performance of $IP3D$ tagger, although the $JetFitter$ tagger will be a bit worse than the case of $p_{\mathrm{T}} > 1$ GeV

If we recalibrate the b-tagging algorithm using these modifications on the ghost-association track selection, this can lead to the future improvements of b-tagging performance, and therefore, the ghost-association algorithm can be used as a standard track-to-jet association algorithm in ATLAS detector. This is the plan for the Run 2.

In order to be applied in the Higgs analysis, the b-tagging algorithms need calibration on data with b-tagging efficiency and mis-tagging rate. The calibration is done on $t\bar{t}$ events. The b-tagging algorithm used in Higgs analysis is the $MV1c$ because of its superior c-jet rejection compared to other algorithms. There are three different category of b-tagging that will be applied, and carried out in the analysis in chapter 5.

Chapter 4

Missing transverse energy trigger

4.1 Introduction

In this chapter, we introduce the reconstruction of missing transverse energy in ATLAS, the triggers of missing transverse energy used for the $ZH \to \nu\bar{\nu}b\bar{b}$ analysis, and the detail of our work on the trigger parametrization for the so-called "delayed stream".

4.1.1 Missing transverse energy

In the ATLAS detector, neutrinos usually go through the whole detector without being detected, resulting in missing energy and momentum in the detector. As a consequence, measuring missing transverse energy (notation $E_{\mathrm{T}}^{\mathrm{miss}}$) is one of the most important measurements in various physics studies in the ATLAS detector. For example, it holds a crucial role in measurement of W boson [75] and top quark [76] properties. It is also an essential asset in the Higgs boson analysis in the production channel where the Higgs boson associates with a Z boson and the Z boson decays to neutrinos.

In principle, $E_{\mathrm{T}}^{\mathrm{miss}}$ is defined as the momentum imbalance in the transverse plane, where the momentum conservation should be fulfilled: it should be zero in the transverse plane if everything is taken into account. This momentum imbalance is calculated from the opposite vector of the vectorial sum of all particles detected in the detector [77].

To measure the $E_{\mathrm{T}}^{\mathrm{miss}}$, it is essential to reduce as much as possible the limitation of detector and its resolution that can cause fake $E_{\mathrm{T}}^{\mathrm{miss}}$. There are various sources of fake $E_{\mathrm{T}}^{\mathrm{miss}}$, such as the inactive transition regions between calorimeters, dead and noisy readout channels in running detector. In this context we will not discuss about reducing noise (more can be found in Ref. [59]). We only focus on the reconstruction of $E_{\mathrm{T}}^{\mathrm{miss}}$ in the detector.

Another important quantity that is measured independently with respect to $E_{\mathrm{T}}^{\mathrm{miss}}$ is the track-based missing transverse momentum (notation $P_{\mathrm{T}}^{\mathrm{miss}}$). It is calculated from the track momenta measured by the ATLAS inner detector [78]. This can be used to validate the measurement of $E_{\mathrm{T}}^{\mathrm{miss}}$ based on the calorimeters and it also serves as an additional tool to reject the multijet background.

4.1.2 $E_{\mathrm{T}}^{\mathrm{miss}}$ reconstruction algorithms

There are two main $E_{\mathrm{T}}^{\mathrm{miss}}$ reconstruction algorithms used in ATLAS: cell–based and object–based.

4.1.2.1 Cell–based algorithm

This algorithm reconstructs and calibrates $E_{\mathrm{T}}^{\mathrm{miss}}$ from the energy deposits in calorimeter cells: using the contributions from transverse energy deposits in the calorimeters, from the correction for energy loss in the cryostat and from the reconstructed muons. Each component x, y of $E_{\mathrm{T}}^{\mathrm{miss}}$ can be determined as the following:

$$E_{x,y}^{\mathrm{miss}} = E_{x,y}^{\mathrm{miss(Calo)}} + E_{x,y}^{\mathrm{miss(Cryo)}} + E_{x,y}^{\mathrm{miss(Muon)}}$$

The Calo term in $E_{\mathrm{T}}^{\mathrm{miss}}$ is calculated from the transverse energy measured in TopoCells (they are calorimeter cells that belong to the TopoClusters, which are 3-dimensional topological clusters of energy deposits in the calorimeter [59]) in x and y directions:

$$(E_{x,y}^{\mathrm{miss}})^{\mathrm{Calo}} = -\Sigma_{\mathrm{TopoCells}} E_{x,y}$$

The muon term of $E_{x,y}^{\mathrm{miss}}$ is calculated from measuring muon momenta covered in pseudo-rapidity range $|\eta|$ <2.7:

$$(E_{x,y}^{\mathrm{miss}})^{\mathrm{Muon}} = -\Sigma_{\mathrm{RecMuons}} E_{x,y}$$

Finally, the $(E_{x,y}^{\mathrm{miss}})^{\mathrm{Cryo}}$ term is determined from energy lost in the cryostat. This loss is due to the fact that the hadronic showers lose some energy when they pass the cryostat between LAr barrel electromagnetic calorimeter and the tile barrel hadronic calorimeter which is about half an interaction length:

$$(E_{x,y}^{\mathrm{miss}})^{\mathrm{Cryo}} = -\Sigma_{\mathrm{RecJets}} Ejet_{x,y}^{\mathrm{Cryo}}$$

The value of $E_{\mathrm{T}}^{\mathrm{miss}}$ is calculated from its x, y components as:

$$E_{\mathrm{T}}^{\mathrm{miss}} = \sqrt{(E_x^{\mathrm{miss}})^2 + (E_y^{\mathrm{miss}})^2}$$

and the direction of $E_{\mathrm{T}}^{\mathrm{miss}}$ is determined from its azimuthal angle in transverse plane $\phi_{E_{\mathrm{T}}^{\mathrm{miss}}}$, which is defined as:

$$\phi_{E_{\mathrm{T}}^{\mathrm{miss}}} = \arctan(E_{\mathrm{y}}^{\mathrm{miss}}, E_{\mathrm{x}}^{\mathrm{miss}})$$

4.1.2.2 Object–based algorithm

The principle of the object–based algorithm is to reconstruct $E_{\mathrm{T}}^{\mathrm{miss}}$ using reconstructed objects. The calorimeter cells are associated with a reconstructed parent object which possesses high p_{T} chosen in the following order: electrons, photons, taus (with hadronic decay), jets, and muons. Cells not associated with any of the listed objects are also taken into account toward the $E_{\mathrm{T}}^{\mathrm{miss}}$ reconstruction, which we name $E_{x,y}^{\mathrm{miss(CellOut)}}$. All objects are corrected using the best correction to our knowledge and used in the $E_{\mathrm{T}}^{\mathrm{miss}}$ calculation. Energy of muons and electrons is smeared and scaled, and the jet (as well as τ and γ) energy is also recalibrated.

When the cells are all associated to the reconstructed objects above, then each component of $E_{\mathrm{T}}^{\mathrm{miss}}$ can be calculated as follows:

$$E_{x,y}^{\mathrm{miss}} = E_{x,y}^{\mathrm{miss(e)}} + E_{x,y}^{\mathrm{miss}(\gamma)} + E_{x,y}^{\mathrm{miss}(\tau)} + E_{x,y}^{\mathrm{miss(jets)}} + E_{x,y}^{\mathrm{miss(softjets)}} + E_{x,y}^{\mathrm{miss(CellOut)}} + E_{x,y}^{\mathrm{miss}(\mu)},$$

where $E_{x,y}^{\mathrm{miss(e)}}, E_{x,y}^{\mathrm{miss}(\gamma)}, E_{x,y}^{\mathrm{miss}(\tau)}$ are the terms reconstructed by cells associated with electrons, photons and taus (from hadronic decay of τ lepton), respectively. $E_{x,y}^{\mathrm{miss(jets)}}$ are calculated from cells associated to jets with p_{T} >20 GeV, the term $E_{x,y}^{\mathrm{miss(softjets)}}$ requires that p_{T} of jet be $7 < p_{\mathrm{T}} < 20$ GeV. $E_{x,y}^{\mathrm{miss}(\mu)}$ is the negative sum of reconstructed muon objects (the muon energy loss in the calorimeters is subtracted to avoid double counting [79]).

Each term in this expression is the negative sum of calibrated cell energies associated to the object in the term.

To improve the $E_{\mathrm{T}}^{\mathrm{miss}}$ reconstruction, the cell calibration is replaced by the calibration of the objects (for example, energy calibration of e, jets, ...) which is supposed to have higher accuracy. This kind of calibration is called *refined calibration* [77]. The $E_{\mathrm{T}}^{\mathrm{miss}}$ reconstructed after this refine step is mainly used for the analysis. The reconstruction of $E_{\mathrm{T}}^{\mathrm{miss}}$ also applies pile-up suppression in $E_{x,y}^{\mathrm{miss(CellOut)}}$ term (using tracks or jet area method) and $E_{x,y}^{\mathrm{miss(jets)}}$ term (using tracks).

4.1.2.3 $\boldsymbol{P}_{\mathbf{T}}^{\mathbf{miss}}$ reconstruction

The track-based missing transverse momentum is measured using the tracks originating from primary vertex and reconstructed with the ATLAS Inner Detector. The primary vertex is required to have at least 3 tracks and those tracks must pass the quality requirements [78]:

- $p_{\mathrm{T}} > 0.5$ GeV
- $|\eta|$ <2.5
- ≥ 1 hit in pixel detector
- ≥ 6 hits in SCT
- Impact parameter requirements with respect to the primary vertex: $|d_0| < 1.5$ mm and $|z_0 \sin\theta| < 1.5$ mm

These requirements guarantee the track momentum is well measured and reduce the rate of reconstructing fake tracks. Then the components x, y of $P_{\mathrm{T}}^{\mathrm{miss}}$ are defined as the following:

$$P_{x,y}^{\mathrm{miss}} = -\Sigma_{\mathrm{Tracks}} p_{x,y}.$$

The tracks from leptons not passing the quality cuts above should also be added to the $P_{\mathrm{T}}^{\mathrm{miss}}$ calculation.

4.1.3 $E_{\mathrm{T}}^{\mathrm{miss}}$ triggers in ATLAS detector

4.1.3.1 $E_{\mathrm{T}}^{\mathrm{miss}}$ at Level 1

The $E_{\mathrm{T}}^{\mathrm{miss}}$ trigger at level 1 uses the L1 calorimeter measurements [58] for transverse energy E_{T} and scalar sum of transverse energy ΣE_{T}, covering the region $|\eta|$ <4.9. The reconstruction of L1 $E_{\mathrm{T}}^{\mathrm{miss}}$ trigger is based on the Jet/Energy modules, which calculate the value E_x, E_y and $E_{\mathrm{T}}^{\mathrm{miss}}$ [58, 80].

The values of ΣE_x and ΣE_y are calculated from L1, then the magnitude of $E_{\mathrm{T}}^{\mathrm{miss}}$ at L1 trigger is defined as the quadratic sum of the x, y components, namely $E_{\mathrm{T}}^{\mathrm{miss\,L1}} = \sqrt{(\Sigma E_x)^2 + (\Sigma E_y)^2}$ [81] and a threshold is placed on this value. The L1 trigger bits are defined as $E_{\mathrm{T}}^{\mathrm{miss(L1)}} > E_{\mathrm{T}}^{\mathrm{miss(threshold)}}$.

In 2012, the noise suppression in the forward region ($|\eta|$ >2.5) of calorimeters at L1 was studied because this region is susceptible to pile up [82], so that the $E_{\mathrm{T}}^{\mathrm{miss}}$ dependence on pile-up contamination in this region is reduced.

4.1.3.2 $E_{\mathrm{T}}^{\mathrm{miss}}$ at High Level Trigger

In 2011 the $E_{\mathrm{T}}^{\mathrm{miss}}$ at L2 was not recalculated and the L1 value was reused. In 2012, thanks to the upgraded readout electronics in the calorimeters, energy sum of all cells can be readout and calculated at L2, therefore the resolution of $E_{\mathrm{T}}^{\mathrm{miss}}$ is better compared to L1 $E_{\mathrm{T}}^{\mathrm{miss}}$ (Fig. 4.1 [82]), and it also reduces the rate by a factor five.

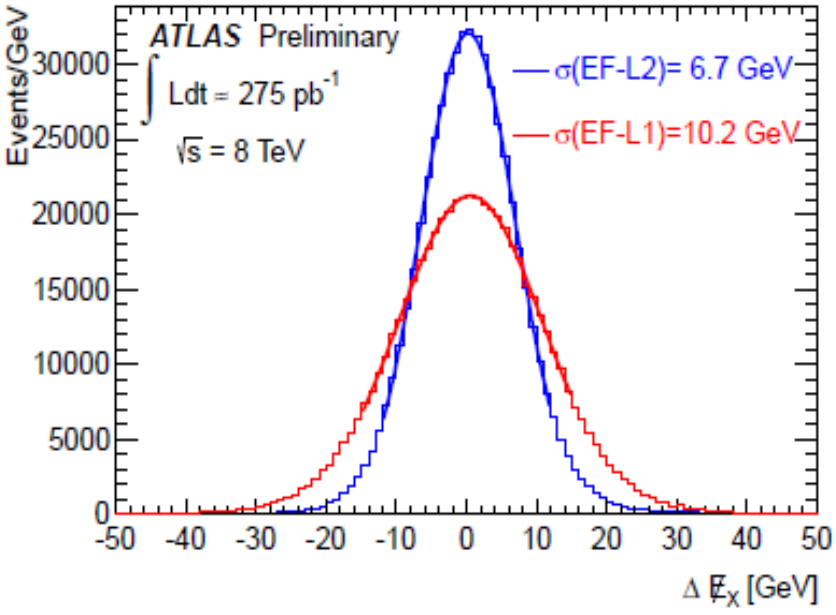

Figure 4.1: Resolution x-component of $E_{\mathrm{T}}^{\mathrm{miss}}$ at L1 (red) and L2 (blue), which are mearsured with respect to EF of $E_{\mathrm{T}}^{\mathrm{miss}}$.

Each component of $E_{\mathrm{T}}^{\mathrm{miss}}$ at L2 is calculated as:

$$E_{x,y}^{\mathrm{miss}} = E_{x,y}^{\mathrm{miss(L2,calo)}} - \Sigma_{muons} p_{x,y}^{(L2)},$$

where $\Sigma_{muons}(\mathrm{L2})p_{x,y}$ is the momenta of all muons reconstructed by L2 algorithm (satisfying the matching of track reconstructed in muon spectrometer and in the inner detector). Actually the L2 trigger can use the muon term, but for our trigger study and during data taking, the muon terms is not taken into account. Note that even without the muon terms at L2, the $E_{\mathrm{T}}^{\mathrm{miss}}$ trigger decision at L2 is still different from L1 (also explained in Ref. [82]). The threshold of $E_{\mathrm{T}}^{\mathrm{miss}}$ at L2 is not the same as at L1.

The EF algorithm takes the sum over clusters after calibration to hadronic scale (multiplying the $E_{\mathrm{T}}^{\mathrm{miss}}$ by a constant related to the hadronic/electromagnetic calorimeter energy fraction in a jet), which leads to further improvement in resolution.

4.1.4 $E_{\mathrm{T}}^{\mathrm{miss}}$ trigger menu used in Higgs analysis in 2012

There are three $E_{\mathrm{T}}^{\mathrm{miss}}$ triggers available in 2012 data that are used in the Higgs analysis:

- EF_xe80_tclcw
- EF_xe80T_tclcw_loose
- EF_xe80_tclcw_loose

with different threshold at each trigger level (Table 4.1). Each trigger is available in certain amount of data processed in some duration of the year that are classified in periods. From period B6, the trigger EF_xe80_tclcw_loose is available thanks to the L1Calo noise suppression in the forward calorimetric region (Sec. 4.1.3.1). Before period B6, the two triggers EF_xe80_tclcw, EF_xe80T_tclcw_loose are available. The trigger EF_xe80T_tclcw_loose has lower thresholds, but it removes the first three bunches of protons in a train, which aims to reduce the high trigger rate bunches at L1.

Table 4.1: Data period and thresholds (in GeV) at each level of $E_{\mathrm{T}}^{\mathrm{miss}}$ triggers that used in the analysis.

Trigger Name	Starting period	Level 1 [GeV]	Level 2 [GeV]	Event Filter [GeV]
EF_xe80_tclcw	A	50	55	80
EF_xe80T_tclcw_loose	A	40	45	80
EF_xe80_tclcw_loose	B6	40	45	80

In the analysis, based on the availability, integrated luminosities (Table 4.2) and trigger thresholds, in order to maximize event acceptance, the three $E_{\mathrm{T}}^{\mathrm{miss}}$ triggers are used as follows: From period A to B5, the trigger EF_xe80T_tclcw_loose is used in the region of $E_{\mathrm{T}}^{\mathrm{miss}} < 160$ GeV, otherwise the trigger EF_xe80_tclcw will be used instead; from period B6 to the end of the year, trigger EF_xe80_tclcw_loose will be used.

Table 4.2: Data period and integrated luminosity at each level of $E_{\mathrm{T}}^{\mathrm{miss}}$ triggers used in the analysis.

Trigger Name	Data period	Luminosity [pb^{-1}]
EF_xe80_tclcw	A–B5	2125.7
EF_xe80T_tclcw_loose	A–B5	1914.6
EF_xe80_tclcw_loose	B6–End	18132.1

4.1.5 $E_{\mathrm{T}}^{\mathrm{miss}}$ trigger in delayed stream

4.1.5.1 Delayed stream of data

Data collected with the ATLAS detector in 2012 from proton-proton collision at $\sqrt{s} = 8$ TeV are divided into different periods from A to L with total delivered luminosity of 20.3 fb^{-1}. There is a part of data collected on top of regular data taking and processed later, due to the limited available computing resources, called delayed stream. This part of data stream takes place from period E1 to the end of the year with the corresponding integrated luminosity 7.29 fb^{-1}. This part of luminosity is included in the full luminosity of data.

4.1.5.2 Triggers in delayed stream

All the nominal $E_{\mathrm{T}}^{\mathrm{miss}}$ triggers are available in the delayed stream data. Apart from these triggers, there are other $E_{\mathrm{T}}^{\mathrm{miss}}$ triggers that exist exclusively in the delayed stream:

- EF_xe60_tclcw_loose_delayed,
- EF_xe60T_tclcw_loose_delayed (with the T meaning that the first three bunches of protons in the train were skipped).

At each level, these triggers have lower thresholds than other nominal triggers: L1 $>$ 35 GeV, L2 $>$ 40 GeV and EF $>$ 60 GeV. Due to the lower integrated luminosity of trigger EF_xe60T_tclcw_loose_delayed (6.67 fb^{-1}), we will use only the trigger EF_xe60_tclcw_loose_delayed in the analysis (with 7.3 fb^{-1}). This trigger was off if the instantaneous luminosity exceeded the value 5.77×10^{33} cm^{-2}s^{-1}.

4.1.5.3 Motivation of using delayed stream trigger

In the previous analysis [83], events are selected from $E_{\mathrm{T}}^{\mathrm{miss}} > 120$ GeV. We aim to move to lower $E_{\mathrm{T}}^{\mathrm{miss}}$ region by lowering the $E_{\mathrm{T}}^{\mathrm{miss}}$ lower threshold to 90 GeV, in order to increase signal acceptance and significance from this region. Thanks to the lower thresholds, the trigger EF_xe60_tclcw_loose_delayed has earlier turn-on than the nominal triggers, resulting in more signal acceptance in the region of $90 < E_{\mathrm{T}}^{\mathrm{miss}} < 120$ GeV, as we can see in Figure 4.2, which shows the distributions of $E_{\mathrm{T}}^{\mathrm{miss}}$ spectrum before applying any $E_{\mathrm{T}}^{\mathrm{miss}}$ trigger, and after applying trigger EF_xe80_tclcw_loose (nominal trigger) or EF_xe60_tclcw_loose_delayed (delayed stream trigger). The signal acceptance is expected to increase about 20% using delayed stream trigger (before any selection).

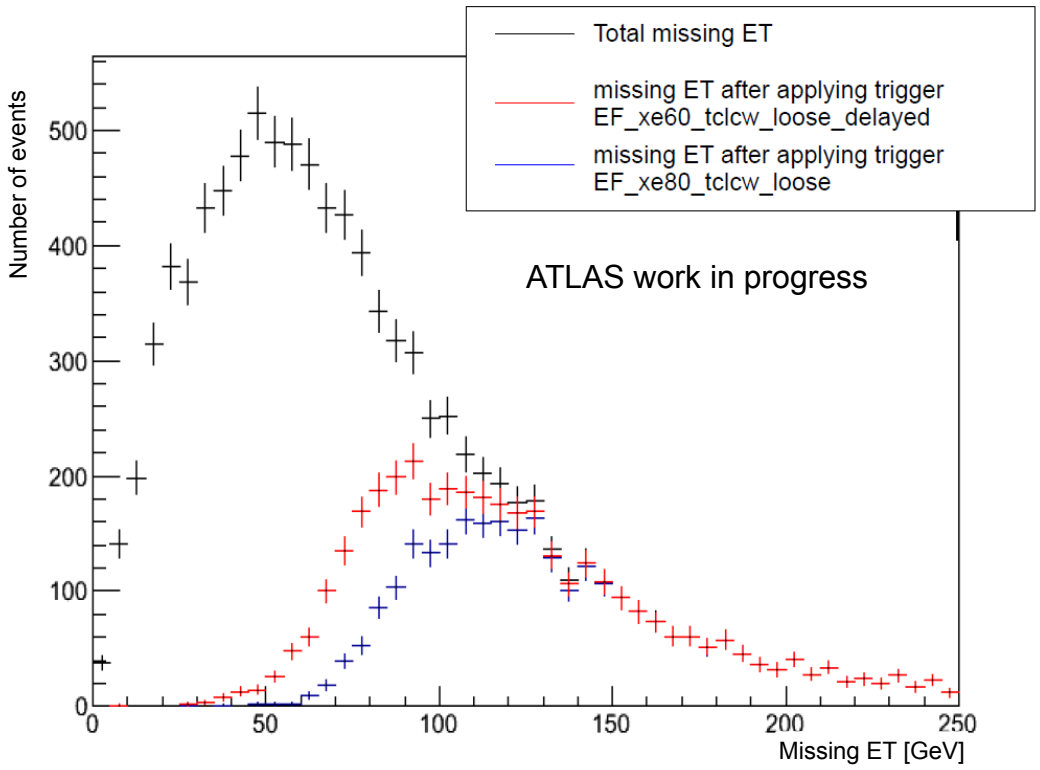

Figure 4.2: $E_{\mathrm{T}}^{\mathrm{miss}}$ after trigger requirements compared with the inclusive $E_{\mathrm{T}}^{\mathrm{miss}}$ spectrum from the $ZH \to \nu\bar{\nu}b\bar{b}$ signal sample.

4.1.6 $E_{\mathrm{T}}^{\mathrm{miss}}$ trigger parametrization study: strategy

The goal of $E_{\mathrm{T}}^{\mathrm{miss}}$ trigger parametrization is to measure the trigger scale factor, which is the ratio of trigger efficiency in data and simulation samples, in order to correct the trigger efficiency in MC samples so that it could match that of data. This ratio is usually referred to as trigger scale factor. In order to obtain the trigger scale factor, we need to calculate firstly the trigger efficiencies (or trigger turn-on) at each trigger level in both data and MC samples, then compute the trigger scale factor by dividing the trigger efficiency of data by the one of MC.

The trigger parametrization will be measured on the channels with two muons (coming from the Z boson decay) and 1 muon (coming from the W boson decay). The reason to choose these 2 channels of muons is that they are events with high purity and also less contribution from multijet than events which contain electrons. We are selecting a channel that is similar to the signal ($Z \to \mu\mu$ compared to $Z \to \nu\bar{\nu}$): the muons can be removed from $E_{\mathrm{T}}^{\mathrm{miss}}$ to simulate the $E_{\mathrm{T}}^{\mathrm{miss}}$ (which will be discussed later). For the $W \to \mu\nu$ channel, although this channel is not similar to the signal (W vs Z), this channel contains true $E_{\mathrm{T}}^{\mathrm{miss}}$ and higher statistics.

We have to obtain trigger turn-ons and trigger scale factors on both channels ($Z \to \mu\mu$ and $W \to \mu\nu$) and compare the results between the two channels.

4.2 Trigger parametrization with $Z \to \mu\mu$ and $W \to \mu\nu$ events

4.2.1 Monte Carlo and data samples

4.2.1.1 MC samples

All the MC samples used in this parametrization are from the MC12a production performed by ATLAS production group [84] using GEANT 4 program [85]. For the trigger parametrization, we mainly care about the backgrounds which simulate the events from $Z \to \mu\mu$ and $W \to \mu\nu$.

Background samples simulate the events from different processes of the pp collisions in the detector, which are generated by several different generators as the following:

- Top processes: Generated by POWHEG [86] interfaced to PYTHIA [87] which requires at least one W from the top decays to a lepton (e, μ or τ). For the single top processes, s–channel and Wt–channel are generated with POWHEG and the t–channel is generated by AcerMC [88].

- Diboson processes: WW, WZ, ZZ events are modelled by POWHEG [86] + PYTHIA generator.

- W/Z+ jets processes: produced with SHERPA generator [89]. A filter is applied to select events containing b, c or light quarks in order to raise statistics of W/Z+ heavy jets samples. An additional filter is used to select the events with different vector boson transverse momentum: $p_{\mathrm{T}}^{W/Z}$ <70 GeV, 70< $p_{\mathrm{T}}^{W/Z}$ <140 GeV, 140< $p_{\mathrm{T}}^{W/Z}$ <280 GeV, 280< $p_{\mathrm{T}}^{W/Z}$ <500 GeV, $p_{\mathrm{T}}^{W/Z}$ >500 GeV, so that the statistics of the high p_{T} could be increased.

4.2.1.2 Data

The data used in this analysis were collected in 2012 from proton–proton collisions with center–of–mass energy of $\sqrt{s}$ = 8 TeV with an integrated luminosity of 20.3 fb^{-1}. The data are required to fulfill the conditions that guarantee the ATLAS detector operates with good efficiency when data are collected. These data requirements are implemented using Good Run Lists (GRL) based on ATLAS Data Quality (DQ). The currently used GRL is data12_8TeV.periodAllYear_DetStatus-v61-pro14-02 _DQDefects-00-01-00_PHYS_StandardGRL_All_Good. The collected data can be classified to specific streams that serve for different physics analyses (Higgs, SUSY, etc...) using corresponding specific trigger (for example, muon stream requires the data to pass muon trigger selection). For the trigger parametrization study, we focus mainly in the muon stream data.

4.2.2 Object and event selection

4.2.2.1 Triggers

Our study involves the selection of events with one or two muons, so we use the following triggers for muon:

- For selecting single muon events, we require the EF_mu24i_tight or EF_mu36_tight triggers for the full data, where the 24 and 36 stand for the p_{T} threshold of muons (in GeV) at EF to be triggered and "i" in EF_mu24i_tight means the isolation requirement at EF.
- For selecting di–muons events, the additional trigger EF_2mu13 will be used, this trigger selects events containing two muons with $p_{\mathrm{T}} > 13$ GeV.

4.2.2.2 Electron selection

Since our $E_{\mathrm{T}}^{\mathrm{miss}}$ trigger study selects events containing muons, we veto any events containing electron. For identifying electron, we require loose selection $E_{\mathrm{T}} > 10$ GeV, $|\eta| < 2.47$ (including crack region $1.37 < |\eta| < 1.52$), isolation (sum of tracks p_{T} divided by p_{T} within cone of ΔR =0.2) less than 0.1, and transverse impact parameter d_0 (with respect to PV) less than 0.1 mm.

4.2.2.3 Muon selection

Muon candidates are selected using the combination of track measurement from the inner detector and muon spectrometer. Muons are selected to lie in the region of $|\eta| < 2.7$, and require transverse momentum $p_{\mathrm{T}} > 20$ GeV. Muon candidates also fulfill the track cuts required by Muon Combined Performance group [90]:

- Number of pixel hits + number of crossed dead pixel sensors > 0
- Number of SCT hits+number of crossed dead SCT sensors > 4
- Number of pixel holes + number of SCT holes < 3
- Define $\mathrm{n} = \mathrm{n}_{\mathrm{TRT}}^{\mathrm{hits}} + \mathrm{n}_{\mathrm{TRT}}^{\mathrm{outliers}}$ where $\mathrm{n}_{\mathrm{TRT}}^{\mathrm{hits}}$ is the number of TRT hits of muon track, $\mathrm{n}_{\mathrm{TRT}}^{\mathrm{outliers}}$ is the number of TRT outliers of muon track. Then, in the region of $0.1 < |\eta| < 1.9$, we require that $\mathrm{n} > 5$ and $\mathrm{n}_{\mathrm{TRT}}^{\mathrm{outliers}} < 0.9\mathrm{n}$.

The impact parameter cut is applied which requires the transverse impact parameter with respect to primary vertex to be less than 0.1 mm. Additionally, the muons are required to pass the isolation cut that the sum of transverse momentum of tracks within a cone of radius 0.2 be less than 10% of the transverse momentum of the muon.

For selecting muons in $Z \to \mu\mu$ events: the muons are required to satisfy the condition of $p_{\mathrm{T}} > 25$ GeV and $|\eta| < 2.5$, which we refer to as medium selection of muon.

For selecting muons in $W \to \mu\nu$ events: muon candidates must fulfill the medium selection, and also the additional tighter isolation cuts which require the ratio sum of calorimetric

energy deposits in a cone of radius 0.3 divided by its transverse momentum is less than 0.07 and less than 0.03 for track–based isolation (in the cone of radius 0.2), which we refer to as tight selection.

4.2.2.4 Jet selection

Jets are reconstructed using the anti–k_t algorithm with a radius parameter of 0.4 [61,62]. For the kinematic part, jets are required to have $p_{\mathrm{T}} > 20$ GeV and $|\eta|$ <2.5 to be considered as signal jets used for the analysis. Jets to be used for veto are required to have $p_{\mathrm{T}} > 30$ GeV and $2.5 < |\eta| < 4.5$. To reduce the contribution of jets from pile–up, jets with $p_{\mathrm{T}} < 50$ GeV and $|\eta| < 2.4$ have to satisfy |JVF| > 0.5 (see definition of JVF in section 3.1.4.1).

For the leading jet, we require an extra condition that the transverse momentum $p_{\mathrm{T}} > 45$ GeV.

For b–tagging procedure to identify b–jets, we use the $MV1c$ algorithm [74] at the 50, 70 and 80% working points (discussed in section 3.4.2).

Jet labelling The flavour of jets in MC samples is determined at hadron level. The jet is labelled as b–jet if there is a B–hadron with $p_{\mathrm{T}} > 5$ GeV within a cone of ΔR =0.4 to the jet axis. If the jet is not labelled as b but there is a c–hadron with $p_{\mathrm{T}} > 5$ GeV in the same cone, it will be labelled as c–jet. If τ is found, then the jet is considered as τ-jet. Otherwise jets are categorized as light jets.

Note that the procedure is slightly different than for chapter 3: hadrons are used instead of quarks.

4.2.2.5 Overlap removal

In order to avoid double–counting the objects, overlaping removal cuts are applied for jets, muons and electrons (leptons satisfy the loose requirements, and only signal jets are selected). If the objects passing the selection are found overlaping with other objects in certain ΔR, a classification is made to keep one of the overlaping objects and remove the others. The classification is as the following in order:

- A jet found with $\Delta R < 0.4$ to an electron with $p_{\mathrm{T}} > 15$ GeV is removed
- A muon found with $\Delta R < 0.4$ to a jet (after jet–electron removal) is removed
- An electron with $p_{\mathrm{T}} < 15$ GeV and with $\Delta R < 0.4$ to a jet is removed
- Electrons with $\Delta R < 0.2$ to a muon is removed

4.2.2.6 $\boldsymbol{E}_{\mathbf{T}}^{\mathbf{miss}}$ calculation for trigger parametrization

In this trigger parametrization, we study the $Z \to \mu\mu$ events and $W \to \mu\nu$ events. $E_{\mathrm{T}}^{\mathrm{miss}}$ in $Z \to \mu\mu$ events is not that large since it would not be expected to contain neutrinos, and in $W \to \mu\nu$ selection the contribution to $E_{\mathrm{T}}^{\mathrm{miss}}$ is mainly from the sole neutrino from leptonic decay of W. So $E_{\mathrm{T}}^{\mathrm{miss}}$ recalculation is needed in order to simulate the $E_{\mathrm{T}}^{\mathrm{miss}}$ in the $Z \to \mu\mu$ and $W \to \mu\nu$ selection as the $E_{\mathrm{T}}^{\mathrm{miss}}$ in the $Z \to \nu\bar{\nu}$ case. The idea is to remove the contribution of muon terms from the $E_{\mathrm{T}}^{\mathrm{miss}}$ calculation as we have seen in section 4.1.2.2 .

For the $P_{\mathrm{T}}^{\mathrm{miss}}$, the measurement is as mentioned in section 4.1.2.3. As for $E_{\mathrm{T}}^{\mathrm{miss}}$ measurement, we also require the muon momentum removal from the $P_{\mathrm{T}}^{\mathrm{miss}}$ measurement.

4.2.2.7 Event selection

To perform our $E_{\mathrm{T}}^{\mathrm{miss}}$ trigger paremetrization, we are interested in three types of events: $Z \to \mu\mu$, $W \to \mu\nu$ and $t\bar{t}$ events, which are selected as follows:

***$Z \to \mu\mu$* selection**:

- Select exactly 2 muons passing the above selection with at least 1 muon passing the medium criteria
- The invariant mass of the 2 muons has to be within the Z mass window $83 < M_{\mu\mu} < 99$ GeV
- 2 or 3 jets with transverse momentum of leading jet $p_{\mathrm{T}} > 45$ GeV

***$W \to \mu\nu$* selection**:

- Exactly 1 muon passing the tight selection
- Transverse mass of W bosons[1] $60 < M_{\mathrm{T}}^{W} < 120$ GeV
- 2 or 3 jets with transverse momentum of leading jet $p_{\mathrm{T}} > 45$ GeV

***$t\bar{t}$* selection**:

- Exactly 2 muons passing the medium selection
- Z mass veto: invariant mass of 2 muons must lie in region $40 < M_{\mu\mu} < 83$ GeV or $M_{\mu\mu} > 99$ GeV
- 2 or 3 jets with 2 b–tagged jets (with b-tagging working point at 70% efficiency).

The MC contributions are normalized to the total integrated luminosity, cross-sections of processes, pile-up reweighting. The results after these selections are shown in Fig. 4.3 ($Z \to \mu\mu$), 4.4 ($W \to \mu\nu$) and 4.5 ($t\bar{t}$). For the event selection of $Z \to \mu\mu$, we obtain a good agreement between the data and MC in terms of $E_{\mathrm{T}}^{\mathrm{miss}}$ and invariant mass of 2 muons. We can see some discrepancy between data and MC in the $W \to \mu\nu$ in the region of low $E_{\mathrm{T}}^{\mathrm{miss}}$ and low M_{T}^{W}, which suggests the potential contribution from multijet processes. In this framework the multijet estimation is not our major study (detailed discussion of multijet background estimation can be found in chapter 5), instead we propose a selection to reject the multijet, which will be discussed in the next part of this section. Due to overall low statistics, the $t\bar{t}$ sample will be used only for cross-checking the consistency with the samples of W and Z bosons.

[1] $M_{\mathrm{T}}^{W} = \sqrt{2p_{\mathrm{T}}^{\mu} E_{\mathrm{T}}^{\mathrm{miss}} (1 - \cos\Delta\phi(\mu, E_{\mathrm{T}}^{\mathrm{miss}}))}$

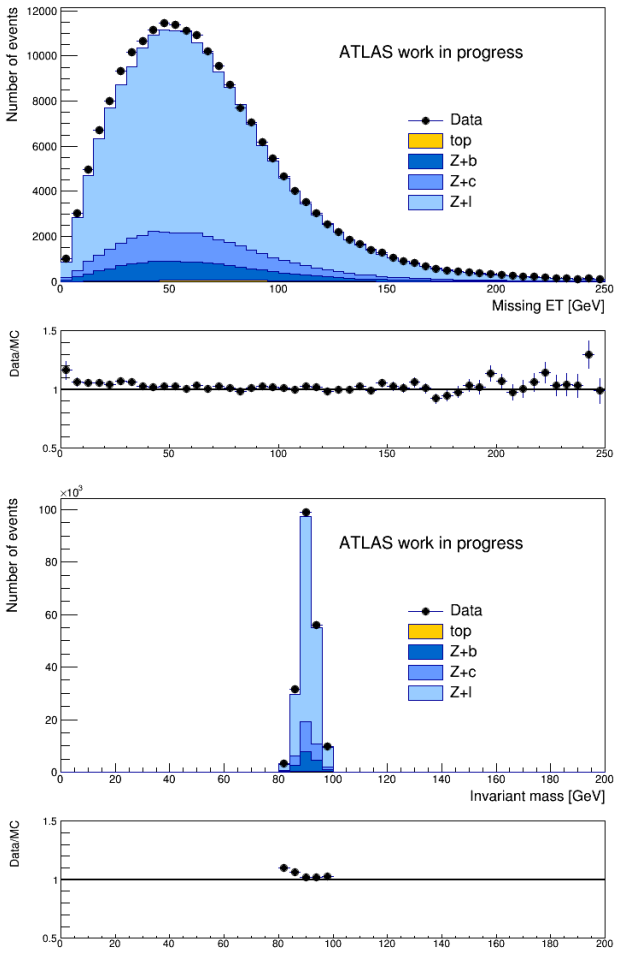

Figure 4.3: $E_{\mathrm{T}}^{\mathrm{miss}}$ without muon contribution (top) and invariant mass of 2 muons (bottom) in $Z \to \mu\mu$ channel without multijet rejection cuts.

4.2.2.8 Additional multijet rejection cuts

These additional cuts are to reduce further the multijet contamination on $W \to \mu\nu$ events and also simulate multijet background rejection cuts applied in 0–lepton channel of the Higgs analysis (more details at section 5.7). These cuts are defined as follows:

- The minimum value of the angular distance between the $E_{\mathrm{T}}^{\mathrm{miss}}$ and jets: $\min \Delta\phi(E_{\mathrm{T}}^{\mathrm{miss}}, \mathrm{jet}) > 1.5$
- Distance between two jets $\Delta R(jet1, jet2) > 0.7$
- Track-based missing transverse momentum $P_{\mathrm{T}}^{\mathrm{miss}} > 30$ GeV
- Angular distance between $E_{\mathrm{T}}^{\mathrm{miss}}$ and $P_{\mathrm{T}}^{\mathrm{miss}}$, $\Delta\phi(E_{\mathrm{T}}^{\mathrm{miss}}, P_{\mathrm{T}}^{\mathrm{miss}}) < \pi/2$

All quantities related to $E_{\mathrm{T}}^{\mathrm{miss}}$ and $P_{\mathrm{T}}^{\mathrm{miss}}$ are considered after muon contribution removal.

The results after these rejection cuts are shown in Fig. 4.6. These cuts actually reduced the contribution of multijet processes from $W \to \mu\nu$ events.

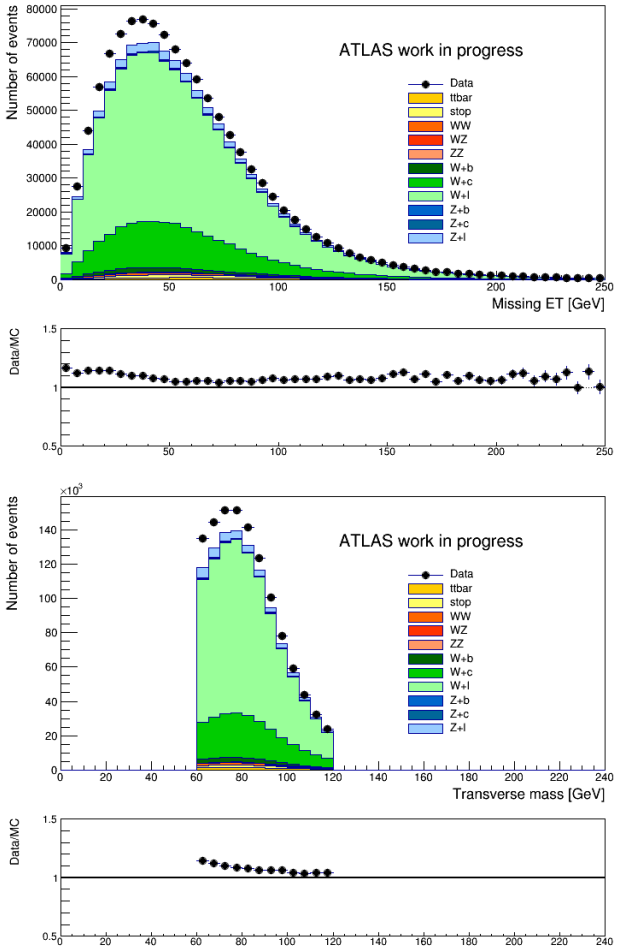

Figure 4.4: $E_{\mathrm{T}}^{\mathrm{miss}}$ without muon contribution (top) and transverse mass (bottom) in $W \to \mu\nu$ channel without multijet rejection cuts.

4.2.3 Trigger emulation

In the MC samples, all the trigger bits of nominal triggers at each level are available and can be applied directly in the parametrization. Nevertheless, unlike the nominal triggers, trigger bits at each level of trigger EF_xe60_tclcw_loose_delayed are not available. We can use another approach as we have already seen in section 4.1.3: utilize the components x, y of $E_{\mathrm{T}}^{\mathrm{miss}}$ at each level (which are always recorded in each event), calculate their modules and put the thresholds on them to reconstruct the $E_{\mathrm{T}}^{\mathrm{miss}}$ trigger bits at each level, then we can perform the normal parametrization as we do for the nominal triggers.

In data, unlike the nominal triggers, the trigger EF_xe60_tclcw_loose_delayed is not available if the instantaneous luminosity exceeds 5.77×10^{33} cm^{-2}s^{-1}. In order to calculate trigger efficiencies using the delayed stream trigger we should remove the part of data in which this trigger is off.

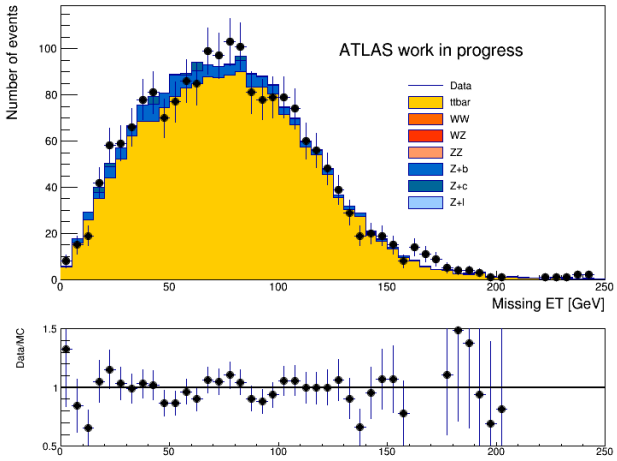

Figure 4.5: $E_{\mathrm{T}}^{\mathrm{miss}}$ without muon contribution in $t\bar{t}$ channel.

4.2.4 Measuring trigger turn–on

To measure the total trigger turn–on, first we parametrize the trigger efficiencies on each level of trigger using the error function, then multiply the trigger efficiency functions to parametrize the total trigger turn–on. The trigger efficiencies at each level are defined as the ratio between the events that passed the trigger bit and the events that pass the requirement prior to the trigger bit. In more details:

$$\text{Efficiency}_{L1} = E_{\mathrm{T}}^{\mathrm{miss}} \text{ pass } L1 \text{ / } E_{\mathrm{T}}^{\mathrm{miss}} \text{ Total}$$

$$\text{Efficiency}_{L2} = E_{\mathrm{T}}^{\mathrm{miss}} \text{ pass } L2 \text{ / } E_{\mathrm{T}}^{\mathrm{miss}} \text{ pass } L1$$

$$\text{Efficiency}_{EF} = E_{\mathrm{T}}^{\mathrm{miss}} \text{ pass } EF \text{ / } E_{\mathrm{T}}^{\mathrm{miss}} \text{ pass } L2$$

$$\text{Efficiency}_{Total} = \text{Efficiency}_{L1} \times \text{Efficiency}_{L2} \times \text{Efficiency}_{EF}$$

The function used for the parametrization of trigger efficiency is defined as:

$$\text{Efficiency} = 0.5 \times \left(1 + \text{erf}\left(\frac{E_{\mathrm{T}}^{\mathrm{miss}} - \text{threshold}}{\sqrt{2} \times \text{width}}\right)\right)$$

where the erf function is defined as:

$$\text{erf}(x) = \frac{2}{\sqrt{\pi}} \int_0^x e^{-t^2} dt$$

Here we define the two parameters: the *threshold* is the value of $E_{\mathrm{T}}^{\mathrm{miss}}$ at which 50% of efficiency is obtained, the *width* determines the "inflection" of the error function. The fitting range for the error functions is chosen from 40 to 200 GeV, because we want to avoid the high fluctuated efficiencies in region of $E_{\mathrm{T}}^{\mathrm{miss}}$ <40 GeV, and for $E_{\mathrm{T}}^{\mathrm{miss}}$ >200 GeV the trigger efficiency is supposed to reach plateau of 1, in which we have no further interest.

The results of the fits are shown in Figs. 4.7, 4.8, 4.9, 4.10, which show the trigger efficiencies at each level and their corresponding fit functions with respect to $E_{\mathrm{T}}^{\mathrm{miss}}$ for W and

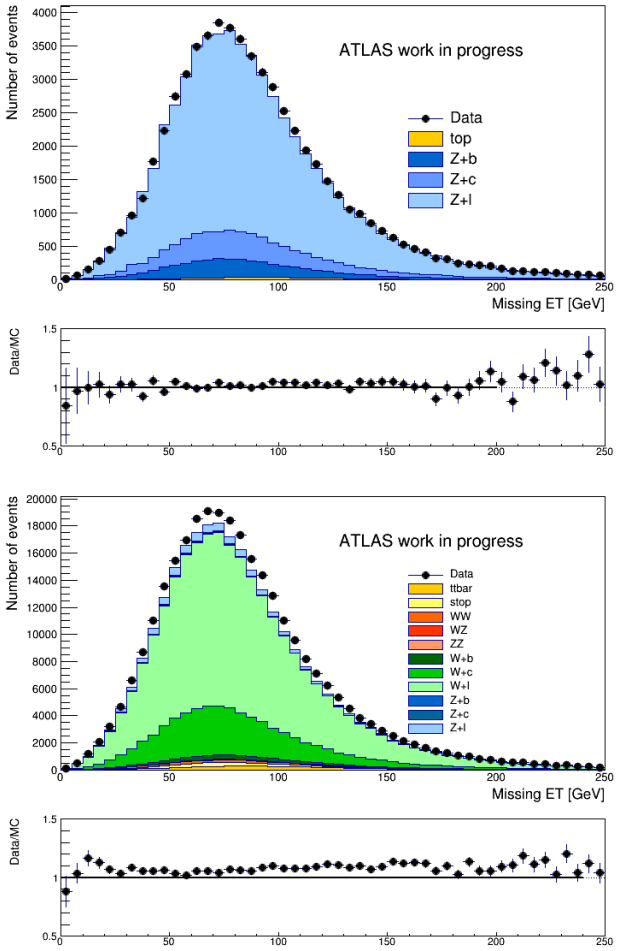

Figure 4.6: $E_{\mathrm{T}}^{\mathrm{miss}}$ without muon contribution for $Z \to \mu\mu$ (top) and $W \to \mu\nu$ (bottom) channel with multijet rejection cuts.

Z samples with 2 jets (for both data and MC samples). The fitting parameters are shown in Table 4.3. The analytic curves of the fit using error functions show good agreement with data points and MC for both $Z \to \mu\mu$ and $W \to \mu\nu$ events, which means that our parametrization is reasonable.

4.2.5 Measuring trigger scale factor

After gathering the $E_{\mathrm{T}}^{\mathrm{miss}}$ trigger turn–ons on both data and MC for $Z \to \mu\nu$ and $W \to \mu\nu$ selection, the trigger scale factors can be calculated as follows:

$$\text{Scale factor} = \frac{\text{Turn-on}^{data}_{W\to\mu\nu/Z\to\mu\mu}}{\text{Turn-on}^{MC}_{W\to\mu\nu/Z\to\mu\mu}},$$

where $\text{Turn–on}^{data/MC}_{W\to\mu\nu/Z\to\mu\mu}$ is the product of error functions at L1, L2, EF obtained in section 4.2.4.

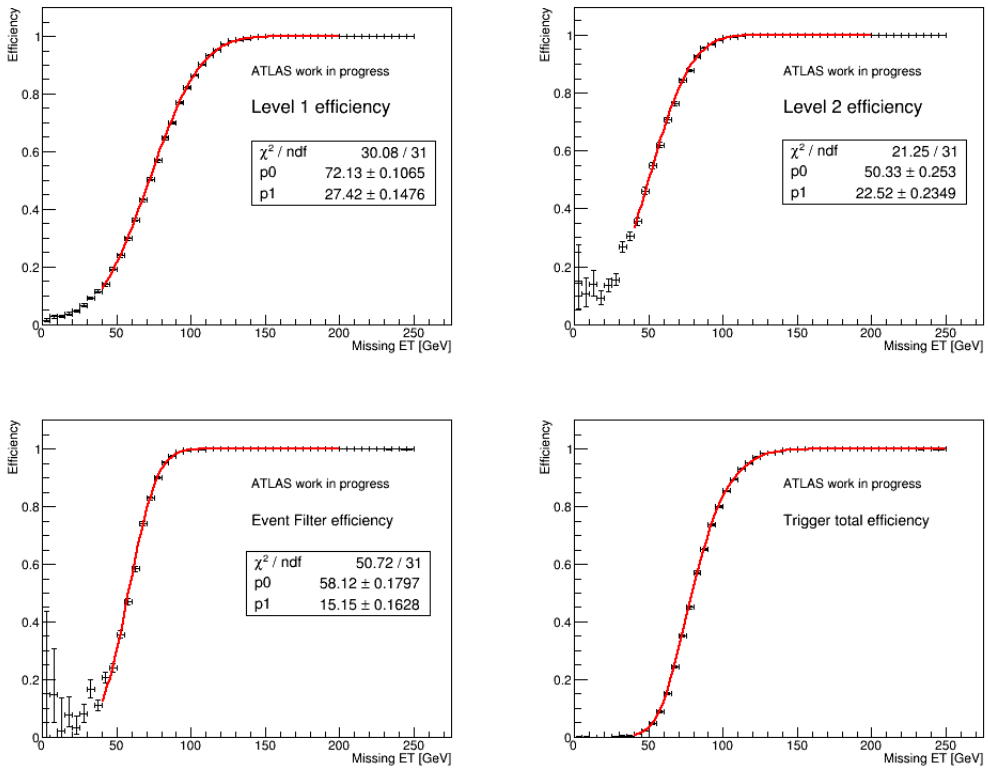

Figure 4.7: $E_{\mathrm{T}}^{\mathrm{miss}}$ trigger efficiencies at level 1 (top left), level 2 (top right), Event Filter (bottom left) and total efficiency (bottom right) for MC in $Z \to \mu\mu$ + 2 jets channel.

Figure 4.11 shows the total trigger scale factors from data points and fit results, which show the overall good agreement between the data points and the curves obtained from fitting results[2] down to $\sim$ 60 GeV of $E_{\mathrm{T}}^{\mathrm{miss}}$. In the analysis we will apply the trigger scale factor in the region of $E_{\mathrm{T}}^{\mathrm{miss}} > 90$ GeV.

4.2.6 Various comparisons for trigger parametrization

In this section we will see if the trigger turn–on and trigger scale factors change in various categories: 2 or 3-jet selection, Z or W samples, applying or not applying multijet rejection cuts. If significant differences are observed among the categories, we need some proper treatment for each of them in the analysis, else we just need to determine the parametrization for one category and apply it for the rest.

4.2.6.1 Comparison between 2 and 3-jet selection

In the Higgs analysis, apart from the 2-jet region, we are also interested in the 3-jet region, so comparing the trigger turn–on between 2-jet and 3-jet bins is necessary to decide if we need to have a separate parametrization of the trigger in 3-jet bin. The results are shown

[2]Note: the curve here is *not* a fit to the points.

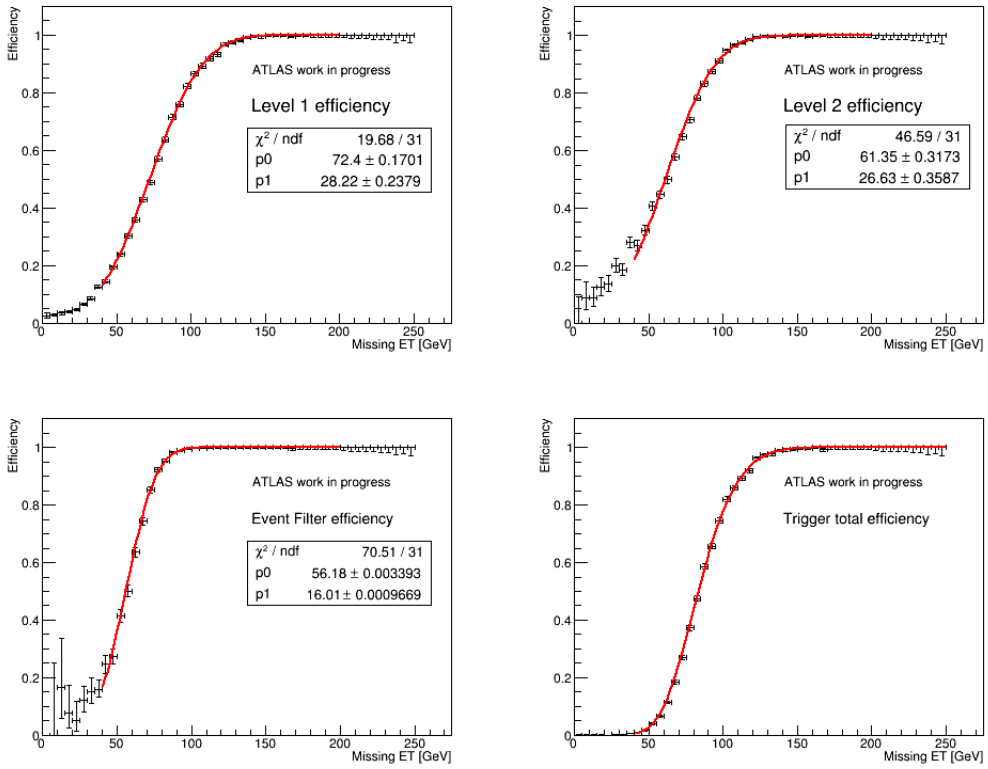

Figure 4.8: $E_{\mathrm{T}}^{\mathrm{miss}}$ trigger efficiencies at level 1 (top left), level 2 (top right), Event Filter (bottom left) and total efficiency (bottom right) for data in $Z \to \mu\mu$ + 2 jets channel.

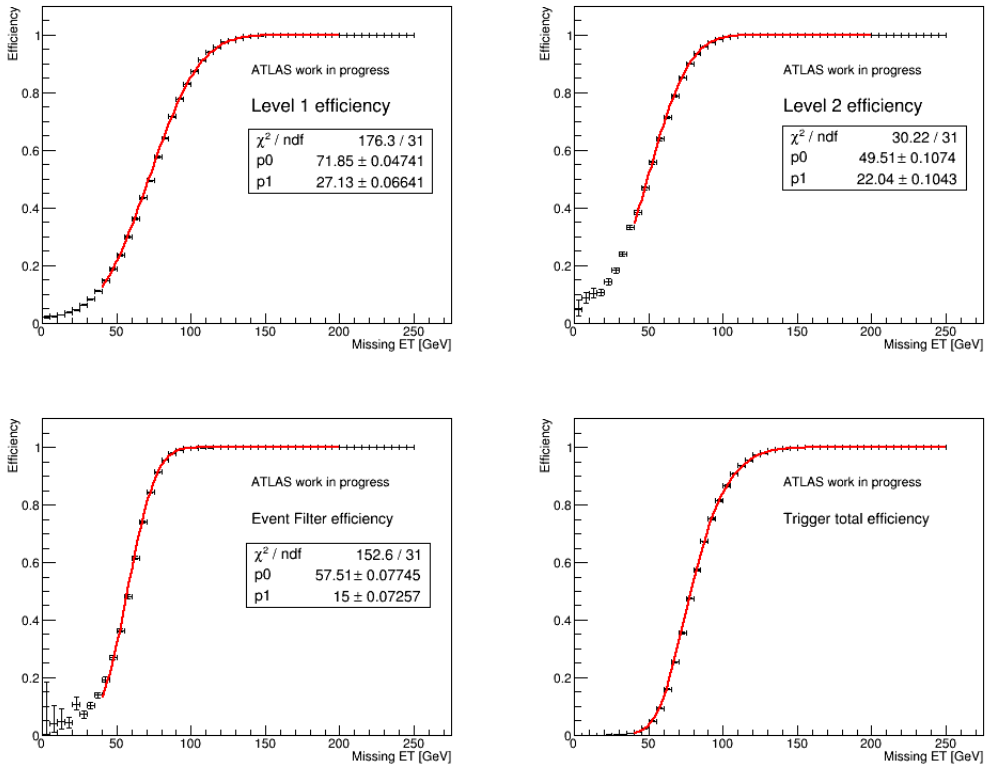

Figure 4.9: $E_{\mathrm{T}}^{\mathrm{miss}}$ trigger efficiencies at level 1 (top left), level 2 (top right), Event Filter (bottom left) and total efficiency (bottom right) for MC in $W \to \mu\nu$ + 2 jets channel.

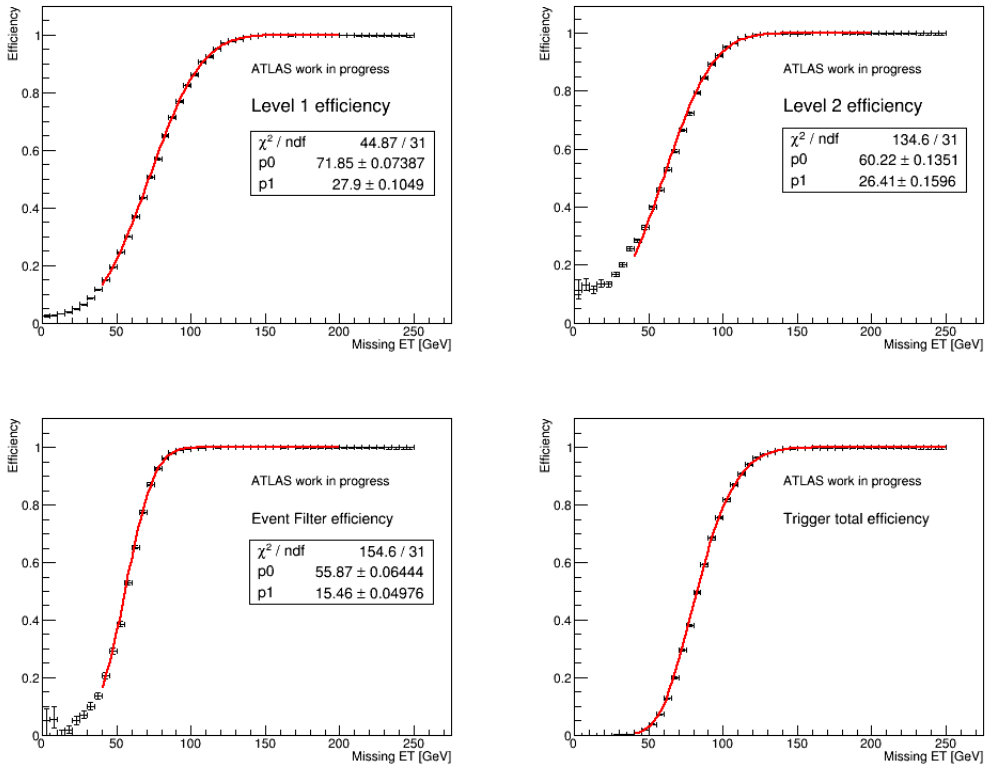

Figure 4.10: $E_{\mathrm{T}}^{\mathrm{miss}}$ trigger efficiencies at level 1 (top left), level 2 (top right), Event Filter (bottom left) and total efficiency (bottom right) for data in $W \to \mu\nu$ + 2 jets channel.

Table 4.3: Fitting parameters at each level of trigger for $Z \to \mu\mu$ and $W \to \mu\nu$ samples for MC and data in 2-jet events.

$Z \to \mu\mu$	MC		data	
	Threshold [GeV]	Width	Threshold [GeV]	Width
Level 1	72.13±0.11	27.42±0.15	72.4±0.17	28.22±0.24
Level 2	50.33±0.25	22.52±0.23	61.35±0.22	26.63±0.36
Event Filter	58.12±0.18	15.15±0.16	56.18±0.01	16.01±0.01
$W \to \mu\nu$	MC		data	
	Threshold [GeV]	Width	Threshold [GeV]	Width
Level 1	71.85±0.11	27.13±0.07	71.85±0.07	27.9±0.1
Level 2	49.51±0.11	22.04±0.1	60.22±0.14	26.41±0.16
Event Filter	57.51±0.08	15±0.07	55.87±0.06	15.46±0.05
$t\bar{t}$	MC		data	
Level 1	66.66±1.14	27.53±1.43	61.3±2.87	32.57±2.96
Level 2	50.09±2.36	20.89±1.97	61.48±2.68	25.13±2.76
Event Filter	57.35±1.79	14.71±1.48	54.08±4.43	20.78±3.43

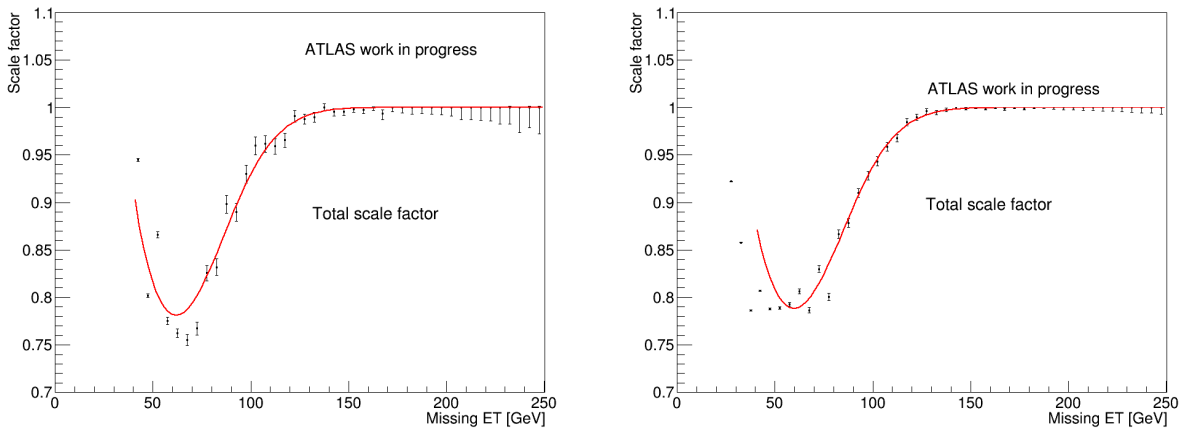

Figure 4.11: Total $E_{\mathrm{T}}^{\mathrm{miss}}$ trigger scale factor from data points (black) and from analytic fit (red curve) in $Z \to \mu\mu$ (left) and $W \to \mu\nu$ (right) channels in 2-jet events.

in Fig. 4.12 for Z samples and Fig. 4.13 for W samples. From the results we can conclude that the trigger turn–on in 2-jet bin and 3-jet bin are almost the same, implying that we can apply the trigger scale factors of 2-jet bin on the 3-jet bin.

4.2.6.2 Comparison before and after applying multijet cuts

It is important to check if the trigger turn–on and trigger scale factors are affected by multijet rejection cuts that are discussed in section 4.2.2.8. For the selection we divide into 2 categories: Applying multijet rejection cuts and no applying these cuts. The results are

shown in Fig. 4.14, 4.15 and indicate that the multijet rejection cuts that we apply in Higgs analysis do not affect the trigger scale factor and trigger turn–on, so we can still apply the trigger parametrization using the events without multijet rejection cuts that we have already done in the previous section because we have better statistical uncertainties without applying multijet cuts.

4.2.6.3 Comparison between W and Z samples

As we have seen in Table 4.3 comparing the fit parameters between W and Z samples, those parameters for W and Z are very similar. More visually, Figure 4.16 shows that the trigger turn–on and trigger scale factors are compatible between the W and Z samples.

Our conclusion is that the trigger scale factors and trigger turn–ons are not dependent on the type of events, so we do not need separate trigger scale factor, and consider the difference between them as systematic uncertainty. The trigger scale factor of W are chosen as nominal since the statistical uncertainty is largely reduced thanks to the high number of W events.

4.2.6.4 Comparison to $t\bar{t}$ sample

For this part we have a comparison among the 3 samples: $Z \to \mu\mu$, $W \to \mu\nu$ and $t\bar{t}$ samples. As shown in Figure 4.17, the consistency among 3 samples is confirmed, the $t\bar{t}$ scale factor curve being indistinguishable from the Z+jets one, and it guarantees that one can use the trigger parametrization on W samples across the other samples in the analysis. One should note that the $t\bar{t}$ sample has low statistics.

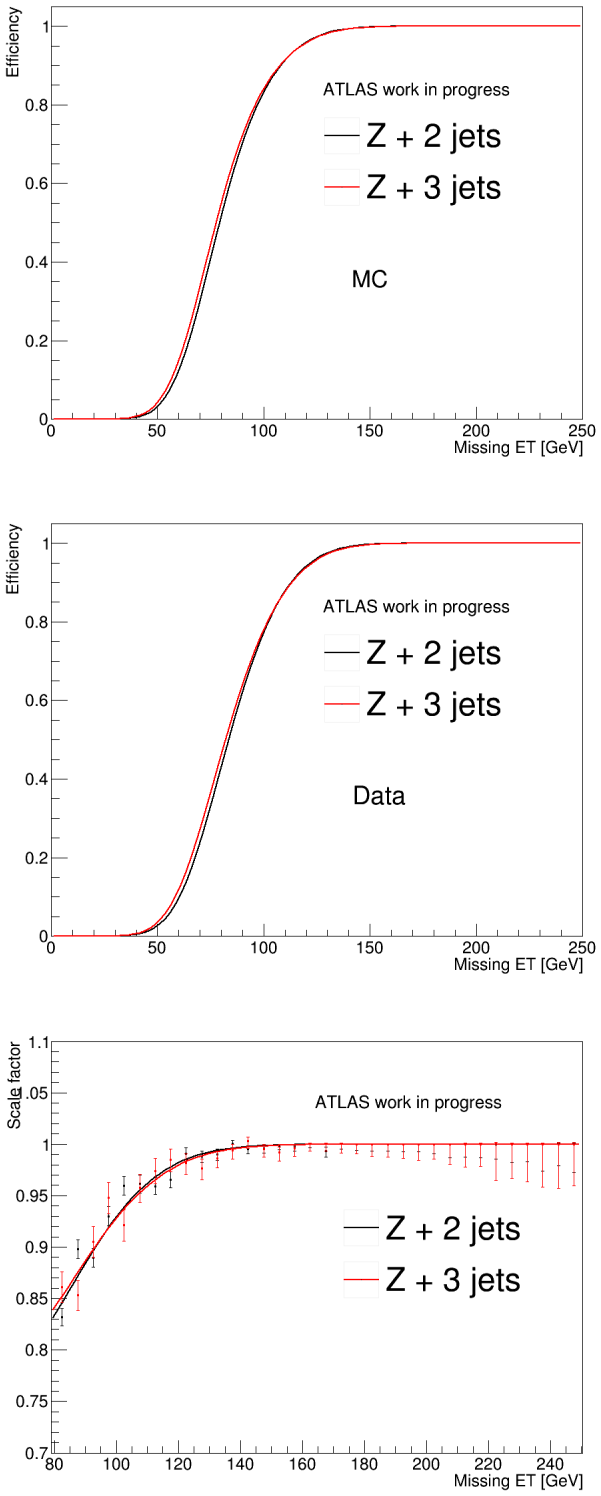

Figure 4.12: Comparison of total $E_{\mathrm{T}}^{\mathrm{miss}}$ trigger turn–on from the fit curves of $Z \to \mu\mu$ for 2 jets and 3 jets bin on MC (top) and data (middle) and trigger scale factor (bottom).

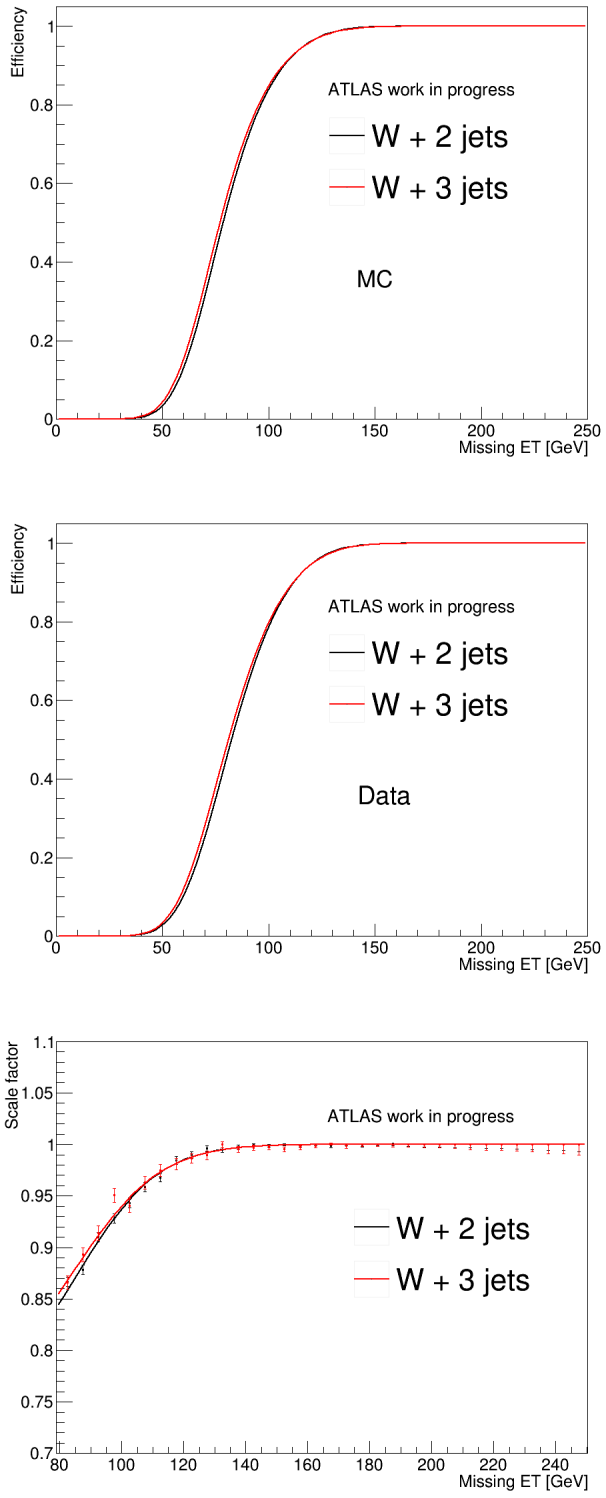

Figure 4.13: Comparison of total $E_{\mathrm{T}}^{\mathrm{miss}}$ trigger turn–on from the fit curves of $W \to \mu\nu$ for 2 jets and 3 jets bin on MC (top) and data (middle) and trigger scale factor (bottom).

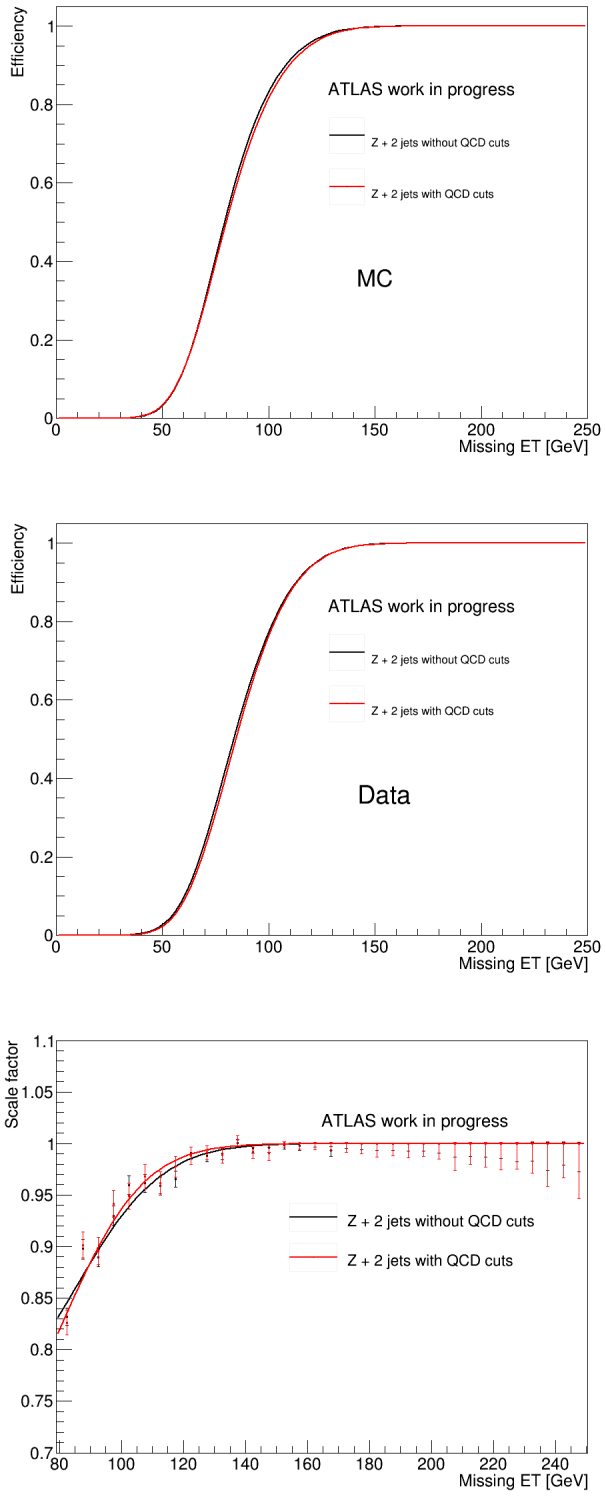

Figure 4.14: Comparison of total $E_{\mathrm{T}}^{\mathrm{miss}}$ trigger turn–on from the fit curves of $Z \to \mu\mu$ between applying/not applying multijet rejection on MC (top) and data (middle) and trigger scale factor (bottom).

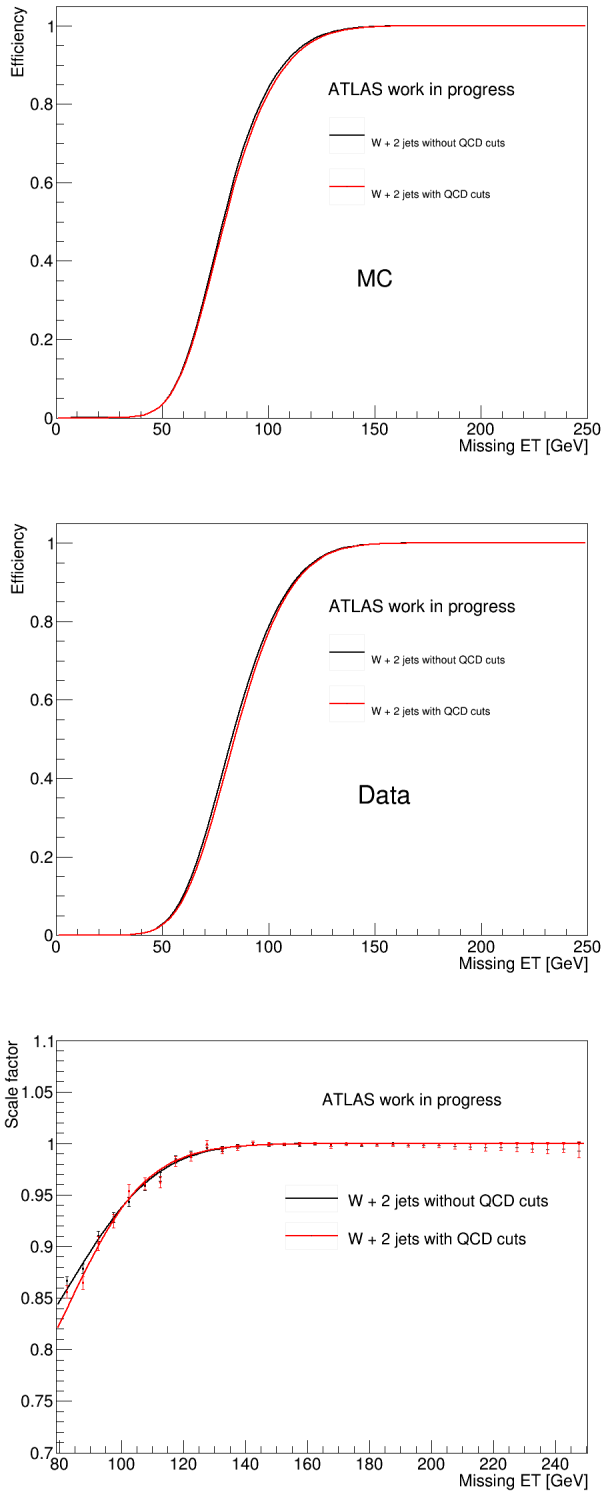

Figure 4.15: Comparison of total $E_{\mathrm{T}}^{\mathrm{miss}}$ trigger turn–on from the fit curves of $W \to \mu\nu$ between applying/not applying multijet rejection on MC (top) and data (middle) and trigger scale factor (bottom).

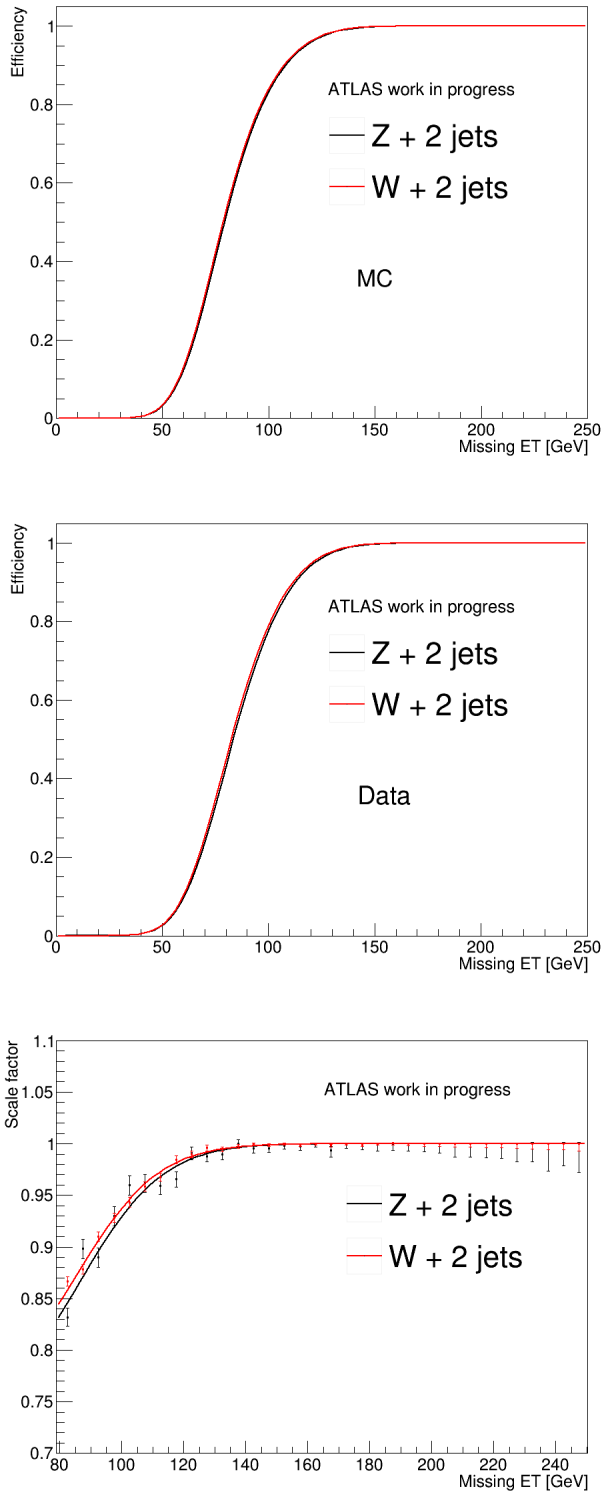

Figure 4.16: Comparison of total $E_{\mathrm{T}}^{\mathrm{miss}}$ trigger turn–on from the fit curves between $Z \to \mu\mu$ and $W \to \mu\nu$ on MC (top) and data (middle) and trigger scale factor (bottom).

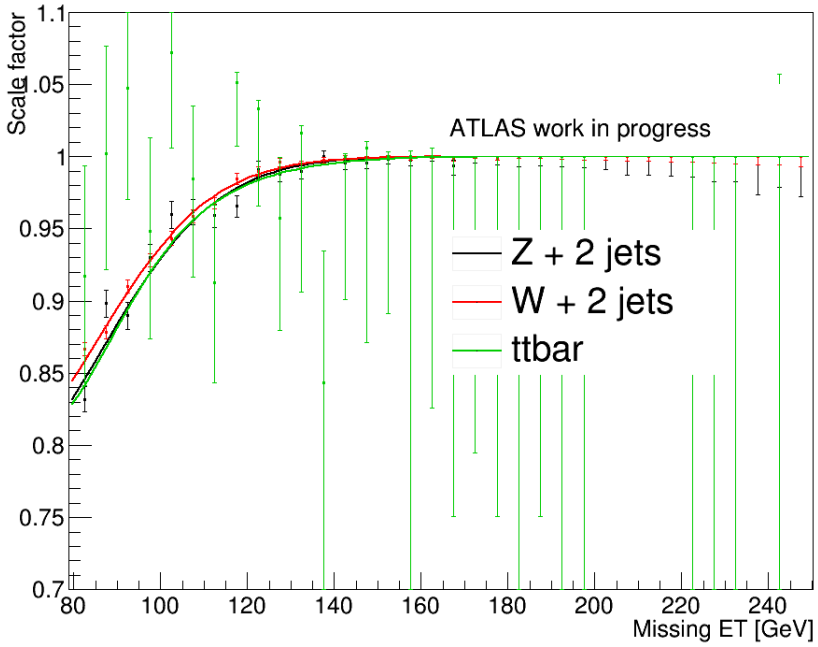

Figure 4.17: Delayed stream $E_{\mathrm{T}}^{\mathrm{miss}}$ trigger scale factor comparison among the three samples: W (red), Z (black) and $t\bar{t}$ (green).

4.2.7 Cleaning cut for trigger

This section is to investigate the trigger dependences with respect to certain variables and how to treat them in the main $ZH \to \nu\bar{\nu}b\bar{b}$ analysis.

4.2.7.1 $E_{\mathrm{T}}^{\mathrm{miss}}$ trigger dependence

Various $E_{\mathrm{T}}^{\mathrm{miss}}$ trigger efficiencies with respect to some variables are studied to test trigger dependence. The trigger efficiency dependences are checked for number of primary vertices and average number of interactions per bunch crossing for nominal triggers and delayed stream trigger (Fig. 4.18, 4.19, 4.20, 4.21[3]) and clearly $E_{\mathrm{T}}^{\mathrm{miss}}$ trigger does not depend on these variables for both nominal triggers and delayed stream.

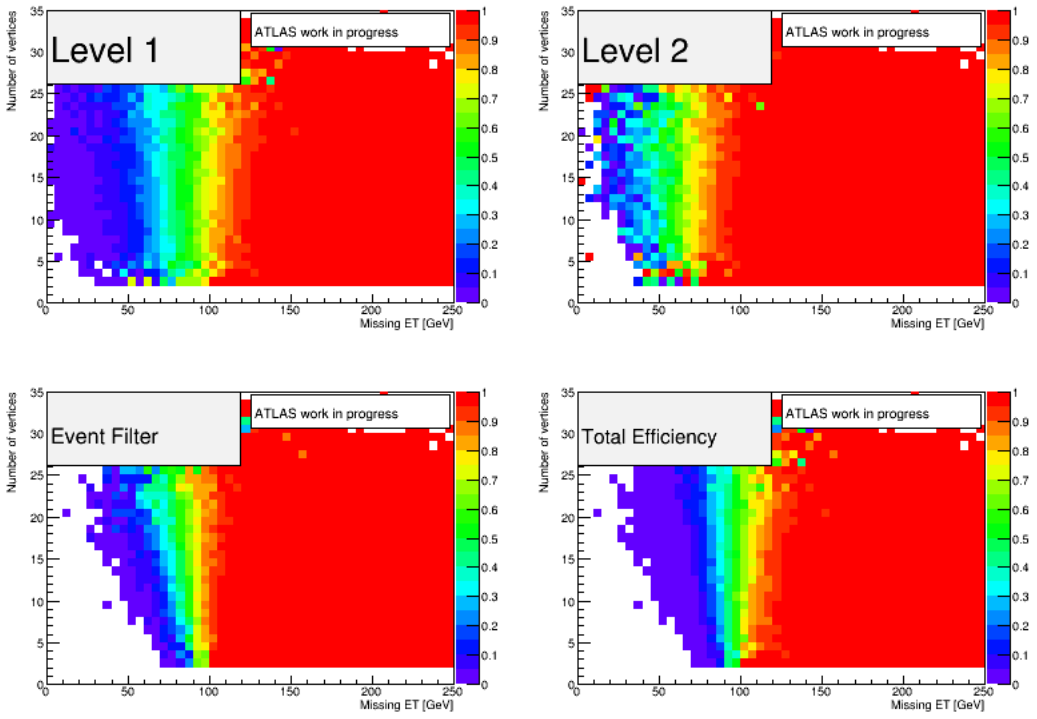

Figure 4.18: $E_{\mathrm{T}}^{\mathrm{miss}}$ trigger turn–on dependence with respect to number of vertices for trigger EF_xe80_tclcw_loose for $Z \to \mu\mu$ sample in 2-jet bin on MC samples. The colors correspond to the efficiency.

More tests show that the $E_{\mathrm{T}}^{\mathrm{miss}}$ triggers depend on the transverse momentum p_{T} of leading jet (Figs. 4.22, 4.23) for p_{T} <100 GeV, and we also found trigger dependence on the scalar sum of p_{T} of the two leading jets ($J12pT$) (Figs. 4.24, 4.25) for $J12pT < 120$ GeV. These results indicate that we need some special treatment to deal with those biases in order to apply in the analysis. We need to define the cleaning cut in term of p_{T} or $J12pT$, and determine which cut is the most optimized for the analysis.

[3]The sharp cut at average number of interactions around 27 is due to the limit on instantaneous luminosity of delayed stream trigger (see section 4.1.5.2).

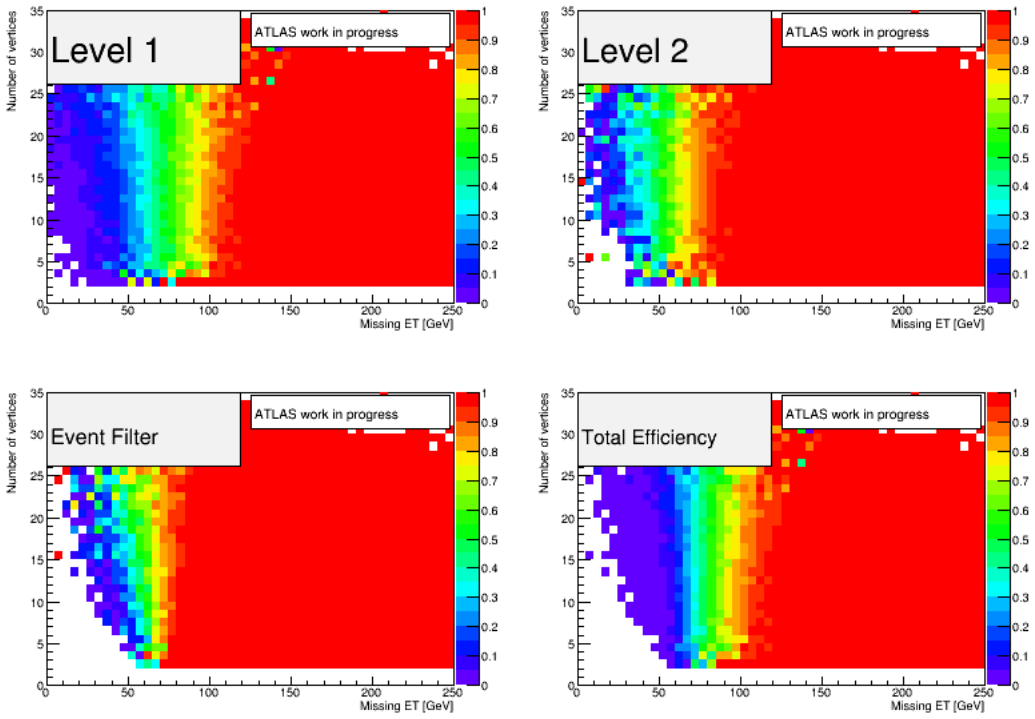

Figure 4.19: $E_{\mathrm{T}}^{\mathrm{miss}}$ trigger turn–on dependence with respect to number of vertices for trigger EF_xe60_tclcw_loose_delayed for $Z \to \mu\mu$ sample in 2-jet bin on MC samples. The colors correspond to the efficiency.

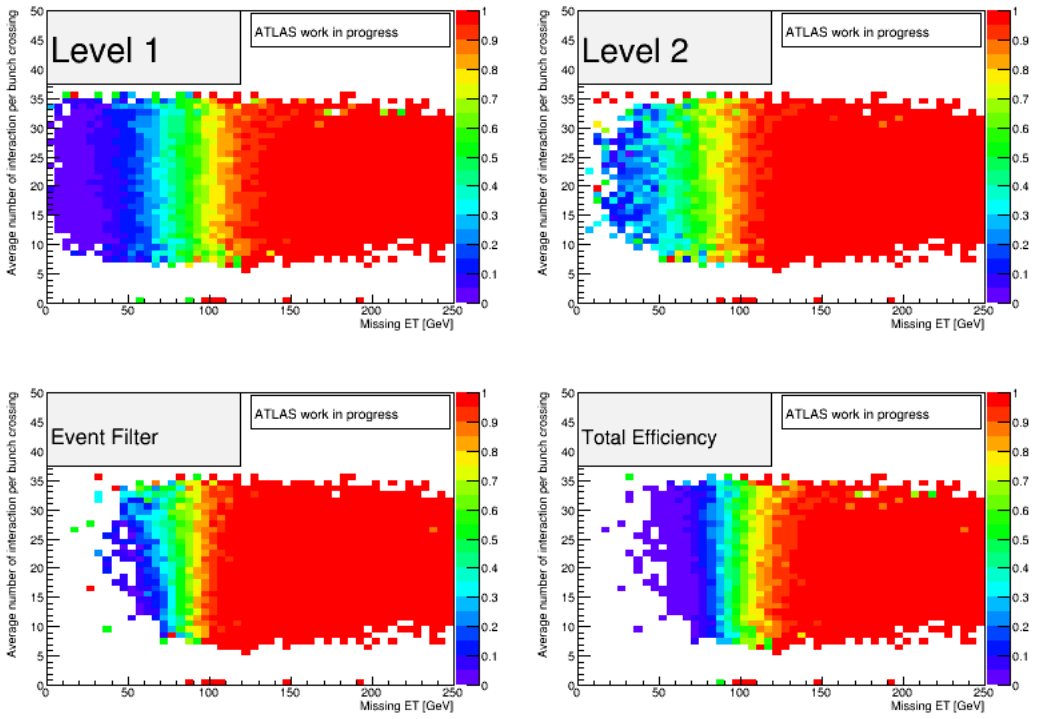

Figure 4.20: $E_{\mathrm{T}}^{\mathrm{miss}}$ trigger turn–on dependence with respect to the average number of interactions per bunch crossing for trigger EF_xe80_tclcw_loose for $Z \to \mu\mu$ sample in 2-jet bin (on data). The colors correspond to the efficiency.

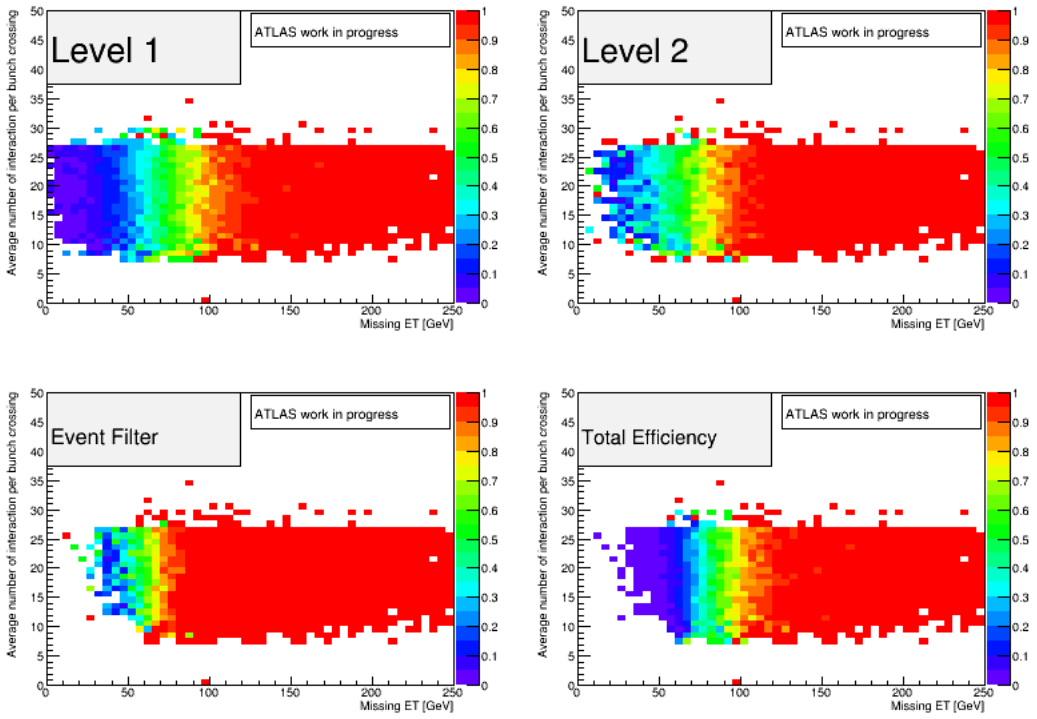

Figure 4.21: $E_{\mathrm{T}}^{\mathrm{miss}}$ trigger turn–on dependence with respect to the average number of interactions per bunch crossing for trigger EF_xe60_tclcw_loose_delayed for $Z \rightarrow \mu\mu$ sample in 2-jet bin (on data) . The colors correspond to the efficiency.

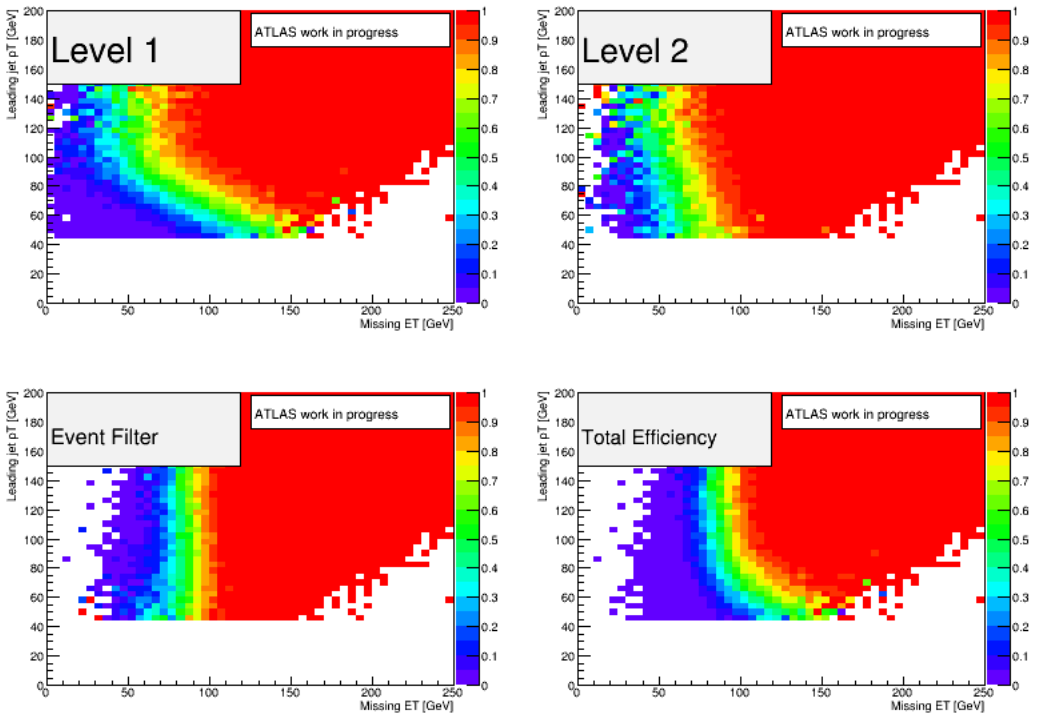

Figure 4.22: $E_{\mathrm{T}}^{\mathrm{miss}}$ trigger turn–on dependence with respect to p_{T} of leading jet for trigger EF_xe80_tclcw_loose for $Z \to \mu\mu$ sample in 2-jet bin on MC. The colors correspond to the efficiency.

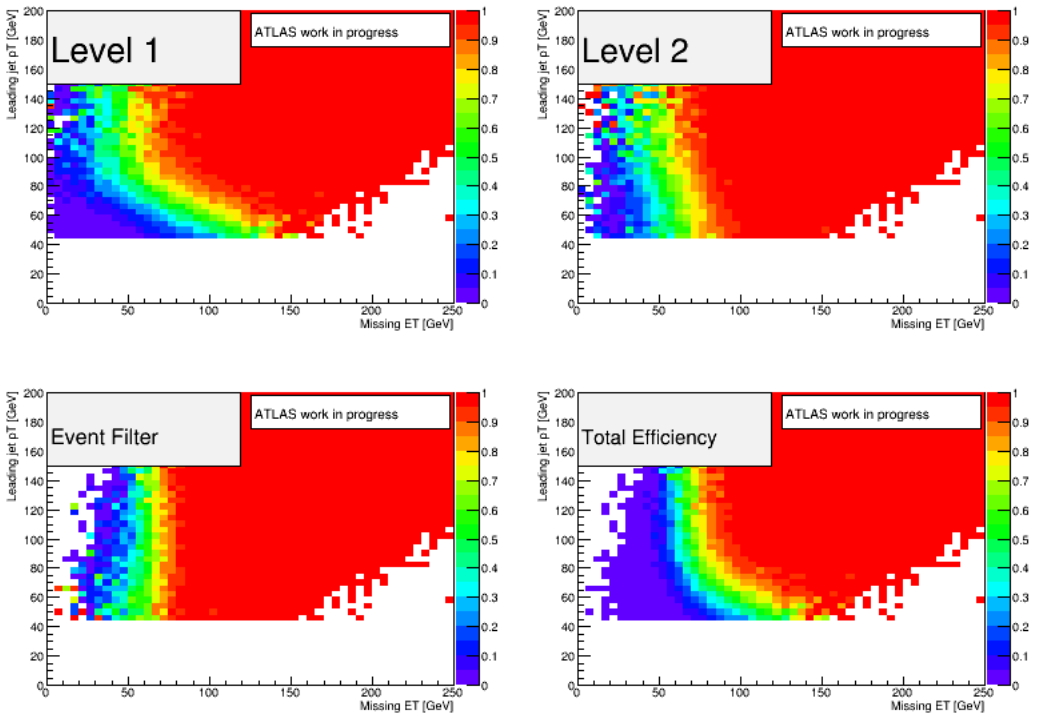

Figure 4.23: $E_{\mathrm{T}}^{\mathrm{miss}}$ trigger turn–on dependence with respect to p_{T} of leading jet for trigger EF_xe60_tclcw_loose_delayed for $Z \to \mu\mu$ sample in 2-jet bin on MC. The colors correspond to the efficiency.

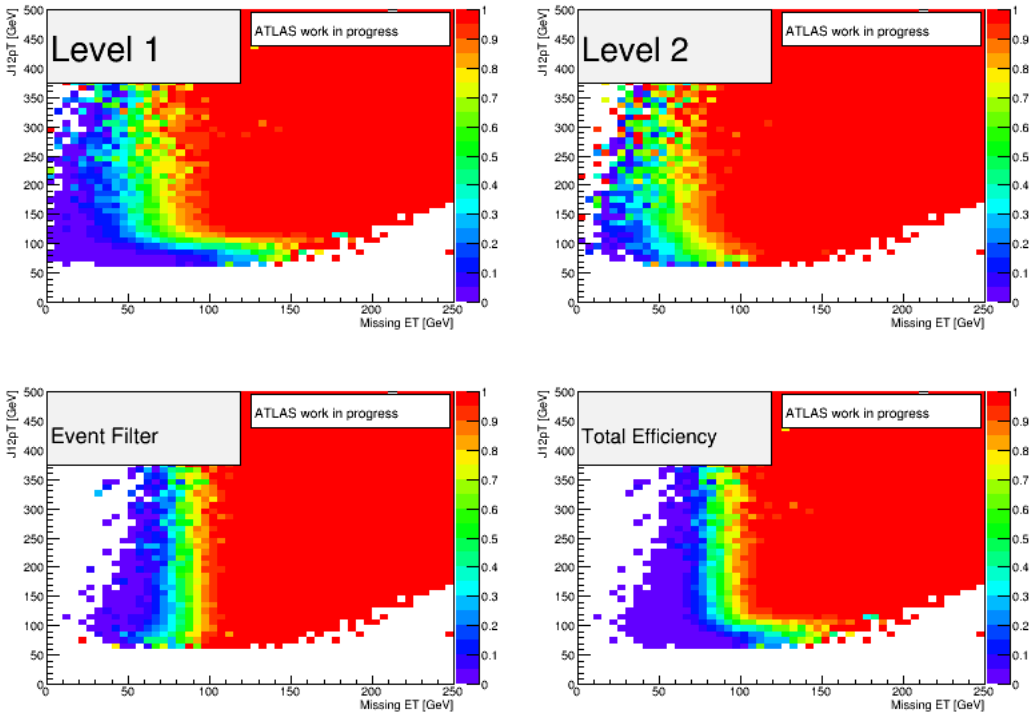

Figure 4.24: $E_{\mathrm{T}}^{\mathrm{miss}}$ trigger turn–on dependence with respect to $J12pT$ for trigger EF_xe80_tclcw_loose for $Z \to \mu\mu$ sample in 2-jet bin on MC. The colors correspond to the efficiency.

4.2.7.2 Defining cleaning cut for $E_{\mathrm{T}}^{\mathrm{miss}}$ trigger

From the last section we have seen the trigger biases with respect to p_{T} and $J12pT$. We will now investigate more the trigger dependence and define cleaning cut for the analysis. This section focuses on the nominal trigger EF_xe80_tclcw_loose, the obtained results are applied in the nominal analysis as well.

Figures 4.22, 4.24 shows that the trigger turn–on bias with respect to p_{T} and $J12pT$ stops at p_{T} =100 GeV and at $J12pT$ =120 GeV respectively. Above these cuts the trigger turn–ons are independent of jet p_{T} and $J12pT$, and the same behaviour can be found with delayed stream trigger (Figs 4.23, 4.25). We apply the cleaning cuts to remove trigger biases using these two thresholds, then re–do the parametrization for triggers again. In order to determine which cleaning cut is optimized for the analysis, we need to estimate the signal significance and also the signal acceptance of the Higgs on $ZH \to \nu\bar{\nu}b\bar{b}$ channel yielded after each cleaning cut. The signal significance is defined as the ratio of number of signal divided by the square root of the number of background; the signal acceptance is determined as the number of signal after applying the cleaning cuts divided by the one before applying any cleaning cuts.

The selection for this study of cleaning cuts will be the same as in $ZH \to \nu\bar{\nu}b\bar{b}$ channel which is defined as follows:

- Lepton veto (no electron or muon in the events)

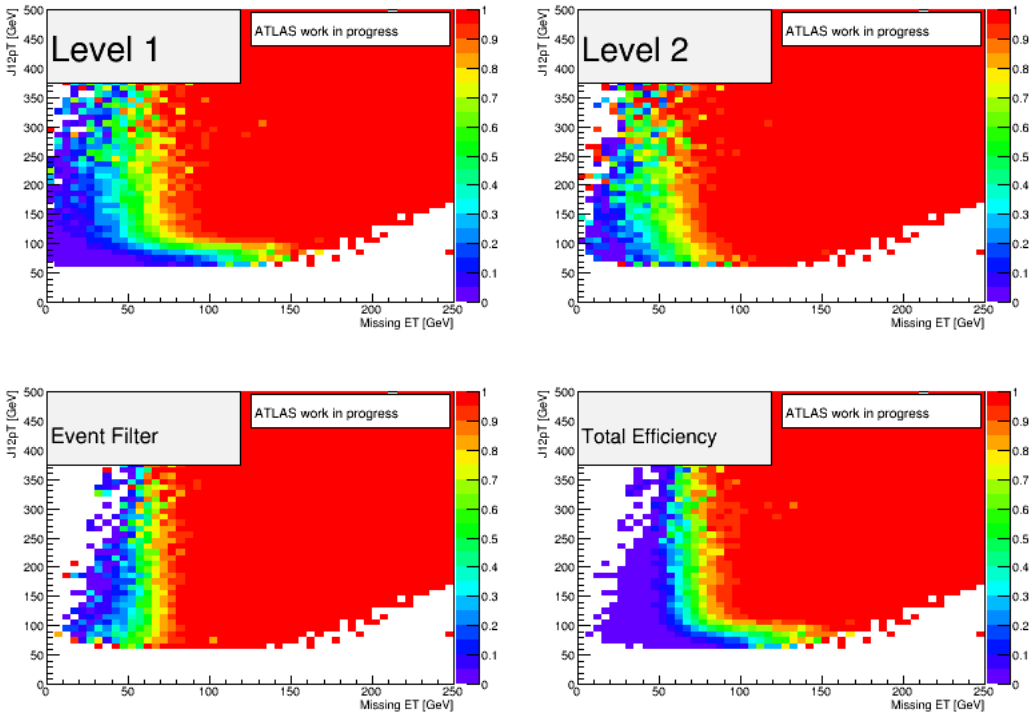

Figure 4.25: $E_{\mathrm{T}}^{\mathrm{miss}}$ trigger turn–on dependence with respect to $J12pT$ for trigger EF_xe60_tclcw_loose_delayed for $Z \rightarrow \mu\mu$ sample in 2-jet bin on MC. The colors correspond to the efficiency.

- $E_{\mathrm{T}}^{\mathrm{miss}}$ trigger EF_xe80_tclcw_loose
- $E_{\mathrm{T}}^{\mathrm{miss}}$ >90 GeV, $P_{\mathrm{T}}^{\mathrm{miss}}$ >30 GeV, $\Delta\phi(E_{\mathrm{T}}^{\mathrm{miss}}, P_{\mathrm{T}}^{\mathrm{miss}}) < \pi/2$
- 2 or 3 jets with p_{T} of leading jet > 45 GeV
- b–tagging: Exactly 2 b–tagged jets, which have to be the two highest p_{T} jets.
- Topological cuts: Angular distance between Z boson and Higgs boson $\Delta\phi(V, H)$ >2.8, minimum value of angular distance between Z boson and jets $\Delta\phi(E_{\mathrm{T}}^{\mathrm{miss}}, jets)$ >1.5
- Distance between two jets:
  - $\Delta R(jet1, jet2)$ >0.7 (for $E_{\mathrm{T}}^{\mathrm{miss}}$ <200 GeV)
  - ΔR <3 (for $E_{\mathrm{T}}^{\mathrm{miss}}$ < 120 GeV)
  - ΔR <2.3 (for $E_{\mathrm{T}}^{\mathrm{miss}}$ < 160 GeV)
  - ΔR <1.8 (for $E_{\mathrm{T}}^{\mathrm{miss}}$ < 200 GeV)
  - ΔR <1.4 (for $E_{\mathrm{T}}^{\mathrm{miss}}$ > 200 GeV).

Figure 4.26 shows the result of the check for $E_{\mathrm{T}}^{\mathrm{miss}}$ after applying the above selection.

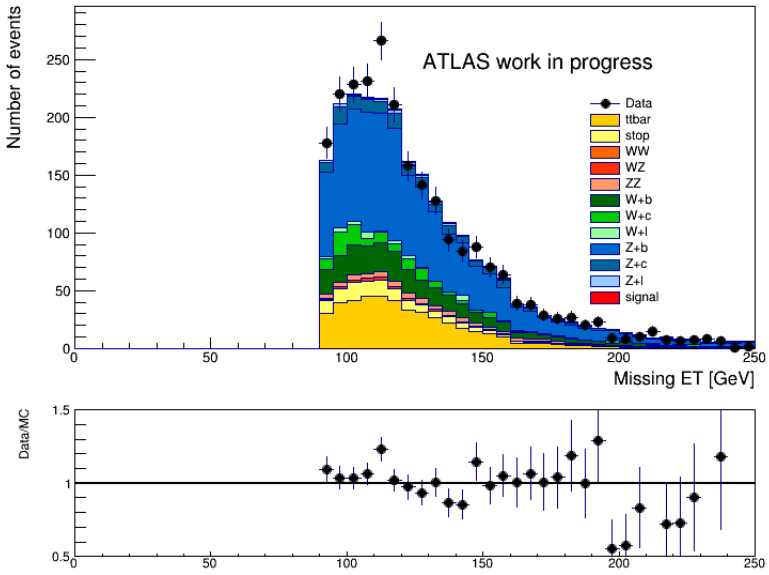

Figure 4.26: Cross-check for $E_{\mathrm{T}}^{\mathrm{miss}}$ using 0-lepton selection in 2-jet bin.

The signal significance and signal acceptance of the Higgs signal will be represented as a function of the cut value of p_{T} of leading jet or $J12pT$. Here we consider our study in 2-jet bin and in 2 $E_{\mathrm{T}}^{\mathrm{miss}}$ bins: 90–120 GeV and 120–160 GeV. Figure 4.27 shows that both signal acceptance and significance in the 90–120 GeV $E_{\mathrm{T}}^{\mathrm{miss}}$ bin are reduced as the cleaning cuts increase, nevertheless, if we apply the proposed cut for p_{T} of leading jet at p_{T} >100 GeV, the acceptance loss is around 14% while at the cut $J12pT$ >120 GeV the acceptance would lose around 10%. For the check on 120–160 GeV $E_{\mathrm{T}}^{\mathrm{miss}}$ bin (Fig. 4.28), we can observe a smaller loss of acceptance: around 5% for cleaning cut of p_{T} of leading jet and 3% for cleaning cut of $J12pT$.

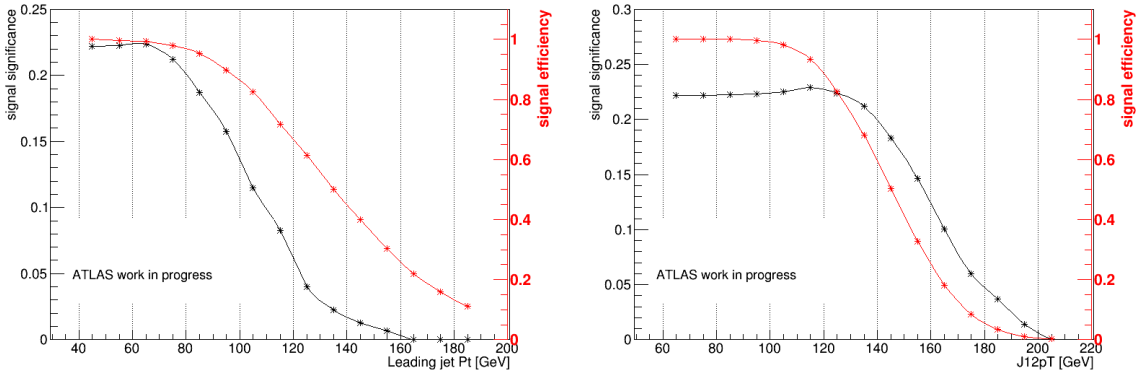

Figure 4.27: Signal significance and signal acceptance as functions of cuts on p_{T} of leading jets (left) and $J12pT$ (right) in $E_{\mathrm{T}}^{\mathrm{miss}}$ bin of 90–120 GeV and 2-jet bin.

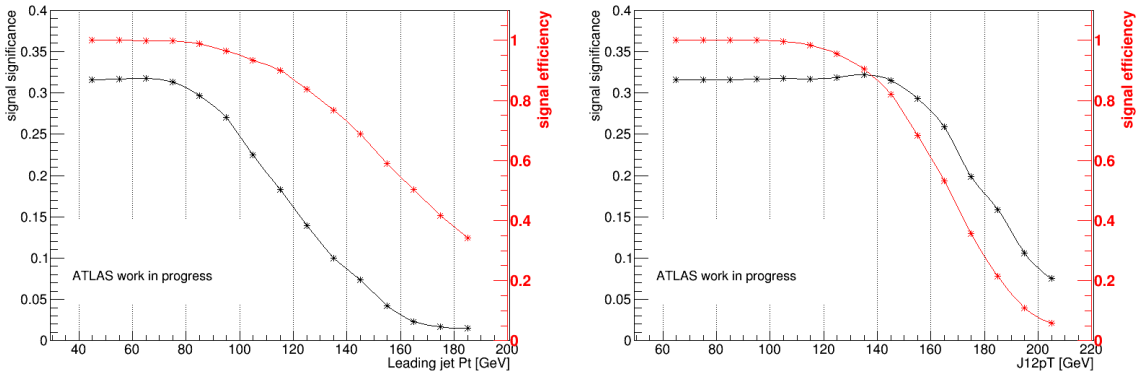

Figure 4.28: Signal significance and signal acceptance as functions of cuts on p_{T} of leading jets (left) and $J12pT$ (right) in $E_{\mathrm{T}}^{\mathrm{miss}}$ bin of 120–160 GeV and 2-jet bin.

For the check of signal significance in 90–120 GeV $E_{\mathrm{T}}^{\mathrm{miss}}$ bin, the cut of $p_{\mathrm{T}} > 100$ GeV causes the significance to decrease significantly (40% of its maximum value) while the cleaning cut for $J12pT$ shows that the significance is maintained at the highest value. If we take a look at the 120–160 GeV $E_{\mathrm{T}}^{\mathrm{miss}}$ bin, we can observe a very similar behavior as in 90–120 GeV $E_{\mathrm{T}}^{\mathrm{miss}}$ bin, with the loss of significance of only 2% for the cleaning cut at $J12pT$ >120 GeV and 22% for the cut of p_{T} >100 GeV. To conclude this part, we choose the optimized solution for cleaning cut for $E_{\mathrm{T}}^{\mathrm{miss}}$ trigger to $J12pT$ >120 GeV.

Cleaning trigger for 3–jet bin We have defined that the cleaning cut in the 2-jet case to remove trigger efficiency bias is the cut on scalar sum of p_{T} of the 2 leading jets $J12pT > 120$ GeV. However, if we come to 3-jet bin we have to determine another cleaning cut. We need to check if we are to apply the scalar sum of p_{T} of 2 leading jets or scalar sum of p_{T} of 3 jets in the events. To do so we estimate which cleaning cut of which variable yields more signal significance and signal acceptance.

Figures 4.29 and 4.30 show that the cleaning cut for scalar sum of p_{T} of leading jets ($J123pT$) for 3-jet case is about 170 GeV (in region $90 < E_{\mathrm{T}}^{\mathrm{miss}} < 120$ GeV) or 150 GeV (in region $E_{\mathrm{T}}^{\mathrm{miss}} > 120$ GeV). As we did for the case of 2 jets, we use the 0–lepton selection and 3 signal jets with 2 b–tagged leading jets, and the significance and signal acceptance are calculated in two $E_{\mathrm{T}}^{\mathrm{miss}}$: 90–120 GeV and 120–160 GeV. Then we represent the signal significance and acceptance as a function of $J12pT$ or $J123pT$ cut.

As can be seen in Figures 4.31, 4.32, at the cut $J12pT$ >150 GeV, in $E_{\mathrm{T}}^{\mathrm{miss}}$ bin of $90 - 120$ GeV, the significance drops about 50% and the acceptance loses around 78%, which are high percentages. On the other hand, for the cut at $J123pT$ >170 GeV the significance loses around 35% and acceptance loss about 60%. If the $E_{\mathrm{T}}^{\mathrm{miss}}$ bin of 120–160 GeV is considered, more significance and acceptance losses are observed for the cut at $J12pT > 150$ GeV with the rate of 20% and 45%, respectively, while the significance is maintained at its maximum value and only about 8% of total acceptance is lost if the cut $J123pT$ >150 GeV is applied.

So to conclude the study of cleaning cut in 3-jet bin, in the region of $90 < E_{\mathrm{T}}^{\mathrm{miss}} < 120$ GeV,

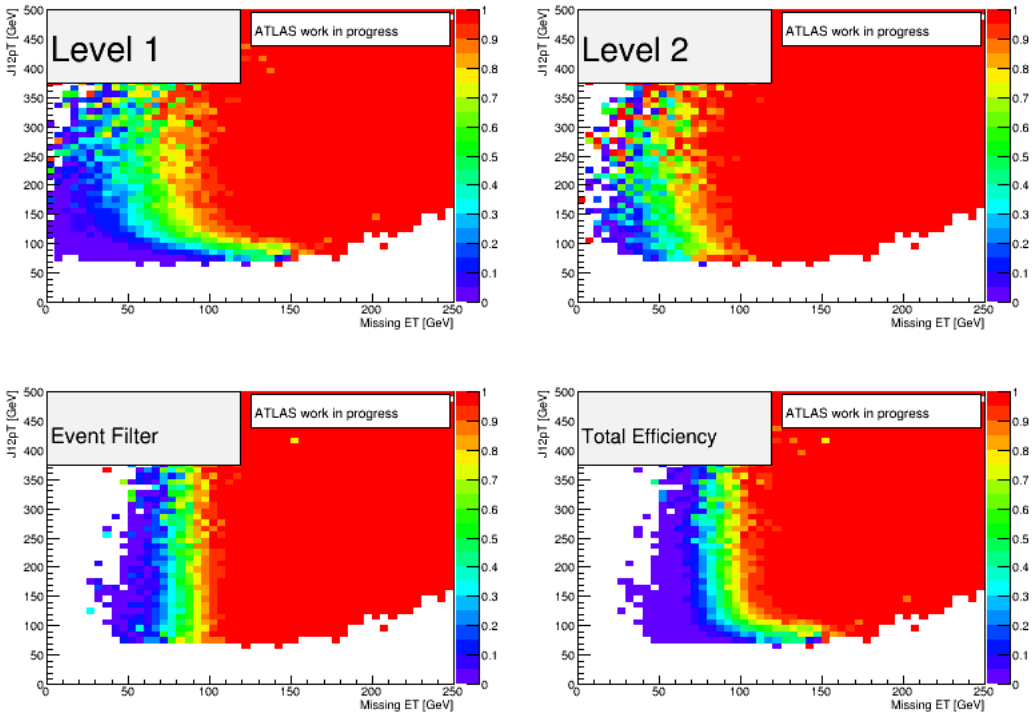

Figure 4.29: $E_{\mathrm{T}}^{\mathrm{miss}}$ trigger turn–on dependence with respect to $J12pT$ for trigger EF_xe80_tclcw_loose for $Z \to \mu\mu$ sample in 3-jet bin.

the cleaning cut is defined as $J123pT$ >170 GeV, and for the region $E_{\mathrm{T}}^{\mathrm{miss}}$ >120 GeV, this cut should be $J123pT$ >150 GeV.

All the cleaning cuts on $J12pT$ and $J123pT$ studied here are included in the main Higgs analysis in 0-lepton channel.

Applying cleaning cuts on trigger parametrization Now the cleaning cuts are defined. The trigger parametrization should be re-done again including those cuts in order to verify the parametrization and also the invariance of trigger across the categories and studied samples. Table 4.4 shows the fitting parameters for $Z \to \mu\mu$ and $W \to \mu\nu$ samples after applying cleaning cut, and those fitting parameters are very similar between the two samples.

To conclude this part, we consider the trigger scale factor and check the consistency among the three dedicated samples: $Z \to \mu\mu$, $W \to \mu\nu$ and $t\bar{t}$. Figure 4.33 indicates that the differences among the three samples are small within the statistical uncertainties of $t\bar{t}$ sample (note that the $t\bar{t}$ sample is always low on statistics).

At low $J12pT/J123pT$ ($J12pT$ <120 GeV or $J123pT$ <150 GeV), we can also apply different trigger scale factors. However the low statistics prevent us from obtaining reliable results.

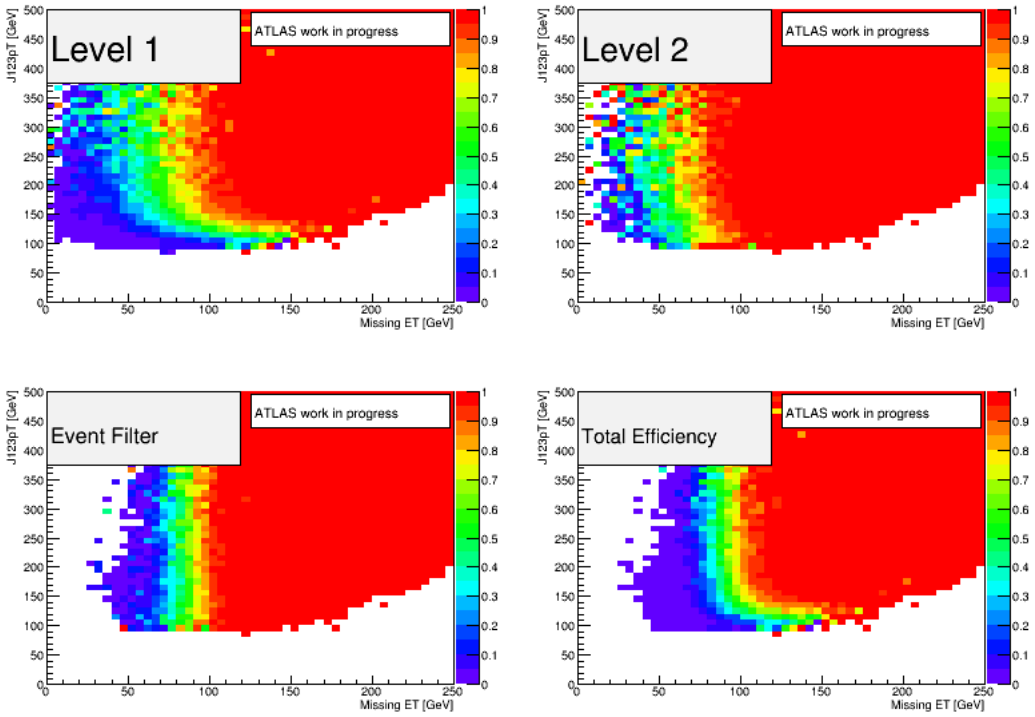

Figure 4.30: $E_{\mathrm{T}}^{\mathrm{miss}}$ trigger turn–on dependence with respect to $J123pT$ for trigger EF_xe80_tclcw_loose for $Z \to \mu\mu$ sample in 3-jet bin.

4.2.8 Trigger uncertainty and systematics

The statistical error estimation for trigger is done by using the statistical errors on calculating trigger efficiencies. We are only interested in the region used in the analysis, $E_{\mathrm{T}} > 90$ GeV. At this point the trigger scale factor uncertainty is around 1.6% for Z samples, and around 1.3% for W samples (Fig. 4.34). The systematic uncertainty is estimated as the difference between the scale factor for W samples and the one for Z samples. The trigger uncertainty with both statistical and systematic errors is presented in Figure 4.35, showing that the overall uncertainty is small. The trigger uncertainty error vanishes when the trigger turn–on reaches the plateau (for $E_{\mathrm{T}}^{\mathrm{miss}} > 130$ GeV).

As we can observe in Figure 4.33, the difference is about 1.3 % at $E_{\mathrm{T}}^{\mathrm{miss}}$ =90 GeV, and vanishes when the scale factor reaches plateau as the two scale factors converge to 1. Moreover the cross–check from last section shows that the scale factor for $t\bar{t}$ sample is also in consistence within statistical uncertainty.

Table 4.4: Fitting parameters at each level of trigger for $Z \to \mu\mu$ and $W \to \mu\nu$ samples for MC and data after applying trigger cleaning cut for 2-jet bin.

$Z \to \mu\mu$	MC		data	
	Mean value [GeV]	Width	Mean value [GeV]	Width
Level 1	52.87±0.26	23.97±0.27	54.24±0.39	25.11±0.42
Level 2	45.51±0.44	21.74±0.37	50.34±0.65	26.13±0.58
Event Filter	59.15±0.24	14.54±0.22	58.32±0.01	15.83±0.02
$W \to \mu\nu$	MC		data	
	Mean value [GeV]	Width	Mean value [GeV]	Width
Level 1	53.88±0.1	23.83±0.12	54.22±0.16	24.99±0.18
Level 2	44.95±0.19	21.39±0.16	49.31±0.28	26.3±0.26
Event Filter	58.64±0.01	14.37±0.09	57.66±0.05	15.21±0.1

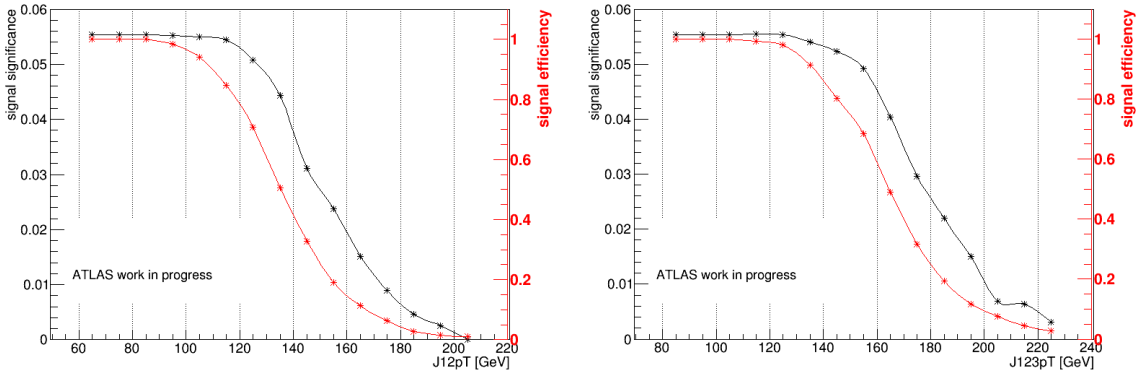

Figure 4.31: Signal significance and signal acceptance as functions of cuts on $J12pT$ (left) and $J123pT$ (right) in $E_{\mathrm{T}}^{\mathrm{miss}}$ bin of 90–120 GeV and 3-jet bin.

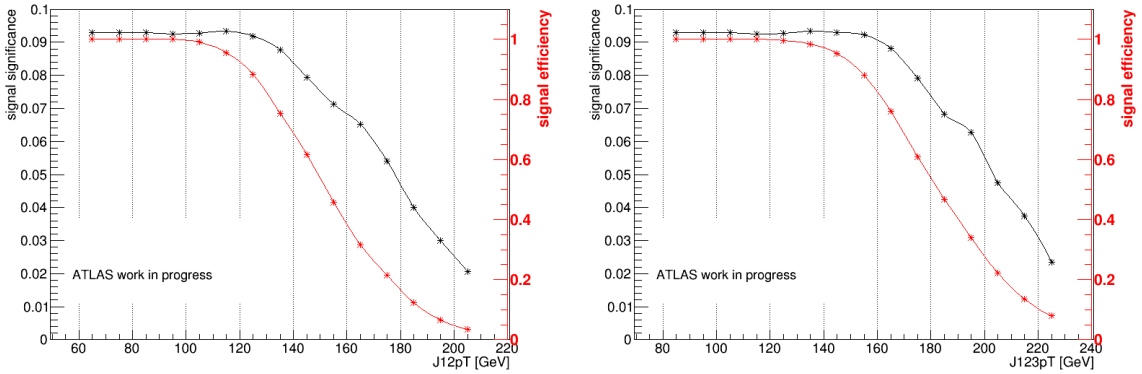

Figure 4.32: Signal significance and signal acceptance as functions of cuts on $J12pT$ of leading jets (left) and $J123pT$ (right) in $E_{\mathrm{T}}^{\mathrm{miss}}$ bin of 120–160 GeV and 3-jet bin.

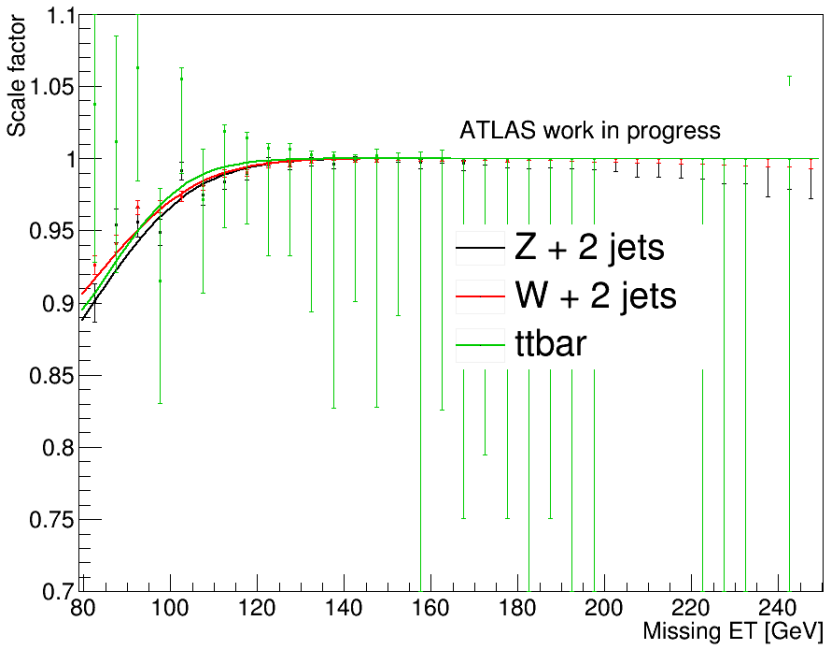

Figure 4.33: Delayed stream trigger scale factors for W, Z, $t\bar{t}$ samples after applying trigger cleaning cut (for 2-jet bin).

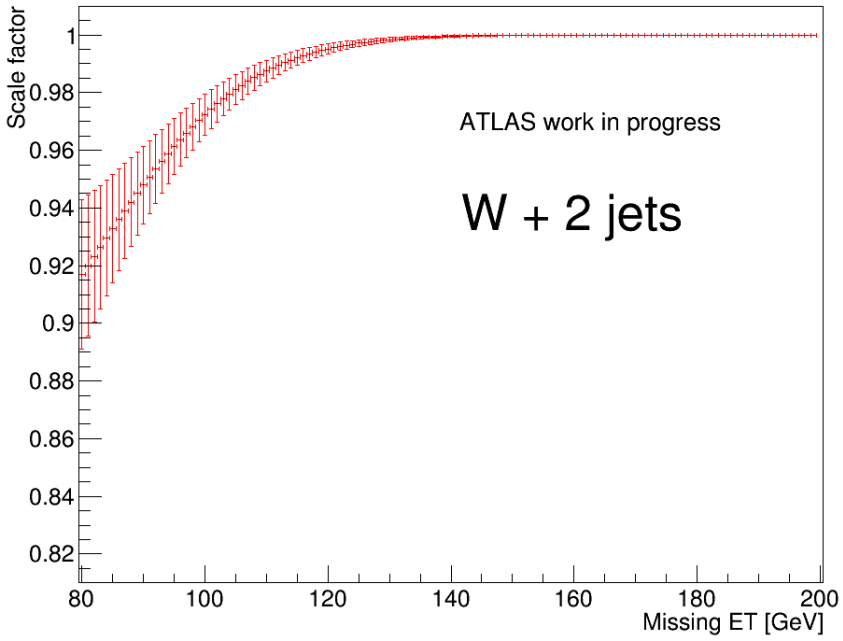

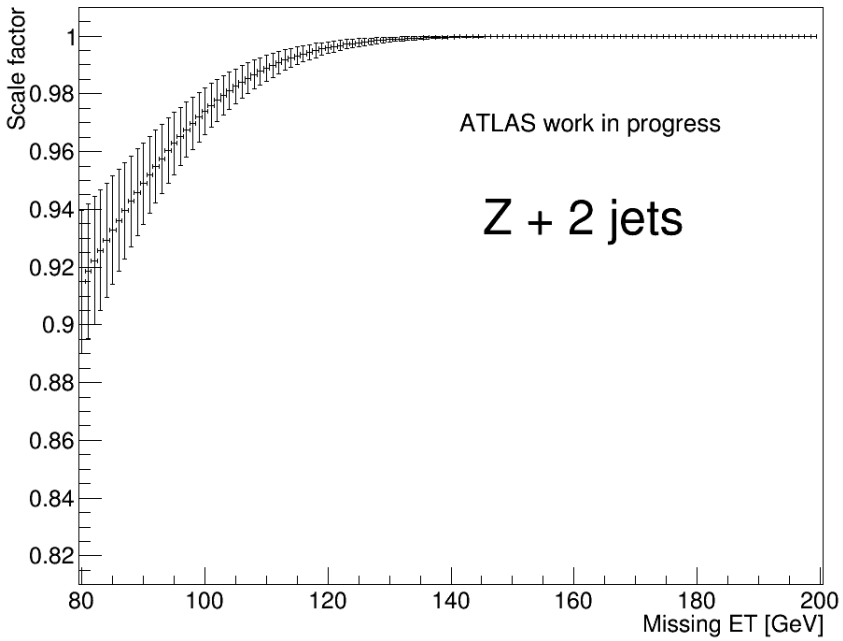

Figure 4.34: Statistical error of trigger scale factor for W (top) and Z (bottom) samples.

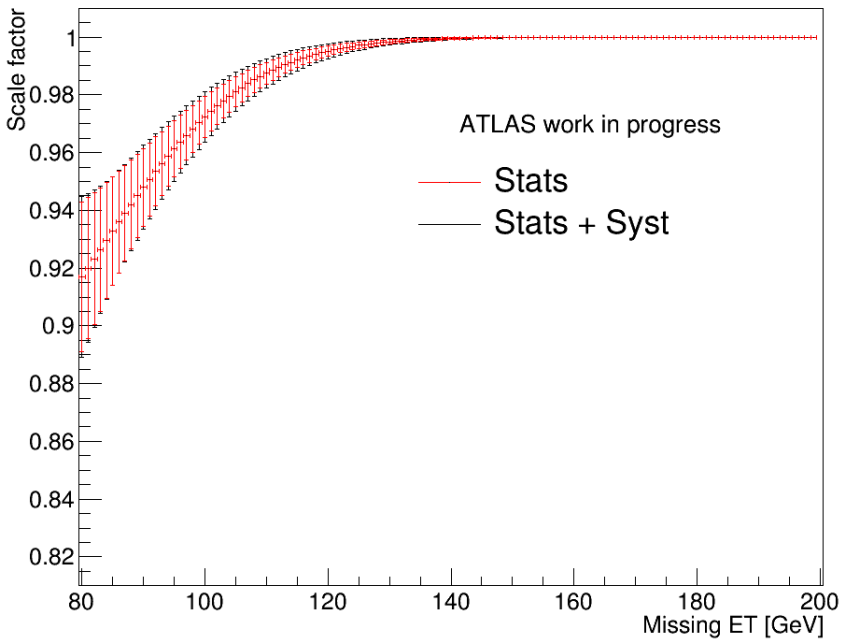

Figure 4.35: Trigger scale factor for W samples with statistical error and statistical + systematics error.

4.3 Conclusion

In this chapter we have discussed the parametrization of the $E_{\mathrm{T}}^{\mathrm{miss}}$ trigger and the main target is the $E_{\mathrm{T}}^{\mathrm{miss}}$ trigger present in the delayed stream of data. Due to the availability of the delayed stream $E_{\mathrm{T}}^{\mathrm{miss}}$ trigger EF_xe60_tclcw_loose_delayed in the 2012 data, in order to be used in the analysis, from period A of data to before period E, the nominal triggers (EF_xe80_tclcw, EF_xe80T_tclcw_loose, EF_xe80_tclcw_loose) are used, and after period E, the delayed stream trigger is used in the fraction of data in which it is available (instantaneous luminosity $<5.77\times10^{33}\,\mathrm{cm}^{-2}\mathrm{s}^{-1}$). If the delayed stream trigger is off at some point, the trigger EF_xe80_tclcw_loose is used instead.

This parametrization uses $Z \to \mu\mu$ and $W \to \mu\nu$ events to model and parametrize the $E_{\mathrm{T}}^{\mathrm{miss}}$ trigger. $t\bar{t}$ events are used for cross-checking consistency only due to its low overall statistics. This parametrization is based on the trigger efficiency calculation and fitting using the error function. The results of the trigger efficiency calculation show an overall good agreement between the efficiency points and the fitting curves, indicating a good trigger modelling. The trigger scale factors (the ratio of data and MC turn-on curves) also show good agreement between points and analytic function curves for $E_{\mathrm{T}}^{\mathrm{miss}}$ >90 GeV (analysis region).

The $E_{\mathrm{T}}^{\mathrm{miss}}$ trigger parametrization also shows the independence of trigger on the number of jets, the application of multijet rejection cuts for 0–lepton channel of Higgs analysis, as well as the event–type ($Z \to \mu\mu$, $W \to \mu\mu$, or $t\bar{t}$). These independences guarantee the universality of the trigger parametrization: it is not necessary to treat the trigger parametrization separately based on the event categories, we only need to parametrize the trigger on just one category and then apply to all other categories. The reference event–type which yields the most statistics was chosen: W events with 2 jets and no multijet rejection applied.

In this study, the trigger turn–on is shown to be dependent on certain variables: p_{T} of leading jet and scalar sum of jets p_{T} ($J12pT$ or $J123pT$). The study shows no other dependence. The cleaning cut for $E_{\mathrm{T}}^{\mathrm{miss}}$ trigger is important in order to remove the trigger biases in the analysis, and we need a cleaning cut that can remove efficiently the bias as well as maintaining the high efficiency and significance of the expected Higgs signal. The optimized cut is on the $J12pT$ and $J123pT$ variables which are defined as follows:

- For 2-jet events: $J12pT$ >120 GeV,
- For 3-jet events in region 90< $E_{\mathrm{T}}^{\mathrm{miss}}$ <120 GeV: $J123pT$ >170 GeV,
- For 3-jet events in region $E_{\mathrm{T}}^{\mathrm{miss}}$ >120 GeV: $J12p3T$ >150 GeV.

The same result is also applied for the nominal analysis. Applying these cleaning cuts in the parametrization again we can use the trigger in the 0–lepton channel of the Higgs analysis. Overall the $E_{\mathrm{T}}^{\mathrm{miss}}$ trigger statistical and systematic uncertainties are small (around 1%).

Chapter 5

Search for the Higgs boson in the $b\bar{b}$ decay channel

As summarized in chapter 1, a Higgs-like boson was discovered at LHC and exhibits coupling with bosons in SM and leptons. Nevertheless, a confirmation of coupling of this Higgs boson to quarks is needed to confirm the discovered Higgs-like particle is the Higgs boson predicted in SM.

5.1 Higgs analysis channel

In this part we want to search for Higgs boson in the $H \to b\bar{b}$ decay mode to test the Higgs coupling to quarks.

5.1.1 Choosing Higgs production mode

Here we consider the search in the proton-proton collisions at $\sqrt{s} = 8$ TeV with 20.3 fb^{-1} of delivered luminosity recorded by ATLAS detector in 2012.

We choose the production mode based on the detectability of the Higgs signal in each channel of Higgs production for the $H \to b\bar{b}$ decay mode: The gluon-gluon fusion has the largest cross section (19.27 pb at $m_H = 125$ GeV), however a challenge of huge background (about 10^8 pb) makes it almost impossible to extract the Higgs signal if we are to search for decay modes of Higgs to pair of quarks. The same difficulty is present with the weak boson fusion production (with a cross section of 1.58 pb at $m_H = 125$ GeV), where the Higgs boson is produced with two quarks. The channels that are useful to detect the Higgs boson signal thanks to their detectable signatures in detector are Higgs-strahlung production, where the Higgs boson associates with a weak boson (either W or Z) and $t\bar{t}H$ production, where the Higgs boson associates with a pair of top-quarks. At $m_H = 125$ GeV, the corresponding cross-sections are: 0.7 pb, 0.42 pb and 0.13 pb. The $t\bar{t}H$ production channel has the lowest cross section overall, so the Higgs-strahlung is our preferable production channel.

We are therefore considering the Higgs production via the Higgs-strahlung process:

$$pp \to Z^* \to ZH.$$

5.1.2 Choosing analysis channel

5.1.2.1 Choosing Z decay mode

As discussed in section 5.1.1, this search concerns the Higgs-strahlung production of Higgs boson associated with a Z boson. Regarding the decay mode of Z boson, it can be divided into 3 categories:

- Leptonic decays: The Z boson decays to a pair of charged leptons (e, μ, τ) with a branching ratio for each flavour of 3.37%.
- Invisible decays: The Z boson decays into neutrino-antineutrino pairs (3 families inclusively) with a total branching ratio of 20%.
- Hadronic decays: The Z boson decays to quarks with inclusive branching ratio of 69.91%.

The leptonic decay of Z boson has pure signatures thanks to the presence of leptons. However, the ATLAS detector can identify electrons and muons with high efficiencies while identifying taus would be harder due to their subsequent decays (leptonic or hadronic). The Z leptonic decay can therefore be well-detected with total branching ratio of 6.7%, which is relatively small. The hadronic decays of Z have the largest branching ratio, nevertheless it would be nearly impossible to extract this channel in the sea of quarks, gluons from the large amount of processes in proton-proton collisions at LHC. So finally, the invisible decay modes, which have relatively large branching ratio, is our preferred channel to perform our search since the neutrinos can be identified as missing transverse energy in the ATLAS detector (more detail discussed in chapter 4).

5.1.2.2 Choosing Higgs decay mode

For $m_H = 125$ GeV, the Higgs boson decays dominantly to a pair of b-quarks ($\sim$57.7% of branching ratio compared to 2.91% of $H \to c\bar{c}$), so it is the most prospective channel for the Higgs boson search. Our analysis concerns the Higgs search in the mode where Higgs decays to a pair of b-quarks.

The topology of our Higgs analysis can be viewed in Figure 5.1.

In total there are three $VH(H \to b\bar{b})$ analysis channels: $ZH \to \nu\bar{\nu}b\bar{b}$, $ZH \to \ell\ell b\bar{b}$ and $WH \to \ell\nu b\bar{b}$, however the latter two are not included in this context. For the name convention, we refer the analysis $ZH \to \nu\bar{\nu}b\bar{b}$ as 0–lepton, $ZH \to \ell\ell b\bar{b}$ as 2–lepton, and the $WH \to \ell\nu b\bar{b}$ channel as 1–lepton.

5.1.2.3 General analysis

The strategy of searching for the Higgs boson in the channel $pp \to ZH \to \nu\bar{\nu}b\bar{b}$ at LHC and in ATLAS detector can be summarized as follows:

1. Select events (trigger) with large $E_{\mathrm{T}}^{\mathrm{miss}}$ (for $Z \to \nu\bar{\nu}$ events), see chapter 4.

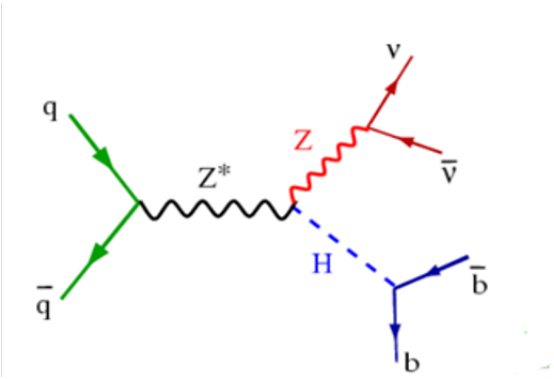

Figure 5.1: Feynman diagram for Higgs production in Higgs-strahlung production channel. The Z boson decays to neutrinos and H decays to a pair of b-quarks.

2. Construct distributions of invariant mass, in this case the invariant mass of two b-jets. Estimate the expected contribution of signal processes, as well as the contributions from other SM processes that can produce the same signature. The detailed steps can be followed from section 5.2 to 5.8.

3. Estimate systematic uncertainties: this step is to estimate how much the signal and background predictions should vary due to the possible measurement errors. This will be discussed in detail in section 5.9

4. Statistical analysis: This takes the signal and background predictions (also data) as inputs, as well as their uncertainties, and evaluates how precisely we can observe or not observe the Higgs boson in our analysis. Section 5.10 will discuss more about the strategy and implementation.

5.2 Data samples

Data used in this analysis were collected by the ATLAS experiment in year 2012 during the operation of LHC at center-of-mass energy $\sqrt{s} = 8$ TeV with total integrated luminosity 21.3 fb^{-1}. We also use the delayed stream of data in this analysis with integrated luminosity of 7.3 fb^{-1} (inclusively with the data 2012).

In order to be used in the analysis, the data must satisfy the requirements of good operation in some essential elements of the ATLAS detector while data are collected. These data quality requirements are implemented in the analysis by the Good Run List (GRL). This quality control is to ensure the good reconstruction of the key objects like electrons, muons, jets, triggers, b-tagging and $E_{\mathrm{T}}^{\mathrm{miss}}$. After applying this GRL the integrated luminosity yields 20.3 fb^{-1}. The GRL used in the Higgs analysis is data12_8TeV.periodAllYear_DetStatus-v61-pro14-02_DQDefects-00-01-00_PHYS_StandardGRL_All_Good.

5.3 Simulation samples

5.3.1 Background samples

The backgrounds used for this analysis are simulated with different generators. W/Z+jets samples are modelled by SHERPA generator [89] with massive $b/c-$quarks, using parton distribution function CT10 [91]. The filter for p_{T}^{V} (V stands for W/Z boson) and flavor categorizing are applied in W and Z samples (unit in GeV): $p_{\mathrm{T}} < 40$, $40 < p_{\mathrm{T}}^{V} < 70$, $70 < p_{\mathrm{T}}^{V} < 140$, $140 < p_{\mathrm{T}}^{V} < 280$, $280 < p_{\mathrm{T}}^{V} < 500$, $p_{\mathrm{T}}^{V} > 500$. The samples of V+jets are applied a filter to select events with at least one b-hadron, then with at least one c-hadron, and then the rest is identified as light flavour in order to increase the statistics of the vital V+heavy-flavour-jets. For $t\bar{t}$ background, the simulation is done with the POWHEG [86] with CT10 PDFs, interface with PYTHIA6 [87] (CTEQ6L1 [92] as PDFs). For single-top-quark simulation, the $s-$ and $Wt-$ channels are produced with POWHEG while $t-$channel are produced with AcerMC [88] generator interfaced with PYTHIA6 with CTEQ6L1 as PDFs. The diboson processes (WW, WZ or ZZ) are simulated by POWHEG with CT10 PDFs, interfaced with PYTHIA8.

Table 5.1 summarizes the generators of each background process and their inclusive cross section for $\sqrt{s} = 8$ TeV.

Table 5.1: MC generators used for modeling the background processes and the cross section times branching ratio (for normalizing purpose) at $\sqrt{s} = 8$ TeV.

Processes	Generator	$\sigma \times BR$	N_{events} (10^6)
$Z \to \ell\ell$ (l $= e, \mu, \tau$)	SHERPA	1.24 nb	66
$Z \to \nu\nu$	SHERPA	6.71 nb	98
$W \to \ell\nu$	SHERPA	12.07 nb	390
WW	POWHEG + PYTHIA8	52.44 pb	10
WZ	POWHEG + PYTHIA8	9.24 pb	15
ZZ	POWHEG + PYTHIA8	3.171 pb	15
$t\bar{t}$	POWHEG + PYTHIA6	252.89 pb	100
single t $s-$channel	POWHEG + PYTHIA6	5.61 nb	6
single t $Wt-$channel	AcerMC + PYTHIA6	22.37 nb	20
single t $t-$channel	AcerMC + PYTHIA6	87.76 nb	9

5.3.2 Signal simulation

The signals of ZH are modeled using the PYTHIA8 MC generator with CTEQ6L1 PDF (for the $qq \to ZH \to \nu\bar{\nu}b\bar{b}/\ell\ell b\bar{b}$ and $qq \to WH \to \ell\nu b\bar{b}$ processes) and POWHEG+PYTHIA8 (for the $gg \to ZH \to \nu\bar{\nu}b\bar{b}/\ell\ell b\bar{b}$ process). Samples are generated in the range of Higgs boson mass between 115 GeV and 150 GeV with intervals of 5 GeV. The total production cross section, the uncertainties of Higgs mass production, as well as $H \to b\bar{b}$ branching ratios are taken from Ref. [45]. The central value of Higgs cross-section are calculated at next-

to-next-leading-order (NNLO) in QCD corrections [93–95] and next-leading-order (NLO) in electro-weak correction [96]. The decay of Z boson is taken from Ref. [28].

5.4 Object selection

For the object selection, we need lepton identification so that we can veto events containing leptons because the $ZH \to \nu\bar{\nu}b\bar{b}$ events have no lepton. We also need jet reconstruction and b-jet identification since our analysis contains two b-quarks.

5.4.1 Electrons

Electron selection is divided into 3 categories based on the purity order: loose, medium and tight. Each category is used depending on the requirements of the analysis channel (0–lepton, 1–lepton or 2–lepton).

Loose selection For loose criteria, all electrons with transverse energy $E_{\mathrm{T}} > 7$ GeV and in the region $|\eta| < 2.47$ are chosen. There is an additional requirement for isolation of tracks $iso^{e}_{track} < 0.1$, which is defined as the ratio of the sum of track transverse momenta around the lepton inside the cone $\Delta R(e, \mathrm{track}) < 0.2$ and the electron transverse momentum:

$$iso^{e}_{\mathrm{track}} = \frac{1}{p^{e}_{\mathrm{T}}} \sum_{track} p_{\mathrm{T}}^{\mathrm{track}\ in\ \Delta R(e,\mathrm{track})<0.2}$$

The electrons are also required to pass another quality cut called likelihood (LH) criterion, which is constructed using the probability density functions (detailed in Ref. [97]). For loose electrons we only require VeryLoose LH selection.

Medium selection The electrons labelled as medium must pass the loose criteria and pass the additional requirement $E_{\mathrm{T}} > 25$ GeV.

Tight selection For the tight selection, electrons must pass the medium criteria and a tighter track isolation cut $iso^{e}_{track} < 0.04$. An additional isolation cut is also applied on the calorimeter isolation iso^{e}_{calo} defined as the sum of transverse energy of topoclusters around the electron for $\Delta R(e, \mathrm{topoclusters}) < 0.3$ divided by the electron E_{T} iso_{calo} <0.04. There is another quality cut of LH, which is categorized as VeryTight LH [97].

Calibration and correction Various electron calibration on identification efficiency, isolation and energy scale are computed using $Z \to e^{+}e^{-}$ samples [98] and applied to electron candidates.

5.4.2 Muons

As for electrons, the muons are also selected in 3 categories of loose, medium and tight based on purity. There are different types of reconstructed muons in detector:

- Combined muons: this muon identification uses independent track reconstruction in muon spectrometer and in ID, then combines the two reconstructions.
- Segment–tagged muons: identified using tracks in ID extrapolated to muon spectrometer and associated with at least one segment in the precision muon chamber. This type of muon is to increase the efficiency of muon reconstruction in poorly covered regions and low transverse momenta.
- Calorimeter tagged muons (Calo muons): identified in calorimeter and associated with ID tracks, to recover the efficiency of muon reconstruction at $|\eta| < 0.1$.
- Muon spectrometer stand–alone muons (StandAlone muons): to extend the muon reconstruction up to $|\eta| < 2.7$ (not using ID track matching because of ID limited range $|\eta| < 2.5$).

Loose selection Muons are required to pass requirements of transverse energy, pseudo–rapidity, impact parameter cuts (transverse d_0 and longitudinal z_0) and track isolation as in Table 5.2.

Table 5.2: Requirements on different types of reconstructed muons

Requirements	Segment–tagged/Combined	Calo	StandAlone
E_{T} [GeV]	> 7	> 20	> 7
$\|\eta\|$	<2.7	< 0.1	[2.5, 2.7]
d_0 [mm]	< 0.1	< 0.1	–
z_0 [mm]	< 10	< 10	–
iso_{track}	< 0.1	< 0.1	–

For quality aspect, muons (except Calo muons) must pass the Tight Muid criteria. The Muon Combined Performance (MCP) hits requirements in Inner Detector are applied as discussed in section 4.2.2.3.

Medium selection For this selection, muons are required to pass the loose criteria, for Segment–tagged and Combined muons the kinematic cuts $p_{\mathrm{T}} > 25$ GeV and $|\eta| <2.5$ are applied. The medium selection applies only on Combined or Segment–tagged, calo and StandAlone muons are excluded.

Tight selection Muons must pass the medium selection and additional tighter cuts for isolation:

- $iso_{track} < 0.04$
- $iso_{calo} < 0.04$

Muon correction The muon reconstruction efficiency is measured on both data and MC samples using $Z \to \mu\mu$, then the scale factor is derived to correct efficiency on MC. The detailed study is presented in Ref. [90].

5.4.3 Jets

Jets are reconstructed using the anti–k_t algorithm with a radius parameter value of R=0.4 [61, 62].

The track selection mentioned in section 4.1.2.3 is used to select tracks with good quality to be associated to jets or vertices (primary vertex or secondary vertices).

To reduce the contribution from jets produced by pile-up interactions, a cut on JVF (defined in section 3.1.4.1) is applied. Tracks with $p_{\mathrm{T}} > 0.5$ GeV are used for JVF calculation.

The JVF is calculated for the vertex with highest $\sum p_{\mathrm{T}}^2$ of tracks, the primary vertex, and the JVF cut is applied only for jets with $p_{\mathrm{T}} < 50$ GeV and $|\eta| < 2.4$. The reason for this limitation is the jets originating from pile-up interaction tend to have softer p_{T} spectrum.

There are two categories of jets: Signal jets (which will be considered to be used in the analysis) and forward jets (jets lying in the forward region of detector). The signal jet with the highest transverse momentum must satisfy $p_{\mathrm{T}} > 45$ GeV; for the other signal jets the cut is loosened to $p_{\mathrm{T}} > 20$ GeV, and all the signal jets must fall within the region $|\eta| < 2.5$. For the forward jets, a cut at $p_{\mathrm{T}} > 30$ GeV and $2.5 < |\eta| < 4.5$ is applied.

Jet labelling The jet labelling showing how to identify b-jets, $c-$jets, $\tau-$jets and light-jets was discussed in section 4.2.2.4.

Events of V+jets are also labeled according to the label of two jets used for Higgs boson reconstruction. If one of those two jets are labelled as b, then the event is listed as Vb category. If b-jet is not found but c-jet, then the event is labeled as Vc. Otherwise the event will be considered as Vl. There are subvisions of those categories: Vbb, Vbc, Vbl, Vcc, Vcl. The combination of Vbb, Vbc, Vbl, Vcc will be listed as V+hf (heavy flavour).

Jet calibration The calibration of jet is applied in order to correct the jet energy measured in calorimeter to the energy at particle level, this is the Jet Energy Scale (JES). The corrections for JES calibration are derived from p_{T} and $|\eta|$ of jets [99]. A method called Global Sequential Calibration (GSC) [99] was developed to improve the resolution of jet response (defined as $\frac{p_{\mathrm{T}}^{\text{reconstructed jet}}}{p_{\mathrm{T}}^{\text{truth jet}}}$) and making the jet response less flavour-dependent.

5.4.4 *b*-jet identification

The identification of jets originating from b-quarks was discussed in chapter 3, and this is a crucial step in the Higgs analysis since we have to identify events containing two b-jets. The $MV1c$ algorithm is used in the analysis thanks to its superior c-rejection compared to the previous version $MV1$. The $MV1c$ is the artificial NN combination of b-tagging algorithms: $IP3D$, $SV1$ and $JetFitterCombNN$, including the information from $b \to c$ decay chain.

To gain higher sensitivity of Higgs signal, the b-tagging is divided into three categories: Loose, Medium and Tight, based on the operating points of $MV1c$ (Table 3.10). The algorithm is calibrated so that the three categories can be used inclusively or exclusively.

***b*-tagging calibration** The calibration for b-tagging was discussed in section 3.4.2.

5.4.5 Missing transverse energy and track-based missing transverse momentum

The $E_{\mathrm{T}}^{\mathrm{miss}}$ is reconstructed by using all standard objects: electrons, muons, photons, taus, jets, and soft terms (unclustered cells in calorimeter), as discussed in chapter 4. All terms, except the terms of photon and tau, are re-calculated, synchronizing all the corrections and systematic uncertainties. For photon and tau, the pre-calculated terms are used. The other quantity of $E_{\mathrm{T}}^{\mathrm{miss}}$ used in the analysis is its direction, which will be used later in multijet background extraction from data in 0–lepton analysis.

The $P_{\mathrm{T}}^{\mathrm{miss}}$ is calculated using tracks. The track selection used for $P_{\mathrm{T}}^{\mathrm{miss}}$ calculation is defined in section 4.1.2.3 (only tracks from primary vertex are considered). This term plays a crucial role in 0–lepton analysis to suppress the multijet background and also clean the events from non collision background. This provides us a better way to deal with the multijet background and non-collision background suppression, rather than the direct cut on jet, which can lead to bias on jet calibration and b-tagging calibration.

5.4.6 Overlap removal

To avoid the double counting in event selection, overlap removal cuts are applied. The order of this removal is as following:

1. Check jet-electron overlap: If a jet is found overlaping an electron within $\Delta R(jet, e) < 0.4$, then the electron is kept while the jet is removed.

2. Check jet-muon overlap: If a jet has number of tracks ≤ 3 with $p_{\mathrm{T}}^{track} > 0.5\,\mathrm{GeV}$ and overlaps with a muon within $\Delta R(jet, \mu) < 0.4$, then the jet is removed.

3. Check muon-jet overlap: If a jet is found to contain more than 3 tracks with $p_{\mathrm{T}}^{track} > 0.5\,\mathrm{GeV}$ and overlaps with a muon within $\Delta R(\mu, jet) < 0.4$, then the muon is removed.

4. Check muon-electron removal: All the remaining loose electrons within a radius $\Delta R(\mu, e) < 0.2$ to a loose muon are removed unless it is a Calo muon, then the electron is kept instead.

5.5 Event selection

5.5.1 Pre-selection for data and MC samples

The data must satisfy the conditions that guarantee some important parts of ATLAS detector operate properly while collecting the data from collisions. These data quality requirements are done in event selection by the Good Run List (GRL).

Apart from GRL requirements, there are other cuts that need to be applied in order to reject the events coming from problems in the detector, in reconstruction processes, etc... :

- Remove the incomplete events which do not contain some detector information (contain Core EventInfo error flag)
- LAr error flag: to remove the data events affected by LAr noise burst (that have LAr EventInfo error flag)
- Corrupted tile events: Since collision at $\sqrt{s} = 7$ TeV, the Tile Calorimeter suffers from frequent module trips. Although these trips are tolerable in data quality and are included in offline reconstruction, with the discovery of new particle, a full understanding of detector is required, therefore applying this cut is needed. The corrupted tile events in data periods from G to J are rejected by using TileTripReader, otherwise they can be rejected using Tile error flag.

On the MC, the events containing no truth particles are rejected.
Finally, we require the following selection that applies to both data and MC samples:

- The events must contain a primary vertex with at least 3 tracks
- $E_{\mathrm{T}}^{\mathrm{miss}}$ cleaning: any events containing loose bad jets (jets not associated to real energy deposits in the calorimeters) with $p_{\mathrm{T}} > 20$ GeV and $|\eta| < 4.5$ (after overlap removal and before applying JVF cut) are removed.

5.5.2 Trigger selection

For the nominal 0-lepton analysis, $E_{\mathrm{T}}^{\mathrm{miss}}$ triggers that are already mentioned in chapter 4 are used. For enhancing the data to be analyzed and trigger availability, the triggers EF_xe80_tclcw_loose, EF_xe80T_tclcw_loose, EF_xe80_tclcw are applied as described in Table 4.2 in the official analysis. In this chapter we will also take into account the delayed stream trigger EF_xe60_tclcw_loose_delayed. The delayed stream trigger EF_xe60_tclcw_loose_delayed should be used in the $ZH \to \nu\bar{\nu}b\bar{b}$ analysis as follows:

- For data periods prior to E, use the nominal triggers EF_xe80T_tclcw_loose, EF_xe80_tclcw, EF_xe80_tclcw_loose.
- For data periods from E onwards, if the delayed stream trigger is available (with instantaneous luminosity $< 5.77 \times 10^{33}$ cm^{-2}s^{-1}), it will be used. Else, the trigger EF_xe80_tclcw_loose is used instead.

In this $ZH \to \nu\bar{\nu}b\bar{b}$ analysis we will show the usage of delayed stream trigger implementation and compare it with analysis using nominal triggers.

5.5.3 Lepton veto

The Higgs analysis in 0-lepton channel only uses the loose criteria for leptons. We reject any event containing any type of loose leptons (electrons, muons).

5.5.4 Jet selection

The events with exactly 2 or 3 jets without any forward jets are selected for the analysis. The reason for forward jet veto is to reduce the contribution from single and pair of top quarks production background (which is one of the main backgrounds).

Events which contain the signal jets then will pass the b-tagging requirements with exactly two b-tagged jets. The b-tagging requirements are divided into categories as shown in figure 5.2 based on the number of b-tagged jets and type of b-tag. The events before applying b-tagging (pre-tag), no b-tagged jet (0tag) and only one b-tagged jet (1tag) categories are also defined for control regions. The double b-tag are divided exclusively into 3 categories:

- Two exclusive tight b-tags: "2TT"
- Two exclusive medium b-tags: "2MM"
- Two exclusive loose b-tags: "2LL"

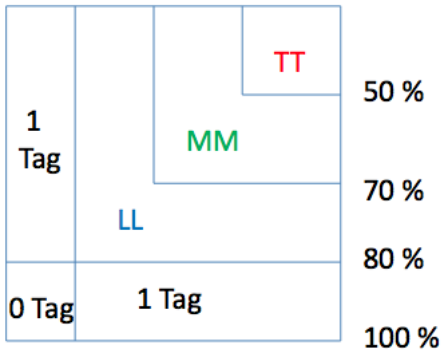

Figure 5.2: Exclusive b-tag categories. The percent shows the b-jet efficiency.

In 3-jet events (we consider the signal jets only), if the lowest p_{T} jet passes the loose b-tag criterion, this event will be vetoed. For 2-tag events we require the first two leading jets to be b-tagged.

5.6 Kinematic selection

From now on, to be more convenient, we use the colors and markers described in figure 5.3 for MC contributions and data.

After the selection above, events then are categorized based on the transverse momentum of vector boson p_{T}^{V} (in 0-lepton channel, this quantity is the $E_{\mathrm{T}}^{\mathrm{miss}}$ itself). Events with $E_{\mathrm{T}}^{\mathrm{miss}} > 90$ GeV and $P_{\mathrm{T}}^{\mathrm{miss}} > 30$ GeV are considered to be analyzed. Our analysis divides the $E_{\mathrm{T}}^{\mathrm{miss}}$ into 4 bins: 100–120 GeV, 120–160 GeV, 160–200 GeV and larger than 200 GeV, that we call first, second, third and fourth bin respectively. We also select events based on the number of jets (2– or 3–jet bins)

For multijet estimation and rejection, we define two cuts:

Figure 5.3: Colors and markers represent the MC contributions and data.

- The difference of azimuthal angle between $E_{\mathrm{T}}^{\mathrm{miss}}$ and the closest jet: $\min(\Delta\phi(E_{\mathrm{T}}^{\mathrm{miss}}, jets)) > 1.5$[1] for signal-like events while for multijet modeling the cut $\min(\Delta\phi(E_{\mathrm{T}}^{\mathrm{miss}}, jets)) < 0.4$ is chosen. This can be explained as follows: the signal-like events of Higgs boson are supposed to have the Higgs boson direction opposite to Z boson direction, therefore $E_{\mathrm{T}}^{\mathrm{miss}}$ seems to be well-separated from the direction of signal jets, while the events originating from multijet processes have $E_{\mathrm{T}}^{\mathrm{miss}}$ close to a jet direction (fake $E_{\mathrm{T}}^{\mathrm{miss}}$ from mis-measured jet energy) (shown in Figure 5.4). We can utilize this fact to reduce the events from multijet processes and also to model and estimate the multijet contribution (details are discussed in section 5.7).

- The difference of azimuthal angle ϕ betweem $E_{\mathrm{T}}^{\mathrm{miss}}$ and $P_{\mathrm{T}}^{\mathrm{miss}}$ [100]: For selecting signal-like events, the cut $\Delta\phi(E_{\mathrm{T}}^{\mathrm{miss}}, P_{\mathrm{T}}^{\mathrm{miss}}) < \pi/2$ is applied, for modeling the multijet contribution, we choose the cut $\Delta\phi(E_{\mathrm{T}}^{\mathrm{miss}}, P_{\mathrm{T}}^{\mathrm{miss}}) > \pi/2$.

If the energy in the collision is large enough, the Z and H are not at rest and tend to travel back-to-back. The larger $E_{\mathrm{T}}^{\mathrm{miss}}$ from decay of Z boson into two neutrinos, the larger boost the Higgs boson has. So the two b-jets from Higgs boson decay tend to be close to each other. To select such events, we define cuts on distance between the two signal jets $\Delta R(\mathrm{jet1}, \mathrm{jet2})$ (shown in Table 5.3).

Table 5.3: Selection of $\Delta R(jet1, jet2)$ in different bin of $E_{\mathrm{T}}^{\mathrm{miss}}$.

$E_{\mathrm{T}}^{\mathrm{miss}}$ [GeV]	100–120	120–160	160–200	> 200
ΔR	0.7–3.	0.7–2.3	0.7–1.8	< 1.4

On the other hand, in the events with large $E_{\mathrm{T}}^{\mathrm{miss}}$, the Higgs boson and Z boson are

[1] this cut is not applied for the first $E_{\mathrm{T}}^{\mathrm{miss}}$ bin, discussed later in this section.

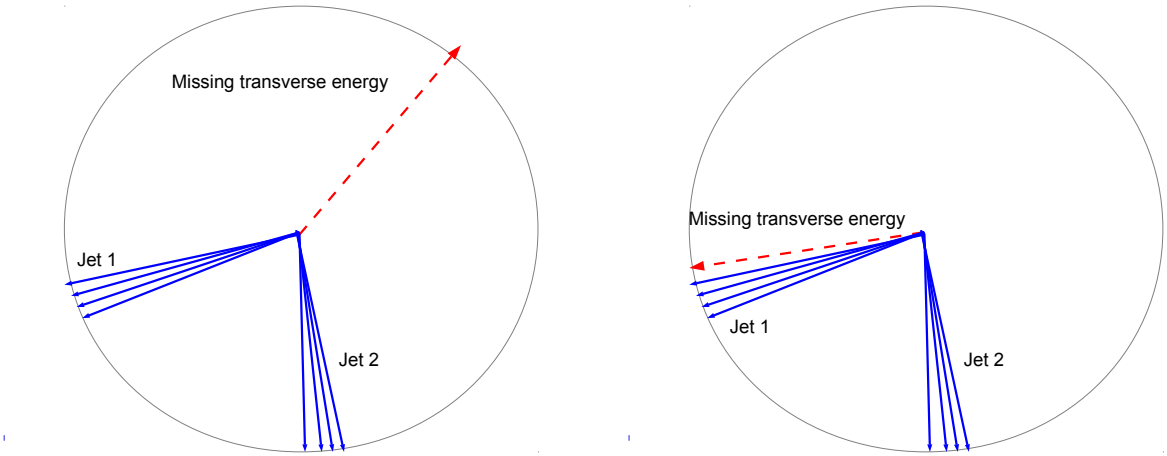

Figure 5.4: Schema of the event topology between two jets and $E_{\mathrm{T}}^{\mathrm{miss}}$ for signal-like events (left) and multijet-like events (right).

expected to be back-to-back, therefore an angular cut $\Delta\phi(Z,H)$[2] is required to select events based on $E_{\mathrm{T}}^{\mathrm{miss}}$:

- $E_{\mathrm{T}}^{\mathrm{miss}} > 120$ GeV: $\Delta\phi(E_{\mathrm{T}}^{\mathrm{miss}}, H) > 2.8$
- $E_{\mathrm{T}}^{\mathrm{miss}} < 120$ GeV: $\Delta\phi(E_{\mathrm{T}}^{\mathrm{miss}}, H) > 2.2$

To avoid $E_{\mathrm{T}}^{\mathrm{miss}}$ trigger biases (already studied in section 4.2.7), cuts on scalar sum of p_{T} of leading jets ($J12pT$ for 2 signal jets and $J123pT$ for 3 signal jets) are applied based on $E_{\mathrm{T}}^{\mathrm{miss}}$ and the number of signal jets present in the events:

- $N_{jets} = 2$: $J12pT > 120$ GeV
- $N_{jets} = 3$: $J123pT > 150$ GeV for $E_{\mathrm{T}}^{\mathrm{miss}} > 120$ GeV, $J123pT > 170$ GeV for $E_{\mathrm{T}}^{\mathrm{miss}} < 120$ GeV

Exclusive selection for low $E_{\mathrm{T}}^{\mathrm{miss}}$ region The $\min(\Delta\phi(E_{\mathrm{T}}^{\mathrm{miss}}, jets))$ cut is efficient to reduce multijet background for high $E_{\mathrm{T}}^{\mathrm{miss}}$, however it loses its potential in the low $E_{\mathrm{T}}^{\mathrm{miss}}$ region ($100 < E_{\mathrm{T}}^{\mathrm{miss}} < 120$ GeV) because it will reject a large fraction of $ZH \to \nu\bar{\nu}b\bar{b}$ signal. To deal with this issue, other cuts are proposed in this region. The $\Delta\phi(\mathrm{jet1}, \mathrm{jet2})$ and $E_{\mathrm{T}}^{\mathrm{miss}}$ significance are chosen to reduce the multijet. The $E_{\mathrm{T}}^{\mathrm{miss}}$ significance is defined as:

$$E_{\mathrm{T}}^{\mathrm{miss}} \text{ significance} = \frac{E_{\mathrm{T}}^{\mathrm{miss}}}{\sqrt{J12pT}}$$

The remaining multijet are rejected using the multivariate likelihood-based technique. We define the likelihood ratio:

$$\text{Likelihood Ratio (LR)} = \frac{\mathrm{LH}^{\mathrm{signal}}}{\mathrm{LH}^{\mathrm{signal}} + \mathrm{LH}^{\mathrm{multijet}}},$$

[2]The output events only contain two b-jets and $E_{\mathrm{T}}^{\mathrm{miss}}$. We suppose that H is the vectorial sum of two b-jets with highest p_{T} and direction of $E_{\mathrm{T}}^{\mathrm{miss}}$ is supposed to be the same direction of Z boson.

where $\mathrm{LH}^{\mathrm{signal}} = \Pi_i^{n_{kin}} P_i^{\mathrm{signal}}$, $\mathrm{LH}^{\mathrm{multijet}} = \Pi_i^{n_{kin}} P_i^{\mathrm{multijet}}$, $P_i^{\mathrm{signal,multijet}}$ are the probabilities derived from PDF functions using Z+jets events before applying any b-tagging requirement, i is the index of kinematic variables used for constructing the likelihood and n_{kin} is the number of those variables. Those variables are:

- $\Delta\phi(\mathrm{jet1}, \mathrm{jet2})$,
- $\Delta\phi(V, H)$,
- Transverse momentum of Higgs boson $p_{\mathrm{T}}^{\mathrm{Higgs}}$ (defined as the vectorial sum of two leading jets in event),
- $p_{\mathrm{T}}^{\mathrm{Higgs}}/J12pT$.

The distribution of the likelihood is shown in Figure 5.5. We can see that there is a discrepancy between data and MC in region of LR < 0.5, suggesting that this region is contaminated by multijet processes, as expected.

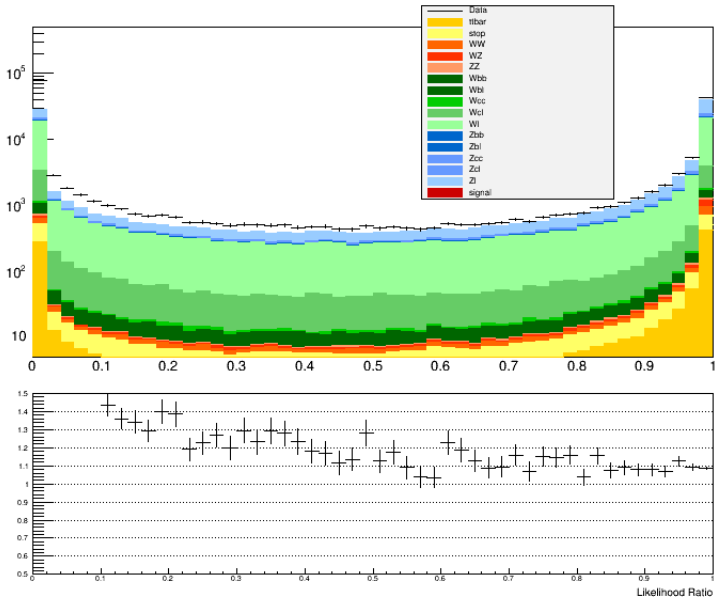

Figure 5.5: Distribution of likelihood ratio in lowest $E_{\mathrm{T}}^{\mathrm{miss}}$ bin.

The 3-jet bin in low $E_{\mathrm{T}}^{\mathrm{miss}}$ region is not supposed to contribute significantly to the signal sensitivity, but it can serve as a test for background modeling with high statistics, particularly for $t\bar{t}$ background, thus we keep the same selection as for $E_{\mathrm{T}}^{\mathrm{miss}} > 120$ GeV. All the cuts applied for $E_{\mathrm{T}}^{\mathrm{miss}}$ between 100–120 GeV are summarized in Table 5.4.

5.7 Multijet background estimation

The multijet background is not well-estimated by the MC simulation due to the complication of modelling the sub-processes of proton-proton collision, and a large amount of events is needed to simulate in high $E_{\mathrm{T}}^{\mathrm{miss}}$ region (>160 GeV). The limitation of computing

Table 5.4: Exclusive selection for $100 < E_{\mathrm{T}}^{\mathrm{miss}} < 120$ GeV and 2-jet region.

$E_{\mathrm{T}}^{\mathrm{miss}}$ [GeV]	100–120
$\Delta\phi(Z, H)$	> 2.2
$\Delta\phi(jet1, jet2)$	< 2.7
$E_{\mathrm{T}}^{\mathrm{miss}}$ significance	> 7.0
Likelihood ratio cut	> 0.5

resources is also another difficulty for simulating multijet processes. Therefore a data-driven method is proposed in order to estimate the multijet contribution.

There are two kinematic variables used to discriminate the region dominated by multijet processes and the one in which EW processes (which is from events of diboson, W/Z+jets, single–top and $t\bar{t}$ production) are preferred:

- azimuthal distance between $E_{\mathrm{T}}^{\mathrm{miss}}$ and $P_{\mathrm{T}}^{\mathrm{miss}}$, $\Delta\phi(E_{\mathrm{T}}^{\mathrm{miss}}, P_{\mathrm{T}}^{\mathrm{miss}})$.
- azimuthal distance between the $E_{\mathrm{T}}^{\mathrm{miss}}$ and the closest jet to it, $\min\Delta\phi(E_{\mathrm{T}}^{\mathrm{miss}}, jets)$.

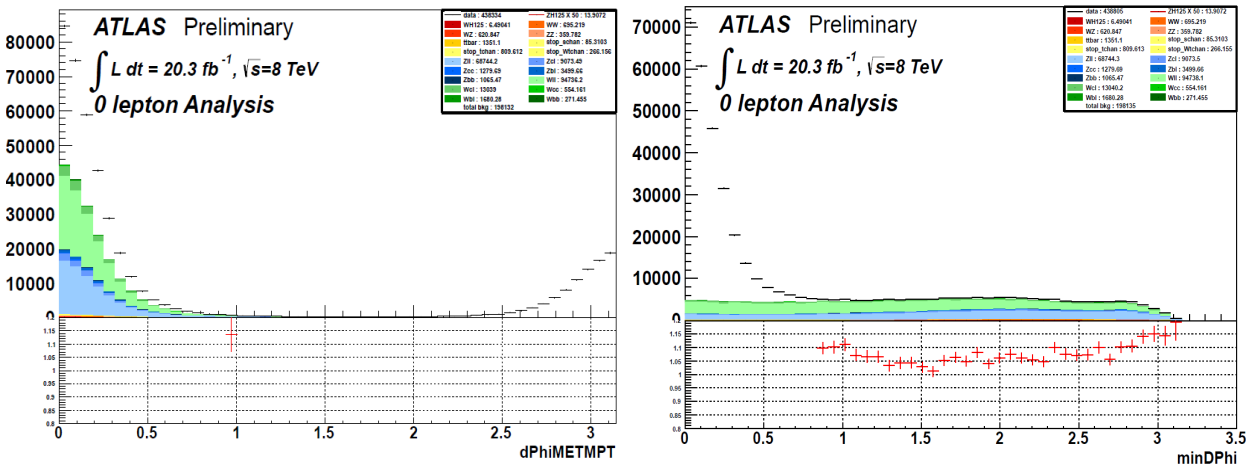

Figure 5.6: Distribution of $\Delta\phi(E_{\mathrm{T}}^{\mathrm{miss}}, P_{\mathrm{T}}^{\mathrm{miss}})$ (left) and $\min\Delta\phi(E_{\mathrm{T}}^{\mathrm{miss}}, jets)$ (right) [101].

One can clearly see in Figure 5.6 that in the region where $\Delta\phi(E_{\mathrm{T}}^{\mathrm{miss}}, P_{\mathrm{T}}^{\mathrm{miss}}) < 1.5$, EW processes are present, although this region is much contaminated by multijet contribution. And for $\min\Delta\phi(E_{\mathrm{T}}^{\mathrm{miss}}, jets) > 1.5$, multijet processes are highly suppressed and EW processes dominate. Thus, we define the 4 regions called A, B, C, D based on the cut values of $\Delta\phi(E_{\mathrm{T}}^{\mathrm{miss}}, P_{\mathrm{T}}^{\mathrm{miss}})$ and $\min\Delta\phi(E_{\mathrm{T}}^{\mathrm{miss}}, jets)$, as shown in Figure 5.7.

The region A is usually referred to as signal region and it is the region where we perform our Higgs analysis. For the first $E_{\mathrm{T}}^{\mathrm{miss}}$ bin, the likelihood ratio cut is chosen instead of $\min\Delta\phi(E_{\mathrm{T}}^{\mathrm{miss}}, jets)$ cut (Fig. 5.5), we choose LR <0.2 for B, D regions definition and LR >0.5 for A, C. The prediction of multijets events in this region is calculated by the following formula:

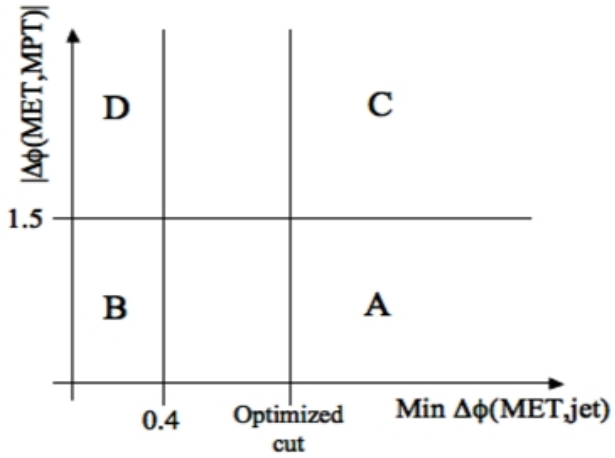

Figure 5.7: Two-dimensional kinematic plane ($\Delta\phi(E_{\mathrm{T}}^{\mathrm{miss}}, P_{\mathrm{T}}^{\mathrm{miss}})$, $\min\Delta\phi(E_{\mathrm{T}}^{\mathrm{miss}}, jets)$) used for defining regions A, B, C, D to estimate the multijet events in signal region (region A). The optimized cut for $\min\Delta\phi(E_{\mathrm{T}}^{\mathrm{miss}}, jets)$ is chosen to be 1.5.

$$N_{QCD}(A) = \frac{N(B)}{N(D)} \times N(C),$$

where $N_{QCD}(A)$ is the number of multijet events estimated in region A, and $N(B), N(C), N(D)$ are the number of events in B, C, D region, respectively. To properly use this formula, we assume that the two variables $\Delta\phi(E_{\mathrm{T}}^{\mathrm{miss}}, P_{\mathrm{T}}^{\mathrm{miss}})$, $\min\Delta\phi(E_{\mathrm{T}}^{\mathrm{miss}}, jets)$ are weakly correlated. This is confirmed on Fig. 5.8, where $\min\Delta\phi(E_{\mathrm{T}}^{\mathrm{miss}}, jets)$ for events with $\Delta\phi(E_{\mathrm{T}}^{\mathrm{miss}}, P_{\mathrm{T}}^{\mathrm{miss}}) > \pi/2$ or $\Delta\phi(E_{\mathrm{T}}^{\mathrm{miss}}, P_{\mathrm{T}}^{\mathrm{miss}}) < \pi/2$ have the same shape.

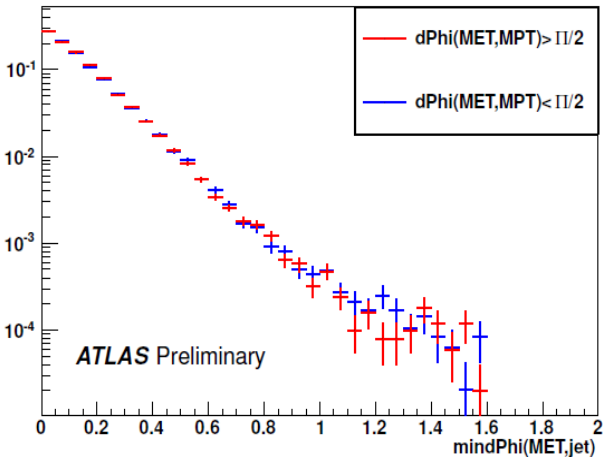

Figure 5.8: Distribution of $\min\Delta\phi(E_{\mathrm{T}}^{\mathrm{miss}}, jets)$ of multijet background in region of $\Delta\phi(E_{\mathrm{T}}^{\mathrm{miss}}, P_{\mathrm{T}}^{\mathrm{miss}}) < \pi/2$ (blue) and $\Delta\phi(E_{\mathrm{T}}^{\mathrm{miss}}, P_{\mathrm{T}}^{\mathrm{miss}}) > \pi/2$ (red) using data [101]. This distribution is made in region of first $E_{\mathrm{T}}^{\mathrm{miss}}$ bin, before applying b-tagging.

Normally this method is applied after selection mentioned in section 5.5. However, the data events present after the selection won't yield much statistics. So, the b-tagging requirement will be ignored in $N(B), N(C), N(D)$ estimation, plus the upper ΔR cuts will also be

removed. Then $N(B)$ and $N(D)$ are estimated by multiplying with the b-tagging rate R_B or R_D, which is defined as ratio between number of events passing b-tagging requirements and those before b-tagging. These rates are calculated using data samples.

Region B is favoured by heavy-flavor jets compared to region D or A (Fig. 5.9), which leads the b-tagging rates in region B to always be larger than that in region D (results are shown in table 5.5 using the estimation on data). Although close to region A, the heavy flavour jet content in region D is still higher. So in the multijet estimation we prefer to apply the R_D to avoid over-estimating of b-tagging rate.

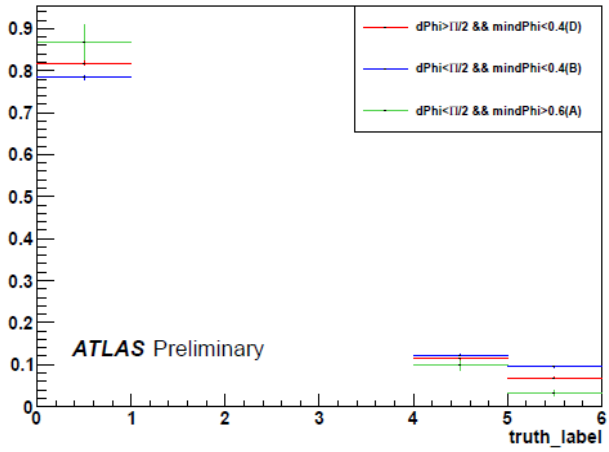

Figure 5.9: Truth label of jet closest to $E_{\mathrm{T}}^{\mathrm{miss}}$ in A, B, D region with label <4 means light jets, label=4 means c-jets and 5 means b-jets [101].

Table 5.5: b-tagging rates for B and D region for each bin of $E_{\mathrm{T}}^{\mathrm{miss}}$ and b-tagging category for 2-jet events using delayed stream trigger on data.

$E_{\mathrm{T}}^{\mathrm{miss}}$ bin [GeV]	b-tag category	Region D	Region B
100–120	LL	0.0058	0.0091
	MM	0.0022	0.0041
	TT	0.0013	0.0035
120–160	LL	0.02	0.036
	MM	0.0094	0.025
	TT	0.0039	0.014
160–200	LL	0.02	0.03
	MM	0.0082	0.016
	TT	0.0035	0.0079
>200	LL	0.019	0.021
	MM	0.0076	0.0096
	TT	0.0019	0.0032

Then the multijet events in signal region is re-estimated as:

$$N_{QCD}(A) = \frac{N(B)}{N(D)} \times N(C) \times R_D$$

The multijet estimation of $N_{QCD}(A)$ is presented in Table 5.6. The multijet events are small compared to EW background with less than 2 % with respect to electroweak background. The template of multijet in region A is derived from region C by subtracting the backgrounds from MC samples. These estimations are added into the distribution of invariant mass in the final analysis.

Table 5.6: Multijet estimation in signal region and its fraction to electroweak background for different $E_{\mathrm{T}}^{\mathrm{miss}}$ bins and b-tagging categories using delayed stream trigger.

N_{jets}	$E_{\mathrm{T}}^{\mathrm{miss}}$ bin [GeV]	b-tag category	$N_{QCD}(A)$	EW background	MJ/EW (%)
2	100–120	LL	10.06±0.39	827.52±63.84	1.2
		MM	3.87±0.15	389.02±59.4	1
		TT	2.32±0.09	279.56±23.63	0.8
	120–160	LL	12.5±0.8	781.8±5.88	1.6
		MM	5.95±0.38	394.21±5	1.5
		TT	2.5±0.16	283.944±4.44	0.9
	160–200	LL	1.18±0.27	244.01±5.15	0.5
		MM	0.48±0.11	112.66±4.38	0.4
		TT	0.21±0.04	77.27±3.88	0.1
	>200	LL	0.41±0.2	182.97±1.98	0.2
		MM	0.16±0.08	75.86±1.52	0.2
		TT	0.04±0.02	50.62±1.29	0.2
3	120–160	LL	2.39±0.33	222.33±1	1.1
		MM	1.3±0.18	141.71±1.2	0.6
		TT	0.6±0.08	100.52±0.87	0.6
	160–200	LL	0.31±0.16	92.53±2.85	0.3
		MM	0.1±0.05	47.4±0.81	0.4
		TT	0.05±0.03	31.02±2.12	0.2
	>200	LL	0.11±0.09	82.99±1.39	0.1
		MM	0.04±0.02	35.12±1.21	0.3
		TT	0.02±0.01	20.6±0.91	0.1

Systematic uncertainty on multijet background The multijet contribution can be changed by varying the cut on $\min \Delta\phi(E_{\mathrm{T}}^{\mathrm{miss}}, jets)$ and also change the b-tagging rate in region D by the one in region B. A systematic uncertainty of 100% is estimated for this small background and not correleted between 2- or 3-jet cases, b-tagging categories.

5.8 Applying delayed stream trigger

5.8.1 Mis–modelling issue

In this part we expand our lowest $E_{\mathrm{T}}^{\mathrm{miss}}$ threshold down to 90 GeV.

In the 0-lepton channel analysis using nominal $E_{\mathrm{T}}^{\mathrm{miss}}$ triggers, there is potential mis-modelling issue occurring in terms of the transverse momentum of Higgs boson [3] in the region of 90–120 GeV of Higgs p_{T} (in Figure 5.10). This mis-modelling issue seems to affect only the lowest $E_{\mathrm{T}}^{\mathrm{miss}}$ bin of the analysis, the other higher $E_{\mathrm{T}}^{\mathrm{miss}}$ bins suffer no such issue.

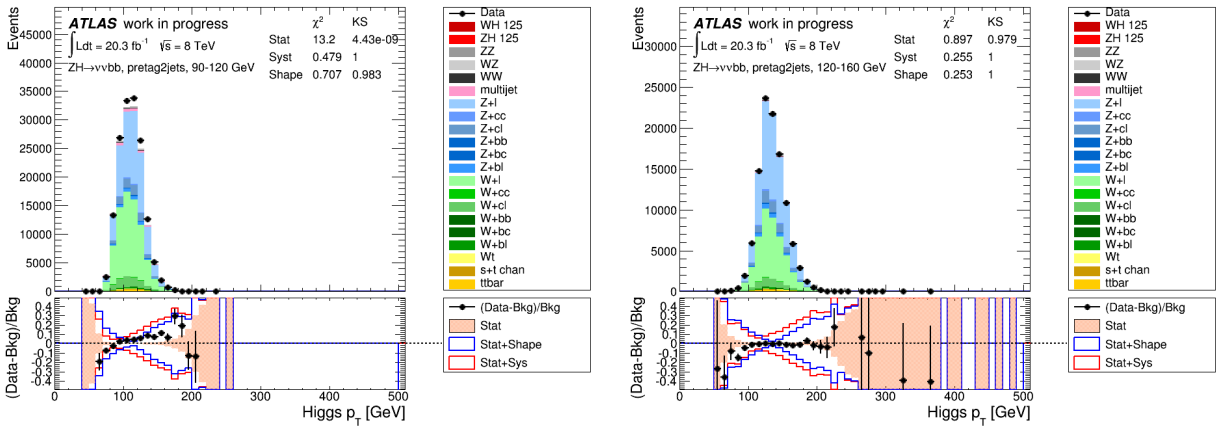

Figure 5.10: Distribution of vectorial sum of momentum of two b-tagged jets (Higgs boson p_{T}) using nominal analysis for pre-tag in first $E_{\mathrm{T}}^{\mathrm{miss}}$ bin (left), pre-tag in second $E_{\mathrm{T}}^{\mathrm{miss}}$ bin (right).

This mis-modelling issue might come from the biases of nominal $E_{\mathrm{T}}^{\mathrm{miss}}$ triggers in low $E_{\mathrm{T}}^{\mathrm{miss}}$ region. We can have the same test using the delayed stream trigger exclusively, which possesses a lower threshold, to see if this issue still exists. To implement this test, the part of data from period E where delayed stream trigger is available is considered, which yields a luminosity of 7.3 fb^{-1}. For the event selection, we keep the selection as described in section 5.5, except for the where the delayed stream trigger (EF_xe60_tclcw_loose_delayed) is used exclusively instead of nominal triggers.

The results after event selection using delayed stream exclusively show that there are contributions from multijet backgrounds, which are shown in distributions of $E_{\mathrm{T}}^{\mathrm{miss}}$, $\Delta\phi(jet, jet)$, $E_{\mathrm{T}}^{\mathrm{miss}}$ significance (Fig. 5.11). In this study of mis-modelling, we will try to determine the stricter multijet rejection compared to the selection in section 5.5.

The cuts we apply for multijet rejection purpose is:

- $\Delta\phi(j, j) < 2.0$
- $E_{\mathrm{T}}^{\mathrm{miss}}$ significance > 9.0

The distributions for $E_{\mathrm{T}}^{\mathrm{miss}}$, $\Delta\phi(j, j)$, $E_{\mathrm{T}}^{\mathrm{miss}}$ significance and likelihood are shown in Figure 5.12. As we can see these multijet rejection cuts yield overall better data/MC agreement,

[3] In our context, this quantity is equivalent to vectorial sum of momentum of two b-tagged jets.

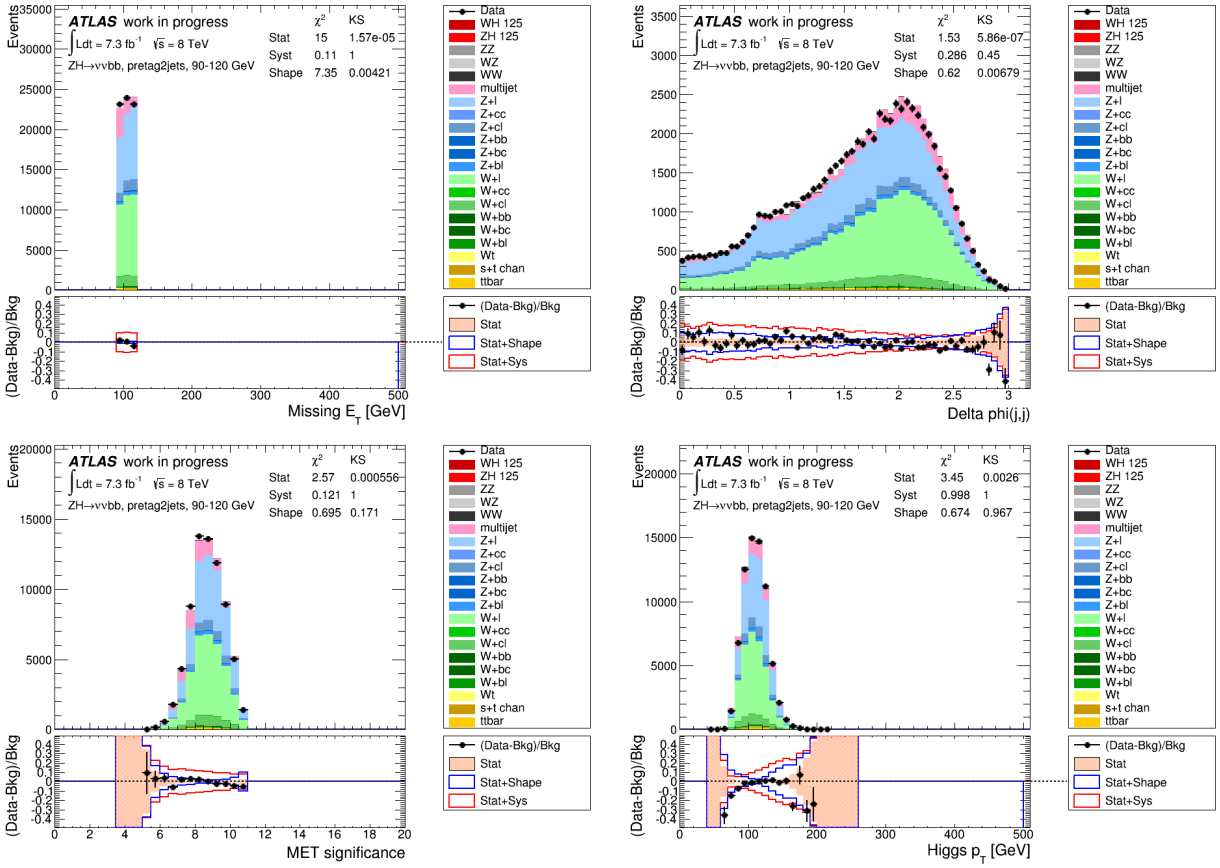

Figure 5.11: Distributions of event selection using delayed stream exclusively in first $E_{\mathrm{T}}^{\mathrm{miss}}$ bin for $E_{\mathrm{T}}^{\mathrm{miss}}$ (top left), $\Delta\Phi(j,j)$ (top right), $E_{\mathrm{T}}^{\mathrm{miss}}$ significance (bottom left), Higgs p_{T} (bottom right).

although the acceptances for all background and signal are clearly impacted. These cuts are not applied in the main analysis and only used for purpose of checking mis-modelling on delayed stream.

The result for this study is shown in Figure 5.13, showing the mis-modelling seems to give no issue with the delayed stream trigger. For the analysis using nominal triggers, after applying the same multijet rejection, the mis-modelling is still visible although it has weaker impact.

We check if applying the delayed stream trigger inclusively with other triggers in the analysis with nominal selection improves the modeling. Figure 5.14 shows that the mis-modelling still exists.

In conclusion, the delayed stream trigger exclusively may provide an analysis with better modelling compared to the nominal triggers, but when using it inclusively with nominal triggers, it does not provide better modelling overall. If we are to maintain the first $E_{\mathrm{T}}^{\mathrm{miss}}$ bin in the main analysis, then the cut $E_{\mathrm{T}}^{\mathrm{miss}} > 100$ GeV is applied. Figure 5.15 shows that the mis-modelling issue on the p_{T} of Higgs still exists but has less impact than the case of $E_{\mathrm{T}}^{\mathrm{miss}} > 90$ GeV.

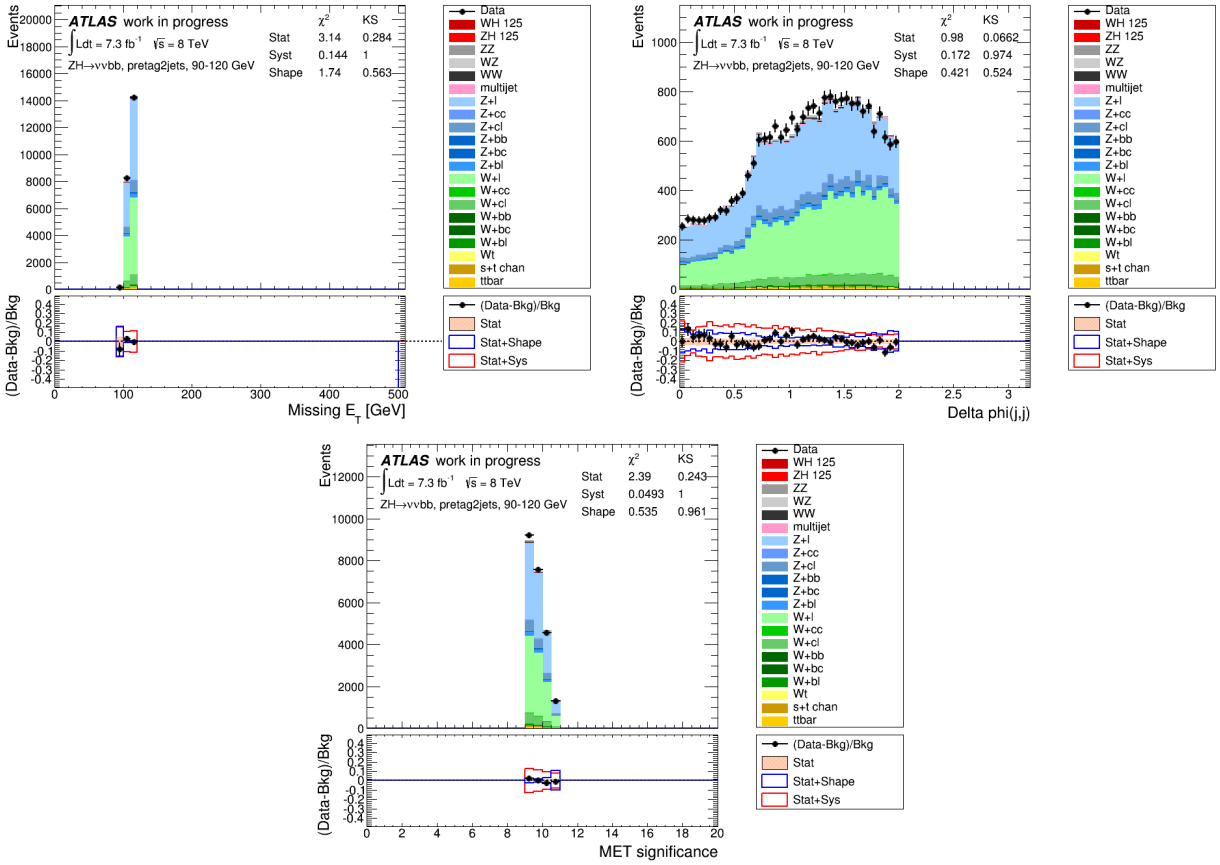

Figure 5.12: Distributions of event selection using delayed stream exclusively after performing tighter multijet rejection cuts in first $E_{\mathrm{T}}^{\mathrm{miss}}$ bin for $E_{\mathrm{T}}^{\mathrm{miss}}$ (top left), $\Delta\phi(j,j)$ (top right), $E_{\mathrm{T}}^{\mathrm{miss}}$ significance (bottom).

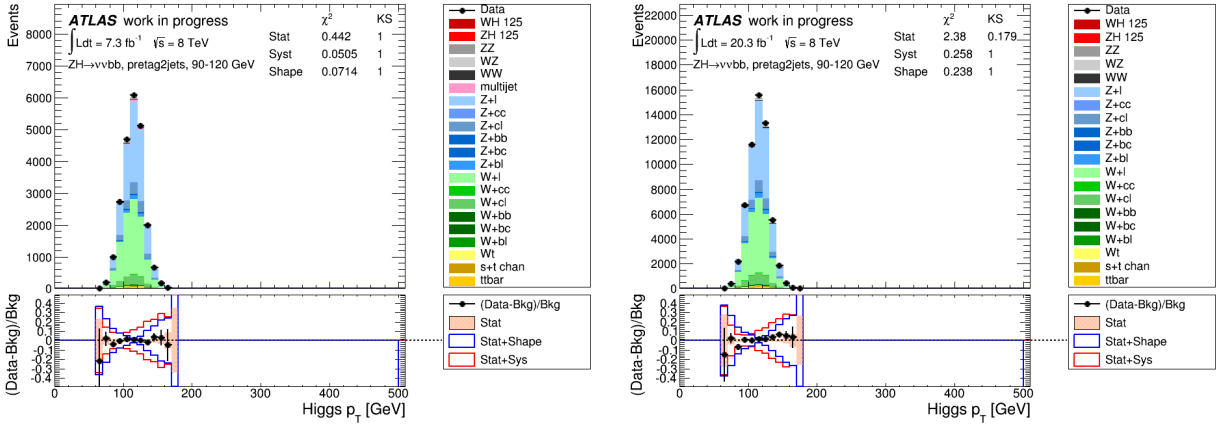

Figure 5.13: Distribution of Higgs boson p_{T} using delayed stream trigger exclusively (left) and nominal triggers (right) using nominal selection.

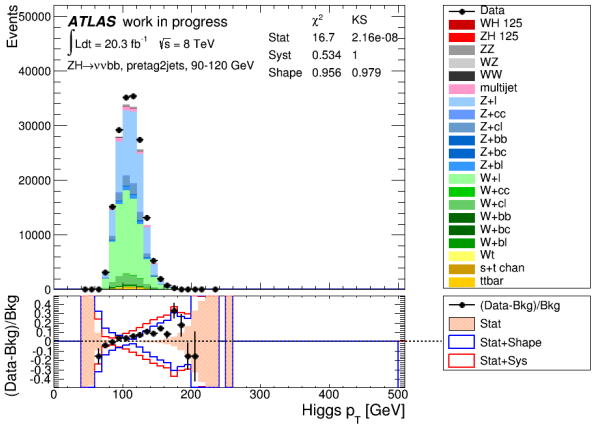

Figure 5.14: Distribution of Higgs boson p_{T} using delayed stream trigger inclusively in region $90 < E_{\mathrm{T}}^{\mathrm{miss}} < 120$ GeV.

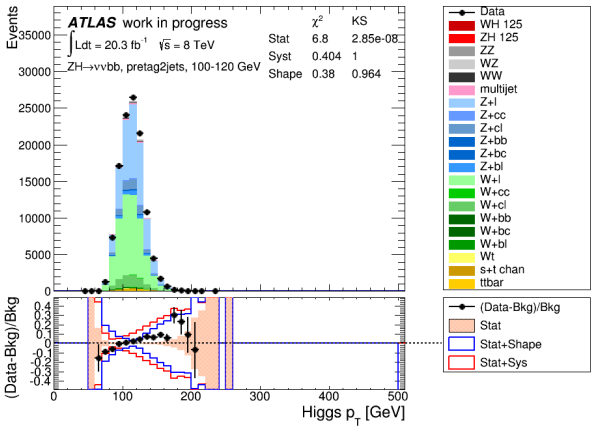

Figure 5.15: Distribution of Higgs p_{T} using nominal triggers with $100 < E_{\mathrm{T}}^{\mathrm{miss}} < 120$ GeV.

5.8.2 Estimation of signal and background

The invariant mass formed by two b-tagged jets is used as input for our future statistical analysis. By definition, this invariant mass should form the mass of the Higgs boson that we are performing our analysis to search for. We make two analyses: one analysis with the implementation of delayed stream trigger, and one using nominal triggers. The two analyses are made before applying any statistical fit (or pre-fit) (which will be discussed later in section 5.10.1). The distributions of this invariant mass are shown in Figure 5.16 for the control regions[4] (pre-tag, 0-tag and 1-tag) in first $E_{\mathrm{T}}^{\mathrm{miss}}$ bin (100–120 GeV) and second $E_{\mathrm{T}}^{\mathrm{miss}}$ bin (120–160 GeV), and also in the 2-tag regions on the first and second $E_{\mathrm{T}}^{\mathrm{miss}}$ bin (Figure 5.17). We can observe the overall good agreement in the control regions (pre-tag, 0-tag and 1-tag) within the uncertainties. In 2–tag regions there are some discrepancies between data and MC because the scale factors for each kind of background are not applied (this is discussed in Sec. 5.11.1).

[4]In control regions, we define the invariant mass formed by the two leading jets.

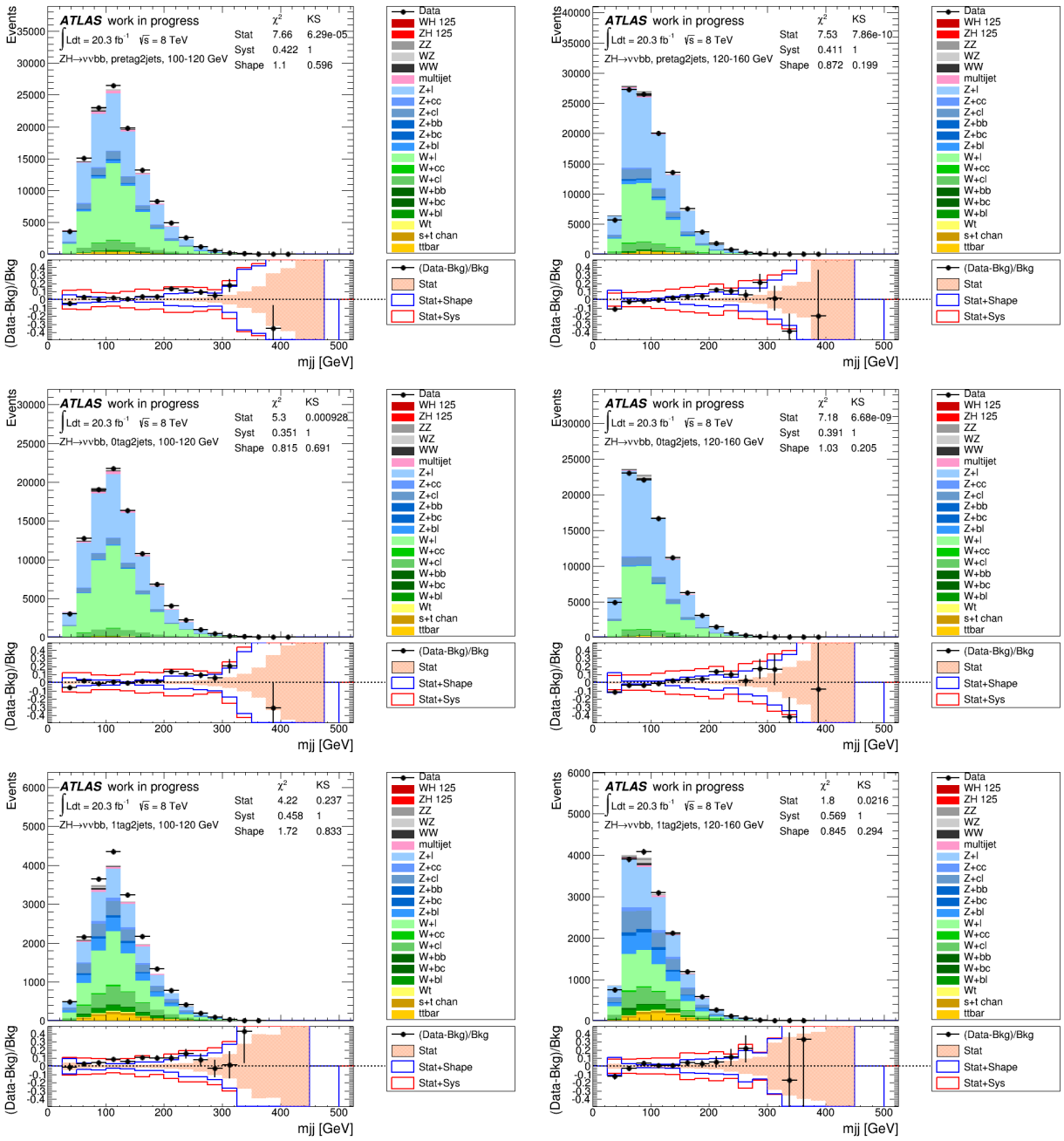

Figure 5.16: Distribution of invariant mass of two b-jets for pre-tag, 0-tag and 1-tag region (in 2-jet bin and in 2 bins of $E_{\mathrm{T}}^{\mathrm{miss}}$: 100–120 GeV and 120–160 GeV) of b-tagging category of the analysis using delayed stream trigger (pre-fit).

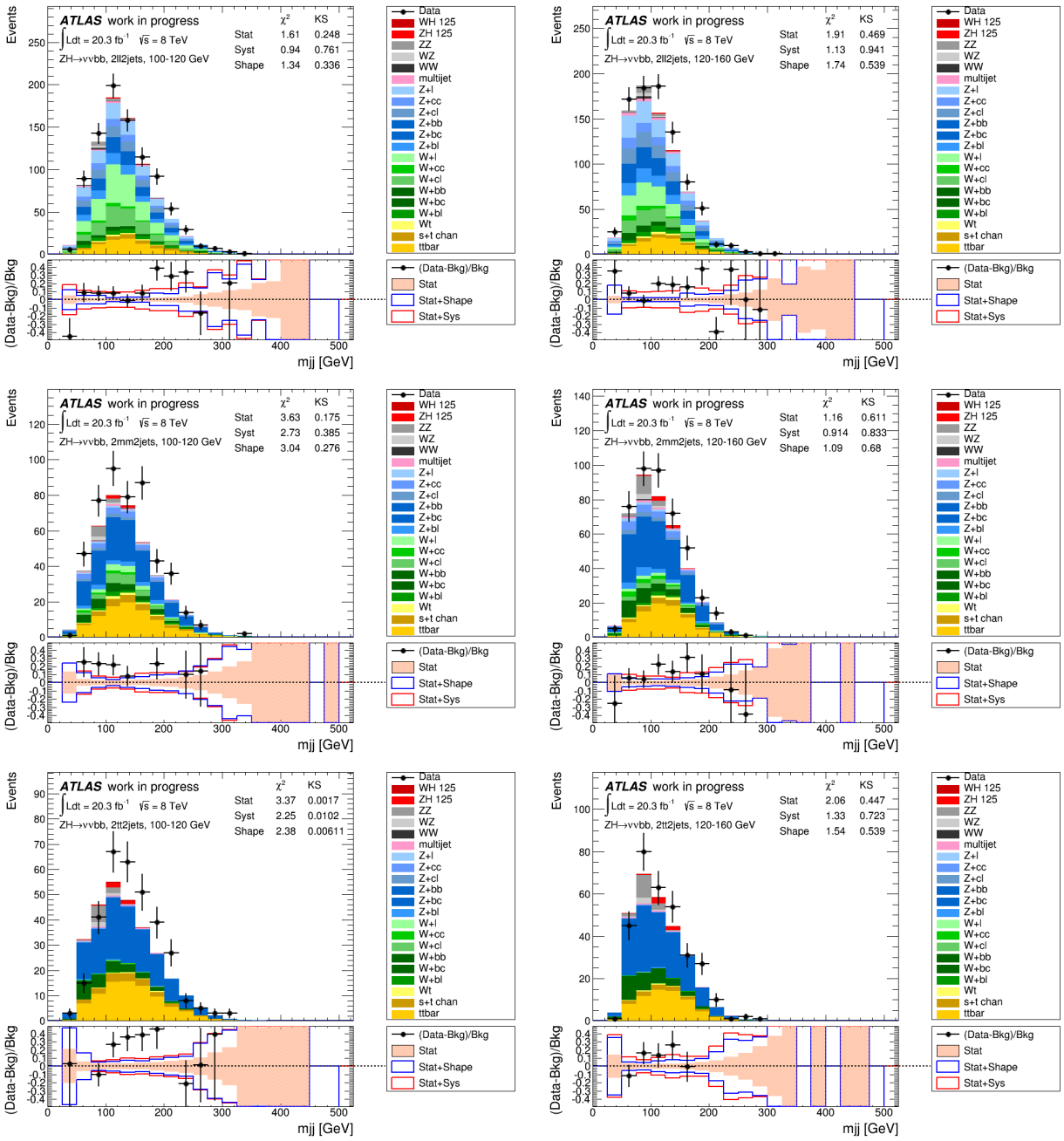

Figure 5.17: Distribution of invariant mass of two b-jets for LL, MM and TT tag regions (in 2-jet bin and in 2 bins of $E_{\mathrm{T}}^{\mathrm{miss}}$: 100–120 GeV and 120–160 GeV) of b-tagging category of the analysis using delayed stream trigger (pre-fit).

Tables 5.7, 5.8 show the comparison of contribution from each sample between the use of delayed stream trigger (inclusively with other nominal triggers) and nominal triggers only in 2TT region in two $E_{\mathrm{T}}^{\mathrm{miss}}$ bins: 100–120 GeV and 120–160 GeV. Tables 5.9, 5.10 show the results for analysis using delayed stream trigger in 2LL and 2MM b-tag regions in the first $E_{\mathrm{T}}^{\mathrm{miss}}$ bin. The errors shown in the tables are statistical uncertainties. There is an overall very slight improvement of signal acceptance and significance when including delayed stream trigger in the analysis regarding the first $E_{\mathrm{T}}^{\mathrm{miss}}$ bin. The higher $E_{\mathrm{T}}^{\mathrm{miss}}$ bins are not affected by the delayed stream trigger implementation because the trigger efficiency is closed to 1 for $E_{\mathrm{T}}^{\mathrm{miss}}$ >120 GeV and reaches a plateau for $E_{\mathrm{T}}^{\mathrm{miss}} > 160$ GeV.

Samples	with delayed stream trigger inclusively	with nominal triggers	ratio
Signal	3.72±0.09	3.58±0.08	1.036
Diboson	3.37±0.22	3.26±0.22	1.034
W+jets	8.84±2.02	8.23±1.89	1.032
Z+jets	48.97±2.66	37.09±2.54	1.037
top	39.08±1.83	37.09±1.75	1.041
multijets	0.89±0.1	0.86±0.11	1.073
All bkgs	101.16±6.84	96.68±6.5	1.046
$S/\sqrt{B}$	0.37	0.365	1.014
data	134	126	1.063

Table 5.7: Comparison of background and signal predictions, signal significance and data in first bin of $E_{\mathrm{T}}^{\mathrm{miss}}$ for the two analysis in 2TT tag region (pre-fit).

Samples	with delayed stream trigger inclusively	with nominal triggers	ratio
signal	5.14±0.10	5.12±0.10	1.004
diboson	3.90±0.22	3.83±0.21	1.018
W+jets	11.45±1.53	11.12±1.45	1.030
Z+jets	49.24±2.23	49.24±2.15	1.000
top	34.77±2.20	34.37±1.72	1.017
multijet	0.80±0.16	0.81±0.16	0.988
all bkgs	100.17±5.92	99.37±5.69	1.008
$S/\sqrt{B}$	0.514	0.513	1.002
data	118	116	1.017

Table 5.8: Comparison of background and signal predictions, the significance and data in second bin of $E_{\mathrm{T}}^{\mathrm{miss}}$ for the two analysis in 2TT tag region (pre-fit).

Samples	Event yield
Signal	1.90±0.06
Diboson	5.26±0.36
W+jets	153.49±5.73
Z+jets	136.23±5.38
top	49.30±2.28
multijets	3.87±0.45
All bkgs	348.16±14.19
$S/\sqrt{B}$	0.102
data	360

Table 5.9: Comparison of background and signal predictions, signal significance and data in first bin of $E_{\mathrm{T}}^{\mathrm{miss}}$ for the analysis using delayed stream trigger inclusively in 2LL tag region (pre-fit).

Samples	Event yield
Signal	3.19±0.08
Diboson	4.20±0.29
W+jets	33.46±4.02
Z+jets	66.22±4.16
top	49.35±2.25
multijets	1.49±0.17
All bkgs	154.72±10.9
$S/\sqrt{B}$	0.256
data	178

Table 5.10: Comparison of background and signal predictions, signal significance and data in first bin of $E_{\mathrm{T}}^{\mathrm{miss}}$ for the analysis using delayed stream trigger inclusively in 2MM tag region (pre-fit).

5.9 Systematic uncertainties

Systematic uncertainties are considered as the errors in measurement that may lead to alternate results from the expected value of the measurememt. The sources of systematics are from experimental and modelling uncertainties. There are uncertainties affecting the normalisation (Norm) and others affecting the shape of m_{bb} distribution.

5.9.1 Experimental uncertainties

Luminosity and pile up The uncertainty on integrated luminosity is 2.8%. The method of deriving this uncertainty is discussed in Ref. [102].

Electrons and muons The uncertainties on electron energy and resolution corrections are named SysElecE and SysElecEResol respectively [103].

For muons, the uncertainty of muon efficiency, as well as isolation, are supposed to be zero in 0-lepton analysis. The non-zero uncertainties of muons come from the muon energy resolution and its smearing in ID and muon spectrometer [104], namely SysMuonEResolID and SysMuonEResolMS, respectively.

In 0-lepton analysis, the uncertainty of lepton veto efficiency should be estimated, named as SysLepVeto.

$\boldsymbol{E}_{\mathbf{T}}^{\mathbf{miss}}$ There are two uncertainties of $E_{\mathrm{T}}^{\mathrm{miss}}$: scale of soft terms SysMETScaleSoftTerms and its resolution SysMETResoSoftTerms [79].

$\boldsymbol{E}_{\mathbf{T}}^{\mathbf{miss}}$ trigger The trigger uncertainty is estimated in detail in chapter 4. The statistical uncertainty is named as SysMETTrigStat, which is estimated from the efficiency of the curve fit. The systematic uncertainty is SysMETTrigZ, which is the difference between W and Z events.

Jets For jet energy scale uncertainty [105]:

- Uncertainty for in-situ jet energy scale calibration: There are six parameters that represent this uncertainty: SysJetNP1 till SysJetNP6rest.
- Uncertainty from η intercalibration: the uncertainty come from the comparison between MC models and also the statistical error of this comparison. They are named as SysJetEtaModel and SysJetEtaStat.
- Uncertainty for MC non-closure with respect to MC12a/Pythia8 simulation: SysJetNonClos.
- Uncertainty for pile-up: there are four of them: SysJetMu, SysJetNPV, for average number of interaction per bunch crossing or number of primary vertices dependence, SysJetPilePt for p_{T} dependence and SysJetPileRho for event energy density.

For flavour and topology uncertainties of jets:

- Uncertainty in b-jet responses in different MC generator: SysJetFlavB.
- Uncertainty in energy from μ and ν from b-hadron decay: SysJetBE.
- Uncertainty for the mixture of light-quarks and gluons SysJetFlavComp_X (with X corresponds to Top, Wjets or Zjets).
- Uncertainty for response between light-quarks and gluons from MC comparison: SysJetFlavResp_X.

There are two jet energy resolution terms [106]: SysJetEResol for jet energy resolution, and SysBJetResol for b-jet resolution.

Jet Fraction Vertex The uncertainty for Jet Fraction Vertex is obtained from the difference between the data and MC in JVF cut, which is named as SysJetJVF.

Flavour tagging The $MV1c$ algorithm is used to distinguish between light and heavy-flavour jets. There are various uncertainties from the scale factors, which are derived from the calibration on data [70, 71]. The uncertainty is a mix of statistical error from data, experimental errors (on Jet Energy Resolution) and theoretical errors (top p_{T} spectrum in $t\bar{t}$ events). The uncertainties depends on p_{T} and interval between operating points of b-tagging algorithm. These uncertainties are decomposed to uncorrelated components and 10 most significant uncertainties for b-jets (SysBTagL0Effic-SysBTagL9Effic) are kept for the analysis, 15 for c-jets (SysCTagL0Effic-SysCtagL14Effic) and 10 for light-jets (SysLTagL0Effic-SysLTagL9Effic).

5.9.2 Modelling uncertainties

These uncertainties relate to the simulation procedures of samples used in the analysis. Those uncertainties are: cross-sections, samples normalizations (Example: W/Z+jets, $t\bar{t}$, QCD and signal), sample modeling (depends on MC generators), shape corrections for MC samples to agree with data (such as $\Delta\phi_{jj}$, p_{T}^{V}, m_{jj} corrections).

$t\bar{t}$ background To correct the measurement on $t\bar{t}$, the top-quark p_{T} reweighting is applied on MC generator level [107], and this correction comes with uncertainty (SysTopPt). The other shape uncertainties (SysTtbarPtWCont for correction on p_{T}^{W} shape, SysTtbarMBBCont for m_{bb} shape, SysTtbarPtB1Cont for leading jet p_{T} shape and SysTtbarMetCont for $E_{\mathrm{T}}^{\mathrm{miss}}$ shape uncertainty) are also taken into account.

single-top background This background has theoretical uncertainties of 4%, 4% and 7% corresponding to each channel of s–channel, t–channel and Wt–channel [108]. The differences on MC generators (AcerMC+Pythia8 for t-channel production and POWHEG+PYTHIA8 for Wt and s production) are compared using 1-lepton channel.

Z+jets background Corrections on $\Delta\phi(\text{jet},\text{jet})$ (SysZDphi) and p_{T}^{Z} (SysZPtV) are applied in order to correct the data/MC agreement, with their corresponding uncertainties. The $\Delta\phi(\text{jet},\text{jet})$ correction is done on 2- and 3-jet events separately, and treated as they are uncorrelated. The shape uncertainty of the m_{bb} distribution (SysZMbb) is compared between data and background in the range of $100 < m_{bb} < 150$ GeV. The uncertainty in flavour fraction (Zbl/Zbb, Zcc/Zbb, Zbc/Zbb) is also taken into account.

W+jets background As for the Z+jets background, the correction on $\Delta\phi(\text{jet},\text{jet})$ (SysWDphi) and p_{T}^{W} (SysWPtV) is also applied on W+jets background for 2- and 3-jet cases separately. The uncertainty of normalisation of Wl background are taken from simulation. The shape uncertainty of the m_{bb} distribution is also taken into account, assuming that it is uncorrelated for Wl, Wcl, $Wbb + Wcc$ and $Wbl + Wbc$, and for $Wbb + Wcc$, it is uncorrelated among the p_{T}^{V} intervals. The uncertainty on flavour fractions (for example, Wbl/Wbb) are also included.

Diboson background The uncertainty on diboson production cross-sections (WW, WZ, ZZ) can be calculated in parton level. There are other uncertainties: the normalisation and factorisation scales, the choice of PDFs. The uncertainty of the PDF choice ranges from 2% to 4%. The scale uncertainties are observed to be largest at high p_{T}^{V}, for 2-jet case, the largest uncertainty is about 22% in WZ channel, and in 3-jet case, the uncertainty is about 17% applied to all channel.

Signal modelling The uncertainties of the signal production cross-sections (from productions of $q\bar{q} \to ZH$, $gg \to ZH$ and $q\bar{q} \to WH$) are assessed from the choice on normalisation/factorisation scales and PDFs. The scale uncertainties are 1% on WH production and 3% on $gg \to ZH$ production. The PDF uncertainties are 17% on $gg \to ZH$ and 2.4% on $q\bar{q} \to (W/Z)H$. The uncertainty on $H \to b\bar{b}$ branching ratio is about 3% at m_H= 125 GeV.

5.9.3 Estimation of systematics

The results of estimation for experimental and modeling uncertainties are listed in Tables 5.11, 5.12, 5.13, 5.14 for the $t\bar{t}$ and Zbb events as an example since they are main backgrounds. The results for the signal are represented in Tables 5.15 and 5.16. Tables 5.11, 5.13 and 5.15 show the effect of systematic uncertainties (experimental or modelling) over the normalisation and shape (up and down) and Tables 5.12, 5.14 and 5.16 show the flavour-tagging uncertainties. For the $t\bar{t}$ background, the experimental uncertainty with largest impact on normalisation is $E_{\text{T}}^{\text{miss}}$ shape uncertainty on $t\bar{t}$ with 15%. The shape uncertainties are small, less than 1%. For Zbb background, we can observe that the uncertainty with largest impact on normalisation is the mixture of light quarks and gluons with 2.8% of variation on normalisation. The largest shape uncertainty on Zbb background is p_T dependence with 25% of variation on shape. For signal, the systematic with largest impact on normalisation is the b-tagging SysBTagB1Effic (2.3%). The largest shape variation for signal is η intercalibration SysJetEtaModel (6.6%).

Name	Experimental uncertainties $t\bar{t}$			
	NormUp(%)	NormDo(%)	ShapUp(%)	ShapDo(%)
SysElecE	-0.2258	0.1458	0.0143	0.0111
SysElecEResol	-0.0312	0.1862	0.0115	0.0227
SysMuonEResolID	-0.0001	-0.0049	0.0138	0.0355
SysMuonEResolMS	0.1020	0.0009	0.0158	0.8946
SysJetNP1	-0.2300	-1.9988	0.4482	0.8666
SysJetNP2	-1.1746	0.7473	0.5407	0.5332
SysJetNP3	0.6771	-0.6437	0.4800	0.7039
SysJetNP4	0.5650	-0.3188	0.0824	0.1982
SysJetNP5	-0.5287	0.5989	0.2163	0.1264
SysJetNP6rest	0.0986	0.3702	0.1823	0.3506
SysJetEtaModel	-0.9149	-0.3419	0.5955	1.2532
SysJetEtaStat	-0.0212	0.1503	0.1922	0.3836
SysJetNPV	-0.3313	0.3919	0.5172	0.6519
SysJetMu	-0.4801	-0.3415	0.2275	0.2138
SysJetPilePt	0.3816	-0.6889	0.5380	0.3755
SysJetPileRho	-0.0725	0.3577	0.2883	0.7465
SysJetFlavComp	-1.4655	4.3015	0.0892	0.1079
SysJetFlavResp	-0.7404	1.8787	0.0693	0.0730
SysJetFlavB	1.3057	-4.1248	0.5465	0.5539
SysJetNonClos	0.8583	-0.3955	0.5692	0.5489
SysJetBE	-0.0190	0.0247	0.2550	0.8920
SysMETResoSoftTerms	0.1530	-0.9601	0.0638	0.0762
SysMETScaleSoftTerms	-2.4272	1.7671	0.0507	0.0774
SysMuScale	0.0110	-0.0203	0.0407	0.0351
SysJVF	1.9286	-2.0729	0.0200	0.0269
SysMETTrigZ	0.3071	-0.3071	0.0003	0.0003
SysMETTrigStat	0.3403	-0.3403	0.0003	0.0003
SysJetEResol	4.3416	4.3416	0.3530	0.3530
SysBJetReso	-0.1311	-0.1311	0.6114	0.6114
Name	Modelling uncertainties $t\bar{t}$			
SysTopPt	0.5412	-0.5412	0.0048	0.0049
SysTtbarPtWCont	3.8421	-3.8421	0.0009	0.0010
SysTtbarMBBCont	0.9387	-0.9387	0.4735	0.4824
SysTtbarPtB1Cont	-0.4888	0.4888	0.0105	0.0104
SysTtbarMetCont	15.2237	-15.2237	0.0034	0.0047

Table 5.11: Estimation of experimental and modelling uncertainties using delayed stream trigger implementation using $t\bar{t}$ sample on 2MM and first $E_{\mathrm{T}}^{\mathrm{miss}}$ region.

Name	Flavour tagging uncertainties $t\bar{t}$			
	NormUp(%)	NormDo(%)	ShapUp(%)	ShapDo(%)
SysBTagL0Effic	-0.2776	0.2776	0.0039	0.0039
SysBTagL1Effic	-0.1893	0.1893	0.0028	0.0028
SysBTagL2Effic	-0.1037	0.1037	0.0026	0.0026
SysBTagL3Effic	0.0098	-0.0098	0.0012	0.0012
SysBTagL4Effic	-0.0492	0.0492	0.0013	0.0013
SysBTagL5Effic	-0.0180	0.0180	0.0004	0.0004
SysBTagL6Effic	-0.0544	0.0544	0.0011	0.0011
SysBTagL7Effic	0.0089	-0.0089	0.0003	0.0003
SysBTagL8Effic	-0.0040	0.0040	0.0002	0.0002
SysBTagL9Effic	-0.0215	0.0215	0.0004	0.0004
SysBTagC0Effic	0.1299	-0.1299	0.0009	0.0009
SysBTagC1Effic	0.5291	-0.5291	0.0031	0.0032
SysBTagC2Effic	-0.2603	0.2603	0.0015	0.0015
SysBTagC3Effic	-0.1000	0.1000	0.0008	0.0008
SysBTagC4Effic	-0.0809	0.0809	0.0009	0.0009
SysBTagC5Effic	0.1881	-0.1881	0.0017	0.0017
SysBTagC6Effic	-0.1781	0.1781	0.0014	0.0014
SysBTagC7Effic	0.4285	-0.4285	0.0025	0.0026
SysBTagC8Effic	-0.1406	0.1406	0.0013	0.0013
SysBTagC9Effic	0.1062	-0.1062	0.0015	0.0015
SysBTagC10Effic	-0.0930	0.0930	0.0011	0.0011
SysBTagC11Effic	0.0670	-0.0670	0.0011	0.0011
SysBTagC12Effic	-0.4636	0.4636	0.0024	0.0024
SysBTagC13Effic	-0.0797	0.0797	0.0021	0.0021
SysBTagC14Effic	0.1272	-0.1272	0.0017	0.0017
SysBTagB0Effic	1.0532	-1.0483	0.0026	0.0027
SysBTagB1Effic	1.9607	-1.9421	0.0028	0.0029
SysBTagB2Effic	0.3389	-0.3392	0.0013	0.0013
SysBTagB3Effic	-0.2527	0.2530	0.0005	0.0005
SysBTagB4Effic	0.8835	-0.8810	0.0029	0.0029
SysBTagB5Effic	1.2422	-1.2347	0.0025	0.0025
SysBTagB6Effic	0.1235	-0.1238	0.0016	0.0016
SysBTagB7Effic	0.0115	-0.0115	0.0006	0.0006
SysBTagB8Effic	-0.0099	0.0097	0.0015	0.0015
SysBTagB9Effic	-0.7749	0.7776	0.0018	0.0018

Table 5.12: Estimation of uncertainty on flavour tagging using delayed stream on $t\bar{t}$ samples on 2MM tag and first $E_{\mathrm{T}}^{\mathrm{miss}}$ region.

Name	Experimental uncertainties Zbb			
	NormUp(%)	NormDo(%)	ShapUp(%)	ShapDo(%)
SysElecE	-0.0022	0.0313	0.0006	0.0051
SysElecEResol	0.0168	0.0002	0.0069	0.0001
SysMuonEResolID	0.0000	0.0002	0.0025	0.0221
SysMuonEResolMS	-0.0427	-0.0002	0.0164	0.0106
SysJetNP1	-0.1862	0.4276	12.7515	5.7906
SysJetNP2	-1.3323	0.3776	17.5091	12.1319
SysJetNP3	1.2493	-1.5751	12.2796	1.0271
SysJetNP4	-0.9979	0.6275	0.1379	0.2362
SysJetNP5	0.1057	-0.1302	0.2091	0.2110
SysJetNP6rest	0.2638	-0.1989	11.6892	0.8241
SysJetEtaModel	1.2481	1.2958	1.6022	0.9364
SysJetEtaStat	-0.4916	-0.3530	12.2549	1.2385
SysJetNPV	-0.4476	-0.2707	11.6622	0.9268
SysJetMu	0.4139	-0.0949	0.1363	0.0912
SysJetPilePt	0.3132	-0.0068	25.0699	2.2191
SysJetPileRho	-0.2893	-0.4048	11.9138	1.3513
SysJetFlavComp	-0.8919	2.7940	0.0208	0.0315
SysJetFlavResp	-0.5711	1.4042	0.0163	0.0230
SysJetFlavB	1.9920	-2.5732	12.2128	2.1818
SysJetNonClos	2.0403	-1.9314	0.7569	2.0865
SysJetBE	-0.1439	0.1150	12.2117	2.4654
SysMETResoSoftTerms	1.2678	0.5635	0.1182	1.5298
SysMETScaleSoftTerms	-1.5152	1.2004	0.0899	1.7405
SysMuScale	-0.7030	0.5808	0.0545	0.0323
SysJVF	0.6740	0.1842	0.0214	0.0159
SysMETTrigZ	0.3025	-0.3025	0.0003	0.0003
SysMETTrigStat	0.3341	-0.3341	0.0002	0.0002
SysJetEResol	1.8288	1.8288	1.8369	1.8369
SysBJetReso	-0.0101	-0.0101	2.9905	2.9905
Name	Modelling uncertainties Zbb			
SysZDPhi	-2.4052	2.4052	0.0147	0.0140
SysZPtV	-2.4401	2.4401	0.0026	0.0025
SysZMbb	1.5924	-1.5924	2.1630	2.2330

Table 5.13: Estimation of experimental and modelling uncertainties using delayed stream trigger implementation using Zbb sample on 2MM and first $E_{\mathrm{T}}^{\mathrm{miss}}$ region.

Name	*Zbb*			
	NormUp(%)	NormDo(%)	ShapUp(%)	ShapDo(%)
SysBTagB0Effic	1.0080	-1.0046	0.0028	0.0028
SysBTagB1Effic	2.0472	-2.0276	0.0025	0.0026
SysBTagB2Effic	0.7175	-0.7186	0.0033	0.0033
SysBTagB3Effic	-0.3416	0.3421	0.0005	0.0005
SysBTagB4Effic	1.7563	-1.7511	0.0056	0.0057
SysBTagB5Effic	1.2192	-1.2131	0.0023	0.0023
SysBTagB6Effic	0.1573	-0.1578	0.0020	0.0020
SysBTagB7Effic	0.0216	-0.0215	0.0007	0.0007
SysBTagB8Effic	-0.1342	0.1338	0.0015	0.0015
SysBTagB9Effic	-0.8354	0.8388	0.0015	0.0015

Table 5.14: Estimation of uncertainty on flavour tagging using delayed stream on *Zbb* samples on 2MM tag and first $E_{\mathrm{T}}^{\mathrm{miss}}$ region.

Name	Experimental uncertainties signal			
	NormUp(%)	NormDo(%)	ShapUp(%)	ShapDo(%)
SysElecE	-0.0427	0.0650	0.0032	0.0034
SysElecEResol	-0.0252	0.0286	0.0058	0.0056
SysMuonEResolID	-0.0001	-	0.0014	0.0024
SysMuonEResolMS	0.0054	0.0001	0.0028	0.0011
SysJetNP1	0.3111	0.3770	0.3491	2.3322
SysJetNP2	-0.1845	1.8853	1.7986	1.8652
SysJetNP3	1.0582	-0.4074	0.3667	1.7774
SysJetNP4	-0.1763	0.1156	0.0584	0.1464
SysJetNP5	-0.1601	-0.0732	0.0627	0.0512
SysJetNP6rest	0.3213	-0.0731	0.3106	0.4253
SysJetEtaModel	1.6716	-0.4977	2.3500	6.6300
SysJetEtaStat	0.0724	0.1569	0.2793	1.5861
SysJetNPV	0.0127	0.3023	0.1479	1.6827
SysJetMu	-0.1574	0.2294	0.0774	0.2549
SysJetPilePt	0.1505	-0.2124	0.1282	1.1442
SysJetPileRho	0.4181	0.2838	0.3663	2.0675
SysJetFlavComp	-0.3405	2.1844	0.3648	0.3500
SysJetFlavResp	-0.2699	1.2059	0.1195	0.1052
SysJetFlavB	2.2411	-1.3481	2.0015	2.2750
SysJetNonClos	1.4455	-0.8082	1.9843	2.0143
SysJetBE	-	-	2.2475	2.0952
SysMETResoSoftTerms	-0.3305	0.3354	0.2053	0.1616
SysMETScaleSoftTerms	-1.1651	1.1692	0.2050	0.0749
SysMuScale	-0.3880	0.3774	0.0732	0.0367
SysJVF	0.3711	-0.1977	0.0148	0.0106
SysMETTrigTop	0.3159	-0.3159	0.0003	0.0003
SysMETTrigStat	0.3391	-0.3391	0.0003	0.0003
SysJetEResol	1.1410	1.1410	1.4133	1.4133
SysBJetReso	-	-	1.7712	1.7712
Name	Modelling uncertainties signal			
SysTheoryHPt	2.0000	-2.0000	-	-
SysTheoryVPtQCD	0.9349	-0.9349	0.0058	0.0059

Table 5.15: Estimation of experimental and modelling uncertainties using delayed stream trigger implementation using signal sample on 2MM and first $E_{\mathrm{T}}^{\mathrm{miss}}$ region.

Name	signal			
	NormUp(%)	NormDo(%)	ShapUp(%)	ShapDo(%)
SysBTagL0Effic	-0.0674	0.0674	0.0054	0.0054
SysBTagL1Effic	-0.0488	0.0488	0.0034	0.0034
SysBTagL2Effic	-0.0080	0.0080	0.0073	0.0073
SysBTagL3Effic	0.0194	-0.0194	0.0024	0.0024
SysBTagL4Effic	-0.0166	0.0166	0.0011	0.0011
SysBTagL5Effic	-0.0046	0.0046	0.0007	0.0007
SysBTagL6Effic	-0.0100	0.0100	0.0019	0.0019
SysBTagL7Effic	-0.0025	0.0025	0.0012	0.0012
SysBTagL8Effic	0.0003	-0.0003	0.0005	0.0005
SysBTagL9Effic	-0.0043	0.0043	0.0006	0.0006
SysBTagC0Effic	-0.3619	0.3619	0.0422	0.0419
SysBTagC1Effic	0.0160	-0.0160	0.0042	0.0042
SysBTagC2Effic	0.0039	-0.0039	0.0034	0.0034
SysBTagC3Effic	0.0172	-0.0172	0.0008	0.0008
SysBTagC4Effic	-0.0094	0.0094	0.0014	0.0014
SysBTagC5Effic	0.0043	-0.0043	0.0008	0.0008
SysBTagC6Effic	0.0061	-0.0061	0.0014	0.0014
SysBTagC7Effic	0.0016	-0.0016	0.0028	0.0028
SysBTagC8Effic	-0.0072	0.0072	0.0004	0.0004
SysBTagC9Effic	-0.0053	0.0053	0.0006	0.0006
SysBTagC10Effic	0.0093	-0.0093	0.0007	0.0007
SysBTagC11Effic	-0.0068	0.0068	0.0010	0.0010
SysBTagC12Effic	-0.0016	0.0016	0.0008	0.0008
SysBTagC13Effic	0.0069	-0.0069	0.0022	0.0022
SysBTagC14Effic	-0.0005	0.0005	0.0032	0.0032
SysBTagB0Effic	1.2519	-1.2457	0.0031	0.0032
SysBTagB1Effic	2.3152	-2.2912	0.0060	0.0063
SysBTagB2Effic	0.4776	-0.4788	0.0031	0.0032
SysBTagB3Effic	-0.2642	0.2645	0.0006	0.0006
SysBTagB4Effic	1.3447	-1.3414	0.0045	0.0046
SysBTagB5Effic	1.2698	-1.2615	0.0034	0.0034
SysBTagB6Effic	0.2612	-0.2618	0.0021	0.0021
SysBTagB7Effic	0.0011	-0.0011	0.0005	0.0005
SysBTagB8Effic	-0.1575	0.1573	0.0008	0.0008
SysBTagB9Effic	-0.8151	0.8182	0.0014	0.0014

Table 5.16: Estimation of uncertainty on flavour tagging using delayed stream on signal samples on 2MM tag and first $E_{\mathrm{T}}^{\mathrm{miss}}$ region.

5.10 Statistical analysis

5.10.1 Test statistic

We use the invariant mass distribution $m_{b\bar{b}}$ as the input for the statistical analysis to determine the upper limit of cross-section of Higgs boson. This analysis use the presence of signal at each value of Higgs mass: 115, 120, 125, 130, 135, and 140 GeV.

Let us consider the expected number of signal and backgrounds are S and B, respectively. Then we define $\mu S + B$ with μ the strength of the signal, defined as σ/σ_{SM}. μ=0 corresponds to the background-only hypothesis while μ=1 corresponds to nominal signal hypothesis.

To extract the signal strength μ from data, a statistical fitting procedure is used, based on RooStat framework [109, 110]. A binned likelihood function is established using the product of Poisson-probability terms over the bins of invariant mass distribution m_{bb} (from four bins of $E_{\mathrm{T}}^{\mathrm{miss}}$, two number-of-jet categories (2 or 3[5]), three b-tagging categories (2LL, 2MM and 2TT)) and weight of $MV1c$ algorithm (in two regions of $E_{\mathrm{T}}^{\mathrm{miss}}$: $E_{\mathrm{T}}^{\mathrm{miss}} < 120$ GeV and $E_{\mathrm{T}}^{\mathrm{miss}} > 120$ GeV, 2- and 3-jet bins and 1-tag region), which contains the number of signal and background yields, by considering floating normalisations of backgrounds and systematic uncertainties.

The normalisation factors applying for each background are extracted from these fitting procedure. The invariant mass distribution after applying those scale factors are called post-fit.

The effect of systematic uncertainties on the predictions of signal and backgrounds is described by the *nuisance parameters* (NP) $\vec{\theta}$, constrained by Gaussian or log-normal[6] probability density functions. The expectations of signal and backgrounds in each bin are functions of $\vec{\theta}$. The NP is parametrised such that signal and background yields in each bin are log-normal distribution for a normally distributed θ.

The test statistic [111] q_μ is constructed from a profile likelihood ratio:

$$q_\mu = -2 \ln \frac{\mathcal{L}(\mu, \hat{\hat{\vec{\theta}}}_\mu)}{\mathcal{L}(\hat{\mu}, \hat{\hat{\vec{\theta}}})},$$

where $\hat{\mu}$, $\hat{\hat{\vec{\theta}}}$ are the parameters that maximise the likelihood (with $0 \leq \hat{\mu} < \mu$), and $\hat{\hat{\vec{\theta}}}_\mu$ are the nuisance parameters that maximise the likelihood for a given μ.

To assess the compatibility between background-only hypothesis and observed data, the test statistic q_0 is used with $q_0 = -2 \ln \frac{\mathcal{L}(0, \hat{\hat{\vec{\theta}}})}{\mathcal{L}(\hat{\mu}, \hat{\hat{\vec{\theta}}})}$.

5.10.2 Confidence levels and limits

The range of μ can be extracted from the test statistic while calculating the upper limit of μ. We can construct the distribution of the test statistic q_μ by considering the different value of signal strength μ. This distribution is defined as:

$$f(q_\mu | \mu, m_H, \vec{\theta})$$

[5] 3-jet events in the first $E_{\mathrm{T}}^{\mathrm{miss}}$ bin are not used.

[6] This is chosen to prevent negative normalisation factors in fitting procedure.

This distribution depends explicitly on Higgs mass m_H and nuisance parameters $\vec{\theta}$. Then we can calculate the p-values for testing a certain value of μ using the distribution established at $\hat{\hat{\vec{\theta}}}(\mu, \text{obs})$ (the maximum likelihood estimated with observed data) as follows:

$$p_\mu = \int_{q_{\mu,\text{obs}}}^{\text{inf}} f(q_\mu|\mu, m_H, \vec{\theta}(\mu, \text{obs}))dq_\mu,$$

where $q_{\mu,\text{obs}}$ is the value of test statistic for the observed data. The p-value for the test statistic under the background-only hypothesis is:

$$p_b = \int_{q_{\mu,\text{obs}}}^{\text{inf}} f(q_\mu|0, m_H, \vec{\theta}(\mu = 0, \text{obs}))dq_\mu.$$

Then, to calculate the upper limit on μ, the quantity CL_s is calculated as:

$$CL_s = \frac{p_\mu}{1 - p_b}.$$

The CL_s upper limit on μ is obtained from solving $CL_s(\mu) = 5\%$, labelled as μ_{up}. The value of μ is considered to be excluded at 95% confidence level if $\mu > \mu_{up}$.

There is other quantity that we want to estimate: the probability for the fluctuation of data using background-only hypothesis produce the same output as signal, called p_0:

$$p_0 = \int_{q_{0,\text{obs}}}^{\text{inf}} f(q_0|0, m_H, \vec{\theta}(\mu = 0, \text{obs}))dq_0,$$

5.10.3 Systematic uncertainty implementation

Systematic uncertainties are included by fluctuating the predictions of signal and backgrounds in each histogram bin. When forming the computation of probabilities and test statistics, they are affected by these systematic uncertainties. To compute this effect, we fluctuate the signal and background estimations in each histogram bin by taking into account both the Poisson statistical uncertainties and Gaussian variations for each systematic uncertainty.

The fit to extract the signal strength in section 5.10.1 uses the templates from the signal and background estimation in the input invariant mass distribution in each bin, with the systematic variations included as the variations of the nominal template for each up-and-down variation ($\pm\sigma$). If the systematic variation ends up as reweighting of the nominal template (such as b-tagging), then no statistical fluctuations are expected in the existing nominal template. If the systematic variation can cause a change to the event selection (for example, JES), additional statistical variations are included, therefore changing the template of systematic variations. To deal with such cases, smoothing procedure is introduced and applied to such systematic variation in each region.

The fit uses a large number of nuisance parameters, which costs a long time to run. To overcome this problem, systematic uncertainties that have negligible impact on the final results are pruned away. A normalisation uncertainty is pruned if the associated variation

is below 0.5% in all bins. Another condition for pruning is the signal contribution is less than 2% of the total background and the systematic variations change the total background estimation by 0.5%.

It is important to understand which systematic variation causes the largest impact to the final results, and need more care. To do this, the NP ranking is introduced. For each systematic uncertainty, the fit is done again using the corresponding fitted NP value $\hat{\theta}$, varied up and down by its fit uncertainty, while other parameters float freely to guarantee the correlation between the systematic uncertainties. The magnitude of the variation on the fitted signal strength μ is expressed as the observed impact of the corresponding NP.

5.11 Results

The results for the statistical analysis will be divided in various cases: in 0-lepton analysis, we will consider the two cases: one case focuses on the first bin of $E_{\mathrm{T}}^{\mathrm{miss}}$ only, the second case will use all $E_{\mathrm{T}}^{\mathrm{miss}}$ bins.

5.11.1 Invariant mass distribution after the fit

The normalisation for each type of background after the fit including all $E_{\mathrm{T}}^{\mathrm{miss}}$ bin is shown in Table 5.17, using the constraints introduced by various bins of $E_{\mathrm{T}}^{\mathrm{miss}}$. Table 5.18 shows the normalisation factors on the first $E_{\mathrm{T}}^{\mathrm{miss}}$ bin, with constraints only on that bin. The new distributions of invariant mass after applying the normalisation scale factors for all $E_{\mathrm{T}}^{\mathrm{miss}}$ bin are shown in Figures 5.18, 5.19. The differences between the scale factors in inclusive $E_{\mathrm{T}}^{\mathrm{miss}}$ bins and in first $E_{\mathrm{T}}^{\mathrm{miss}}$ bin are due to the constraints on high $E_{\mathrm{T}}^{\mathrm{miss}}$ regions: the large contribution of the Z+jets background and clear shape difference between Z+jets, W+jets and $t\bar{t}$ shown in Figure 5.19 for $E_{\mathrm{T}}^{\mathrm{miss}} > 160$ GeV provide a control on the normalisation of the Z+jets and $t\bar{t}$ backgrounds, contrary to what can be obtained in the first $E_{\mathrm{T}}^{\mathrm{miss}}$ bin. Figure 5.20 shows the results after applying normalisation scale factors on the first $E_{\mathrm{T}}^{\mathrm{miss}}$ bin using Tables 5.17 and 5.18, showing that the normalisation scale factors on 5.18 yields a slightly better data/MC agreement, as expected from a fit on that bin only. The normalisation factors are nevertheless better motivated in the fit with inclusive $E_{\mathrm{T}}^{\mathrm{miss}}$ bins.

Background	Normalisation factor
Zl	0.93 ± 0.07
Zcl	0.98 ± 0.22
Zhf	1.00 ± 0.14
Wl	1.04 ± 0.09
Wcl	1.22 ± 0.27
Whf	0.73 ± 0.23
single t	1.05 ± 0.21
$t\bar{t}$	1.49 ± 0.23

Table 5.17: The normalisation factor for each type of background after the likelihood fit for all $E_{\mathrm{T}}^{\mathrm{miss}}$ bin. The "hf" means heavy-flavors bb, bc, bl and cc.

Impact of systematic uncertainties The impact of systematic uncertainties on the fitted signal-strength $\hat{\mu}$ (inclusive $E_{\mathrm{T}}^{\mathrm{miss}}$ bin) is represented in Figure 5.21. The uncertainties are listed in decreasing order of impact on the signal strength. The five systematic uncertainties which have largest impact to the signal strength are: m_{bb} shape for Wbb and Wcc background (with $p_{\mathrm{T}}^{W} > 120$ GeV), 1-component of b-tagging efficiency, $E_{\mathrm{T}}^{\mathrm{miss}}$ scale of soft terms, normalisation on Zbb background and Zbl/Zbb normalisation for 2-jet case.

Background	Normalisation factor
Zl	1.07 ± 0.12
Zcl	1.24 ± 0.32
Zhf	0.69 ± 0.32
Wl	1.01 ± 0.10
Wcl	1.14 ± 0.28
Whf	0.99 ± 0.35
single t	1.12 ± 0.35
$t\bar{t}$	2.38 ± 0.57

Table 5.18: The normalisation factor for each type of background after the likelihood fit for first $E_{\mathrm{T}}^{\mathrm{miss}}$ bin. The "hf" means heavy-flavors *bb*, *bc*, *bl* and *cc*.

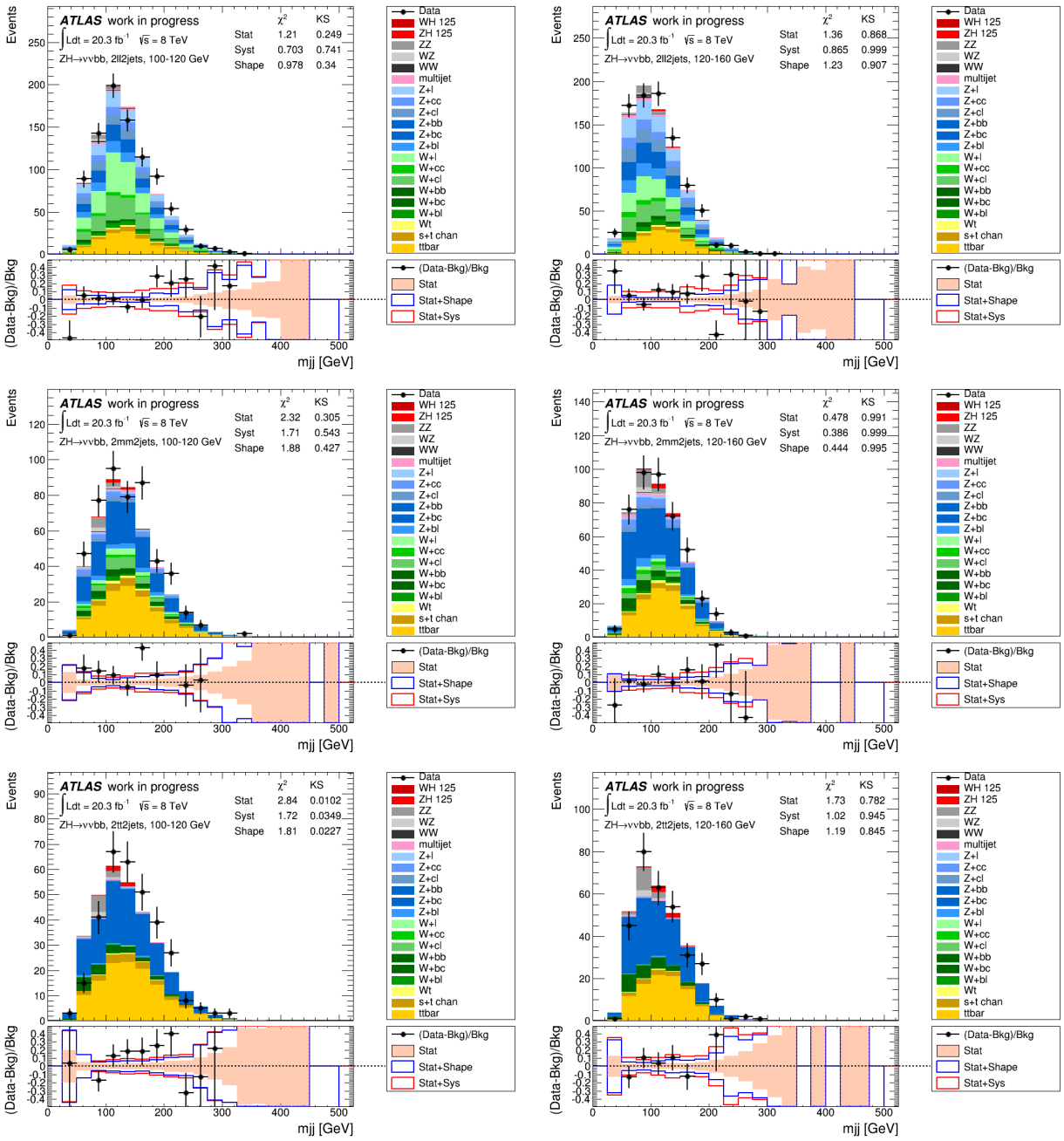

Figure 5.18: Invariant mass distribution for analysis using delayed stream trigger after applying scale factors in Table 5.17. From top to bottom are plots for 2LL, 2MM, 2TT b-tagging categories, left plots are for first $E_{\mathrm{T}}^{\mathrm{miss}}$ bin, and right ones for second $E_{\mathrm{T}}^{\mathrm{miss}}$ bin.

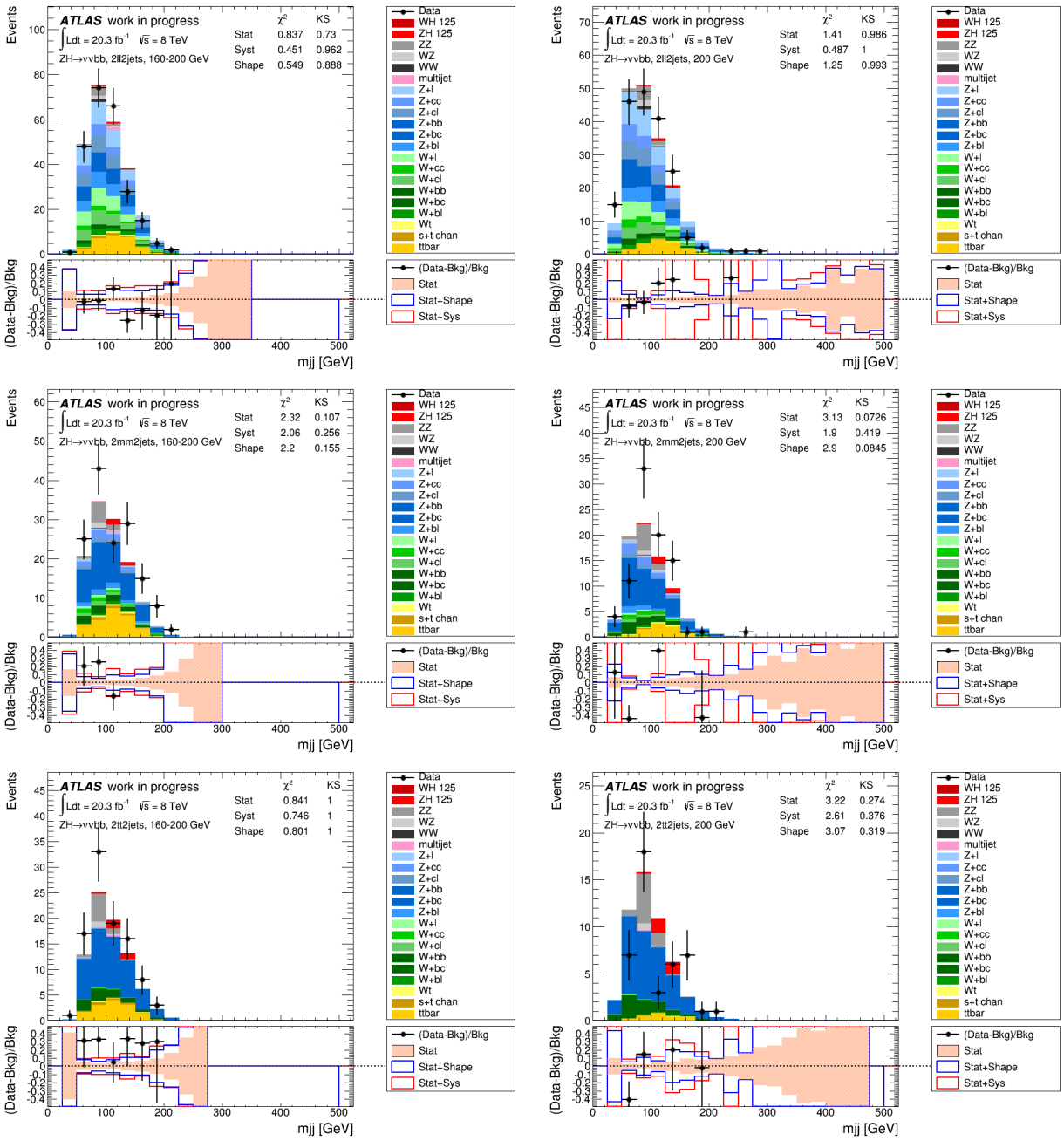

Figure 5.19: Invariant mass distribution for analysis using delayed stream trigger after applying scale factors in Table 5.17. From top to bottom are plots for 2LL, 2MM, 2TT b-tagging categories, left plots are for third $E_{\mathrm{T}}^{\mathrm{miss}}$ bin, and right ones for fourth $E_{\mathrm{T}}^{\mathrm{miss}}$ bin.

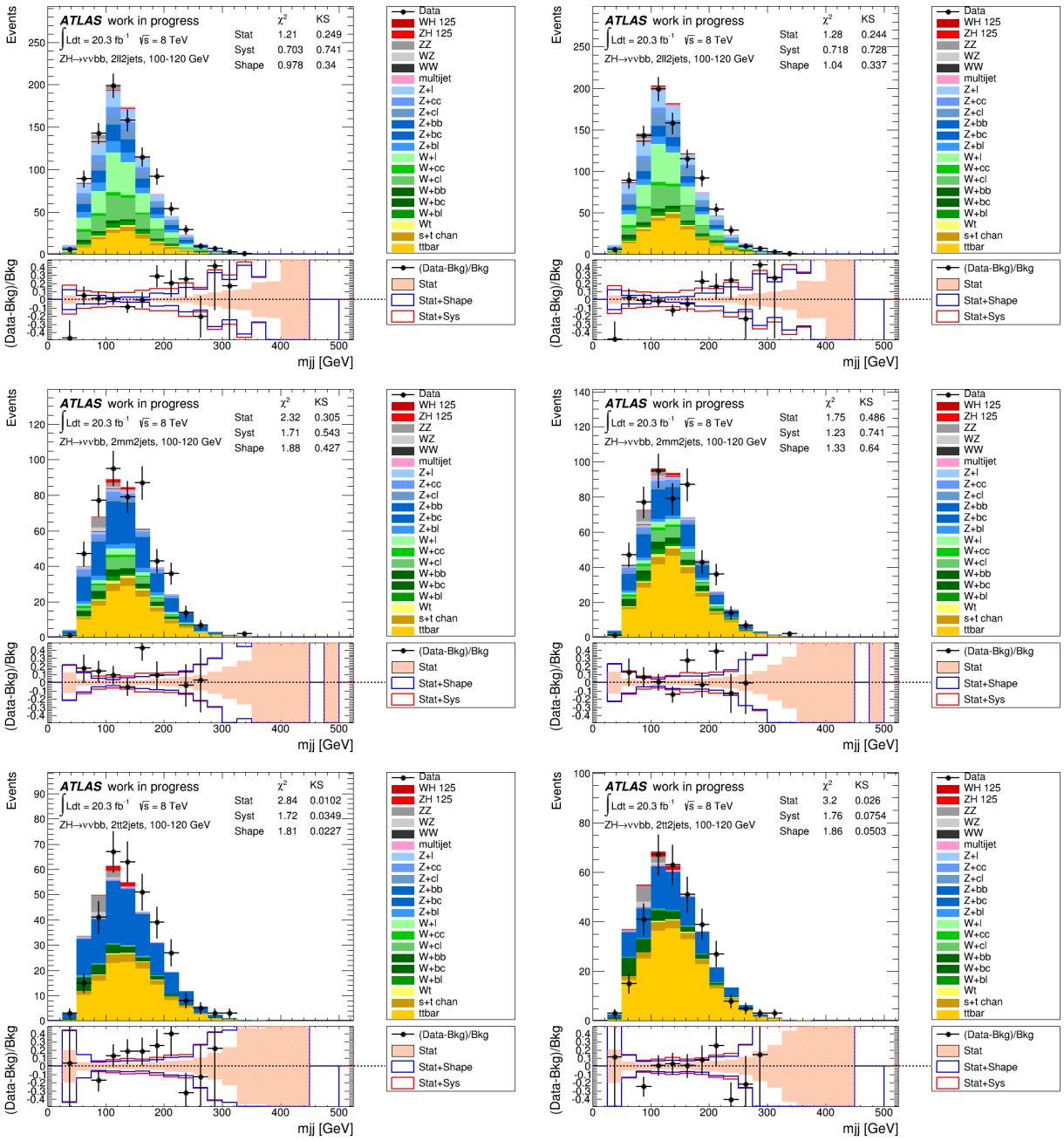

Figure 5.20: Comparison of invariant mass distribution for analysis using delayed stream trigger after applying scale factors in Table 5.17 (left plots) and Table 5.18 (right plots). From top to bottom are plots for 2LL, 2MM, 2TT b-tagging categories.

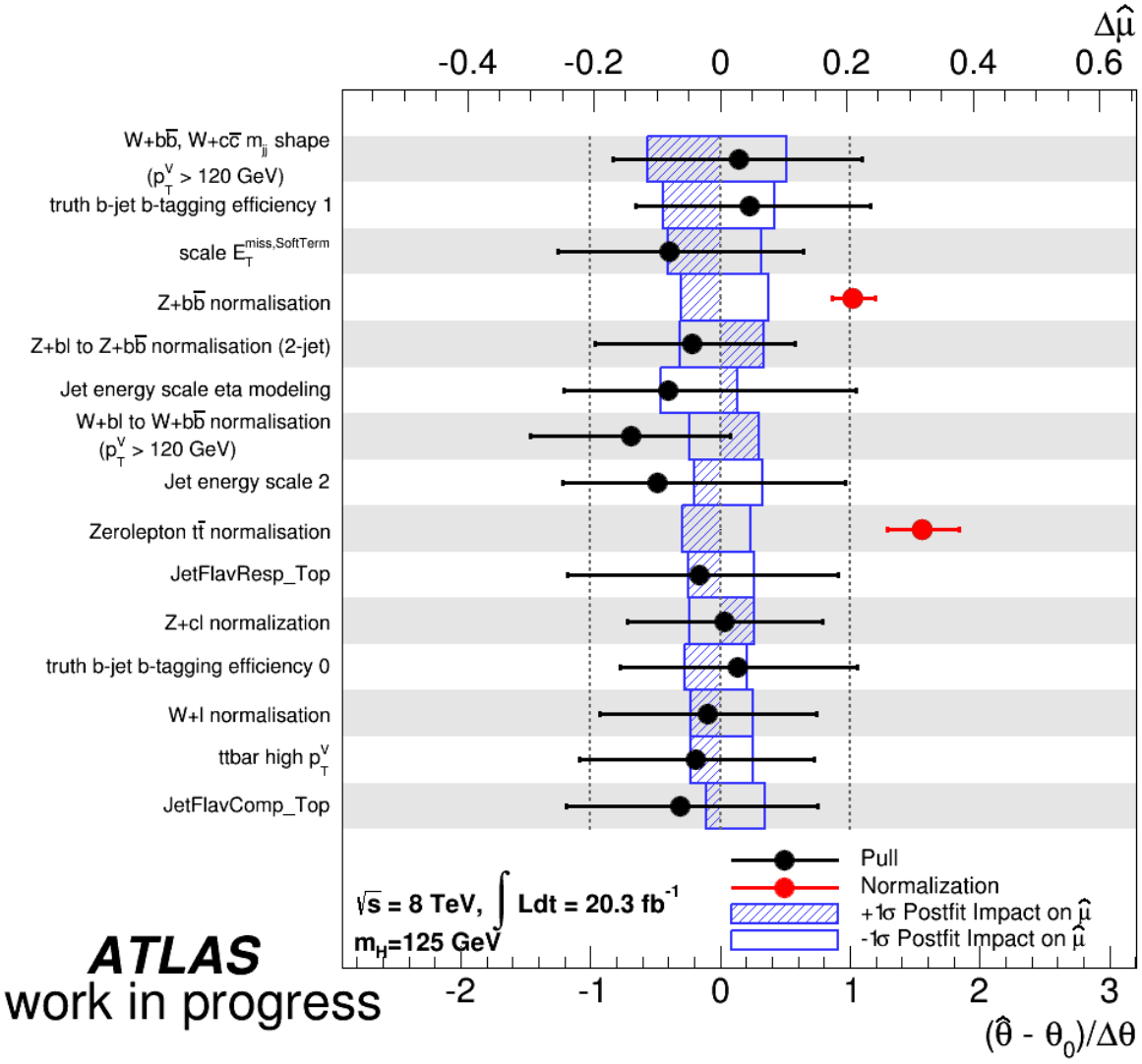

Figure 5.21: Impact of systematic uncertainties on the fitted signal-strength parameter $\hat{\mu}$ for all $E_{\mathrm{T}}^{\mathrm{miss}}$ bin using delayed stream implementation. The systematic uncertainties are listed in decreasing order of their impact on $\hat{\mu}$ on y-axis. The boxes show the variation of $\hat{\mu}$ (the top x-axis) when setting the corresponding nuisance parameter θ to its $\pm 1\sigma$ post-fit variations while fixing every other nuisance parameters to their post-fit values. The black filled points (referring to the bottom x-axis) show the deviation of the fitted nuisance parameters $\hat{\theta}$ with respect to their nominal values θ_0, expressed in $(\hat{\theta} - \theta_0)/\Delta\theta$ ($\Delta\theta$ is their nominal uncertainties). The associated error bars are the post-fit uncertainties of the NPs. The red filled points and their error bars (also referring to the bottom x-axis) are the fitted values of the normalisation parameters.

5.11.2 0-lepton analysis with first $E_{\mathrm{T}}^{\mathrm{miss}}$ bin

Here we consider two cases of analysis: using nominal triggers and using delayed stream trigger. Figure 5.22 displays the limit on signal strength μ in the first $E_{\mathrm{T}}^{\mathrm{miss}}$ bin of the 0-lepton analysis, followed by Tables 5.19 for analysis using delayed stream trigger and 5.20 for analysis using nominal triggers, with mass range from 115 GeV to 140 GeV (with 5 GeV bin). The expected limit upper range for delayed stream is between 3.79 to 13.92 for analysis using delayed stream trigger, and between 3.84 and 13.65 for analysis using nominal triggers at 95% of confidence level. At 125 GeV, the expected limits for analyses using delayed stream trigger and nominal triggers are 5.77 and 5.89, respectively. It can be seen that there is a slight improvement ($\sim 2\%$) with the analysis using delayed stream trigger.

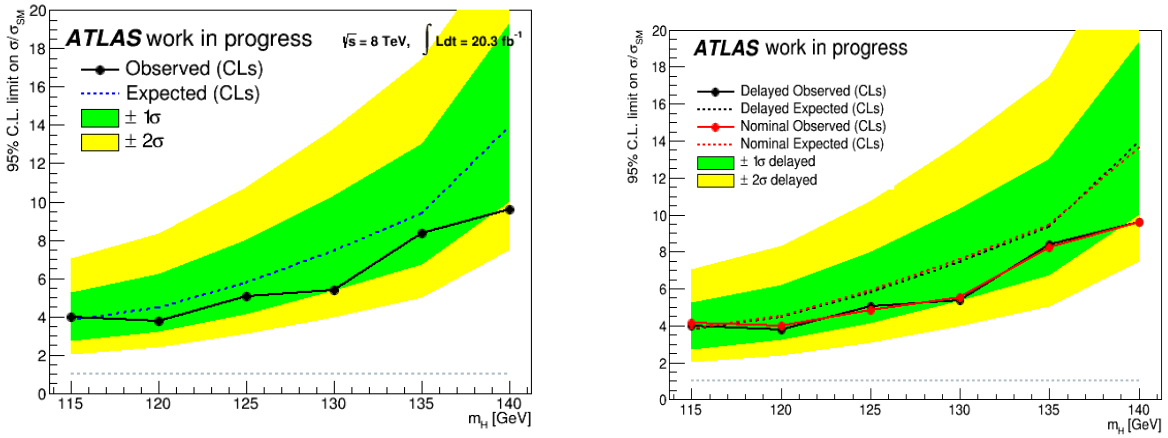

Figure 5.22: Plots of confidence levels for signal strength in terms of Higgs mass for first $E_{\mathrm{T}}^{\mathrm{miss}}$ bin using delayed stream implementation (left) and compared to nominal analysis (right). The 1σ and 2σ variation bands of the analysis with delayed stream trigger are also included.

mass [GeV]	Exp.	$+2\sigma$	$+1\sigma$	-1σ	-2σ	Obs.
115	3.79	7.07	5.28	2.73	2.04	4.00
120	4.48	8.35	6.23	3.23	2.40	3.76
125	5.77	10.76	8.03	4.16	3.10	5.03
130	7.44	13.87	10.35	5.36	3.99	5.36
135	9.36	17.47	13.03	6.75	5.03	8.38
140	13.92	25.97	19.38	10.03	7.47	9.61

Table 5.19: Expected, observed values and their $1{+}2\sigma$ variations of limit on μ in first $E_{\mathrm{T}}^{\mathrm{miss}}$ bin for analysis using delayed stream trigger.

mass [GeV]	Exp.	$+2\sigma$	$+1\sigma$	-1σ	-2σ	Obs.
115	3.84	7.17	5.35	2.77	2.06	4.14
120	4.53	8.46	6.31	3.27	2.43	3.99
125	5.89	10.99	8.19	4.24	3.16	4.86
130	7.57	14.12	10.53	5.45	4.06	5.54
135	9.45	17.63	13.15	6.81	5.07	8.20
140	13.65	25.47	19.00	9.84	7.33	9.62

Table 5.20: Expected, observed values and their $1+2\sigma$ variations of limit on μ in first $E_{\mathrm{T}}^{\mathrm{miss}}$ bin for analysis using nominal triggers.

5.11.3 0-lepton analysis with all $E_{\mathrm{T}}^{\mathrm{miss}}$ bin

Like the previous section, the evaluation of the limit on μ is implemented in the two analyses: one with delayed stream trigger included and one with the official analysis. In this section we will also present the results of p_0 values. Figure 5.23 and Tables 5.21, 5.22 show the results of the limit obtained in function of Higgs mass with range from 115 GeV to 140 GeV (with 5 GeV bin). The expected limit on μ for analysis using delayed stream trigger is ranged from 1.17 to 3.95, and from 1.17 to 3.44 for using nominal triggers at 95% of confidence level. The limit on m_H=125 GeV, the expected limit is 1.59 for using delayed stream trigger, and 1.61 for using nominal triggers. The two analyses show very close results.

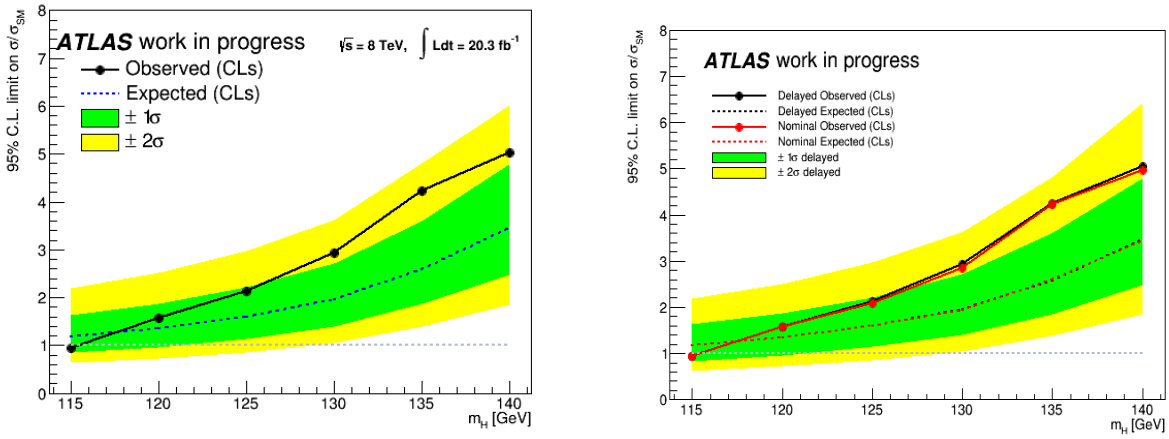

Figure 5.23: Plots of confidence levels for signal strength in terms of Higgs mass for all $E_{\mathrm{T}}^{\mathrm{miss}}$ bins using delayed stream implementation (left) and compared to nominal analysis (right). The 1σ and 2σ variation bands for analysis with delayed stream trigger are also included.

According to these results, the implementation of delayed stream trigger is consistent with the nominal analysis.

The results for p_0 value (the observed probability for background processes to provide results that look like the Higgs signal's, see section 5.10.2) in terms of Higgs boson mass

mass [GeV]	Exp.	$+2\sigma$	$+1\sigma$	-1σ	-2σ	Obs.
115	1.17	2.19	1.63	0.84	0.63	0.94
120	1.35	2.51	1.87	0.97	0.72	1.57
125	1.59	2.97	2.21	1.15	0.85	2.12
130	1.95	3.63	2.71	1.40	1.04	2.92
135	2.58	4.82	3.60	1.86	1.39	4.24
140	3.45	6.43	4.80	2.48	1.85	5.04

Table 5.21: Expected, observed values and their $1{+}2\sigma$ variations of limit on μ including all $E_{\mathrm{T}}^{\mathrm{miss}}$ bins for analysis using delayed stream trigger.

mass [GeV]	Exp.	$+2\sigma$	$+1\sigma$	-1σ	-2σ	Obs.
115	1.17	2.19	1.63	0.85	0.63	0.93
120	1.34	2.50	1.86	0.96	0.72	1.58
125	1.60	2.99	2.23	1.15	0.86	2.09
130	1.94	3.63	2.71	1.40	1.04	2.85
135	2.59	4.84	3.61	1.87	1.39	4.23
140	3.44	6.42	4.79	2.48	1.85	4.97

Table 5.22: Expected, observed values and their $1{+}2\sigma$ variations of limit on μ including all $E_{\mathrm{T}}^{\mathrm{miss}}$ bins for analysis using nominal triggers.

are shown in Fig. 5.24 and Table 5.23. The expected p_0 at m_H=125 GeV is at 0.93% for analysis using delayed stream trigger and 0.96% using nominal triggers. This corresponds to an excess expected with a significance of $\sim 1.3\sigma$ for the analysis using the delayed stream. The observed value shows the excess of 0.9σ using delayed stream trigger.

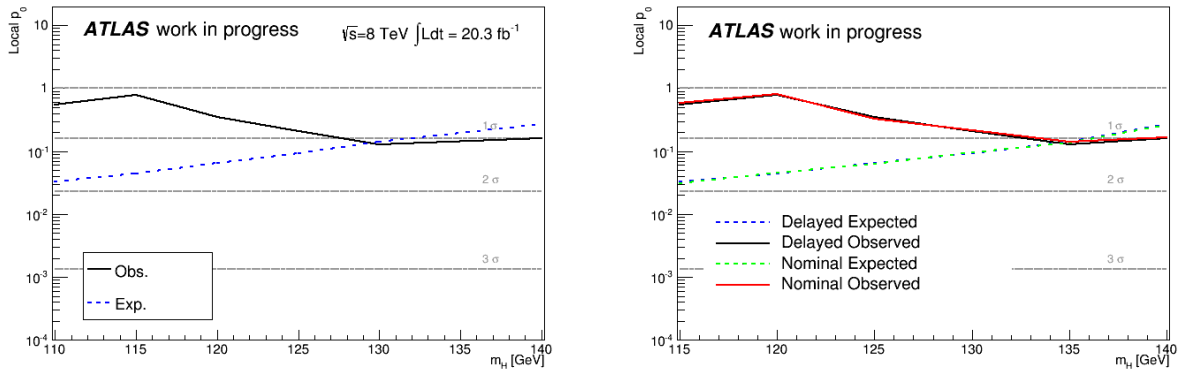

Figure 5.24: Expected, observed values of p_0 as function of Higgs mass in 0-lepton channel including all $E_{\mathrm{T}}^{\mathrm{miss}}$ bins for analysis using delayed stream trigger (left) and compared with nominal triggers (right)

mass [GeV]	delayed stream		nominal	
	Exp p_0	Obs p_0	Exp p_0	Obs p_0
110	0.03244	0.54291	0.03062	0.59031
115	0.04466	0.78582	0.04518	0.79482
120	0.06425	0.34551	0.06312	0.3315
125	0.09349	0.2078	0.09575	0.21271
130	0.13873	0.12672	0.13837	0.14129
140	0.26465	0.15881	0.26445	0.16634

Table 5.23: Expected and observed values of p_0 in 0-lepton channel including all $E_{\mathrm{T}}^{\mathrm{miss}}$ bins for analysis using delayed stream trigger and nominal triggers.

Conclusion

The main work of this thesis is to search for the Standard Model Higgs boson in the decay channel $ZH \to \nu\bar{\nu}b\bar{b}$ channel. This search is done with the data provided by the LHC and collected by the ATLAS detector with an integrated luminosity of 20.3 fb^{-1} in the year of 2012. This Higgs analysis is concerned by:

- Higgs decay channel $H \to b\bar{b}$, therefore the identification of jets originating from b-quark is vital, which lead to the study of b-tagging algorithms.
- Z boson decay channel $Z \to \nu\bar{\nu}$: the two neutrinos go undetected in the ATLAS detector, leaving missing transverse energy behind. So improving the $E_{\text{T}}^{\text{miss}}$ trigger is also important for this analysis: we use the new trigger available in the delayed stream of data, which is expected to increase the signal acceptance.

Regarding the b-tagging algorithm performance study, we made our study of b-tagging performance using the new track-to-jet association: the ghost-association. The ghost-association provides a different approach that can help us deal with the situation where high pile-up and jet substructure are expected, especially in collisions with high luminosity and high center-of-mass energy. This kind of association suggested some improvements to the b-tagging performance. If the b-tagging algorithms using ghost-association of track on jet is re-calibrated, we can expect a higher b-tagging performance and therefore this can become one of the main track-to-jet association algorithm in ATLAS for the Run 2.

In the $E_{\text{T}}^{\text{miss}}$ trigger study, we introduced the new $E_{\text{T}}^{\text{miss}}$ trigger called delayed stream trigger, which is expected to help gaining signal acceptance in the analysis. Such trigger needs deriving data/MC scale factor in order to be applied in the analysis and for that purpose, we needed parametrisation of trigger turn–ons. The results showed that our model of parametrisation and scale factor is good. The further study proved that the parametrization can be extracted on one sample, $W \to \mu\nu$+jets, thanks to its high number of events, so the statistical uncertainty is reduced. The $E_{\text{T}}^{\text{miss}}$ trigger study also showed some trigger dependence on certain kinematic variables, and a method was provided to treat these dependences and maintain high signal acceptance and sensitivity. Those treatments of trigger dependences are approved and applied in the main Higgs analysis in 0-lepton channel, currently under collaboration review, for publication this fall [112]. The uncertainty estimation of $E_{\text{T}}^{\text{miss}}$ trigger was done with overall small variations. The delayed stream trigger was also prepared to be used in the analysis, but this improvement was eventually dropped from the official analysis because of time constraints.

Profiting from the delayed stream $E_{\text{T}}^{\text{miss}}$ trigger, we applied it to the Higgs analysis in 0-lepton channel. We made the comparison between the analysis using delayed stream trigger

with the one using nominal triggers. There was a mis-modelling observed in the analysis using nominal triggers. However using the delayed stream trigger inclusively does not improve the modelling. The tighter cut on $E_{\mathrm{T}}^{\mathrm{miss}}$ at 100 GeV was applied to prevent the affect of this mis-modelling in the analysis. The results showed good agreement between data and MC for both analyses, and the implementation of delayed stream trigger marginally helped our analysis gain a bit more signal significance, but not significantly high ($\sim$3% of signal acceptance and $\sim$1% of signal sensitivity higher than the analysis with nominal triggers for pre-fit). The statistical analysis showed that using delayed stream trigger can provide better (although small, around 1%) limit on signal strength of Higgs boson in the first $E_{\mathrm{T}}^{\mathrm{miss}}$ bin exclusively. However, the results of the two analyses become consistent when all the $E_{\mathrm{T}}^{\mathrm{miss}}$ bins are included. The expected p_0 is about 1.3σ for both analyses.

Bibliography

[1] E. Schrödinger, *An Undulatory Theory of the Mechanics of Atoms and Molecules*, Physical Review **28** (1926) 1049–1070.

[2] M. Born, W. Heisenberg, and P. Jordan, *Zur Quantenmechanik. II.*, Zeitschrift fur Physik **35** (1926) 557–615.

[3] P. A. M. Dirac, *The Quantum Theory of the Electron*, Royal Society of London Proceedings Series A **117** (1928) 610–624.

[4] R. Feynman, *Space-time approach to nonrelativistic quantum mechanics*, Rev.Mod.Phys. **20** (1948) 367–387.

[5] J. S. Schwinger, *Quantum electrodynamics. I. A covariant formulation*, Phys.Rev. **74** (1948) 1439.

[6] S. Tomonaga, *On a Relativistically Invariant Formulation of the Quantum Theory of Wave Fields*, Progress of Theoretical Physics **1** no. 2, (1946) 27–42.

[7] E. Fermi, *Trends to a Theory of beta Radiation. (In Italian)*, Nuovo Cim. **11** (1934) 1–19.

[8] S. Glashow, *Partial Symmetries of Weak Interactions*, Nucl.Phys. **22** (1961) 579–588.

[9] S. Weinberg, *A Model of Leptons*, Phys.Rev.Lett. **19** (1967) 1264–1266.

[10] A. Salam, *Weak and Electromagnetic Interactions*, Conf.Proc. **C680519** (1968) 367–377.

[11] K. G. Wilson, *Confinement of Quarks*, Phys.Rev. **D10** (1974) 2445–2459.

[12] D. J. Gross and F. Wilczek, *Ultraviolet Behavior of Nonabelian Gauge Theories*, Phys.Rev.Lett. **30** (1973) 1343–1346.

[13] D. Gross and F. Wilczek, *Asymptotically Free Gauge Theories. 1*, Phys.Rev. **D8** (1973) 3633–3652.

[14] H. D. Politzer, *Reliable Perturbative Results for Strong Interactions?*, Phys.Rev.Lett. **30** (1973) 1346–1349.

[15] M. Gell-Mann and Y. Ne'emam, *The Eightfold way: a review with a collection of reprints*, ISBN-9780738202990, ISBN-9781114735705, W.A. Benjamin, 1964.

[16] M. Gell-Mann, *A schematic model of baryons and mesons*, Physics Letters **8** (1964) 214–215.

[17] G. Zweig, *An SU(3) model for strong interaction symmetry and its breaking. Version 1*, CERN-TH-401, 1964.

[18] S. L. Glashow, J. Iliopoulos, and L. Maiani, *Weak Interactions with Lepton-Hadron Symmetry*, prd **2** (1970) 1285–1292.

[19] SLAC-SP-017 Collaboration, J. Augustin et al., *Discovery of a Narrow Resonance in e+ e- Annihilation*, Phys.Rev.Lett. **33** (1974) 1406–1408.

[20] E598 Collaboration, J. Aubert et al., *Experimental Observation of a Heavy Particle J*, Phys.Rev.Lett. **33** (1974) 1404–1406.

[21] J. Christenson, J. Cronin, V. Fitch, and R. Turlay, *Evidence for the 2 pi Decay of the k(2)0 Meson*, Phys.Rev.Lett. **13** (1964) 138–140.

[22] M. Kobayashi and T. Maskawa, *CP Violation in the Renormalizable Theory of Weak Interaction*, Prog.Theor.Phys. **49** (1973) 652–657.

[23] S. Herb et al., *Observation of a Dimuon Resonance at 9.5 GeV in 400-GeV Proton-Nucleus Collisions*, Phys. Rev. Lett. **39** (1977) 252–255.

[24] CDF Collaboration, F. Abe et al., *Observation of top quark production in $\bar{p}p$ collisions*, Phys.Rev.Lett. **74** (1995) 2626–2631, arXiv:hep-ex/9503002 [hep-ex].

[25] D0 Collaboration, S. Abachi et al., *Search for high mass top quark production in $p\bar{p}$ collisions at $\sqrt{s} = 1.8$ TeV*, Phys.Rev.Lett. **74** (1995) 2422–2426, arXiv:hep-ex/9411001 [hep-ex].

[26] UA1 Collaboration, G. Arnison et al., *Experimental Observation of Isolated Large Transverse Energy Electrons with Associated Missing Energy at $\sqrt{s} = 540$-GeV*, Phys.Lett. **B122** (1983) 103–116.

[27] UA2 Collaboration, M. Banner et al., *Observation of Single Isolated Electrons of High Transverse Momentum in Events with Missing Transverse Energy at the CERN anti-p p Collider*, Phys.Lett. **B122** (1983) 476–485.

[28] Particle Data Group Collaboration, J. Beringer et al., *Review of Particle Physics (RPP)*, Phys.Rev. **D86** (2012) 010001.

[29] "Neutrino properties." http://pdg.lbl.gov/2012/listings/rpp2012-list-neutrino-prop.pdf.

[30] D. Griffiths, *Introduction to elementary particles*, ISBN-9783527406012, Wiley, 2008.

[31] G. 't Hooft and M. Veltman, *Regularization and renormalization of gauge fields*, Nuclear Physics B **44** (1972) 189–213.

[32] Super-Kamiokande Collaboration, Y. Fukuda et al., *Measurements of the solar neutrino flux from Super-Kamiokande's first 300 days*, Phys.Rev.Lett. **81** (1998) 1158–1162, arXiv:hep-ex/9805021 [hep-ex].

[33] F. Englert and R. Brout, *Broken Symmetry and the Mass of Gauge Vector Mesons*, Phys.Rev.Lett. **13** (1964) 321–323.

[34] P. W. Higgs, *Broken symmetries, massless particles and gauge fields*, Phys.Lett. **12** (1964) 132–133.

[35] P. W. Higgs, *Broken Symmetries and the Masses of Gauge Bosons*, Phys. Rev. Lett. **13** (1964) 508–509.

[36] N. Cabibbo, *Unitary Symmetry and Leptonic Decays*, Phys.Rev.Lett. **10** (1963) 531–533.

[37] B. Pontecorvo, *Neutrino Experiments and the Problem of Conservation of Leptonic Charge*, Sov.Phys.JETP **26** (1968) 984–988.

[38] Z. Maki, M. Nakagawa, and S. Sakata, *Remarks on the unified model of elementary particles*, Prog.Theor.Phys. **28** (1962) 870–880.

[39] J. Goldstone, A. Salam, and S. Weinberg, *Broken Symmetries*, Phys.Rev. **127** (1962) 965–970.

[40] N. Cabibbo, L. Maiani, G. Parisi, and R. Petronzio, *Bounds on the Fermions and Higgs Boson Masses in Grand Unified Theories*, Nucl.Phys. **B158** (1979) 295–305.

[41] A. Djouadi, *The Anatomy of electro-weak symmetry breaking. I: The Higgs boson in the standard model*, Phys.Rept. **457** (2008) 1–216, arXiv:hep-ph/0503172 [hep-ph].

[42] LEP Working Group for Higgs boson searches, ALEPH Collaboration, DELPHI Collaboration, L3 Collaboration, OPAL Collaboration, R. Barate et al., *Search for the standard model Higgs boson at LEP*, Phys.Lett. **B565** (2003) 61–75, arXiv:hep-ex/0306033 [hep-ex].

[43] CDF Collaboration, D0 Collaboration, T. Aaltonen et al., *Higgs Boson Studies at the Tevatron*, Phys.Rev. **D88** no. 5, (2013) 052014, arXiv:1303.6346 [hep-ex].

[44] A. Sopczak, *Highlights of Current Higgs Boson Searches*, arXiv:1011.0681 [hep-ph].

[45] LHC Higgs Cross Section Working Group Collaboration, S. Heinemeyer et al., *Handbook of LHC Higgs Cross Sections: 3. Higgs Properties*, arXiv:1307.1347 [hep-ph].

[46] ATLAS Collaboration, *Observation of a new particle in the search for the Standard Model Higgs boson with the ATLAS detector at the LHC*, Phys.Lett. **B716** (2012) 1–29, arXiv:1207.7214 [hep-ex].

[47] CMS Collaboration, *Observation of a new boson at a mass of 125 GeV with the CMS experiment at the LHC*, Phys.Lett. **B716** (2012) 30–61, arXiv:1207.7235 [hep-ex].

[48] ATLAS Collaboration, *Evidence for Higgs Boson Decays to the $\tau^+\tau^-$ Final State with the ATLAS Detector*, ATLAS-CONF-2013-108, 2013.

[49] CMS Collaboration, *Evidence for the 125 GeV Higgs boson decaying to a pair of τ leptons*, JHEP **1405** (2014) 104, arXiv:1401.5041 [hep-ex].

[50] ATLAS Collaboration, *Updated coupling measurements of the Higgs boson with the ATLAS detector using up to 25 fb^{-1} of proton-proton collision data*, ATLAS-CONF-2014-009, 2014.

[51] J. M. Campbell, J. Huston, and W. Stirling, *Hard Interactions of Quarks and Gluons: A Primer for LHC Physics*, Rept.Prog.Phys. **70** (2007) 89, arXiv:hep-ph/0611148 [hep-ph].

[52] ATLAS Collaboration, *ATLAS inner detector: Technical design report. Vol. 2*, CERN-LHCC-97-17, 1997.

[53] ATLAS Collaboration, *ATLAS inner detector: Technical design report. Vol. 1*, CERN-LHCC-97-16, ATLAS-TDR-4, 1997.

[54] A. Abdesselam et al., *The integration and engineering of the ATLAS SemiConductor Tracker barrel*, JINST **3** (2008) P10006.

[55] ATLAS Collaboration, A. Abdesselam et al., *The ATLAS semiconductor tracker end-cap module*, Nucl.Instrum.Meth. **A575** (2007) 353–389.

[56] ATLAS TRT Collaboration, E. Abat et al., *The ATLAS TRT barrel detector*, JINST **3** (2008) P02014.

[57] ATLAS Collaboration, *ATLAS calorimeter performance Technical Design Report*, CERN-LHCC-96-40, 1996.

[58] ATLAS Collaboration, *ATLAS first level trigger: Technical design report*, CERN-LHCC-98-14, ATLAS-TDR-12, 1998.

[59] ATLAS Collaboration, *Expected Performance of ATLAS Detector, Trigger and Physics*, CERN-OPEN-2008-020, 2008.

[60] G. Blazey et al., *Run II jet physics*, arXiv:hep-ex/0005012 [hep-ex].

[61] M. Cacciari, G. P. Salam, and G. Soyez, *The Anti-k_t jet clustering algorithm*, JHEP **0804** (2008) 063, arXiv:0802.1189 [hep-ph].

[62] M. Cacciari and G. P. Salam, *Dispelling the N^3 myth for the k_t jet-finder*, Phys.Lett. **B641** (2006) 57–61, arXiv:hep-ph/0512210 [hep-ph].

[63] ATLAS Collaboration, *Jet energy scale and its systematic uncertainty in proton-proton collisions at sqrt(s)=7 TeV with ATLAS 2011 data*, ATLAS-CONF-2013-004, 2013.

[64] M. Cacciari, G. P. Salam, and G. Soyez, *The Catchment Area of Jets*, JHEP **0804** (2008) 005, arXiv:0802.1188 [hep-ph].

[65] R. Zaidan, *Recherche du boson de Higgs chargé dans le canal $H+ \to tb$ et étiquetage des jets b avec l'expérience ATLAS auprès du LHC.* PhD thesis, 2009.

[66] ATLAS Collaboration, *Performance of the ATLAS Secondary Vertex b-tagging Algorithm in 7 TeV Collision Data*, ATLAS-CONF-2010-042, 2010.

[67] G. Piacquadio, *Identification of b-jets and investigation of the discovery potential of a Higgs boson in the $WH \to l\nu b\bar{b}$ channel with the ATLAS experiment.* PhD thesis, Freiburg U., Freiburg, 2010. Presented on 11 Jan 2010.

[68] G. Piacquadio and C. Weiser, *A new inclusive secondary vertex algorithm for b-jet tagging in ATLAS*, J.Phys.Conf.Ser. **119** (2008) 032032.

[69] ATLAS Collaboration, *Measurement of the b-tag Efficiency in a Sample of Jets Containing Muons with 5 fb^{-1} of Data from the ATLAS Detector*, ATLAS-CONF-2012-043, 2012.

[70] ATLAS Collaboration, *Calibration of b-tagging using dileptonic top pair events in a combinatorial likelihood approach with the ATLAS experiment*, ATLAS-CONF-2014-004, 2014.

[71] ATLAS Collaboration, *Calibration of the performance of b-tagging for c and light-flavour jets in the 2012 ATLAS data*, ATLAS-CONF-2014-046, 2014.

[72] ATLAS Collaboration, *Calibration of the b-tagging efficiency for c jets with the ATLAS detector using events with a W boson produced in association with a single c quark*, ATLAS-CONF-2013-109, 2013.

[73] I. Burmeister et al., *Measurement of the b-tagging performance in the 2012 ATLAS data*, ATL-COM-PHYS-2013-456, 2013.

[74] P. Berta et al., *Continuous b-tagging for the ATLAS experiment*, ATL-COM-PHYS-2014-035, 2014.

[75] ATLAS Collaboration, *Measurement of the $W \to \ell\nu$ and $Z/\gamma^* \to \ell\ell$ production cross sections in proton-proton collisions at $\sqrt{s} = 7$ TeV with the ATLAS detector*, JHEP **1012** (2010) 060, arXiv:1010.2130 [hep-ex].

[76] ATLAS Collaboration, *Measurement of the top quark pair production charge asymmetry in proton-proton collisions at $\sqrt{s} = 7$ TeV using the ATLAS detector*, JHEP **1402** (2014) 107, arXiv:1311.6724 [hep-ex].

[77] ATLAS Collaboration, *Performance of Missing Transverse Momentum Reconstruction in Proton-Proton Collisions at 7 TeV with ATLAS*, Eur.Phys.J. **C72** (2012) 1844, arXiv:1108.5602 [hep-ex].

[78] ATLAS Collaboration, *Measurement of the missing transverse momentum based on tracks in proton-proton collisions at $\sqrt{s}$ = 900 GeV centre-of-mass energy with the ATLAS detector*, ATLAS-CONF-2010-020, 2010.

[79] ATLAS Collaboration, *Performance of Missing Transverse Momentum Reconstruction in ATLAS studied in Proton-Proton Collisions recorded in 2012 at 8 TeV*, ATLAS-CONF-2013-082, 2013.

[80] ATLAS Collaboration, *Performance of the ATLAS Trigger System in 2010*, Eur.Phys.J. **C72** (2012) 1849, arXiv:1110.1530 [hep-ex].

[81] D. Casadei et al., *The implementation of the ATLAS missing Et triggers for the initial LHC operation*, ATL-DAQ-PUB-2011-001, 2011.

[82] B. A. Petersen, *The ATLAS Trigger Performance and Evolution*, PoS **ICHEP2012** (2013) 493.

[83] ATLAS Collaboration, *Search for the bb decay of the Standard Model Higgs boson in associated W/ZH production with the ATLAS detector*, ATLAS-CONF-2013-079, 2013.

[84] ATLAS Collaboration, *The ATLAS Simulation Infrastructure*, Eur. Phys. J. **C70** (2010) 823–874, arXiv:1005.4568 [physics.ins-det].

[85] GEANT4 Collaboration, S. Agostinelli et al., *GEANT4: A simulation toolkit*, Nucl. Instrum. Meth. **A506** (2003) 250–303.

[86] S. Alioli, P. Nason, C. Oleari, and E. Re, *NLO Higgs boson production via gluon fusion matched with shower in POWHEG*, JHEP **0904** (2009) 002, arXiv:0812.0578 [hep-ph].

[87] T. Sjostrand, S. Mrenna, and P. Z. Skands, *PYTHIA 6.4 Physics and Manual*, JHEP **0605** (2006) 026, arXiv:hep-ph/0603175 [hep-ph].

[88] B. P. Kersevan and E. Richter-Was, *The Monte Carlo event generator AcerMC versions 2.0 to 3.8 with interfaces to PYTHIA 6.4, HERWIG 6.5 and ARIADNE 4.1*, Comput.Phys.Commun. **184** (2013) 919–985, arXiv:hep-ph/0405247 [hep-ph].

[89] T. Gleisberg et al., *Event generation with SHERPA 1.1*, JHEP **0902** (2009) 007, arXiv:0811.4622 [hep-ph].

[90] ATLAS Collaboration, *Preliminary results on the muon reconstruction efficiency, momentum resolution, and momentum scale in ATLAS 2012 pp collision data*, ATLAS-CONF-2013-088.

[91] H.-L. Lai et al., *New parton distributions for collider physics*, Phys.Rev. **D82** (2010) 074024, arXiv:1007.2241 [hep-ph].

[92] J. Pumplin et al., *New generation of parton distributions with uncertainties from global QCD analysis*, JHEP **0207** (2002) 012, arXiv:hep-ph/0201195 [hep-ph].

[93] J. Ohnemus and W. J. Stirling, *Order alpha-s corrections to the differential cross-section for the W H intermediate mass Higgs signal*, Phys.Rev. **D47** (1993) 2722–2729.

[94] H. Baer, B. Bailey, and J. F. Owens, $O(\alpha_s)$ *Monte Carlo approach to W+ Higgs-boson associated production at hadron supercolliders*, Phys. Rev. D **47** (1993) 2730–2734.

[95] O. Brein, A. Djouadi, and R. Harlander, *NNLO QCD corrections to the Higgs-strahlung processes at hadron colliders*, Phys.Lett. **B579** (2004) 149–156, arXiv:hep-ph/0307206 [hep-ph].

[96] M. Ciccolini, S. Dittmaier, and M. Kramer, *Electroweak radiative corrections to associated WH and ZH production at hadron colliders*, Phys.Rev. **D68** (2003) 073003, arXiv:hep-ph/0306234 [hep-ph].

[97] ATLAS Collaboration, *Electron efficiency measurements with the ATLAS detector using the 2012 LHC proton-proton collision data*, ATLAS-CONF-2014-032, 2014.

[98] ATLAS Collaboration, *Electron reconstruction and identification efficiency measurements with the ATLAS detector using the 2011 LHC proton-proton collision data*, Eur.Phys.J. **C74** (2014) 2941, arXiv:1404.2240 [hep-ex].

[99] ATLAS Collaboration, *Jet energy measurement with the ATLAS detector in proton-proton collisions at* $\sqrt{s} = 7$ *TeV*, Eur.Phys.J. **C73** (2013) 2304, arXiv:1112.6426 [hep-ex].

[100] D. Jamin, *Search for the Higgs boson in the* $ZH \to \nu\nu bb$ *channel: Development of a b-tagging method based on soft muons*. PhD thesis, 2010.

[101] F. Ahmadov et al., *Supporting Document for the Search for the bb decay of the Standard Model Higgs boson in associated (W/Z)H production with the ATLAS detector*, ATL-COM-PHYS-2014-051, CERN, 2014.

[102] ATLAS Collaboration, *Improved luminosity determination in pp collisions at* $\sqrt{s} = 7$ *TeV using the ATLAS detector at the LHC*, Eur.Phys.J. **C73** (2013) 2518, arXiv:1302.4393 [hep-ex].

[103] ATLAS Collaboration, *Electron performance measurements with the ATLAS detector using the 2010 LHC proton-proton collision data*, Eur.Phys.J. **C72** (2012) 1909, arXiv:1110.3174 [hep-ex].

[104] ATLAS Collaboration, *Preliminary results on the muon reconstruction efficiency, momentum resolution, and momentum scale in ATLAS 2012 pp collision data*, ATLAS-CONF-2013-088, 2013.

[105] ATLAS Collaboration, *Jet energy measurement and its systematic uncertainty in proton-proton collisions at $\sqrt{s} = 7$ TeV with the ATLAS detector*, submitted to Eur.Phys.J. C (2014), arXiv:1406.0076 [hep-ex].

[106] ATLAS Collaboration, *Jet energy resolution in proton-proton collisions at $\sqrt{s} = 7$ TeV recorded in 2010 with the ATLAS detector*, Eur.Phys.J. **C73** (2013) 2306, arXiv:1210.6210 [hep-ex].

[107] ATLAS Collaboration, *Measurements of normalized differential cross-sections for $t\bar{t}$ production in pp collisions at $\sqrt{s}$=7 TeV using the ATLAS detector*, submitted to Phys. Rev. D (2014), arXiv:1407.0371 [hep-ex].

[108] N. Kidonakis, *Differential and total cross sections for top pair and single top production*, arXiv:1205.3453 [hep-ph].

[109] L. Moneta et al., *The RooStats Project*, arXiv:1009.1003.

[110] W. Verkerke and D. Kirkby, *The RooFit toolkit for data modeling*, physics/0306116.

[111] G. Cowan, K. Cranmer, E. Gross, and O. Vitells, *Asymptotic formulae for likelihood-based tests of new physics*, Eur.Phys.J. **C71** (2011) 1554, arXiv:1007.1727 [physics.data-an].

[112] ATLAS Collaboration, *Search for the $b\bar{b}$ decay of the Standard Model Higgs boson in associated $(W/Z)H$ production with the ATLAS detector*, submitted to JHEP (2014), arXiv:1409.6212 [hep-ex].